Trous noirs et leurs perturbations dans la recherche d'une nouvelle physique

Anna Chrysostomou

THÈSE de DOCTORAT DE L'UNIVERSITÉ DE LYON

Opérée au sein de

l'Université Claude Bernard Lyon 1 – France

en cotutelle avec

l'Université de Johannesburg – Afrique du Sud

Ecole Doctorale N° ED 52
Physique et Astrophysique de Lyon (PHAST)

Discipline : Physique

Soutenue publiquement le 11/06/2024, par :

Anna Chrysostomou

Black holes and their perturbations in the search for new physics

---

Devant le jury composé de :

MAHMOUDI Farvah (Professeure des Universités, Université Lyon 1)	**Présidente**
BENAKLI Karim (Chercheur CNRS, Université Paris Sorbonne)	**Rapporteur**
KONOPLYA Roman (Professeur des Universités, Silesian University)	**Rapporteur**
HOROWITZ William (Professeur des Universités, University of Cape Town)	**Examinateur**
SORDINI Viola (Chercheuse CNRS, Université Lyon 1)	**Examinatrice**
TONAZZO Alessandra (Professeure des Universités, Université Paris Diderot)	**Examinatrice**
DEANDREA Aldo (Professeur des Universités, Université Lyon 1)	**Directeur de thèse**
CORNELL Alan (Professeur des Universités, University of Johannesburg)	**Co-Directeur de thèse**

ὁ Ὁ βίος βραχύς, ἡ δὲ τέχνη μακρή

Life is short; the craft is long

Declaration of Authorship

I hereby declare that, except where specific reference is made to the work of others, the contents of this dissertation are authentic and original; they have not been submitted in whole or in part for the consideration for any other degree or qualification in these or any other universities.

Anna Chrysostomou
2118165 | 220024472
June 2024

The work presented in this thesis is based on the following manuscripts and publications produced during the course of the student's PhD studies (July 2021 - June 2024).

1. C. Chen, H. T. Cho, A. Chrysostomou, and A. S. Cornell, "A semi-analytic treatment of quasinormal excitation factors in the eikonal regime", arXiv: 2407.18644 [gr-qc]

2. A. Chrysostomou, A. S. Cornell, A. Deandrea, H. Noshad, and S. C. Park, "Reissner-Nordström black holes in de Sitter space-time: bounds with quasinormal frequencies", *Submitted to PRD*, arXiv:2310.07311 [gr-qc]

3. A. Chrysostomou, A. S. Cornell, A. Deandrea, E. Ligout, and D. Tsimpis, "Black holes and nilmanifolds: quasinormal modes as fingerprints of extra dimensions?", *Eur. Phys. J. C 83, 325 (2023)*, arXiv:2211.08489 [gr-qc]

Posters, talks, and conference proceedings have not been included in this list. Collaborators and references used have been cited accordingly. Except for guidance in the translation of the abstract into French, no artificial intelligence tools were used in the writing of this thesis or any work derived from it.

Black holes and their perturbations in the search for new physics

Anna Chrysostomou

Abstract

Black hole quasinormal modes (QNMs) serve as an indispensable tool in the study of (semi-) classical and alternative theories of gravity, capable of describing the intricate dynamics of perturbed black hole systems and of fully characterising their black hole source. Since their identification in the 1970s, QNMs and their corresponding complex quasinormal frequencies (QNFs) have provided insight into the nature of singularities, the stability of black hole space-times, and the validity of principles like cosmic censorship and the no-hair conjecture that pervade general relativity (GR) but remain without formal mathematical proof. Within the newly-established era of gravitational-wave (GW) astronomy, we can exploit the phenomenological applications of the extant theoretical QNM framework; we can perform quantitative analyses of GWs emitted in the wake of black hole merger events and employ these in searches for new physics.

We explore these ideas within this thesis, in the context of fixed spherically-symmetric black hole backgrounds upon which a scalar test field propagates. In this vein, we seek to understand how parameters from the black hole space-time and the propagating field influence the QNF spectrum, the constraints we can derive as a result, and whether QNMs can be used in the search for extra dimensions.

We focus on three space-times in particular: the Schwarzschild black hole, which we choose for its simple structure; the charged Reissner-Nordström background embedded in an asymptotically-de Sitter space-time, which reflects the most complicated spherically-symmetric background with GR; an extra-dimensional space-time made up of a Schwarzschild black hole embedded in a space-time of mixed curvature.

Within the Schwarzschild space-time, we investigate the influence of a field mass on the scalar QNF spectrum, where an upper bound can be derived beyond which QNMs fail to propagate. The corresponding QNFs lie in the quasiresonance regime, related to the phenomenon of superradiance.

As an additional investigation within the Schwarzschild space-time, we extend our analysis of the semi-classical tools used to compute QNFs to the computation of the QNM wavefunction and "quasinormal excitation factor" (QNEF). Since tests of GR are mode-specific, QNEFs provide a measurement of relative excitation required to identify a particular mode within the detected GW spectrum that is independent of the black hole's initial perturbing stimulus. In section 2.4, we discuss the procedure we have developed to construct higher-order QNEFs, based on the Dolan-Ottewill and Schutz-Iyer-Will formalisms.

We then expand our interrogation of the effect of field and black hole parameters on the QNFs by examining the QNF spectrum of a spin-0 field with mass μ and charge q within the Reissner-Nordström de Sitter (RNdS) black hole space-time with mass M, charge Q, and cosmological constant $\Lambda > 0$. Using a phase space diagram, we show how the cosmological constant enforces upper limits on the black hole mass and charge. With this diagram, we review the Weak Gravity Conjecture (WGC) that extracts mass and charge constraints from black hole mechanics, the Festina-Lente (FL) bound that provides a lower bound of field mass and charge from black hole decay processes, and the cosmic censorship conjectures that preserve the deterministic nature of GR.

Through a semi-classical computation method tailored to the calculation of charged and massive scalar QNMs in the RNdS black hole background, we show how QNFs evolve within the phase space; we demonstrate regular and anomalous QNF behaviour and its dependence on black hole and field parameters. In particular, we focus on the application of this QNM analysis in the study of stability, superradiance, and cosmic censorship violations within extremised regions of the RNdS black hole. We find regions in the phase space predisposed to superradiance, as well as QNFs in violation of cosmic censorship.

Our final investigation is focused on the search for signatures of new physics using GWs from binary black hole collisions. We investigate an extra-dimensional model of mixed curvature whose higher-dimensional manifold is a compact negative space. Specifically, we are concerned with a product space comprised of a

four-dimensional Schwarzschild black hole space-time and a three-dimensional nilmanifold (twisted torus). We show how we can model the black hole perturbations as a scalar test field, with the extra-dimensional geometry stylised in the QNM effective potential as a squared mass-like term representing a Kaluza–Klein tower of states. This allows us to apply our understanding of massive QNMs to the search for new physics.

Finally, we consider how GW data from the LIGO-Virgo-KAGRA Collaboration can be incorporated in QNMs studies of extra dimensions. As a proof of concept, we demonstrate how parametric deviations from GR can be used in the search for new physics with QNMs. For more stringent limits, we compare the QNF spectrum for the "Schwarzschild-nilmanifold model" against the hierarchical tests of GR performed by the LIGO-Virgo-KAGRA Collaboration to determine a possible "detectability bound" beyond which extra dimensions cannot be detected using QNFs.

Trous noirs et leurs perturbations dans la recherche d'une nouvelle physique

Anna Chrysostomou

Résumé

Les modes quasi-normaux des trous noirs constituent un outil indispensable dans l'étude des théories (semi-)classiques et alternatives de la gravité, capables de décrire la dynamique complexe des systèmes de trous noirs perturbés et de caractériser pleinement les sources des trous noirs. Depuis leur introduction dans les années 1970, les modes quasi-normaux et leurs fréquences complexes, ont permis de mieux comprendre la nature des singularités, la stabilité des espaces-temps des trous noirs et la validité de principes tels que la censure cosmique et la « théorème de calvitie », qui sont omniprésents dans la relativité générale mais qui n'ont pas encore été prouvés mathématiquement. Dans la nouvelle ère de l'astronomie des ondes gravitationnelles, nous pouvons espérer exploiter les applications phénoménologiques des modes quasi-normaux; nous pouvons effectuer des analyses quantitatives des ondes gravitationnelles émises dans le sillage des événements de fusion de trous noirs et les utiliser dans la recherche de nouvelle physique.

Nous explorons ces idées dans cette thèse, dans le contexte d'arrière-plans fixes de trous noirs sphériquement symétriques sur lesquels se propage un champ test scalaire. Nous commençons par une introduction pédagogique aux modes quasi-normaux dans l'espace-temps des trous noirs de Schwarzschild, afin de présenter les techniques de calcul des fréquences quasi-normales et d'illustrer le comportement caractéristique des modes quasi-normaux et l'effet des paramètres de champ. Cela permet d'introduire la fonction d'onde des modes quasi-normaux et le "facteur d'excitation quasi-normal". Comme les tests de la relativité générale sont spécifiques à un mode, les facteurs d'excitation quasi-normaux fournissent une mesure de l'excitation relative nécessaire pour identifier un mode particulier dans le spectre détecté, indépendamment du stimulus perturbateur initial du trou noir. Dans la Section 2.4, nous discutons de la procédure que nous avons développée pour construire des facteurs d'excitation quasi-normaux d'ordre supérieur, sur la base des formalismes Dolan-Ottewill et Schutz-Iyer-Will.

Dans les Chapitres 3 et 4, nous étendons notre examen de l'effet des paramètres du champ et du trou noir sur les fréquences quasi-normales en examinant le spectre d'un champ de spin-0 avec une masse μ et une charge q dans un espace-temps de trou noir de Reissner-Nordström de Sitter (RNdS) avec une masse M, une charge Q, et une constante cosmologique $\Lambda > 0$. Pour ce faire, nous explorons d'abord l'espace des paramètres et la structure globale du trou noir RNdS dans le Chapitre 3. Cela permet de développer les nuances des concepts physiques fondamentaux qui seront abordés par nos analyses, *viz*. la conjecture de faible gravité qui extrait les contraintes de masse et de charge de la mécanique des trous noirs, la limite de Festina-Lente qui fournit une limite inférieure de la masse et de la charge des champs à partir des processus de désintégration des trous noirs, et les conjectures de censure cosmique qui préservent la nature déterministe de la relativité générale.

Nous procédons à l'analyse des modes quasi-normaux dans le Chapitre 4. Avec une méthode de calcul semi-classique adaptée au calcul des champs scalaires chargés et massifs dans l'arrière-plan du trou noir RNdS, nous démontrons le comportement régulier et anormal des fréquences quasi-normales et la dépendance aux paramètres du trou noir et du champ. En particulier, nous nous concentrons sur l'application de cette analyse dans l'étude de la stabilité, de la superradiance et des violations de la censure cosmique dans les régions extrémisées du trou noir RNdS.

Enfin, nous nous intéressons à la recherche de signatures de la physique au-delà du modèle standard à l'aide des ondes gravitationnelles provenant de collisions de trous noirs binaires. Nous expliquons d'abord le scénario au-delà du modèle standard qui nous intéresse : un modèle extradimensionnel de courbure mixte dont le manifold de dimension supérieure est un espace négatif compact. Le Chapitre 5 est donc dédié à la motivation et à la construction de ce modèle extra-dimensionnel. Plus précisément, nous nous intéressons

à un espace produit composé d'un espace-temps quadridimensionnel de trous noirs de Schwarzschild et d'un nilmanifold tridimensionnel (tore torsadé). Nous montrons comment nous pouvons modéliser les perturbations comme un champ test scalaire, la géométrie extradimensionnelle étant décrite dans le potentiel effectif sous la forme d'un terme de masse au carré représentant une tour d'états de Kaluza-Klein.

Le Chapitre 6 se concentre sur les techniques d'acquisition, de traitement et d'interprétation des données des ondes gravitationnelles utilisées par la collaboration LIGO-Virgo-KAGRA, et comment elles peuvent être utilisées dans les tests de relativité générale. Nous expliquons ensuite comment nous utilisons l'infrastructure LVK dans notre propre étude. Nous calculons le spectre des fréquences quasi-normales pour le modèle "Schwarzschild-nilmanifold" en utilisant trois méthodes numériques différentes, et nous les comparons aux tests hiérarchiques de la relativité générale effectués par la collaboration LVK afin de déterminer une possible "limite de détectabilité" au-delà de laquelle les masses de Kaluza-Klein ne peuvent pas être détectées à l'aide des fréquences quasi-normales.

Acknowledgments

First and foremost, my heartfelt thanks go to my supervisors, who offered me this life-changing Ph.D experience. Thank you for countless convivial conversations, from the nuances of nilmanifolds to the writings of Proust and Melville; whether through the windows of laptop screens or dining together at the South African coast. Since our very first encounter, they have looked out for my personal and professional interests, guiding me towards deeply enriching opportunities and truly extraordinary people who − like them − are as brilliant as they are kind. I will always appreciate this.

Thank you to Aldo, my guide on all things European, and ever generous with his knowledge, enthusiasm, and fine Italian chocolate. What a thrill it has been to go from reading your papers in a crowded office at Wits to indulging in pizza with you and the theory group. With your unparalleled kindness towards everyone and your ability to absorb ideas instantly (even when far outside your usual topics), it is a true pleasure to work with you. I will treasure the stimulating hours we have enjoyed discussing in your office.

And equal thanks to Alan, who first initiated me into academic life, and who lured me towards the theoretical with his work on extra dimensions and black holes. Between your wry sense of humour and your capacity for connecting ideas across disciplines − as well as our many digressions during our weekly meetings − working with you is a delight. As a researcher of many hats, you have shared many of your skills with me, opening doors that I had never known existed. Thank you for this, and for always being in my corner.

Thanks also to the institutions whose support made my doctoral studies possible: Campus France (avec un grand merci à Madame Derudder), the SA-CERN programme, the L'Oréal-UNESCO *For Women in Science* programme, and their respective partners and financiers. My thanks also to the staff and administration of the University of Johannesburg (UJ) and the Claude Bernard University Lyon 1 (UCBL1), where I am especially indebted to the good people of the Institute of Physics of the Two Infinities (IP2I) of Lyon for welcoming a thrice-foreign student so warmly into the lab.

Special thanks to Anele and Hajar of our little UJ group, to the IP2I theory and gravitational-waves groups, to the IP2I doctorants − and particularly to Theodoros, Viola, Nazila, Fabio, and my dear office mates of past and present: Marco, Wanda, Antoine, and Sharam. My sincere thanks are also due to Lara Mason, who first charted the *terra incognita* of the UJ-UCBL1 cotutelle agreement and carved out a path that I could blindly follow.

I express my sincere gratitude to my collaborators: the ever-supportive Wade; Dr Chen and Professor Cho; Dimitrios and Etienne; Professor Park; Luc, in particular, for our many discussions and your inspired guidance. Working with each of you has been personally and professionally enriching. I have thoroughly enjoyed our time together, and I look forward to our fruitful collaborations in the future. In this same vein, I extend my warm thanks to my dedicated reviewers, whose input and advice have led to greater refinement and deeper insights, in this manuscript and beyond.

To my friends, who kept me sane and human − Erinn, Stef, Hadj, and Perdikis from the days of SAHETI; Liam, Mvelo, Tam, Roy, Rowan, Cas, and Lex from the days of Wits; my fellow adventurers, Amy and Dave. Thank you for your ever-present support, and your patience with my near-constant "MIA" status. To Michelle, Priyal, and the Supernova Foundation, whose support reminds me of my love for this field.

And finally, to my family. To Mioara, my mentor, who showed me the way and who always believed in me; to Ana, Daniel, David, and Elise, for their endless warmth and hospitality. My gratitude extends to each branch: Galanis, Mathaiou, Chrysostomou, Mandea. But especially to the ones in South Africa, whose love and support are the reasons I am here today. My parents, Maria, Mauritz, Panteleimon, Linah − thank you for everything.

Contents

Declaration of Authorship v

Abstract vii

Resumé ix

Acknowledgments xi

List of Figures xv

List of Tables xvii

1 Introduction 1
- 1.1 Black holes and their QNMs in the new-found era of gravitational-wave astronomy . . . 2
- 1.2 Black holes and their QNMs as probes of fundamental physics . . . 6
- 1.3 Black holes and their QNMs as probes of new physics . . . 7
- 1.4 Thesis outline and objectives . . . 9

2 Quasinormal modes in Schwarzschild black hole space-times 10
- 2.1 QNMs in scattering theory . . . 11
  - 2.1.1 The Green's function approach and quasinormal excitation . . . 13
- 2.2 Semi-classical approaches to QNM problems . . . 17
- 2.3 The massive QNM eigenvalue problem . . . 21
  - 2.3.1 Interpreting the mass-like QNM term in the astrophysical context . . . 25
- 2.4 Quasinormal wavefunctions and excitation factors . . . 27
  - 2.4.1 Preliminaries . . . 28
  - 2.4.2 Interior solution: using the parabolic cylinder function . . . 29
  - 2.4.3 Exterior solution: using the Dolan-Ottewill ansatz . . . 32
  - 2.4.4 Matching procedure . . . 34
  - 2.4.5 The quasinormal excitation factor . . . 36
  - 2.4.6 Discussion . . . 39

3 Einstein-Hilbert-Maxwell theory in de Sitter space-time 41
- 3.1 The Reissner-Nordström de Sitter black hole . . . 42
  - 3.1.1 RNdS black hole structure . . . 43
  - 3.1.2 RNdS black hole phase space . . . 45
- 3.2 The Festina-Lente mass bound . . . 47
- 3.3 Strong Cosmic Censorship . . . 49
  - 3.3.1 Preserving strong cosmic censorship in spherically-symmetric space-times . . . 52

4 Probing the RNdS black hole space-time with QNMs **56**
4.1 QNMs for a charged massive scalar field in the RNdS space-time . . . 56
4.1.1 Superradiance for $\ell = 0$ in the RNdS black hole space-time . . . 59
4.1.2 The behaviour of the potential within the RNdS phase space for $\ell > 0$ . . . 60
4.2 The QNF spectrum in RNdS space-time . . . 63
4.2.1 The semi-classical calculation of QNFs in a RNdS background . . . 63
4.2.2 Classifying charged QNMs in the RNdS space-time . . . 64
4.2.3 On the scalar field mass of the QNF . . . 65
4.3 On the issue of Strong Cosmic Censorship . . . 68
4.3.1 Comparisons with other works . . . 69
4.4 Discussion on the behaviour of QNMs within the RNdS space-time . . . 70

5 Compact negative spaces as higher-dimensional manifolds **72**
5.1 Constructing the 3D nilmanifold . . . 73
5.1.1 Constraints from a dark matter model . . . 78
5.2 The effective 4D QNM problem . . . 79
5.2.1 The interpretation of a mass-like term in the context of new physics . . . 80

6 Searching for extra-dimensions in gravitational-wave ringdown **83**
6.1 Identifying and processing signals with the LVK network . . . 84
6.1.1 Model comparisons: the matched filter . . . 84
6.1.2 Signal-to-noise ratio and template banks . . . 85
6.1.3 Inferring waveforms and physical parameters . . . 86
6.2 Using PyRing to search for deviations in GR . . . 88
6.3 Constraints from GWs using QNMs . . . 90

7 Conclusions **92**

A Philosophical and mathematical preliminaries on cosmic censorship **94**

B Horizons and conformal diagrams: the Schwarzschild example **97**

C The Nariai black hole solution **101**

D Quasinormal excitation factor computation at leading-order **104**
D.1 Interior solution: using parabolic cylinder function . . . 104
D.2 Exterior solution: using the Dolan-Ottewill ansatz . . . 106
D.3 Matching procedure . . . 107
D.4 Ingoing and outgoing coefficients . . . 109
D.5 The leading-order quasinormal excitation factor . . . 110

E Perturbed components of the QNM wavefunction at higher orders **111**

F Details on the semi-classical method **114**

References **116**

List of Figures

1.1 *Top: the observed GW signal for the binary black hole merger event GW150914, as measured at the Livingston (L1) and Hanford (H1) LIGO detectors. Bottom: inspiral, merger, and ringdown of the waveforms modelled using the parameters extracted from the GW150914 event [43].* 4

2.1 *The Schwarzschild effective potential plotted against the tortoise coordinate.* 12
2.2 *Conformal diagrams of the Schwarzschild black hole space-time depicting the linearly-independent solutions to the scalar wave equation, Eqs (2.16) and 2.17) (adapted from Ref. [139]).* 14
2.3 *The magnitude of the $\ell = 0, 1, 2, 3$ QNEFs for increasing values of n at leading order.* 16
2.4 *The effective QNM potential Eq. (2.49) for $M = 1$, $n = 0$, $\ell = 2$, and increasing values of μ.* 22
2.5 *The massive scalar QNF spectrum for $M = 1$ and $\mu \in \{0, 1\}$, computed using the Dolan-Ottewill method.* 24
2.6 *The real part of the massive scalar QNF spectrum for $M = 1$ and $\mu \in \{0, 1\}$, computed using the Dolan-Ottewill method.* 24
2.7 *The imaginary part of the massive scalar QNF spectrum for $M = 1$ and $\mu \in \{0.0, 0.2\}$, computed using the Dolan-Ottewill method.* 25
2.8 *Diagrammatic representation of the solutions, where asymptotics are matched across the shaded regions. At leading-order, $g(z) \sim z$.* 28
2.9 *The real and imaginary parts of the QNEF at orders L^0, L^{-1}, and L^{-2} for the fundamental mode. We compare against the numerical results generated using the MST formalism [194, 195], listed in Table II of Ref. [193].* 39

3.1 *The conformal diagram for the extended RNdS space-time.* 44
3.2 *A two-dimensional projection of the parameter space for $H^2 = \Lambda/3 = 1$ for the 4D RNdS black hole. Dark (light) shading corresponds to cold (warm) black holes.* 46
3.3 *Conformal diagram for the extended RN black hole space-time, with Cauchy surface Σ.* 53
3.4 *From the RNdS Penrose diagram of Fig. 3.1, we consider the competing blue-shift and red=shift mechanisms.* 55

4.1 *For $L^2_{dS} = 1$, $M = 0.112$, and $Q = 0.016$, we plot the scalar QNM potential with $\mu = q = 0.1$ and $\ell = 0$. Observe the "valley" following the barrier potential indicative of superradiant amplification.* . 59
4.2 *For $M = Q = 0.25$ and $L^2_{dS} = 1$ (point E of Fig. 3.2), we plot the scalar QNM potential with $\ell = 1$ and $\mu = q = 0.1$.* 61
4.3 *For $M = 0.2425$, $Q = 0.249$, and $L^2_{dS} = 1$ (above the $M = Q$ line of Fig. 3.2), we plot the scalar QNM potential with $\ell = 1$ and $\mu = q = 0.1$.* 61
4.4 *The evolution of the QNM scalar potential within Fig. 3.2 for $L^2_{dS} = 1$, $\ell = 1$, and $\mu = q = 0.1$.* . . 62
4.5 *The influence of scalar field parameters on the QNM scalar potential within Fig. 3.2 for $L^2_{dS} = 1$, $M = 0.185$, $Q = 0.016$, and $\ell = 1$.* 63

4.6 *A graphical indication of the critical mass $\mu_{cit} \sim 1.4083$ at Point N, where $r_+ \sim r_c$ for $L^2_{dS} = 1$, $M = 1/\sqrt{27}$, and $Q = 0$.* 66
4.7 *At Point E, where $M = Q = 0.104$ for $L^2_{dS} = 1$, the critical mass is $\mu_{crit} \sim 2.065$ for $q = 0$.* 66
4.8 *At Point E, where $M = Q = 0.104$ for $L^2_{dS} = 1$, there is no longer an intersection to denote μ_{crit} for $q = 0.1$.* 67
4.9 *With $L^2_{dS} = 1$ and for $\mu = \ell = 1$ and $q = 0.1$, we shade the parameter space in which ω_+ (blue), ω_c (orange), and both families (magenta) violate the condition for SCC preservation.* 68
4.10 *With $L^2_{dS} = 1$ and for $\mu = 0.1$, $q = 1$, and $\ell = 1$, we shade the parameter space in which ω_+ (blue), ω_c (orange), and both families (magenta) violate the condition for SCC preservation.* 69
4.11 *For $L^2_{dS} = 1$, $M = 0.157$, and $Q = 0.158$, we plot the critical mass $\mu_{crit} \sim 1.7$ corresponding to a violation of the condition for SCC preservation.* 70

5.1 *Mass ratios $R^2_{nil} \leq 6$ corresponding to Eq. (5.32) for $\mathcal{N}_3$ for $\kappa = 1$ (purple) and $\kappa = 2$ (orange).* . . 77
5.2 *Ratios $R^2_{st} \leq 6$ corresponding to Eq. (5.33) and Table 5.2 for $\mathbb{T}^3$.* 78
5.3 *An illustration of the scales probed by QNFs for $M\mu \sim 1$ using Eqs (5.47) and (5.48).* 81

6.1 *1D and 2D marginal posteriors for source-frame masses, using O1 posterior samples.* 88
6.2 *A rudimentary parameter estimation of GR deviations using PyRing for event GW150914.* 90

B.1 *Conformal diagram for the maximally-extended Schwarzschild space-time.* 99

List of Tables

2.1 *The $(n, \ell) = (0, 2)$ scalar QNFs for $M = 1$ and increasing μ, calculated using the Pöschl-Teller approach, and the sixth-order WKB and Dolan-Ottewill methods.* 23

2.2 *The real and imaginary components of the QNEF at orders L^0, L^{-1}, and L^{-2} for the fundamental mode.* 40

3.1 *RNdS space-time regions (Fig. 3.1) and the dominant force within each.* 43

5.1 *Mass ratios R_{nil} for the 3D nilmanifold $\mathcal{N}^3$, corresponding to Eq. (5.32) for $\kappa = 1, 2$.* 77

5.2 *Mass ratios R^2_{st} for the standard 3D torus $\mathbb{T}^3$, corresponding to Eq. (5.33).* 77

6.1 *QNFs computed with the Dolan-Ottewill method as parametric deviations from GR* 91

B.1 *Notation for asymptotic regions depicted in a standard conformal space-time diagram.* 99

F.1 *Error estimation for the WKB-based method used in Chapter 4, with $M = Q = 0.1$ and $L_{dS} = 1$.* . . 115

Chapter 1

Introduction

> The gravitation attraction of a star with a diameter 250 times that of the Sun and comparable in density to the earth would be so great no light could escape from its surface. The largest bodies in the universe may thus be invisible by reason of their magnitude...
>
> Pierre-Simon de Laplace in *Exposition du Système du Monde*[1] (1796)

Einstein's theory of general relativity (GR) relates the curvature of the space-time of the universe to the energy and momentum of the matter therein, providing a geometric theory of gravity that has withstood each experimental challenge levelled against it [3]. The mathematical formulation of GR can be succinctly summarised through the Einstein field equations,

$$R_{\mu\nu} - \frac{1}{2}Rg_{\mu\nu} + \Lambda g_{\mu\nu} = \kappa^2 T_{\mu\nu} \,, \tag{1.1}$$

where Newton's constant G can be related to the reduced Planck mass through the gravitational constant $\kappa^2 = 8\pi G/c^4 = 1/M_P^2$ (see Refs [4–8] for introductions and reviews). Space-time curvature is encoded in the metric tensor $g_{\mu\nu}$, the Ricci curvature tensor $R_{\mu\nu}$, and the Ricci scalar $R = g^{\mu\nu}R_{\mu\nu}$; the stress-energy tensor $T_{\mu\nu}$ contains the characteristic information about the matter content of the universe. Within this thesis, we consider scenarios inclusive and exclusive of a cosmological constant $\Lambda \geq 0$, which corresponds to asymptotically-de Sitter and asymptotically flat space-times, respectively.

To determine exact solutions to the Einstein field equations, we rely on the introduction of simplifying assumptions, usually informed by physically-motivated symmetries and corresponding to gravitational phenomena [9]. In this work, we focus on the vacuum solutions under spherical symmetry. By Birkhoff's theorem, these spherically-symmetric vacuum solutions are the Schwarzschild and the Reissner-Nordström (RN) black holes [10]. For $\Lambda > 0$, these are the Schwarzschild de Sitter (SdS) and Reissner-Nordström de Sitter (RNdS) solutions, respectively.

To describe dynamical systems, we require additional approximations. Einstein's summation convention disguises the highly nonlinear behaviour within GR, which renders the prospect of determining exact solutions for such dynamical systems impractical. As such, we impose that deviations from the metric are small; terms that are quadratic and beyond in $g_{\mu\nu}$ are considered to contribute negligibly to the equations of motion. In this way, we develop linearised gravity and, by extension, the black hole perturbation theory that has played an essential role in the development of gravitational theory over the last century, culminating in the successful realisation of gravitational-wave (GW) astronomy [11].

[1] Laplace [1] is considered among the first to predict the existence of black holes [2].

GR predicts the existence of black hole quasinormal modes (QNMs), the proper modes at which a black hole oscillates when excited by a non-radial perturbation[2]. Unlike the normal modes of Newtonian gravity, these modes are damped by the emission of GWs; the corresponding eigenfrequencies are therefore complex [13, 14]. We begin our discussion with the contextualisation of QNM research within GW investigations, and emphasise its importance in the broader field of gravitational physics. To do so, we briefly review how black holes and their QNMs can be studied within GW astronomy, formal theory, and phenomenology. We then conclude our introduction with a summary of our objectives and an outline of the thesis, highlighting how our novel results contribute to the GR community and beyond.

1.1 Black holes and their QNMs in the new-found era of gravitational-wave astronomy

In analogy to the electromagnetic waves produced by accelerating charges, GWs are generated by any massive body undergoing acceleration. However, for a GW signal to be observable from millions of lightyears away (i.e. for the amplitude of the GW to rise above the background noise), its source must be sufficiently massive and/or rapidly accelerating [15]. In principle, observable GW sources include coalescing compact bodies, pulsars, supernovae (all of which are sources of "deterministic" GWs), and a "cosmic GW background" comprised of the stochastic GWs created by the superposition of a large number of independently ringing sources, analogous to the cosmic microwave background [15–17]. In 2015, the first direct detection of GWs was captured by the Laser Interferometer Gravitational-Wave Observatory (LIGO). This much-anticipated achievement represents the culmination of painstaking numerical and experimental development spanning decades, as detailed in Ref. [18], and facilitated unprecedented access to the universe beyond the reach of the electromagnetic spectrum. To date, over 90 GW events have been confirmed – 83 of which are classified as binary black hole mergers – with a probability of astrophysical origin $p_{astro} > 0.5$ [19–21], providing us with the novel opportunity to scrutinise GR in the relativistic strong-field regime and placing us firmly in the era of GW astronomy.

Such success in the 10 Hz $\leq f \leq$ 10 kHz frequency range motivates the planned upgrades for present observatories, as well as the establishment of other international GW efforts, with the intention of establishing a network of strategically placed GW detectors of varying configurations positioned across the globe. Advanced LIGO consists of two identical interferometers, located in Hanford (Washington) and Livingston (Louisiana) in the United States. Each of these detectors has 4 km-long orthogonal arms and is sensitive to strains of the order of 10^{-23}. The Virgo GW detector near Pisa (Italy) has arms of 3 km and is consequentially slightly less sensitive than LIGO; in comparison, the GEO600 near Sarstedt (Germany) has effective optical arm lengths of 1.2 km. The Kamioka Gravitational Wave Detector [3] (KAGRA) in Hida (Japan) is built beneath the Kamioka Observatory, and is characterised by cryogenic mirrors that aid in reducing seismic and thermal noise [22]. In so doing, KAGRA enriches the global network's sensitivity, forcing the detection threshold further towards the fundamental limits of quantum noise [23]. Through consistent efforts by the LIGO-Virgo-KAGRA (LVK) Collaboration, LIGO-India has been approved for construction in the Maharashtra province, and will come online within the next decade, with a strain sensitivity of $\sim 10^{-24}$ over the 10 Hz $\leq f \leq$ 10 kHz frequency range [24]. Consistency between the observations of these detectors enables the suppression of noise as well as coherent analysis and the sky localisation of GW signals that in turn promote multi-messenger follow-ups of events [25].

Moreover, this access to GW astrophysics additionally motivates the exploration of the broader GW spectrum. For example, the North American Nanohertz Observatory for Gravitational Waves (NANOGrav), active in the lower-frequency band, relies on the precise timing of pulsars to detect GW remnants from past

[2]These perturbations refer to common astrophysical processes like matter accretion, incoming radiation, entry into the gravitational field of another astrophysical body, and – most significantly – black hole merger events [12].
[3]formerly the Large Scale Cryogenic Gravitational Wave Telescope (LCGT)

mergers of supermassive black holes [26].[4]. The approved space-based Laser Interferometer Space Antenna (LISA) will trace the evolution of black holes from the early Universe through the peak of the star formation era [28]). With plans for broadly-sensitive detectors like the Cosmic Explorer [29], we are poised to observe GW sources ranging from the stochastic background at $\sim 10^{-10}$ Hz to pulsars at $\sim 10^{6}$ Hz [30].

This newfound position allows us to test directly the strong-field dynamics[5] of gravity for the first time, as well as to probe the principles we consider sound, such as the "no-hair" conjecture [32–34] − which indicates that isolated Kerr-Newman black holes in equilibrium can be fully characterised by their Arnowitt-Deser-Misner (ADM) mass (M), charge (Q), and spin parameter (a) [4, 11]. We are also equipped to pursue tantalising hypotheticals like extra-dimensions [35–37] and supersymmetry [38]; recent considerations suggest that signals from primordial black holes could lie within the sensitivity range of LISA, or even future iterations of LIGO for $M_{PBH} \leq 100 M_{\odot}$ [39, 40].

Although GWs, by definition, are generated by all massive accelerating bodies, GWs interact weakly with matter and are thus difficult to detect. The merger of compact bodies such as black holes or neutron stars, however, releases enough energy to produce detectable signals (where the associated violence is considered in Ref. [13] as second only to the big bang). Furthermore, models of black hole binary mergers are the most comprehensive and accurate of the two-body systems [17]. For these reasons, the most frequently detected GWs are those sourced from binary black hole collisions [21].

As we see in Fig. 1.1, the gravitational waveform modelled via the techniques of numerical relativity (refined over the course of several decades [14]) finely predicted the behaviour of the data captured by the LIGO detectors. It is well known [11, 12, 14, 41, 42] that specific waveform features correspond to particular stages for the coalescence of a black hole binary system:

(i) inspiral: long, adiabatic stage as orbit shrinks and GW emission increases;

(ii) plunge: violent merger into a single black hole and GW emission peaks;

(iii) ringdown: final black hole emits damped GWs as it relaxes into a stationary state.

The "inspiral phase" marks an orbital decay; within GR, the compact objects spiral closer together due to their loss of energy and angular momentum in the form of GWs. As the orbit shrinks, the frequency and amplitude of these GWs increase. Note how this is in contrast to Newtonian binary systems, where bodies can follow closed elliptical orbits. However, since the overall scenario remains non-relativistic, it can be modelled quite accurately through the post-Newtonian approximation, where expansions in powers of v/c may be used to describe quantities like energy and flux [11, 41]. Inspiral ends with a final stable orbit, the innermost stable circular orbit (ISCO). The subsequent "plunge" represents the merging of the black holes, a stage dominated by strong-field dynamics and involving the maximal release of energy via GW emission [13, 41]. This is modelled using numerical relativity. The resultant, distorted black hole then "rings down" with characteristic frequencies, as it settles into a final quiescent state. The damped GWs emitted by this final black hole are a superposition of QNMs; they dominate the GW spectrum at late times, as first demonstrated in Ref. [44]. The corresponding characteristic frequencies are the quasinormal frequencies (QNFs). Typical models presume that one mode dominates soon after the black hole merger, and an exponentially damped oscillation at constant frequency can be observed as the black hole settles towards its final state [14].

The relevance of these QNMs lies in the physical quantities encoded within them. From the amplitude of the QNM, details concerning the initial black hole binary system may be extracted [11, 14]. The authors of Ref. [45], for example, captured information regarding the mass ratio and spins of the progenitor black holes through a comprehensive numerical interrogation of coalescing black holes.

The QNF, however, is considered "the most physically meaningful quantity after merger" [41]. Superficially, we recognise it to a be a complex quantity, where the real part represents the physical oscillation

[4]Through their analysis of 15 years of pulsar timing data, the NANOGrav collaboration recently released promising results indicative of a stochastic GW background from supermassive black hole binaries [27].

[5]The strong-field regime represents the limit at which the post-Newtonian ($v \ll$ c) approximation of gravity fails, such as when relativistic objects are concerned [31]. Since GWs carry energy outward at $v \sim c$, they are considered a strong-field system [11].

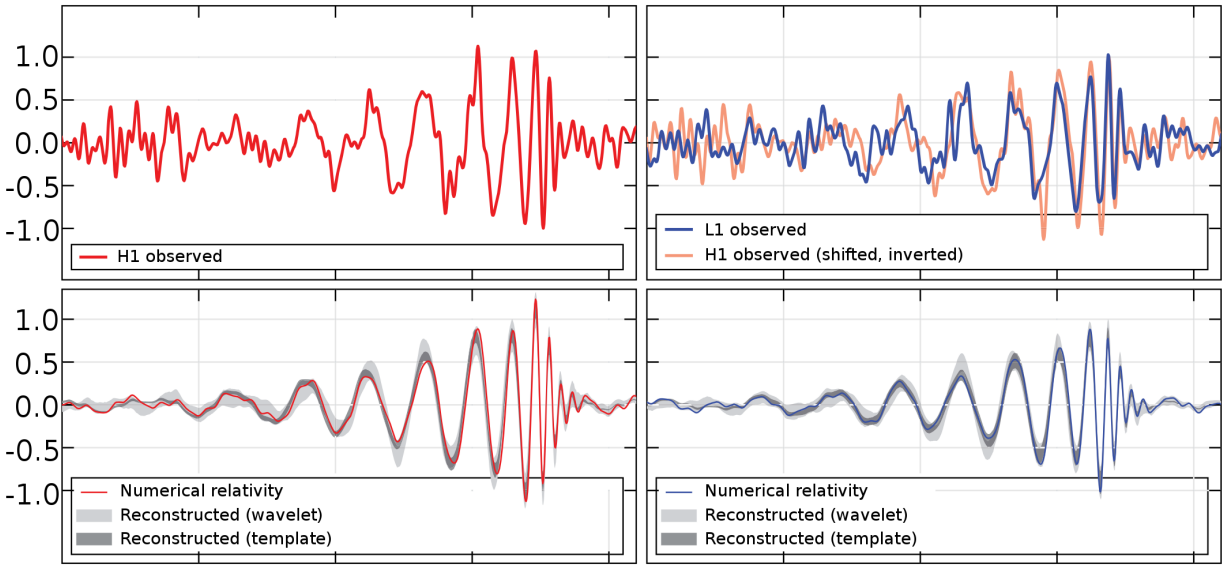

Figure 1.1: *Top: the observed GW signal for the binary black hole merger event GW150914, as measured at the Livingston (L1) and Hanford (H1) LIGO detectors. Bottom: inspiral, merger, and ringdown of the waveforms modelled using the parameters extracted from the GW150914 event* [43].

frequency and the imaginary part expresses the damping of the system [14, 42]. Of greater astrophysical interest, however, is its connection to the character of the final black hole. While the behaviour of the inspiral stage is specified by the nuances of the initial perturbation, ringdown depends exclusively on the parameters of the final black hole, *viz*. the ADM mass, charge, and spin parameter [46]. In studying a single QNM, these parameters may be extracted, and the black hole fully described[6].

As such, QNM studies allow for a means of investigating and cataloguing black holes according to their characteristic parameters. This offers the opportunity to test the "no-hair conjecture" directly [11, 14]. Such investigations are already underway, as demonstrated in Ref. [48], where the analysis was performed using data from the first detected merger event. The authors also noted that in their identification of multiple ringdown modes in the data, they established a measure of progress in the pursuit of black hole spectroscopy. Since we expect to experience a veritable GW data deluge in the coming years, the gravitational physics community shall have ample opportunities to expand upon this work.

However, with this additional volume of data, it is necessary to consider the accuracy with which we calculate QNMs and their associated quantities. As explained in Ref. [47], maximising accuracy in QNM calculations is imperative because of the relationship between QNF and black hole parameters: a slight change in the former corresponds to a considerable change in the latter. For this reason, a significant portion of QNM research has been dedicated to the establishment of highly accurate approaches to the QNM problem.

Furthermore, the increased sensitivity in our detectors suggests an increase in the capturing of higher overtones and harmonics. As discussed in Ref. [49], identifying an individual mode within the superposition of QNMs observed is necessary for the development of waveform models and the testing of GR. Since the detectability of each mode depends on its relative excitation, a means by which to quantify the excitation of a QNM that is independent of the initial perturbing stimulus is vital.

As the name suggests, quasinormal excitation factors (QNEF) indicate how and by how much QNMs are excited [50]. Few papers are available on the subject, due in part to the complexity of the problem of determining the QNM wavefunction. A seminal attempt at the QNEF computation was carried out by

[6]This is in accordance with the "no-hair conjecture", which presumes a perfectly isolated black hole at equilibrium — something impossible to attain, for even in a space-time devoid of matter and fields, a black hole interacts with the vacuum [47].

Andersson in 1995 [51]. Following Nollert and Schmidt's construction of the QNMs as singularities of a Green's function [52], Andersson applied the "phase-integral method"[7] to the case of scalar QNMs in a Schwarzschild background. The final formulae he generated carried over naturally to the gravitational counterpart. It was only recently that the semi-analytic computation of QNEFs for the case of the Kerr black hole was been successfully carried out in Ref. [55] using a WKB analysis at leading order.

A further important example is Ref. [56], focused on a Kerr black hole spacetime and carried out using numerical techniques. For corotating modes, the authors found that the excitation factors tend to zero in the extremal limit, and that the contribution of the overtones should be more significant when the black hole is fast rotating. They also present the first analytical calculation of the large-damping asymptotics of the excitation factors for static black holes. An extensive numerical follow-up by Oshita [57] explored Kerr QNEFs to the 20th overtone.

The calculation of a QNEF has received renewed interest following the regular detection of GWs from binary black hole merger events [58–60]. This accumulation of GW data has allowed for thorough examination of the aforementioned relationship between QNFs and the parameters of post-merger black holes, enabling improved testing of GR in the strong regime [58–61]. However, it has also emphasised the importance of quantifying QNM excitations. Isolating the QNM-dominated phase of the post-merger gravitational radiation from the gravitational waveform is known to be highly non-trivial [61], due to the low signal-to-noise ratio (SNR) of the post-merger phase and the technical challenges in combining posterior probability densities from multiple events [15, 62]. Quantifying QNM excitations is expected to become more complicated as GW detector sensitivity to higher overtones [57] and harmonics [63] increases [64].

To observe how the QNEF contributes to the GWs, we may describe the evolution of the post-merger gravitational radiation propagating in the black hole background as a superposition of QNMs. On the basis of the spherical symmetry of the black hole spacetime at hand, the QNMs may be subjected to a variable-separable decomposition. As such, we can express the GW spectrum as

$$h_+ + ih_\times = \frac{1}{r}\sum_{\ell mn} \mathcal{C}_{\ell n}\, Y_{\ell m}(\theta,\phi)\, e^{-i\omega_{n\ell}t}\,. \tag{1.2}$$

where h_+ and $h_\times$ are the strain amplitudes for the two polarisations of the GW. Since we assume a static and spherically-symmetric background, the spheroidal harmonics $Y_{\ell m}(\theta,\phi)$ reduce to their spherical counterparts, defined in terms of the multipolar number ℓ and azimuthal number m. The QNFs can be decomposed as

$$\omega_{n\ell} = \omega_R - i\omega_I\,, \qquad \omega_R, \omega_I \in \mathbb{R}\,, \tag{1.3}$$

where ω_R represents the real oscillation frequency and ω_I is proportional to the inverse damping time. The magnitude of the imaginary part increases monotonically with n, the "overtone" number. The "fundamental mode" that dominates ringdown is $n = 0$. For a harmonic time dependence $\psi(t) \sim e^{-i\omega t}$, the imaginary part of the QNF must be negative to ensure black hole stability [44].

While the Schwarzschild QNFs depend exclusively on the mass of the black hole by virtue of the no-hair conjecture [32], the "quasinormal excitation coefficient" $\mathcal{C}_{\ell n}$ depends also on the initial perturbing stimulus [14]. In Ref. [57], the excitation factor is expressed as a product of the QNEF $\mathcal{B}_{\ell n}$ and a source factor $\mathcal{T}_{\ell n}$. The latter depends on the initial data of the black hole, where Gaussian wavepackets were traditionally considered in earlier works [51, 52]. The QNEF, on the other hand, is independent of the initial perturbing stimulus and may be considered a quantifying factor for the ease with which QNMs are excited [57]. In Section 2.4, we perform a dedicated calculation of this QNEF, extending the lower-order result of Ref. [50] and demonstrating how the QNEF allows us to distinguish between higher harmonics and overtones in the QNM spectrum.

[7] A semi-analytical technique used to approximate the solution to a second-order ordinary differential equation by integrating an introduced "phase function" along a complex contour [53], applied by Andersson to the computation of QNMs [54].

1.2 Black holes and their QNMs as probes of fundamental physics

While precise definitions may vary within the broader physics community, the general relativist's standard interpretation of a spherically-symmetric black hole includes an event horizon and a singularity, with the former concealing the latter [65]. Common lore then suggests that classical GR breaks down at the singularity and quantum effects manifest [66]. That black holes could serve as the intermediary between classical and quantum gravity is a well-proliferated belief – with the hope that black hole studies could usher in a paradigm shift, much like analyses of the hydrogen atom catalysed modern quantum mechanics [67]. Within the subject of black hole thermodynamics, the heuristic connections between classical and quantum aspects of gravity become more concrete: for example, intrinsically quantum attributes such as entropy and temperature are related to classical quantities such as horizon area and surface gravity through the works of Mukhanov, Bekenstein, Hawking, Gibbons [67–71], and their contemporaries.

As an example, Hod in 1998 established a connection between black hole thermodynamics and the QNFs of a Schwarzschild black hole in the highly-damped regime: from Nollert's numerical results [72],

$$\mathfrak{Re}\left\{\lim_{n\to+\infty}\omega_{n\ell}\right\} \approx \frac{0.0437123}{M} \xrightarrow{\text{Hod}} \frac{\ln 3}{8\pi M} . \tag{1.4}$$

Here, $1/8\pi M$ is the Hawking temperature T_+ of the Schwarzschild black hole, which is defined in terms of the event horizon surface gravity k_+ as $T_+ = k_+/2\pi$ [73]. From this result, Hod determined that Eq. (1.4) could imply a fundamental scaling of the "quantum Schwarzschild black hole" area [74].

A more active line of inquiry lies in the "Swampland programme". Upon compactification, string theories defined in space-times of dimension $d > 4$ should reduce to effective field theories (EFTs) containing both the Standard Model (SM) and gravity at the low-energy scale. This can be achieved for a landscape of choices in compactification parameters. In the pursuit of a falsifiable field theory limit, however, this diversity in consistent theories becomes problematic: there exists a staggering number of string vacua about which the low-energy EFTs are constructed, such that deriving any constraint thereof is extremely difficult.

However, as suggested in Ref. [75], not all semi-classically consistent low-energy EFTs can be completed to a full theory. These EFTs occupy the "Swampland", in antithesis to the "Landscape" of self-consistent EFTs that can be derived from a UV-complete theory of quantum gravity. Under the "Swampland programme", low-energy EFTs that do not satisfy conjectured selection criteria for the Landscape (i.e. the "Swampland conjectures" [76]) are retired to the Swampland.

Many of the Swampland conjectures are constructed using heuristic arguments from black hole mechanics. One of the most well-established results thereof is the Weak Gravity Conjecture (WGC), where considerations of black hole emission of particles with mass m and charge q led to constraints on EFTs inclusive of gravity and $U(1)$ abelian gauge fields in asymptotically-flat space-time [77]. The formulation of the conjecture is as follows. At (super)extremality, a black hole in asymptotically-flat space-time has a mass M (greater than or) equal to its charge Q, such that $M/|Q| \geq 1$ in natural units. Black hole decay occurs by means of the radiation of elementary particles. If such elementary particles have a mass-charge ratio $m/|q| > 1$, then the black hole would radiate all of its mass before losing its charge, resulting in a "black hole" remnant of zero mass but non-zero charge. Citing the logical inconsistency of such a result, the WGC requires the existence of an elementary particle whose ratio of mass to gauge field charge is less than one. We can write this as

$$m < g_1 M_P , \tag{1.5}$$

where M_P is the Planck mass and g_1 is the $U(1)$ gauge coupling [77]. Within this work, we take $U(1)$ to be electromagnetism, unless stated otherwise.

However, the WGC is confined to the Minkowski context, whereas asymptotically-de Sitter space-time better relates to our current dark-energy-dominated cosmological era. Two key experiments in 1998 [78, 79] provided the initial empirical evidence that the universe is expanding at an accelerated rate, and modern

surveys continue to support the existence of a positive cosmological constant [80]. Within theory, interest in de Sitter space-time is ubiquitous [81] due to its holographic dual description via conformal field theory [82], the still-unresolved question of de Sitter stability in quantised theories [83, 84], and its generalisable thermodynamic properties [85].

This last point is particularly interesting. As a consequence of the exponential expansion associated with the positive vacuum energy, a black hole in an asymptotically-de Sitter universe is surrounded by a cosmological horizon beyond which information becomes inaccessible. Hawking radiation [70, 86] emanates from this horizon, such that the cosmological horizon is associated with a de Sitter temperature $T_{\rm dS}$ and Gibbons-Hawking entropy $S_{\rm dS}$ [71]. Except in specific cases, the black hole temperature $T_{\rm BH}$ differs from $T_{\rm dS}$. For a sufficiently large black hole, however, the system drifts towards thermal equilibrium.

It is worth noting that the fundamental nature of black holes is qualitatively and quantitatively altered upon introducing this non-zero cosmological constant. In the case of $\Lambda > 0$, as considered in this work, it is immediately clear that the maximum possible mass of a black hole is reduced: during stellar collapse, for example, the gravitational attraction must compete against the repulsive vacuum energy. More subtle concerns include the impact of the Gibbons-Hawking entropy [71] on the black hole system, particularly with respect to black hole decay (see Ref. [87] and references therein), as well as the question of defining mass [88] and black hole observables in de Sitter space-times [81]. Naturally, these have direct implications for any *gedankenexperiment* conducted within the black hole laboratory.

The development of Swampland criteria in de Sitter space-times therefore requires the careful consideration of the influence of $\Lambda > 0$. For example, Benakli *et al.* recently extended the WGC argument to charged black holes in (anti-)de Sitter space-times [89]. To do so, they combined the WGC with the Weak Cosmic Censorship (WCC) conjecture [90] forbidding naked singularities to establish a new WGC-de Sitter bound. In their study on charged black hole emission in de Sitter space-time, Montero *et al.* derived the "Festina-Lente" (FL) bound [91, 92], a lower bound on the mass of charged particles. We address this in further detail in Section 3.2. In Chapters 3 and 4, we shall demonstrate explicitly the influence of the cosmological constant on the black hole and its perturbations, respectively.

1.3 Black holes and their QNMs as probes of new physics

Our ability to detect GWs directly has immediate astrophysical [93] and cosmological [94] relevance. However, there is a significant interest in the theoretical implications of GWs [95] and the insights they might provide in the search for new physics [96].

This is in part due to their weakly-interacting nature: GWs propagate unimpeded through the universe, piercing both the cosmic microwave and cosmic neutrino backgrounds, possibly providing unique insights into the inflationary epoch and beyond [97–99]. These high and ultra high frequency "stochastic" GWs correspond to energies of the TeV range and higher, towards the Planck scale; in this way, GWs serve as a complementary laboratory to collider physics experiments [100–102]. Searches for new physics focused on early-universe dynamics are well-underway, with examples such as Ref. [103] demonstrating that models based at scales of Grand Unified Theories can be good candidates for detection via next-generation GW detectors [30]. This has encouraged new lines of inquiry into cosmic strings [104, 105], leptogenesis [106], dark matter [107], and other beyond the Standard Model (BSM) challenges. In this vein, GWs are also being applied to searches for extra dimensions (see Refs [37, 108, 109]). Compact extra dimensions feature a variety of different geometries (Ricci-flat [35, 110, 111], toroidal [112], warped toroidal [113] extra dimensions, etc.). These, on the other hand, have so far predicted GWs whose frequencies are of the order of $10^{12} - 10^{14}$ Hz, far exceeding the $10^3 - 10^4$ Hz upper limit of present and planned detectors [99, 100].

Here, however, we are guided by the capabilities of modern detectors, and investigate whether we can exploit present-day GW observations of merger events to infer constraints on new physics. In particular, we shall focus on binary black hole collisions, where the post-merger "ringdown" phase is dominated by

quasinormal ringing [41]. For this reason, we can apply known theoretical and numerical QNM techniques to experimental observations. Logistically, we concentrate on black holes because the dynamics of binary black hole collisions have been studied extensively [11, 13, 41]; the success of the LVK Collaboration is a testament to the gravitational waveform modelling expertise, Bayesian statistical analysis techniques, and experimental prowess carefully honed over several decades (see Ref. [15] for the LVK Collaboration's guide on data acquisition, processing, and analysis).

Furthermore, since the SNR ratio of the post-merger signal is usually fairly low and therefore not always characterisable [58–60], the higher-mass and louder black hole merger events are more likely to produce good candidates for ringdown analyses. The first detected GW event GW150914 [43, 114] was sufficiently loud to accommodate a QNM study, so we shall restrict our discussion to this event within this work, unless otherwise stated.

Current searches for evidence of new physics from available GW observations are dominated by model-agnostic null tests for deviations from GR predictions. These include: consistency checks between data and GR-based models for the evolution of a merger event; tests of the generation and propagation of GWs, where the latter involves searching for modifications to the dispersion relation and in turn constraining the Compton wavelength associated with the graviton mass; tests for additional polarisation modes beyond the tensor plus and cross modes; analyses of the post-merger properties for parametric deviations from GR [58–60, 115], etc. At present, there have been no statistically significant deviation from GR reported.

However, this latter category of testing has been a subject of growing fascination, and motivates investment in more precise measurements of QNFs [116–118]. Furthermore, hopes for the establishment of "black hole spectroscopy" [49] are beginning to be realised: although the $n = 0$, $\ell = 2$ mode is known to dominate the QNM spectrum, higher harmonics [119, 120] and overtones [121] are being investigated. Tests of the no-hair conjecture are of particular interest [61, 119, 122–124], as a violation thereof may be evidence of an exotic object or new physics.

As such, we shall focus here on this use of parametric deviations from GR in the QNF spectrum in an attempt to outline a search for extra dimensions. In fact, there have already been considerations for extra dimensions using black hole QNMs, concentrated for example on the five-dimensional (5D) Randall-Sundrum II [125] model: through the formalism of Shiromizu *et al.* [126] and Dadhich *et al.*, a 4D effective framework can be established from a 5D general relativity construction, leading to a (neutral) black hole solution that resembles the (charged) RN metric. The so-called "tidal charge" $\beta = Q^2/(4M^2)$ (in natural units $G = c = 1$) is a manifestation of the influence of the extra dimension. In Ref. [127], this is the observable utilised to constrain extra dimensions, but is found to disfavour the case of $d > 4$.

It is not clear how to extend the Shiromizu *et al.* formalism to a broader category of extra-dimensional models with $d > 5$, nor is it obvious whether this tidal charge observable can be probed for general cases. Moreover, it may be that alternate geometries could lead to successful GW detection. Bearing these points in mind, we shall consider as an example a particularly simple partially-compactified setup: a direct product space featuring a 4D Minkowski space-time and a 3D negative compact space $\mathcal{M}_4 \times \mathcal{N}_3$. Within this space-time, we shall embed a 4D Schwarzschild black hole. The higher-dimensional component will then be comprised of a twisted torus − known as a "nilmanifold" − constructed from the non-trivial fibrations of layered tori. The nilmanifold is one of the few geometries that allows for analytic calculations of mass spectra and Kaluza-Klein (KK) reductions [128], and boasts a number of phenomenologically-interesting properties that we shall discuss in Section 5.1.

While the higher-dimensional manifold is highly specific, we shall show that the variable-separable nature of our extra-dimensional space-time in the absence of coupling between components of $\mathcal{M}_4$ and $\mathcal{N}_3$ and the QNM problem we consider, allows for a KK reduction that expresses the extra-dimensional behaviour as a mass-like term that can be incorporated into the QNM effective potential. We shall demonstrate how this enables the application of QNM literature on massive oscillating fields, as well as studies on parametric deviations from GR employed by the LVK Collaboration. In so doing, we demonstrate an estimate for a detectability bound on the sensitivity of observable QNFs to signatures of new physics.

1.4 Thesis outline and objectives

The purpose of this introduction was to contextualise the QNMs and their corresponding frequencies within the GW framework, to establish the relevance of QNM research within the broader field of GR, and to provide an overview of the applications of black hole QNMs in the search for new physics. We explore these ideas within this thesis, in the context of fixed spherically-symmetric black hole backgrounds upon which a scalar test field propagates. In this vein, we seek to understand how parameters from the black hole space-time and the propagating field influence the QNF spectrum, the constraints we can derive as a result, and whether QNMs can be used in the search for extra dimensions.

We begin with a pedagogical introduction to QNMs within Schwarzschild black hole space-times in Chapter 2, in order to outline QNF computational techniques (Section 2.2) as well as to illustrate characteristic QNM behaviour and the effect of field parameters of mass μ and the angular momentum number ℓ on the QNF ω (Section 2.3). Our novel results for the massive QNF are integrated into the discussion of Section 2.3; in Section 2.3.1, we use this result to derive a detectability bound for such QNFs. We then introduce the QNM wavefunction and the QNEF. Since tests of GR are mode-specific, QNEFs provide a measurement of relative excitation required to identify a particular mode within the detected GW spectrum that is independent of the black hole's initial perturbing stimulus. In Section 2.4, we discuss the procedure we have developed to construct higher-order QNEFs, based on the Dolan-Ottewill and Schutz-Iyer-Will formalisms.

In Chapters 3 and 4, we extend our interrogation of the effect of field and black hole parameters on the QNFs by examining the QNF spectrum of a spin-0 field with mass μ and charge q within a RNdS black hole space-time with mass M, charge Q, and cosmological constant $\Lambda > 0$. To do so, we first explore the parameter space and the global structure of the RNdS black hole in Chapter 3. This allows for a dedicated elaboration on the nuances of the fundamental physics concepts that shall be addressed by our QNM analyses, *viz*. the influence of Λ on the RNdS phase space (Section 3.1, especially 3.1.2), the FL bound that provides a lower bound of field mass and charge from black hole decay processes (Section 3.2), and the cosmic censorship conjectures that preserve the deterministic nature of GR (Section 3.3).

We proceed with our novel QNM analysis in Chapter 4, beginning with a study of the evolution of the QNM potential within the RNdS phase space in Section 4.1. With a semi-classical computation method tailored to the calculation of charged and massive scalar QNMs in the RNdS black hole background (Section 4.2), we demonstrate regular and anomalous QNF behaviour and its dependence on black hole and field parameters in Section 4.2.3. We then focus on the application of this QNM analysis in the study of cosmic censorship violations within extremised regions of the RNdS black hole in Section 4.3.

Finally, we turn our attention to the search for signatures of physics beyond the Standard Model (BSM) using GWs from binary black hole collisions. We first explain the BSM scenario of interest: an extra-dimensional model of mixed curvature whose higher-dimensional manifold is a compact negative space known as a "nilmanifold" (i.e. a twisted torus). Chapter 5 is thus dedicated to the motivation and construction of this extra-dimensional model, with Section 5.1 dedicated to the study of the nilmanifold itself. Specifically, we are concerned with a product space comprised of a four-dimensional Schwarzschild black hole space-time and a three-dimensional nilmanifold. There, we show how we can model the black hole perturbations as a scalar test field, with the extra-dimensional geometry stylised in the QNM effective potential as a squared mass-like term representing a Kaluza–Klein (KK) tower of states. We discuss this QNM problem and the possible analytic constraints that can be derived in Section 5.2.

Chapter 6 focuses on the LVK Collaboration's GW data capturing, processing, and interpreting techniques, and how they can be used in tests of GR. We begin with a brief introduction to the LVK infrastructure and methodology in Section 6.1. We then elaborate on how we can utilise the LVK software for ringdown analyses in our own study in Section 6.2. Finally, we compare QNF spectrum for the "Schwarzschild-nilmanifold model", treating this as a massive QNM problem, and comparing this against the hierarchical tests of GR in Section 6.3. In so doing, we are able determine a possible "sensitivity bound" beyond which BSM signatures cannot be detected using QNFs. We then summarise our conclusions in Chapter 7.

Chapter 2

Quasinormal modes in Schwarzschild black hole space-times

> You mean, if you had perfect pitch could you find the shape of a drum?
>
> Lipman Bers in Kac's *Can One Hear the Shape of a Drum?* [129]

The study of QNMs, the characteristic modes of a vibrating object, is a ubiquitous topic that can enrich our understanding of a vast array of phenomena across various disciplines: from quantum mechanics to fluid dynamics, and from nuclear physics to optics; the phonon modes in crystals, the microwave cavities in amplifiers, and the oscillating strings of a guitar all display this intrinsically damped oscillatory behaviour. Such characteristic modes are particularly interesting for their ability to reveal the structure and composition of the object whence they came, allowing us to "hear" the shape of the perturbing object [14, 129]. As implied in the introduction, the black hole QNM framework boasts a dense and well-cultivated history whose development is chronicled in four comprehensive reviews [14, 42, 47, 130]. Rather than attempt a summary of the sixty-odd years of QNM research in this chapter, we discuss instead the foundational formalism required to contextualise the QNM-based investigations we perform in Section 2.4 and in Chapters 4 and 6.

We begin this chapter with a description of QNMs through the familiar lens of a scattering problem, where Section 2.1 is written in consultation with Refs [131–133]. The black hole scattering problem is particularly interesting, as the curvature of the space-time informs the boundary conditions and serves as the fixed background upon which the test field propagates; it is also the material upon which the incoming radiation scatters. In studying the massless scalar field scattering on a Schwarzschild black hole, we can introduce the fundamental QNM behaviour, as well as the concepts of stability and superradiance that inform later chapters. In Section 2.2, we provide a brief overview of the semi-classical techniques used to compute QNFs. Then in Section 2.3, we introduce the QNMs of massive scalar field in a Schwarzschild background as an eigenvalue problem, emphasising the role of scalar field parameters and the relationship between QNMs and photon orbits in the eikonal regime. We showcase how the mass of a scalar field can influence QNM nature. The final section is dedicated to our higher-order calculation of the QNEF.

2.1 QNMs in scattering theory

The birth of black hole perturbation theory can be traced back to the 1957 Schwarzschild stability analysis of Regge and Wheeler [134]. It was there that the symmetries of the space-time were shown to be exploitable in the analysis of the gravitational radiation from a black hole: the separation of angular, radial, and temporal components using a tensor spherical harmonic decomposition. In so doing, they derived two decoupled equations of "odd" and "even" parity: the "axial" and "polar" modes, respectively.[8] With the application of a Fourier expansion of the perturbed functions and a suitable gauge transformation, Regge and Wheeler established the "Schrödinger-like" ordinary differential equation suitable for describing the radial behaviour of the linearised perturbations of the metric. Let us consider the explicit example of a perturbed scalar test field within a Schwarzschild black hole space=time/

An application of black hole perturbation theory begins with the modification of the metric by a disturbance,

$$g'_{\mu\nu} = g^{\rm BH}_{\mu\nu} + \delta_{\mu\nu} \,, \tag{2.1}$$

where the unperturbed black hole metric $g^{\rm BH}_{\mu\nu}$ is referred to as the "background" and the "perturbations" $\delta_{\mu\nu}$ are considered to be very small ($\delta_{\mu\nu} \ll g^{\rm BH}_{\mu\nu}$). Similarly, we may consider a perturbed background field $\Phi' = \Phi^{\rm BG} + \phi$. We may then substitute $g'_{\mu\nu}$ and Φ' into the Einstein field equations (c.f. Eq. (1.1)), linearise the system of equations with respect to $\delta_{\mu\nu}$ and ϕ, and thereby deduce the linearised set of differential equations satisfied by the perturbations. An ordinary differential equation, taking the form of a wave equation, can then be constructed for each variable; the system of equations can be subsequently reduced in complexity on the basis of symmetries.

We can illustrate this explicitly using a scalar test field. In particular, we focus on the scattering of a massless scalar test field minimally coupled to gravity within a Schwarzschild black hole space-time, under linearised gravity (i.e. assuming there is negligible backreaction from the space-time). The metric is of the form,

$$g^{\rm BH}_{\mu\nu} dx^\mu dx^\nu = -f(r) dt^2 \; + \; f(r)^{-1} dr^2 \; + \; r^2 \left({\rm d}\theta^2 + \sin^2\theta {\rm d}\phi^2 \right) \,, \tag{2.2}$$

written in terms of the Schwarzschild coordinates (t, r, θ, ϕ), with $t \in (-\infty, +\infty)$, $\theta \in (0, \pi)$, and $\phi \in (0, 2\pi)$; ${\rm d}\theta^2 + \sin^2\theta {\rm d}\phi^2$ serves as the line element on the 2-sphere $\mathbb{S}^2$. Here, the metric function is $f(r) = 1 - r_+/r$, with an event horizon given by $r_+ = 2M$ in geometric units, $c = G = 1$ [4, 131]. The black hole is thus static, electrically-neutral, and spherically-symmetric; it is fully characterised by its mass M [32].

Though massless scalar fields do not feature in the SM, the wave equation governing the behaviour of a weak gravitational field in curved space-time closely resembles its spin-0 counterpart, and suffices to relay the main characteristics of the perturbing field.

To describe the full system, we consider the Einstein-Hilbert gravitational action,

$$S = \frac{1}{16\pi G} \int d^4x \sqrt{-g} R + \int d^4x \sqrt{-g} \left[- \left(\partial_\mu \Phi \right)^\dagger \partial^\mu \Phi \right] \,, \tag{2.3}$$

following the conventions of Eq. (1.1). The equations of motion satisfied by the fields $g_{\mu\nu}$ and Φ are the massless Klein-Gordon equation for a curved space-time,

$$\nabla_\mu \nabla^\mu \Phi = \frac{1}{\sqrt{-g}} \partial_\mu \left(\sqrt{-g} g^{\mu\nu} \partial_\nu \Phi \right) = 0 \tag{2.4}$$

and the 4D Einstein field equations, Eq. (1.1), with $T_{\mu\nu}$ quadratic in Φ. For maximally-symmetric vacuum solutions, $T^{\rm BG}_{\mu\nu} = 0$.

[8] In Refs [135–137], it was shown that for gravitational perturbations in arbitrary dimensions, a third parity is required to capture the additional degrees of freedom: a "tensor-mode". Following this convention, we refer to the odd-parity/axial/Regge-Wheeler [134] and even-parity/polar/Zerilli [138] as "vector-mode" and "scalar-mode", respectively.

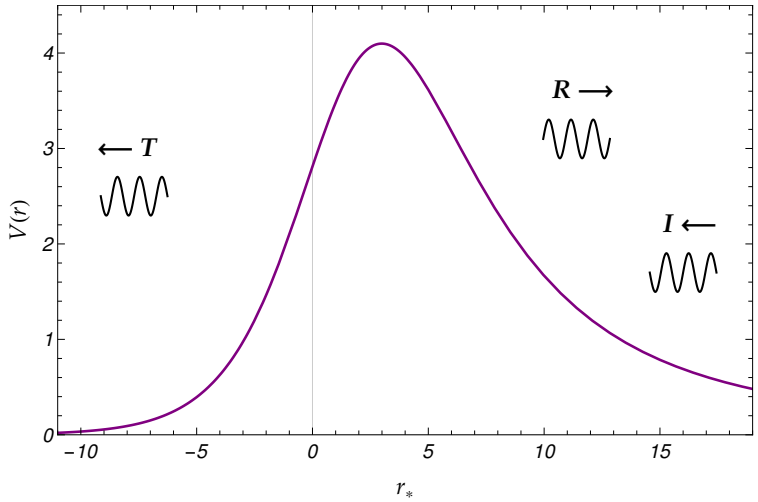

Figure 2.1: *The Schwarzschild effective potential plotted against the tortoise coordinate.*

As detailed in Chandrasekhar's book [131], the behaviour of a perturbed black hole within a classical GR context can be inferred by substituting the perturbed metric and ansatz into the Einstein field equations, and then solving for the vacuum solution. In this context, the linearised equations of motion for ϕ and $\delta_{\mu\nu}$ decouple when $\Phi^{\rm BG} = 0$, allowing for the metric fluctuations $\delta_{\mu\nu}$ to be set to zero.

On the basis of the black hole's static nature and spherical symmetry, the ansatz can be subjected to the decomposition,

$$\phi_{\ell mn}(t, r, \theta, \varphi) = \int_{-\infty}^{+\infty} d\omega \sum_{\ell,m}^{\infty} \frac{\psi_{\ell n}(r)}{r}\, Y^{s}_{m\ell}(\theta)\, e^{-i\omega_{\ell n} t} e^{+i\omega_{\ell n}\varphi}\,, \tag{2.5}$$

where the angular behaviour is described through scalar spherical harmonics

$$\nabla^2 Y^{s}_{m\ell}(\theta,\phi) = -\frac{\ell(\ell+1)}{r^2} Y^{s}_{m\ell}(\theta,\phi)\,. \tag{2.6}$$

For notational simplicity, we shall drop subscripts from this point onwards.

Since the black hole is static and non-rotating, the behaviour of the system is fully encapsulated by the radial component. We introduce the tortoise coordinate $r_\star = \int dr/f(r)$ which acts as a bijection from $(r_+, +\infty)$ to $(-\infty, +\infty)$, thereby mapping the event horizon to negative spatial infinity. With this and some minor algebraic manipulation $\phi = \psi/r$, we obtain the ordinary differential equation,

$$\frac{d^2\psi}{dr_\star^2} + \Big(\omega^2 - V_{eff}\Big)\,\psi(r_\star) = 0\,, \tag{2.7}$$

where

$$V_{eff} = f(r)\left(\frac{\ell(\ell+1)}{r^2} + \frac{f'(r)}{r}\right)\,. \tag{2.8}$$

V_{eff} serves as the model-dependent component of the wave equation, and encodes information about the curvature of the black hole space-time and the character of the test-field. In Fig. (2.1), we demonstrate that the potential is real and asymptotes towards constant values at the boundaries, *viz*.

$$V_{eff}(r_\star \to -\infty) \sim k_+^2\,, \qquad V_{eff}(r_\star \to +\infty) \sim k_\infty^2\,. \tag{2.9}$$

Recall that the distinguishing feature of the black hole is its event horizon, which we classically consider to be a one-way membrane from which no interior object can escape. As such, any physical solution to

Eq. (2.7) must then obey purely ingoing boundary conditions at the horizon. If we consider a scattering problem with monochromatic frequency ω, the asymptotic boundary conditions

$$\psi \sim \begin{cases} \mathcal{T} e^{-ik_+ r_\star} , & r_\star \to -\infty , \\ \mathcal{I} e^{-ik_+ r_\star} + \mathcal{R} e^{+ik_+ r_\star} , & r_\star \to +\infty . \end{cases} \tag{2.10}$$

These describe an incident wave of amplitude $\mathcal{I}$ ingoing from spatial infinity, then partially reflected and transmitted with amplitudes $\mathcal{R}$ and $\mathcal{T}$, respectively.

We emphasise that the nature of the potential (real) and symmetries of the system (*viz.* $t \to -t$ and $\omega \to -\omega$) allow for the additional solution to Eq. (2.7): $\overline{\psi}$, the complex conjugate of ψ. The Wronskian of ψ and $\overline{\psi}$ evaluated near the horizon and spatial infinity is

$$W\big|_{r_\star \to -\infty} = -2ik_+ |\mathcal{T}|^2 , \qquad W\big|_{r_\star \to +\infty} = 2ik_\infty \left(|\mathcal{R}|^2 - |\mathcal{I}|^2 \right) . \tag{2.11}$$

A constant non-zero Wronskian implies linearly-independent solutions. From Eq. (2.11), we obtain the relationship between reflection and transmission coefficients,

$$|\mathcal{R}|^2 = |\mathcal{I}|^2 - \frac{k_+}{k_\infty} |\mathcal{T}|^2 . \tag{2.12}$$

For scattering off of a "perfect absorber", $k_+/k_\infty > 0$ such that $|\mathcal{R}|^2 < |\mathcal{I}|^2$. When $k_+/k_\infty < 0$, however, $|\mathcal{R}|^2 > |\mathcal{I}|^2$. This latter condition is known as "superradiance": at the classical level, this describes the mechanism by which incoming radiation is reflected and amplified as it scatters off of a barrier potential. We shall discuss how this phenomenon occurs in the black hole context in Section 2.3.1 and elaborate on the charged black hole case in Section 4.1.1.

To elevate Eq. (2.7) under Eq. (2.10) to a QNM problem, we impose a further physically-motivated boundary condition: purely outgoing radiation at infinity. From the Green's function analysis, we obtain a formal justification for this additional constraint.

2.1.1 The Green's function approach and quasinormal excitation

When studying the QNM contribution to the full black hole response in the wake of a perturbation, we may consider the Green's function solution to the inhomogeneous wave equation [51, 52]. We consider here a retarded Green function for a scalar field on a Schwarzschild background spacetime,

$$\Box_x G_{\rm ret}(x, x') = \frac{1}{\sqrt{-g}} \partial_\mu \left(\sqrt{-g} g^{\mu\nu} \partial_\nu \right) G_{\rm ret} = \delta^{(4)}(x - x') . \tag{2.13}$$

Eq. (2.13), the scalar wave equation, is separable in the frequency domain for spherically-symmetric black hole spacetimes. We may therefore express the Green function through a spectral decomposition in the Schwarzschild spacetime

$$G_{\rm ret}(x, x') = \frac{1}{2\pi r r'} \int_{-\infty + ic}^{+\infty + ic} d\omega \; \tilde{G}_{\ell\omega}(r, r') e^{-i\omega(t - t')} \times \sum_{\ell=0}^{\infty} (2\ell + 1) P_\ell(\cos\gamma) . \tag{2.14}$$

Here, x, x' represent spacetime points at radii r, r' that are separated by the coordinate time $t - t'$ and the spatial angle γ (for which $\cos\gamma = \cos\theta \cos\theta' + \sin\theta \sin\theta'$). The constant c is positive. $\tilde{G}_{\ell\omega}(r, r')$ is the radial Green function that satisfies

$$\left[\frac{d^2}{dr_\star^2} + \omega^2 - V(r) \right] \tilde{G}_{\ell\omega}(r, r') = -\delta(r_\star - r'_\star) . \tag{2.15}$$

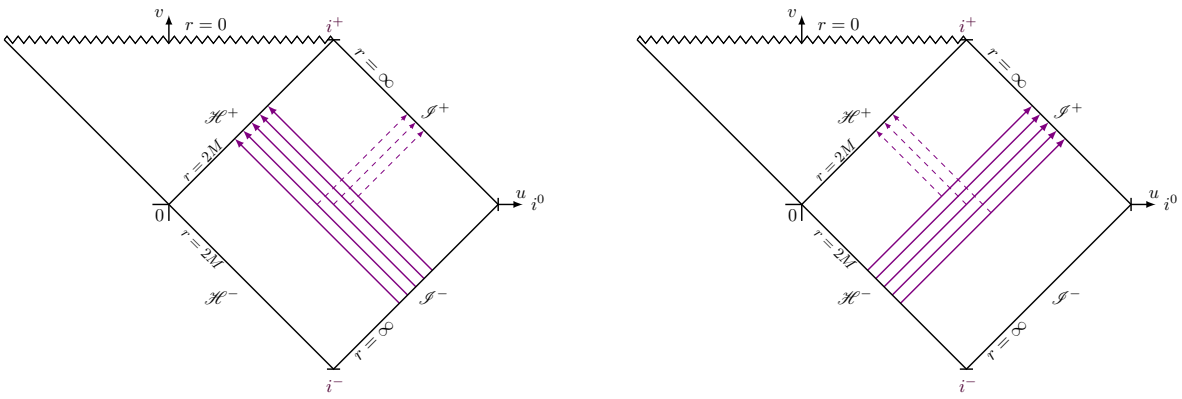

(a) *In-mode: purely ingoing waves at* $\mathscr{H}^+$. (b) *Up-mode: purely outgoing waves at* $\mathscr{I}^+$.

Figure 2.2: *Conformal diagrams of the Schwarzschild black hole space-time depicting the linearly-independent solutions to the scalar wave equation, Eqs* (2.16) *and* 2.17) (*adapted from Ref.* [139]).

We make use of the tortoise coordinate $r_\star = \int dr/f(r)$ which acts as a bijection from $(r_H, +\infty)$ to $(-\infty, +\infty)$, promoting the range of the mode propagation to the whole real line. For Eq. (2.15), an ingoing boundary condition is used at the black hole horizon and an outgoing is used at spatial infinity. The Green function is constructed using the two homogenous solutions of this Eq. (2.15), such that at the horizon

$$u^{in}_{\ell\omega} \sim \begin{cases} e^{-i\omega r_\star}\,, & r_\star \to -\infty\,, \\ A^{out}_{\ell\omega} e^{+i\omega r_\star} + A^{in}_{\ell\omega} e^{-i\omega r_\star}\,, & r_\star \to +\infty\,, \end{cases} \tag{2.16}$$

while at spatial infinity,

$$u^{up}_{\ell\omega} \sim \begin{cases} B^{out}_{\ell\omega} e^{+i\omega r_\star} + B^{in}_{\ell\omega} e^{-i\omega r_\star}\,, & r_\star \to -\infty \\ e^{+i\omega r_\star}\,, & r_\star \to +\infty\,. \end{cases} \tag{2.17}$$

$A^{out}_{\ell\omega}$, $A^{in}_{\ell\omega}$, $B^{out}_{\ell\omega}$, and $B^{in}_{\ell\omega}$ are complex constants. QNMs are modes with complex frequencies such that $A^{in}_{\ell\omega}, B^{out}_{\ell\omega} = 0$. QNMs are purely ingoing at the horizon and purely outgoing at spatial infinity.

Specifically, the radial Green function can be written as

$$\tilde{G}_{\ell m\omega}(r, r') = -\frac{u_{in}(r_<) u_{out}(r_>)}{W_{\ell\omega}}\,, \tag{2.18}$$

where we denote $\min(r, r')$ and $\max(r, r')$ by $r_<$ and $r_>$, respectively. The Wronskian is

$$W_{\ell\omega} = u^{in}_{\ell\omega} \frac{d}{dr_\star} u^{up}_{\ell\omega} - u^{up}_{\ell\omega} \frac{d}{dr_\star} u^{in}_{\ell\omega} = 2i\omega A^{in}_{\ell\omega}\,. \tag{2.19}$$

By the Wronskian theorem, the solutions are linearly independent. However, the poles of the Green's function are located at the zeroes of $A^{in}_{\ell\omega}$ in the complex ω-plane, which we shall call $\{\omega_p\}$. When $\omega = \omega_p$, $u^{in}_{\ell\omega}$ and $u^{up}_{\ell\omega}$ become equivalent. This follows naturally, with $W_{\ell\omega} = 0$ implying linearly-dependent solutions. This yields the QNM boundary conditions,

$$\psi(t, r_\star) \sim e^{-i\omega(t + r_\star)}\,, \qquad r_\star \to -\infty \tag{2.20}$$

$$\psi(t, r_\star) \sim e^{-i\omega(t - r_\star)}\,, \qquad r_\star \to +\infty\,. \tag{2.21}$$

and demonstrates explicitly that QNFs correspond to the poles of the Green's function.

Let us elaborate on how the boundary conditions are refined to extract the QNFs. For some complex

frequencies $\omega_{\ell n}$, the ingoing wave solution u^{in} (Eq. (2.16)) also satisfies an outgoing boundary condition at infinity, namely $A^{in}_{\ell\omega} = 0$. This implies that the ingoing solution is a multiple of the outgoing solution, which in turn tells us that u^{in} and u^{up} are degenerate at these frequencies. Consequently, u^{up} (Eq. (2.17)) must satisfy an ingoing wave condition at the black hole horizon, namely $B^{out}_{\ell\omega} = 0$. At these QNFs, we observe that $B^{in}_{\ell\omega_{\ell n}} A^{out}_{\ell\omega_{\ell n}} = 1$.

As a visual aide, we plot the boundary conditions Eq. (2.16) and Eq. (2.17) in Fig. 2.2, which correspond to the future horizon $\mathscr{H}^+$ and the future null infinity $\mathscr{I}^+$, respectively (see Table B.1 for details on these conventions). In each of these figures, we have used solid lines to denote those corresponding exclusively to the QNM boundary conditions of Eqs (2.20) and Eq. (2.21), respectively.

We evaluate the Green function by substituting Eq. (2.18) into the spectral decomposition, Eq. (2.14). To evaluate the integral, we apply the residue theorem and divide into:

(i) the "direct part" i.e. the integral over the high frequency component;

(ii) the integral on the branch cut along the $\mathfrak{I}m\{\omega\}$ axis;

(iii) the QNM contribution.

Part (i) quickly approaches zero after the initial pulse [140], whereas part (ii) influences the power-law spectrum at late times while also contributing to intermediate and late times. Here, the focus is on part (iii), where the QNMs affect intermediate and early times.

With this in mind, let us return to the problem at hand. If we exploit the fact that u^{up} and u^{in} are degenerate at the QNFs, we can write the QNM contribution to the Green function within the Schwarzschild spacetime using Eq. (2.14),

$$G_{\rm QNM}(x,x') = \frac{2}{rr'}\mathfrak{R}e\left\{\sum_{\ell}^{\infty}\sum_{n}^{\infty}(2\ell+1)P_\ell(\cos\gamma)\times\mathcal{B}_{\ell n}\tilde{u}_{in}(r)\tilde{u}_{in}(r')e^{-i\omega_{\ell n}T}\right\}, \tag{2.22}$$

where the normalised ingoing wavefunction,

$$\tilde{u}^{in}(r) \equiv u_{in}(r)\times\left[A^{out}_{\ell\omega}e^{i\omega_{\ell n}r_\star}\right]^{-1}, \tag{2.23}$$

behaves as $\tilde{u}_{in}(r)\sim 1$ for $r\to+\infty$. The "reflection time" [50],

$$T = t - t' - r_\star - r'_\star, \tag{2.24}$$

refers to the estimate of the time taken for the incident wave to travel from its initial position at $r'_\star$ to the black hole, and for the reflected wave to reach an observer at $r_\star$ [139]. QNMs are expected to dominate the spectrum when $T > 0$. In this regime, Eq. (2.22) converges: higher overtones are suppressed in the sum over n. However, when $T < 0$, Eq. (2.22) becomes ill-defined due to the exponential divergence of the $e^{-i\omega_{\ell n}T}$ factor. Within this black hole context, we make the reasonable assumption that the initial data (i.e. the incident radiation) only has compact support far away from the black hole, and that the observer is also located in the large-$r_\star$ regime. In this way, we need only consider the asymptotic behaviour of the wavefunctions at large $r_\star$.

Finally, this brings us to the data-independent contribution to Eq. (2.22): the QNEF, defined as the amount by which the QNMs are excited by the δ-function in Eq. (2.13), and expressed as

$$\mathcal{B}_{\ell n} \equiv \left[\frac{A^{out}_{\ell\omega}}{2\omega}\left(\frac{\partial A^{in}_{\ell\omega}}{\partial\omega}\right)^{-1}\right]_{\omega=\omega_{\ell n}}. \tag{2.25}$$

Recall that in Chapter 1, we introduced the QNEF as a quantity that indicates how and by how much a

particular QNM is excited. With the increasing sensitivity of GW detectors to higher harmonics, the need to distinguish one mode from another within the superposition of observed QNMs becomes more pressing. For this reason, precise values of the QNEF are required. Furthermore, as a "no-hair" factor dependent exclusively on its associated black hole's parameters, the QNEF is especially useful in the development of waveform models and the testing of GR [49]. With these motivations in mind, we dedicate Section 2.4 to the computation of the QNEF at higher orders in ℓ for the massless scalar QNMs within a Schwarzschild black hole space-time.

Let us close this section with an example of the leading-order QNEF of Ref. [50],

$$\mathcal{B}_{\ell n} = i^{1/2} L^{-1/2} \frac{\sqrt{27}\ \exp\{\zeta/\sqrt{27}\}}{(2+\sqrt{3})\sqrt{\pi}} \exp\{2i\zeta L/\sqrt{27}\} \frac{(-iL)^n}{n!} \left(\frac{216\ \exp\{2\zeta/\sqrt{27}\}}{(2+\sqrt{3})^2} \right)^n , \tag{2.26}$$

for $\zeta = 3 - \sqrt{27} + 4\ln 2 - 6\ln(2+\sqrt{3})$ and $L = \ell + 1/2$. We plot the results for the $\ell = 2$ QNEF for the first several harmonics and overtones in Fig. 2.3. There, the QNEF can be seen to increase with n, bar the slight fall for $n = 1$. We note with interest that the contribution is at a maximum when $\ell = n$ for each QNEF, and that the $(\ell, n) = (0, 0)$ and $(\ell, n) = (2, 1)$ points are of a similar magnitude.

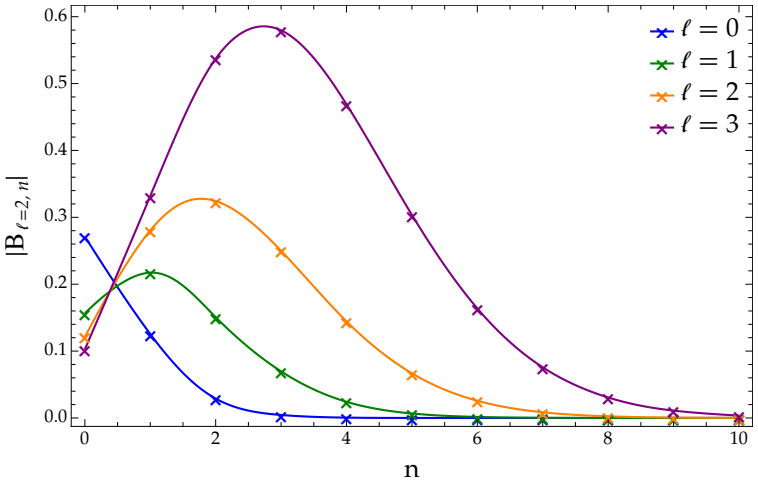

Figure 2.3: *The magnitude of the $\ell = 0, 1, 2, 3$ QNEFs for increasing values of n at leading order.*

Through this description of the QNM as a scattering problem, we have derived the boundary conditions that must be imposed upon Eq. (2.7) in order to perform the QNM computation. However, note carefully that Eq. (2.22) conveys only the late-time component of the black hole signal for some specified initial data. Though there is a countable infinity of QNMs for each multipolar number ℓ for each overtone n, QNMs do not form a complete set. Recall that Eq. (2.22) diverges for early times $T < 0$ and fails to represent the power-law tail that dominates at very late times.

Intuitively, we can appreciate this on the basis that the QNM system is intrinsically damped and therefore not time-symmetric. As a consequence, the eigenvalue problem is non-Hermitian and the eigenvalues are complex. The corresponding eigenfunctions are then not normalisable and therefore do not form a complete set (see [130, 139] for further discussion). To confront these technical difficulties, a wide array of tools have been established to compute QNFs. We address this topic in the next section, and highlight a few key methods that we utilise in our QNM-based investigations.

2.2 Semi-classical approaches to QNM problems

On the basis of spherical symmetry and harmonic time dependence, the QNM behaviour in static black hole space-times can be shown to reduce to a simple radial wave equation, as first demonstrated in Refs [134, 138] for the Schwarzschild case. A wide range of methods have been developed to determine QNM solutions from such wave equations, including methods that are "exact" (e.g. direct integration methods [141, 142], the continued fraction method [143], pseudospectral methods [144, 145], etc.) and numerical (e.g. the asymptotic iteration method [146, 147], the Horowitz-Hubeny approach [148], etc.). Of these, we highlight

(*i*) "inverse-potential methods" that approximate the effective potential with an inverse Pöschl-Teller potential [149] for which bound-state solutions are known to determine the QNF spectrum [150];

(*ii*) "WKB-based methods" that adapt the semi-classical technique to the QNM problem to compute QNFs in the $\ell \geq n$ regime [151–153] at sixth-order [154] and beyond (see Ref. [155]);

(*iii*) "photon-orbit methods" such as the inverse multipolar expansion method [156] that harnesses the known link between QNMs and unstable null geodesics [157] to construct an iterative technique that solves Eq. (2.7) with increasing accuracy for large values of ℓ [158].

This is by no means an exhaustive list; for further insights, consider Refs [14, 47, 159, 160].

The notion that QNM computation is an art in and of itself [161] can be attributed to the extensive research that has accumulated over the course of several decades to establish specialised techniques tailored to generate accurate results for specific QNM scenarios (see Refs [14, 47]). As enforced by Ref. [155], the method chosen must be informed by the nature of the problem at hand to avoid producing misleading results. Here and in Chapter 6, we are interested in computing QNFs that are the most likely to be detected by modern or future GW detectors; we need to consider QNFs that dominate the QNM spectrum. As such, we focus on the fundamental (and least damped) mode corresponding to $n = 0$ and $\ell = 2$. Though the QNMs of a Kerr black hole would represent the most physically relevant case, we focus on the Schwarzschild black hole spacetime as a starting point for the sake of simplicity. The azimuthal number m is therefore taken to be zero and is subsequently inconsequential to our analysis.

In this section, we shall outline three techniques that prove accurate for the $\ell \geq n$ regime, referred to in the literature as the Pöschl-Teller [150, 162, 163] method, the WKB [151–153] technique, and the Dolan-Ottewill [156] inverse multipolar expansion method. We apply these to the computation of massive QNFs and present the results thereof in Section 2.3.

The Pöschl-Teller method

There are few techniques established within the QNM literature that generate exact solutions for QNFs. As stipulated earlier, this is due in part to the mathematical difficulties introduced by the slowly decaying nature of the potential as $r \to \infty$. To circumvent this problem, a method was developed in Refs [150, 162, 163] that exploits the relationship between the QNMs of a potential barrier and the bound states of the inverted potential [162]. The procedure involves fitting the effective QNM potential featured in Eq. (2.7) to a well-understood substitute (characterised by exponential decay and other key common features) for which analytic solutions are known.

The justification for this rests on the symmetry of the boundary conditions of Eqs (2.20) and (2.21). Suppose we can parametrise the potential of Eq. (2.7) as $V(r_\star, p)$, where p represents a set of parameters associated with the potential; let us also claim that $\psi = \psi(r_\star, p)$ and $\omega = \omega(p)$. From the boundary conditions, we can introduce the transformations $r_\star \to -ir$ and $p \to p'$. We may consider the potential to be invariant under these transformations,

$$V(r_\star, p) = V(-ir_\star, p') \,. \tag{2.27}$$

If we define also $\psi(r_\star, p) = \varphi(-ir_\star, p')$ and $\omega(p) = \Omega(p')$, then we may rewrite Eq. (2.7) as

$$\frac{d^2\varphi}{dr_\star^2} + \left(-\Omega^2 + V\right)\varphi = 0\,, \tag{2.28}$$

for which the boundary conditions become $\varphi \sim e^{\mp\Omega r_\star}$ as $r_\star \to \mp\infty$. In other words, the wavefunction vanishes at the boundaries. The QNM problem is thereby reduced to a bound-state problem for an inverted potential $V \to -V$.

In the case of several black hole spacetimes[9], the Pöschl-Teller potential [149]

$$V_{PT} = \frac{V_0}{\cosh^2 p(r_\star - r_\star^{max})} \tag{2.29}$$

can serve as V in Eq. (2.28). Here, $r_\star = r_\star^{max}$ is the point at which V_{PT} attains its maximum, the height of which is given by $V_0 = V(r_\star^{max})$; the curvature of V_{PT} at its maximum is $V'' = -2V_0p^2$.

From the well-known bound-state solutions [150]

$$\Omega = p'\left[-\left(n + \frac{1}{2}\right) + \left(\frac{1}{4} + \frac{V_0}{(p')^2}\right)\right]\,, \tag{2.30}$$

the use of the inverse transformation $p' = ip$ then yields the QNF spectrum,

$$\omega = \pm\sqrt{V_0 - \frac{1}{4}p^2} - ip\left(n + \frac{1}{2}\right)\,, \qquad n \in \mathbb{N}\,. \tag{2.31}$$

The WKB method

For a spherically-symmetric black hole, QNMs can be understood as waves trapped at the unstable circular null geodesic, albeit gradually leaking [157]. In Refs [151–153], this scenario was interpreted as a scattering problem, where the effective QNM potential serves as a potential barrier that tends to constant values in the opposing asymptotic limits. From this framing, a modified WKB method was developed that exploited the Bohr-Sommerfield quantisation condition of quantum mechanics to establish a semi-analytical technique to compute black hole QNFs.

As a starting point, Eq. (2.7) is rewritten as

$$\frac{d^2\psi}{dx^2} + Q(x)\psi(x) = 0\,, \tag{2.32}$$

where $x = r_\star$ and $Q(x) = \omega^2 - V$. Following the usual procedure, the method requires the matching of asymptotic WKB expansions with a solution constructed around the peak of the potential $Q_0 = Q(x_0)$. This matching is performed across "matching regions" defined near the classical turning points defined at $Q(x) = 0$. If the turning points lie close to one another (i.e. $-Q_0 \ll Q(\pm\infty)$), then a Taylor series expansion about x_0 may be introduced such that

$$Q(x) \approx Q_0 + \frac{1}{2}Q_0''(x - x_0)^2 + ... \tag{2.33}$$

This expansion is then substituted into Eq. (2.32) and solved using parabolic cylinder functions [164]. In

[9] While the use of the inverted Pöschl-Teller potential leads to the production of QNFs with errors $> 1\%$ for Schwarzschild black holes with $\ell > 2$, greater accuracy can be found for Schwarzschild-de Sitter and RNdS black hole spacetimes, where the Pöschl-Teller potential exactly matches [47].

the asymptotic regions, the WKB solution is given by

$$\psi \sim \exp\left\{\sum_{k=0}^{\infty}\frac{S_k(x)\epsilon^k}{\epsilon}\right\}, \tag{2.34}$$

where ϵ is a parameter used to keep track of the expansion orders. The expressions for $S_k(x)$ are solved for by collecting like terms. It is important to note that Eq. (2.34) corresponds to four solutions, to account for ingoing and outgoing solutions on both sides of the potential.

Upon the completion of the matching procedure, an expression for the QNF may be extracted. At the sixth order, it was determined in Ref. [154]that

$$\frac{i(\omega^2-V_0)}{\sqrt{-2V_0''}}-\sum_{i=2}^{6}\Lambda_i = n+\frac{1}{2}, \qquad n\in\mathbb{N}. \tag{2.35}$$

Here, Λ_i represents correction terms dependent on the value of the potential and its derivatives (up to and including order i). While the WKB method is far more successful than we would expect [53], it is understood that this method produces more accurate results for QNFs when $\ell \gtrsim 2$ at lower orders [165]. However, even at higher orders (i.e. see the 12th-order WKB method established in Refs [166, 167]), the method still works best for $\ell > n$, with further accuracy found at higher multipolar values. In other words, results are not guaranteed to be more precise with each subsequent WKB order. The WKB method converges only asymptotically, and is truly accurate only in the eikonal regime [155].

The Dolan-Ottewill method

In the eikonal limit, the spin-2 QNF spectrum corresponding to a 4D Schwarzschild black hole is given by

$$\omega_{n,\ell\to\infty} = \Omega\left(\ell+\frac{1}{2}\right) - i\overline{\Lambda}\left(n+\frac{1}{2}\right)+\mathcal{O}(\ell^{-1}), \qquad \Omega=\overline{\Lambda}=\frac{1}{\sqrt{27}M}, \tag{2.36}$$

for fixed n [157]. Ω here refers to the orbital frequency of the $r_{orb} = 3r_+/2 = 3M$ photon sphere[10]; in the large-ℓ limit, it is equivalent to the Lyapunov exponent $\overline{\Lambda}$ that indicates the decay time scale of the gravitational perturbations. This behaviour has been observed in perturbing test fields of spin $s \in \{0, 1/2, 1, 3/2\}$ within the region of a Schwarzschild black hole [158, 163, 168–172]. Note that this correspondence between eikonal QNMs and the parameters of circular null geodesics does not necessarily hold in other contexts e.g. for black holes in asymptotically-de Sitter space-time [173, 174].

In Ref. [156], Dolan and Ottewill presented a method by which to compute QNM wavefunctions and frequencies invoking this relationship between photon orbits and the large-ℓ asymptotics of QNMs. The method centres on an ansatz for the wavefunction that is inspired by the trajectory of a distant photon along a null geodesic that ends on the photon sphere, locked in orbit about a spherically-symmetric black hole. Here, we shall briefly present a derivation of this ansatz. To extract the parameters of interest, we follow Refs [131, 168] in studying the equation of motion for a test particle near the spherically-symmetric black hole. The Lagrangian in the equatorial plane ($\theta = \pi/2$) is written as

$$\mathcal{L} = \frac{1}{2}g_{\mu\nu}\dot{x}^\mu\dot{x}^\nu = \frac{1}{2}\left(-f(r)\dot{t}^2+f(r)^{-1}\dot{r}^2+r^2\dot{\phi}^2\right), \tag{2.37}$$

where the overdot represents a derivative with respect to an affine parameter. From the corresponding

[10] "Photon sphere" refers to the surface formed from the collection of null geodesics along which gravitationally-entrapped photons orbit a black hole. For a static black hole, photons orbit a black hole at this fixed radius; the orbit itself is unstable against radial perturbations.

conjugate momenta, we obtain the angular momentum $\overline{L}$ and the photon energy $\overline{E}$,

$$\dot{\phi} = \frac{\overline{L}}{r^2} , \qquad \dot{t} = \frac{\overline{E}}{f(r)} . \tag{2.38}$$

These expressions allow us to write the Hamiltonian as

$$\begin{aligned} \mathcal{H} &= \left(p_t \dot{t} + p_\phi \dot{\phi} + p_r \dot{r} - \mathcal{L}\right) \\ &\Rightarrow \quad 2\mathcal{H} = \overline{E}\dot{t} - \overline{L}\dot{\phi} - f(r)^{-1}\dot{r}^2 = \delta_1 , \end{aligned} \tag{2.39}$$

for which $\delta_1 = 0$ for null geodesics. Combining $\dot{r} \equiv V_r$ [168] with the condition for circular orbits $V_r = V_r' = 0$ [175] produces

$$0 = \frac{\overline{E}^2}{\overline{L}^2} - \frac{f(r)}{r^2} . \tag{2.40}$$

From this, Dolan and Ottewill define the function

$$k(r) = \frac{1}{b^2} - \frac{f(r)}{r^2} , \tag{2.41}$$

where $b = \overline{L}/\overline{E}$ is the impact parameter. From these considerations, the Dolan-Ottewill ansatz is established as

$$u_{\ell\omega}(r) = e^{i\omega z(x)} v(r) , \quad z(x) = \int^x \rho(r) dx , \tag{2.42}$$

where the QNF is expressed as a linear expansion in inverse multipolar numbers parameterised as $L = \ell + 1/2$,

$$\omega_{\ell n} = \sum_{k=-1} \overline{\omega}_k L^{-k} . \tag{2.43}$$

The coefficients $\overline{\omega}_k$ are functions of the overtone number n. Similarly, the function $v(r)$ is a series expansion in L^{-k},

$$v_{\ell n}(r) = \left[\left(1 - \frac{3}{r}\right)^n + \sum_{i=1}^{n} \sum_{j=1}^{\infty} \alpha_{ijn} L^{-j} \left(1 - \frac{3}{r}\right)^{n-i} \right] \times \exp\left\{ \sum_{k=0} S_{kn}(r) L^{-k} \right\} , \tag{2.44}$$

where we have set $M = 1$. For the least-damped case of $n = 0$, the function simplifies to

$$v_{\ell 0}(r) = \exp\left\{ \sum_{k=0} S_k(r) L^{-k} \right\} . \tag{2.45}$$

The function within the integrand of Eq. (2.42) is given by $\rho(r) = b_c k_c(r)$, with $x = \int dr/f(r)$ serving as the usual tortoise coordinate. The subscript c denotes a quantity evaluated at the critical radius $r_c = 2f(r)/\partial_r f(r)|_{r=r_c}$ at which $k^2(r, b_c)$ has repeated roots and satisfies the condition $k^2(r_c, b_c) = \partial_r k^2(r_c, b_c) = 0$.

The ansatz must satisfy the boundary conditions,

$$f(r) \to 0 , \quad b_c k_c(r) \to -1 \quad \text{as} \quad x \to -\infty , \tag{2.46}$$

$$f(r)/r^2 \to 0 , \quad b_c k_c(r) \to +1 \quad \text{as} \quad x \to +\infty . \tag{2.47}$$

These convey that the event horizon is encountered as $x \to -\infty$ and an asymptotically-flat region is approached as $x \to +\infty$. Finally, the ansatz may be substituted into Eq. (2.7) to obtain

$$f(r)\frac{d}{dr}\left(f(r)\frac{dv}{dr}\right) + 2i\omega\rho(r)\frac{dv}{dr} + \left[i\omega f(r)\frac{d\rho}{dr} + \left(1 - \rho(r)^2\right)\omega^2 - V(r)\right] v(r) = 0 . \tag{2.48}$$

The primary objective of the Dolan-Ottewill multipolar expansion method is to solve for the coefficients of Eq. (2.43) using Eq. (2.48) in an iterative fashion, order by order. To compute $\overline{\omega}_{k+1}$ for $k \geq 0$, we require an expression for dS_{kn}/dr. Through solving for the quantities of $\overline{\omega}_k$ and dS_{kn}/dr, the QNF can be generated as a function of L. Similarly, the radial component of the wavefunction in Eq. (2.44) can be constructed from the explicit expressions for $S_{kn}(r)$. We shall see in Section 2.4 how the latter enables us to express the wavefunction, as well as the QNEF defined in Eq. (2.25).

For the Schwarzschild black hole spacetime, the components of the ansatz are given by $r_c = 3$, $b_c = \sqrt{27}$ for $M = 1$, and thus $\rho(r) = (1 - 3/r)\,(1 + 6/r)^{1/2}$. For a scalar field, Eq. (2.43) to order $\mathcal{O}(L^{-6})$ yields

$$\sqrt{27}\omega_{\ell 0} = L - \frac{i}{2} + \frac{7}{216}L^{-1} - \frac{137i}{7776}L^{-2} + \frac{2615}{1259712}L^{-3} + \frac{590983i}{362797056L}L^{-4} - \frac{42573661}{39182082048}L^{-5} + \frac{11084613257i}{8463329722368}L^{-6}$$

for $n = 0$, as demonstrated in Ref. [156] and confirmed in Ref. [158]. Note that odd (even) values of k correspond to real (imaginary) expansion terms.

We shall now apply these techniques to a QNM problem: the massive scalar perturbations of a Schwarzschild black hole. Within the QNM literature, massive scalar QNMs have been approached primarily as a numerical problem (see e.g. Refs [176–178]). However, a study of the mass parameter μ can also offer insights into the fundamental nature of QNMs and their behaviour in astrophysical contexts. In the section that follows, we shall illustrate the role played by μ in QNM studies, which shall in turn provide the foundations for our later analyses in Chapters 4 and 6.

2.3 The massive QNM eigenvalue problem

As demonstrated in Eq. (2.7), the radial component of black hole QNMs can be written as a source-less wave equation. With the introduction of the QNM boundary conditions, we have already discussed how we can approach the intrinsically dissipative QNM system as a technically-challenging eigenvalue problem. In the case of the massive spin-0 QNM, we consider a massive Klein-Gordon equation in curved (Schwarzschild) space-time. After introducing the spherical harmonic decomposition, the radial component of the QNM reduces to Eq. (2.7). The effective potential for the scalar test field is augmented with a mass term μ,

$$V(r) = f(r)\left[\frac{\ell(\ell+1)}{r^2} + \frac{f'(r)}{r} + \mu^2\right] . \tag{2.49}$$

Let us briefly discuss how the QNM boundary conditions manifest in the case of a non-zero field mass.

Recall that in the frequency-domain representation, the exponentially decaying behaviour within an asymptotically-flat space-time follows the harmonic temporal dependence,

$$\psi(t,r) = \psi(\omega,r)e^{-i\omega t} , \tag{2.50}$$

where $\Im m\{\omega\} < 0$. As we approach the horizon (spatial infinity), $V(r) \sim 0$ ($V(r) \sim \mu$) and the boundary conditions are

$$\psi(\omega,r) \sim \begin{cases} e^{-i\omega r_\star} , & r_\star \to -\infty , \\ A(\omega)e^{-wr_\star} + B(\omega)e^{+wr_\star} , & r_\star \to +\infty , \end{cases} \tag{2.51}$$

Here, $A(\omega)$ and $B(\omega)$ are complex coefficients and $w = \sqrt{\mu^2 - \omega^2}$ for $\Re e\{w\} > 0$. From the values of the complex coefficients, we can discriminate between "quasibound states" and "QNMs". Upon setting $B(\omega) = 0$, we obtain the former: "quasibound states" localised within the vicinity of the black hole decay exponentially as they travel outwards from the black hole. For QNM behaviour, $A(\omega) = 0$ such that waves

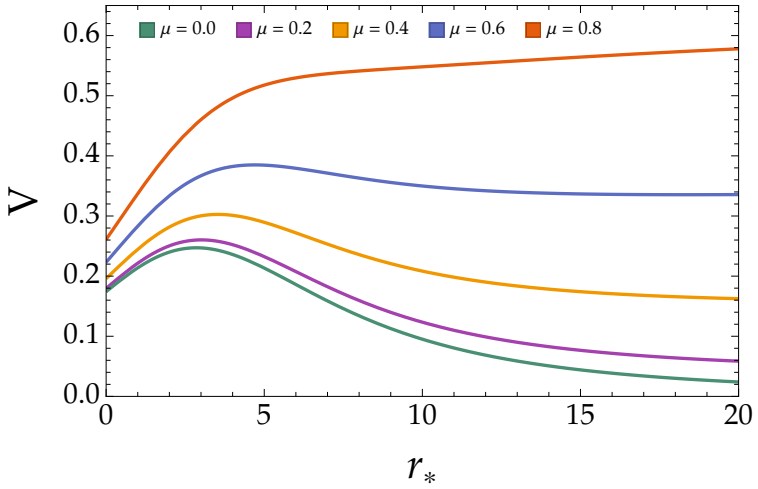

Figure 2.4: *The effective QNM potential Eq. (2.49) for $M = 1$, $n = 0$, $\ell = 2$, and increasing values of μ.*

are purely outgoing at spatial infinity; the imposed boundary conditions are of the form of Eqs (2.20) and (2.21), leading to a discrete spectrum of allowed QNFs that we can write as $\{\omega_{n\ell}(M\mu)\}$ [143, 176, 178–180].

To obtain wavelike solutions far from the black hole event horizon, the modes must satisfy the condition $\omega > \mu$ [176]. Consequentially, Percival and Dolan in Ref. [165] distinguish between "propagative modes", for which $\Re e\{\omega^2\} - \mu^2 > 0$, and "evanescent modes", where $\Re e\{\omega^2\} - \mu^2 < 0$. As we shall explore in Chapter 6, this suggests that there exists some $\mu = \mu_{max}$ that serves as the upper bound for which we can observe QNFs. Here, we shall focus on the features of the effective potential in Eq. (2.49), plotted in Figure 2.4, and the insights into QNM behaviour that they provide.

Recall that a necessary condition for the existence of QNMs is a background whose potential can "trap waves"; the QNMs are then the trapped waves gradually escaping [177]. We observe in Fig. 2.4 that for $\mu = 0$, $V \to 0$ as $r_\star \to \infty$ and the effective potential has a distinct peak. For $\mu \neq 0$, $V \to \mu^2$ as $r_\star \to +\infty$. In other words, μ elevates the potential: as $r_\star$ increases, the potential no longer asymptotes to zero but instead approaches μ^2. When $\mu^2 \gtrsim V(r_0)$ as μ exceeds 0.6, the peak is smoothed out and the local maximum is removed; the potential barrier is transformed into a potential step. Consequentially, waves can no longer be "trapped" and QNM behaviour is lost.

To compute the QNF spectrum, we use the Pöschl-Teller, WKB, and Dolan-Ottewill methods (see Table 2.1). For the massive scalar field propagating in a Schwarzschild spacetime[11], we compute in Ref. [182] the novel Dolan-Ottewill QNF expression to order $\mathcal{O}(L^{-6})$ for $n = 0$. Explicitly, this is

$$\begin{aligned}\omega = &+\frac{1}{3}L - \frac{i}{6}L^0 + \left[\frac{3\mu^2}{2} + \frac{7}{648}\right]L^{-1} + \left[\frac{5i\mu^2}{4} - \frac{137i}{23328}\right]L^{-2} \\ &+ \left[\frac{9\mu^4}{8} - \frac{379\mu^2}{432} + \frac{2615}{3779136}\right]L^{-3} + \left[\frac{27i\mu^4}{16} - \frac{2677i\mu^2}{5184} + \frac{590983i}{1088391168}\right]L^{-4} \\ &+ \left[\frac{63\mu^6}{16} - \frac{427\mu^4}{576} + \frac{362587\mu^2}{1259712} - \frac{42573661}{117546246144}\right]L^{-5} \\ &+ \left[\frac{333i\mu^6}{32} + \frac{6563i\mu^4}{6912} + \frac{100404965i\mu^2}{725594112} + \frac{11084613257i}{25389989167104}\right]L^{-6}\,. \end{aligned} \tag{2.52}$$

From Table 2.1 demonstrating the fundamental QNM mode, we observe that $\Re e\{\omega\}$ increases steadily

[11] Though Decanini *et al.* reformulated the photon orbit analysis to accommodate massive particles for their complex momentum analysis [181], we find that this is not necessary for our purposes (i.e. in the regime where $\omega < \mu$): as shown in Table 2.1, we produce fairly accurate results using the Dolan-Ottewill method as it was originally constructed, albeit with the potential augmented by the μ term.

Table 2.1: *The $(n, \ell) = (0, 2)$ scalar QNFs for $M = 1$ and increasing μ, calculated using the Pöschl-Teller approach, and the sixth-order WKB and Dolan-Ottewill methods.*

μ	ω (WKB)	ω (PT)	ω (DO)
0.0	$0.4836 - 0.0968i$	$0.4874 - 0.0979i$	$0.4836 - 0.0968i$
0.1	$0.4868 - 0.0957i$	$0.4909 - 0.0968i$	$0.4868 - 0.0957i$
0.2	$0.4963 - 0.0924i$	$0.5015 - 0.0936i$	$0.4963 - 0.0924i$
0.3	$0.5123 - 0.0868i$	$0.5192 - 0.0881i$	$0.5124 - 0.0868i$
0.4	$0.5351 - 0.0787i$	$0.5443 - 0.0800i$	$0.5352 - 0.0787i$
0.5	$0.5649 - 0.0676i$	$0.5770 - 0.0690i$	$0.5653 - 0.0676i$
0.6	$0.6022 - 0.0528i$	$0.6181 - 0.0541i$	$0.6032 - 0.0532i$
0.7	$0.1396 + 0.2763i$	$0.6695 - 0.0312i$	$0.6500 - 0.0343i$
0.8	$0.8000 - 5.8370 \times 10^{-28}i$	$0.8000 - 5.8370 \times 10^{-28}i$	$0.7070 - 0.0010i$
0.9	$0.9000 - 6.2510 \times 10^{-28}i$	$0.9000 - 6.2510 \times 10^{-28}i$	$0.7761 + 0.0218i$

with μ whereas $\mathfrak{Im}\{\omega\}$ decreases. As μ approaches 0.7, there is a discernible change in the QNF behaviour: a large jump in both the real and imaginary parts is observed for all three methods, with a pronounced difference in the WKB result for $\mu = 0.7$: a sudden drop in $\mathfrak{Re}\{\omega\}$ and shift from negative to positive in $\mathfrak{Im}\{\omega\}$. This represents a breakdown in the method: while there is a known increase in the relative error for $\mu = 0.7$ [155], we observe explicitly from Fig. 2.4 that $\mu^2 > V(r_0)$ when μ exceeds 0.6; we lose the barrier potential. In this way, we quantify that for $\mu \gtrsim 0.6$ and $(n, \ell) = (0, 2)$, all three methods listed in Table 2.1 become unreliable.

In the absence of a local maximum, the WKB method cannot be applied. For this reason, it is noted in Ref. [155] that the WKB method should not be used to compute QNFs near the "quasiresonance regime": when $\mathfrak{Im}\{\omega\} \approx 0$, denoting arbitrarily long-lived modes (see Section 2.3.1). By definition, "inverse potential techniques" like the Pöschl-Teller method cannot be applied when the shape of the potential is distorted. For this reason, we see a loss of agreement between the Pöschl-Teller results and those of the other methods in Table 2.1 even for small μ. The fitting of the inverse Pöschl-Teller potential fails to describe the effective QNM potential once $\mu > V(r_0)$. In contrast, the Dolan-Ottewill method shows greater consistency with results in the literature even at larger μ (c.f. Fig. 2 of Ref. [165], with QNFs computed using the continued fraction method). As such, the Dolan-Ottewill method allows us to identify with greater precision the value of μ for which the sign of the imaginary component of the QNF changes. However, for accurate values of the QNFs themselves in this regime, other techniques should be used i.e. methods relying on continued fractions, direct time-domain integration, Frobenius series, etc.

However, there is also the physical interpretation to consider. In the geodesic picture, we understand that the flattening of the potential forbids the quantum tunnelling that allows the waves to "leak out" from the system. In Ref. [165], massive QNMs for which $\mathfrak{Re}\{\omega^2\} > \mu^2$ are defined as "propagative" and behave similarly to their massless counterparts, whereas $\mathfrak{Re}\{\omega^2\} < \mu^2$ are "evanescent" and contribute negligibly to the QNM spectrum for a perturbed black hole. This shift from propagative to evanescent is characterised by a change in sign in the imaginary part, as observed in Fig. 2.5. As μ increases, the QNMs transition from propagative to evanescent; as the imaginary part goes to zero, the QNMs enter the quasiresonance regime [177], where the QNMs are arbitrarily long-lived. In this regime, the ingoing wave amplitude at the event horizon of the black hole is considered much smaller than the amplitude far from the black hole; since energy no longer "leaks" from the system at spatial infinity, the QNMs behave as standing waves [178].

At high energies, it is known that massive QNMs behave as massless ones [181]. This can be confirmed from Fig. 2.5: even for small multipolar numbers, the data points become more closely spaced for increasing ℓ; they converge as $\ell \to \infty$. Such behaviour is expected from the form of the potential given in Eq. (2.49), which produces the familiar form $V(r) \sim f(r)\ell^2/r^2$ in the eikonal limit irrespective of the μ. We also observe

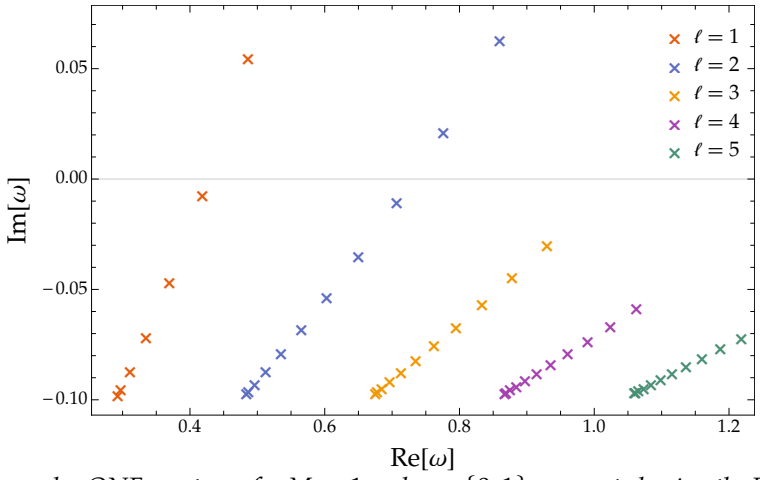

Figure 2.5: *The massive scalar QNF spectrum for $M = 1$ and $\mu \in \{0, 1\}$, computed using the Dolan-Ottewill method.*

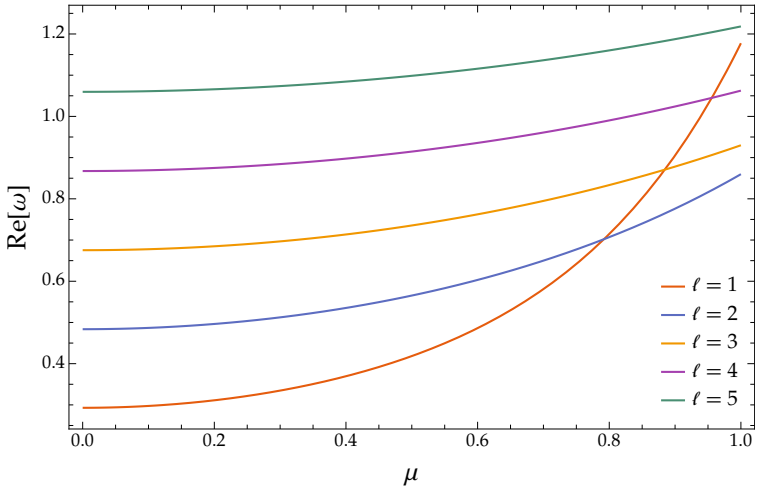

Figure 2.6: *The real part of the massive scalar QNF spectrum for $M = 1$ and $\mu \in \{0, 1\}$, computed using the Dolan-Ottewill method.*

in Fig. 2.5 that the oscillation timescale increases with the angular momentum number. This corresponds well to classical and quantum systems with which we are familiar, where the frequency of an oscillating wave increases with energy. Note, however, that as ℓ increases, the influence of μ wanes: the range of the QNF values converge to their massless counterpart for larger multipolar numbers.

Finally, we comment on the influence of ℓ on the oscillation and decay rate of the massive QNMs. In Table 2.1, we see that for a fixed ℓ, $\mathfrak{Re}\{\omega\}$ scales with μ while the $|\mathfrak{Im}\{\omega\}|$ decreases with increasing μ. In Fig. 2.6, $\mathfrak{Re}\{\omega\}$ scales with ℓ for lower values of μ, with near-equal spacing between the modes as $\mu \to 0$. As μ increases, the lower values of ℓ scale faster than the higher harmonics: beyond $\mu = 2$, $\mathfrak{Re}\{\omega_{\ell=5}\}$ is the least of the plotted QNMs and $\mathfrak{Re}\{\omega_{\ell=1}\}$ is the largest.

For the imaginary part, the least damped QNMs correspond to those with the higher multipolar number for low values of μ (i.e. $|\mathfrak{Im}\{\omega\}|$ decreases with increasing ℓ). However, when μ is larger, the least damped QNMs have lower values of ℓ. We see this explicitly in Fig. 2.7: the magnitude $|\mathfrak{Im}\{\omega_{\ell=5}\}|$ is largest of the five plotted harmonics while $|\mathfrak{Im}\{\omega_{\ell=1}\}|$ is the smallest for larger μ. For $\mu \lesssim 0.7$, however, we observe $|\mathfrak{Im}\{\omega_\ell\}| > |\mathfrak{Im}\{\omega_{\ell+1}\}|$. In other words, for larger μ, the scalar field fluctuations become increasingly smooth, with lower multipolar modes dominating and disappearing last as the black hole settles towards an equilibrium state.

As observed also in Ref. [183], this low-mass behaviour is therefore in opposition to our intuition on the

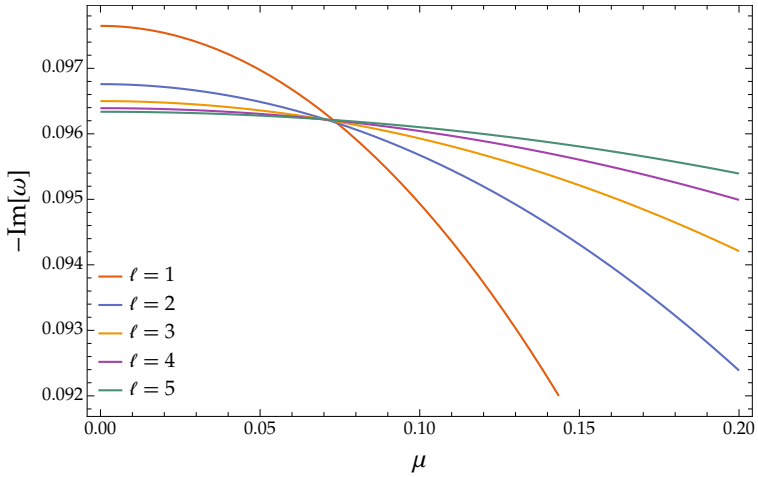

Figure 2.7: *The imaginary part of the massive scalar QNF spectrum for* $M = 1$ *and* $\mu \in \{0.0, 0.2\}$*, computed using the Dolan-Ottewill method.*

QNF spectrum, where we expect the imaginary part to grow with ℓ. This is in line with the hierarchy we expect also from physical systems, where more energetic modes typically decay more quickly. For example, electrons bound to an atom in higher energy states experience spontaneous decay rates to the ground state that are faster than their lower-energy counterparts. We explore the anomalous decay rate in greater detail in Section 4.2.3, with the added contributions of a black hole and a scalar field charge.

While we have addressed the influence of a mass term on the QNM potential and the QNF spectrum, the massive scalar QNM has been the subject of much discussion in the literature concerning the superradiant amplification of bosonic perturbing fields within the vicinity of a black hole. Since classical superradiance informs our analyses in Sections 4.1.1 and 5.2.1, we close this section on the massive QNM eigenvalue problem with a brief aside on the subject.

2.3.1 Interpreting the mass-like QNM term in the astrophysical context

As mentioned earlier, when $\Im m\{\omega\} \approx 0$, QNMs enter the "quasiresonance regime" in which modes become arbitrarily long-lived. This occurs when the field mass reaches some critical value, such that the damping rate asymptotically approaches zero and the QNM behaviour resembles that of a bound state [177]. The mass responsible for this decay in the damping rate is associated with a local minimum generated far from the black hole. Waves scattered off of the black hole (recall Fig. 2.1) become reflected and enhanced within this local minimum [184], resulting in "superradiance".

Following the definition provided in Eq. (2.12), "superradiance" occurs when the amplitude of the reflected wave $\mathcal{R}$ exceeds that of the incident wave $\mathcal{I}$ for a particular frequency. Classical superradiance was first addressed in the black hole context in 1973, for rotating [185, 186] and electrically charged [187] black holes. We discuss the latter in Section 4.1.1; here, we shall briefly consider the Kerr case.

For a scattered bosonic field with mass $m = \mu\hbar/c^2$ in the vicinity of a Kerr black hole [185, 186], rotational energy is carried away from the spinning black hole; the superradiant amplification can be augmented by the confining potential of the massive bosonic field, leading to a runaway self-amplification of the field and the formation of a bosonic condensate around the black hole source (see Refs [14, 47, 133]). This process has become a subject of renewed interest due to the possibility of detecting such a phenomenon through GW astronomy [188]. Since the bosonic cloud and its black hole source both encode information about the perturbing field, GW observations could in principle be used to constrain the mass of the bosonic field. GW analyses performed in Refs [189, 190] suggest that LIGO and LISA may be able to probe the parameter space of light bosons at $m \sim 10^{-13} - 10^{-11}$ eV and $m \sim 10^{-19} - 10^{-14}$ eV, respectively. These constraints overlap

well with hypothetical ultralight fields [3, 191], which we elaborate upon in Section 5.2.1.

In such astrophysical settings, particular importance is placed on the parameter $M\mu$, where M is the usual black hole Arnowitt-Deser-Misner mass and $m = \mu\hbar/c^2$ is the bosonic field mass. Recall that the black hole mass serves as a length scale and μ has inverse units of length. In geometric units ($c = G = 1$), this $M\mu$ parameter is a dimensionless constant. In SI units, this mass coupling can be related to the Planck mass M_P [180], as well as to the black hole horizon radius r_+ over the Compton wavelength $\lambda_C = h/(mc)$ of the perturbing field [165, 179],

$$M\mu = \frac{M\mu}{M_P^2} \equiv \frac{GM\mu}{\hbar c} \sim \frac{r_+}{\lambda_C} \,. \tag{2.53}$$

Recall that the Compton wavelength can also be related to the mass in eV using

$$\lambda_C \times m = 1.24 \times 10^{-9} \,. \tag{2.54}$$

For Compton wavelengths corresponding to astrophysical black holes $M \sim 10M_\odot$, μ will correspond to very light particles of mass $m \sim 10^{-10}$ eV/c^2 [183, 192]. For astrophysical black holes, it is expected that $M\mu$ will be fairly large for $M\mu \geq \ell$ [180]. As noted in Ref. [165], this is evident from elementary dimensional analysis (using SI units):

$$M\mu = \frac{M\mu}{m_P^2} \approx 7.52 \times 10^9 \times \left(\frac{M}{M_\odot}\right)\left(\frac{\mu c^2}{eV}\right) \,. \tag{2.55}$$

However, there is broad variability to contend with *viz*. for a neutral pion field of mass $\mu_{\pi^0} \sim 134.96 \times 10^3$ eV/c^2 and a $10M_\odot$ black hole, $M\mu \sim 4.8 \times 10^3$; for that same black hole and a W-boson, $M\mu \sim 6 \times 10^{21}$. In a study of Proca field QNMs in the Kerr space-time [165], Dolan and Percival found $M\mu$ to be exceedingly large in the case of SM vector bosons, and extremely small for the photon with $\mu \lesssim 10^{-27}$ eV/c^2. Furthermore, they found that in the SM case, only evanescent modes for QNFs with $\ell + 1/2 \lesssim \mathcal{O}(M\mu)$ were predicted. For these extremely light photons, the QNF spectrum was anticipated to replicate that of the electromagnetic field, albeit with one extra longitudinal polarisation matching the QNF spectrum of a massive scalar field.

Furthermore, when the Compton wavelength of the massive bosonic field is of the order of the black hole's radius, the scaling for the suppression of the instability timescale is governed by $M\mu \lesssim 1$.This leads to the strongest superradiant instabilities for the Kerr black hole [14, 47]. In the case of ultralight scalar fields, this instability timescale is of the order of seconds for black holes of mass $M \sim M_\odot$, or hundreds of years for the heavier $M \sim 10^9 M_\odot$ black holes [47, 133].

As such, if we are to observe QNMs, we can consider $M\mu \sim \mathcal{O}(1)$. As we demonstrated in Ref. [182], we can then utilise dimensional analysis to isolate a mass range for the scalar field. Using SI units $M = m_{\rm BH}G/c^2$ and $\mu = mc/\hbar$, we can express the mass of a bosonic field as

$$m = \frac{1}{m_{\rm BH}}\frac{\hbar c}{G} M\mu \,. \tag{2.56}$$

Since $\hbar c/G \sim 10^{-16}$ kg^2 and $1M_\odot \sim 10^{30}$ kg, we can scale the black hole mass as $m_{\rm BH} \sim 10^\chi M_\odot$. Returning to natural units with $c = 1$ (c.f. Eq. (4.25) of Ref. [133]), we then have

$$m \sim 10^{-(\chi+10)} M\mu \text{ eV} \,. \tag{2.57}$$

Eq. (2.57) serves as a rough detectability bound on the sensitivity of the QNF spectrum corresponding to an astrophysical black hole to ultralight scalar fields. We shall make use of this order-of-magnitude estimate in Sections 4.2.3 and 6.3, as a guide on the detectability of charged massive scalar fields and extra dimensional signatures, respectively.

Finally, we shall close this chapter with a higher-order calculation of the QNEF, introduced in Chapter 1 and defined in Eq. (2.25). For completeness, we have included a review of the leading-order QNEF

calculation in Appendix D.

2.4 Quasinormal wavefunctions and excitation factors

During the course of the iterative process needed to generate the QNF series Eq. (2.43), the Dolan-Ottewill method produces as a by-product the elements of the $S_{kn}(r)$ series contained within the exponential contribution to the wavefunction Eq. (2.44). From the ansatz, Eq. (2.42), recall that can write the wavefunction to order $\mathcal{O}(L^{-1})$ as

$$\begin{aligned}\overline{u}_{\ell\omega}(r) \approx A_n \left[\left(1-\frac{3}{r}\right)^n + \sum_{i=1}^{n} \alpha_{i(1n)} L^{-1} \left(1-\frac{3}{r}\right)^{n-i}\right] \times \exp\left\{S_{0n}(r) + S_{1n}(r) L^{-1}\right\} \\ \times \exp\{i\omega_{\ell n} \int_3^r \left[\left(1-\frac{3}{r}\right)\sqrt{1+\frac{6}{r}} - 1\right] \frac{1}{f(r)} dr\,,\end{aligned} \tag{2.58}$$

for $M = 1$, where A_n is a normalisation constant determined from the condition

$$\lim_{r\to+\infty} \overline{u}_{\ell\omega}(r) = 1\,. \tag{2.59}$$

If we set $y = \sqrt{1+6/r}$, then

$$\exp\left\{\int_3^r \left[\left(1-\frac{3}{r}\right)\sqrt{1+\frac{6}{r}} - 1\right] \frac{1}{f(r)} dr\right\} = \frac{1}{4}(2-\sqrt{3})^6 e^{2-\sqrt{27}-r(1-x)} \left(\frac{1+y}{2-y}\right)^4\,. \tag{2.60}$$

Finally, we can obtain $S_{0n}(r)$ by integrating the derivative $S'_{0n}(r)$. This yields

$$S_{0n}(r) = +\frac{1}{2}\ln\left\{\frac{2}{y}\right\} + 2N \ln\left\{\frac{2+\sqrt{3}}{y+\sqrt{3}}\right\}, \tag{2.61}$$

where the value of the integration constant,

$$c = \frac{1}{2}\ln\{2\} + 2N \ln\left\{2+\sqrt{3}\right\},$$

is chosen in order to satisfy the condition $S_{0n}(r=2) = 0$. Following Ref. [156], we make use of the constant

$$\xi = \frac{2+\sqrt{3}}{2-\sqrt{3}} = (2+\sqrt{3})^2 = 7+4\sqrt{3}\,. \tag{2.62}$$

S_{0n} is consistent irrespective of the spin of the field; it is the first term in the L expansion of the QNM for all overtones n. For the next-to-leading-order term, S_{1n}, this is not so. We shall demonstrate this in the calculation that follows.

The QNM excitation factors indicate how (and by how much) the QNMs are excited by a given initial data. To compute this $\mathcal{B}_{\ell n}$ of Eq. (2.25), Dolan and Ottewill extended their QNF analysis of Ref. [156] discussed in Section 2.2. However, a hallmark of that method is a breakdown at the critical orbit $r = r_c = 3$ that cannot be circumvented in the case of the wavefunction computation. As such, the solution space is divided into an "interior" region near $r = 3$ and "exterior" regions defined by $r > (3+\epsilon')$ and $r < (3-\epsilon')$ for some infinitesimally-small ϵ'. While the exterior solution is based on the photon-sphere arguments of the QNF calculation made in Refs [50, 156], the interior solution follows the low-order WKB method of Refs [151, 152]; specifically, the interior solution reduces to the asymptotic form of the parabolic cylinder function

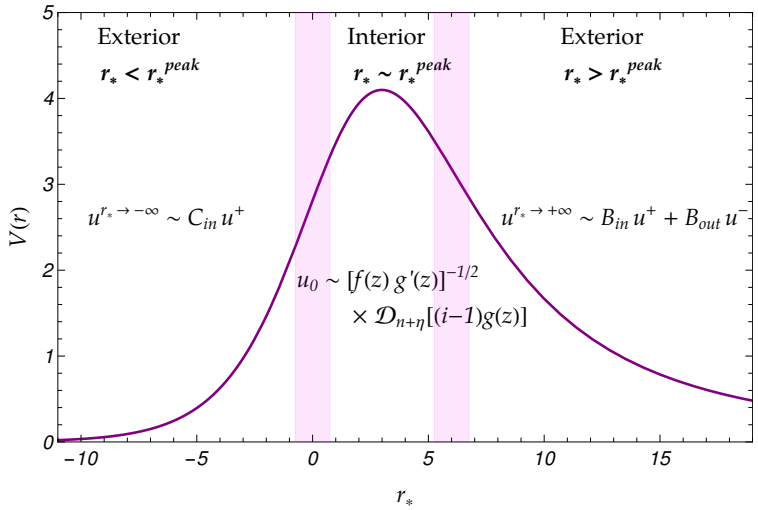

Figure 2.8: *Diagrammatic representation of the solutions, where asymptotics are matched across the shaded regions. At leading-order, $g(z) \sim z$.*

$\psi_1 \sim D_a((-1+i)z)$.

In Appendix D, we provide a review of the leading-order calculation of the QNEF using the Dolan-Ottewill method. In this section, we demonstrate a detailed calculation of our QNEF computation up to $\mathcal{O}(L^{-2})$. To elevate the interior solution to higher orders, we follow the strategy of Ref. [153] in which a solution of the form $\psi \sim (g'(z))^{-1/2} D_a[g(z)]$ is used to achieve a third-order expression, where $D_a[g(z)]$ is the parabolic cylinder function. For the exterior solution, higher-order expressions can be achieved if we use the Dolan-Ottewill method to compute expressions for the first few $S_{kn}(r)$ functions of Eq. (2.44). The final step of the QNEF calculation then primarily involves the appropriate matching of the solutions.

2.4.1 Preliminaries

We begin with the effective QNM potential for a scalar test field for $f(r) = 1 - 2/r$,

$$\frac{d^2\psi}{dr^2} + U(r)\psi = 0\,, \qquad U(r) = \frac{1}{f(r)^2}\left[\omega^2 - f(r)\left(\frac{L^2 - \frac{1}{4}}{r^2}\right) + \frac{1}{r^4}\right]\,, \tag{2.63}$$

where the perturbed QNF is given by

$$\begin{aligned}\widetilde{\omega}_{\ell n} &= \omega_{\ell n} + \epsilon \\ &\approx \overline{\omega}_{-1} L + \overline{\omega}_0 + \overline{\omega}_1 L^{-1} + \overline{\omega}_2 L^{-2} + \epsilon + \mathcal{O}\left(L^{-3}\right)\,.\end{aligned} \tag{2.64}$$

Here, we shall retain terms from the QNF series expansion of Eq. (2.43) up to order $\mathcal{O}(L^{-2})$. Following the standard Schultz-Iyer-Will technique [151–153], we expand the barrier potential $U(r)$ in a Taylor series about the maximum $r = r_p$,

$$U(r) \approx U(r_p) + \frac{1}{2}U''(r_p)(r - r_p)^2 + \frac{1}{6}U^{(3)}(r - r_p)^3 + \ldots\,. \tag{2.65}$$

If we solve for $r_p = r_0 + r_1 L^{-1} + r_2 L^{-2} + \ldots$ using $U'(r_p) = 0$ in the large-ℓ limit, we find that at order $\mathcal{O}(L^{-2})$,

$$r_p = 3 + 12\sqrt{3}\overline{\omega}_0 L^{-1} + \left(\frac{11}{6} + 342\overline{\omega}_0^2 + 12\sqrt{3}\overline{\omega}_1\right) L^{-2} + \mathcal{O}\left(L^{-3}\right)\,. \tag{2.66}$$

Upon substituting Eq. (2.66) into Eq. (2.63),

$$U(r_p) = 2\sqrt{3}L\overline{\omega}_0 + \left(\frac{7}{36} - 39\overline{\omega}_0^2 + 2\sqrt{3}\overline{\omega}_1\right) + \frac{2\left(504\sqrt{3}\overline{\omega}_0^3 - 22\sqrt{3}\overline{\omega}_0 - 351\overline{\omega}_1\overline{\omega}_0 + 9\sqrt{3}\overline{\omega}_2\right)}{9}\frac{1}{L} + ... \tag{2.67}$$

for large-ℓ at higher orders. We continue in this way for each term of Eq. (2.65),

$$\begin{aligned}
\frac{1}{2}U''(r_p) &= \frac{L^2}{9} - \frac{16\overline{\omega}_0}{\sqrt{3}}L + \left(-\frac{233}{324} + \frac{888\overline{\omega}_0^2}{3} - \frac{16\overline{\omega}_1}{\sqrt{3}}\right) + ... \,, \\
\frac{1}{6}U^{(3)}(r_p) &= -\frac{20L^2}{81} + \frac{1160L\overline{\omega}_0}{27\sqrt{3}} + ... \,, \\
\frac{1}{24}U^{(4)}(r_p) &= \frac{95L^2}{243} - \frac{6544L\overline{\omega}_0}{81\sqrt{3}} + ... \,,
\end{aligned} \tag{2.68}$$

parameterising r_p as

$$r - r_p = \frac{z}{\alpha} \,. \tag{2.69}$$

At leading order, $r_p = 3$ and $\alpha = \sqrt{L/3}$ (c.f. Eq. (D.1.3) of Appendix D). We determine α by substituting Eqs. (2.68) and (2.69) into Eq. (2.65). However, the introduction of Eq. (2.69) into the ordinary differential equation implies that the new equation to solve is

$$\frac{d^2}{d(r_p + z/\alpha)^2} \to \alpha^2\frac{d^2}{dz^2} \quad \Rightarrow \quad \frac{d^2\psi}{dz^2} + \frac{1}{\alpha^2}U(z)\psi = 0 \,. \tag{2.70}$$

This brings us to

$$\begin{aligned}
\frac{1}{\alpha^2}U(z) \approx &\left[2\sqrt{3}L\overline{\omega}_0 + \left(\frac{7}{36} - 39\overline{\omega}_0^2 + 2\sqrt{3}\overline{\omega}_1\right) + ...\right]\frac{1}{\alpha^2} + \left[\frac{L^2}{9} - \frac{16\overline{\omega}_0}{\sqrt{3}}L + ...\right]\frac{z^2}{\alpha^4} \\
&+ \left[-\frac{20L^2}{81} + \frac{1160L\overline{\omega}_0}{27\sqrt{3}} + ...\right]\frac{z^3}{\alpha^5} + \left[\frac{95L^2}{243} - \frac{6544L\overline{\omega}_0}{81\sqrt{3}} + ...\right]\frac{z^4}{\alpha^6} + ... \,.
\end{aligned} \tag{2.71}$$

The coefficient of the quadratic term in z is expected to be 1 [151–153], which allows us to solve for α. Therefore, we can rewrite Eq. (2.69) as

$$r(z) - \alpha^{-1}z = 3 + 12\sqrt{3}\overline{\omega}_0 L^{-1} + \left(\frac{11}{6} + 342\overline{\omega}_0^2 + 12\sqrt{3}\overline{\omega}_1\right)L^{-2} + \mathcal{O}\left(L^{-3}\right) \,, \tag{2.72}$$

where

$$\alpha^{-1} = \frac{\sqrt{3}}{\sqrt{L}} + \frac{36\overline{\omega}_0}{L^{3/2}} + \left[\frac{233}{48\sqrt{3}} + 414\sqrt{3}\overline{\omega}_0^2 + 36\overline{\omega}_1\right]\frac{1}{L^{5/2}} + \mathcal{O}\left(L^{-\frac{7}{2}}\right) \,. \tag{2.73}$$

2.4.2 Interior solution: using the parabolic cylinder function

While the spin of the perturbing field is irrelevant at leading order, deviations emerge at higher orders of L^{-k}. Here, we consider $s = 0$ perturbations, which allows us to use Eq. (2.7) as before in order to obtain a new effective potential (c.f. Eq. (D.1.5)). Following Refs [151–153], we elevate the leading-order expressions to next-to-leading order by substituting a power series expansion in $g(z)$ (c.f. Eq. (3.16) of Ref. [153]) in place of z within the ordinary differential equation. Thereafter, we solve the resultant ordinary differential equation (c.f. Eq. (3.14) of Ref. [153]) using functions of the parabolic cylinder functions of the form $\psi \sim (g'(z))^{-1/2}D_a[g(z)]$.

We begin by substituting Eqs (2.69) and (2.72) into Eq. (2.65), such that the radial equation becomes,

$$\frac{d^2\psi}{dz^2} + \left(\left[6\sqrt{3}\overline{\omega}_0 + \left(\frac{7}{12} + 315\overline{\omega}_0^2 + 6\sqrt{3}\overline{\omega}_1 \right) \frac{1}{L} + ... \right] + z^2 \right.$$
$$\left. + \left[-\frac{20\sqrt{3}}{9}\frac{1}{L^{1/2}} - \frac{40\overline{\omega}_0}{3}\frac{1}{L^{3/2}} + ... \right] z^3 + \left[\frac{95}{9}\frac{1}{L} + \frac{296\sqrt{3}\overline{\omega}_0}{9}\frac{1}{L^2} + ... \right] z^4 + ... \right) \psi = 0 \,, \tag{2.74}$$

$$\Rightarrow \quad \frac{d^2\psi}{dz^2} + Q(z)\psi = 0 \,. \tag{2.75}$$

Analogous to Eq. (3.15) of Ref. [153] and Eq. (D.1.5), we can rewrite the potential as

$$Q(z) = \sum_{n=1}^{\infty} \left(\frac{1}{L} \right)^{n/2} U_{n/2}(z) \,, \tag{2.76}$$

and solve for each term, *viz.*

$$U_0 = 6\sqrt{3}\overline{\omega}_0 + z^2 \,, \tag{2.77}$$
$$U_{1/2} = -\frac{20\sqrt{3}z^3}{9} \,, \tag{2.78}$$
$$U_1 = \frac{7}{12} + 315\overline{\omega}_0^2 + 6\sqrt{3}\overline{\omega}_1 + \frac{95z^4}{9} \,, \tag{2.79}$$
$$U_{3/2} = -\frac{40\overline{\omega}_0 z^3}{3} - \frac{392\sqrt{3}z^5}{27} \,, \tag{2.80}$$
$$U_2 = 5088\sqrt{3}\overline{\omega}_0^3 + \frac{75\sqrt{3}\overline{\omega}_0}{4} + 630\overline{\omega}_0\overline{\omega}_1 + 6\sqrt{3}\overline{\omega}_2 + \frac{296\sqrt{3}\overline{\omega}_0 z^4}{9} + \frac{1499z^6}{27} \,. \tag{2.81}$$

Following Eq. (3.14) of Ref. [153] and Eq. (D.1.8), we set the solution of Eq. (2.75) as

$$\psi = \left(\frac{dg}{dz} \right)^{-1/2} \mathcal{D}_a((-1+i)g(z)) \,, \tag{2.82}$$

where $\mathcal{D}_a((-1+i)g(z))$ satisfies the parabolic cylinder function,

$$\left(\frac{d^2}{dg^2} + \lambda + g^2(z) \right) \mathcal{D}_a((-1+i)g(z)) = 0 \,, \tag{2.83}$$

and λ is an unsolved variable that is constant in z, and $a = -(1-i\lambda)/2$. With Eq. (2.82), we can rewrite Eq. (2.75) in terms of $g(z)$,

$$\left(\frac{dg}{dz} \right)^2 \left[\lambda + g(z)^2 \right] + \frac{1}{2}\left(\frac{dg}{dz} \right)^{-1} \left(\frac{d^3g}{dz^3} \right) - \frac{3}{4}\left(\frac{dg}{dz} \right)^{-2} \left(\frac{d^2g}{dz^2} \right)^2 - \sum_{n=0}^{\infty} \left(\frac{1}{L} \right)^{n/2} U_n(z) = 0 \,. \tag{2.84}$$

Solving the above equation by taking

$$g(z) = z + \sum_{n=1}^{\infty} \left(\frac{1}{L} \right)^{n/2} A_{n/2}(z) \,, \tag{2.85}$$

and

$$\lambda = \sum_{k=0}^{\infty} \left(\frac{1}{L}\right)^k \lambda_k \ , \ \ A_{n/2}(z) \sim \sum_{k=0}^{\infty} p_{nk} z^k \ , \tag{2.86}$$

we can solve for λ and $A_{n/2}(z)$ iteratively by considering each coefficient of $L^{-n/2}$. For example, at the order of L^0 and $L^{-1/2}$, we generate

$$L^0 : \quad \lambda_0 - 6\sqrt{3}\overline{\omega}_0 = 0 \ , \tag{2.87}$$

$$L^{-1/2} : \quad \frac{1}{18}\left(9A^{(3)}_{1/2}(z) + 36z^2 A'_{1/2}(z) + 72(\lambda_0 - 3\sqrt{3}\overline{\omega}_0)A'_{1/2}(z) + 36zA_{1/2}(z) + 40\sqrt{3}z^3\right) = 0 \ , \tag{2.88}$$

and solve for each coefficient of z. Following this procedure, we find the result up to and including $\mathcal{O}(L^{-2})$:

$$\lambda = \sum_{n=0}^{4} \left(\frac{1}{L}\right)^{n/2} U_{n/2}(0) - \frac{\Lambda}{L} - \frac{\Omega}{L^2} \ ; \tag{2.89}$$

$$A_{1/2} = \frac{40\overline{\omega}_0}{9\sqrt{3}} - \frac{10z^2}{9\sqrt{3}} \ ; \tag{2.90}$$

$$A_1 = \frac{1265z^3}{1944} + \frac{2605\overline{\omega}_0 z}{216\sqrt{3}} \ , \qquad \Lambda = \frac{155}{216} + \frac{645\overline{\omega}_0^2}{2} \ ; \tag{2.91}$$

$$A_{3/2} = \frac{254179\overline{\omega}_0^2}{1215\sqrt{3}} + \frac{40\overline{\omega}_1}{3} - \frac{58987z^4}{43740\sqrt{3}} - \frac{185179\overline{\omega}_0 z^2}{43740} + \frac{6781}{3645\sqrt{3}} \ ; \tag{2.92}$$

$$A_2 = \frac{7702759z^5}{7558272} + \frac{4699901\overline{\omega}_0 z^3}{629856\sqrt{3}} + \left(\frac{108646309\overline{\omega}_0^2}{839808} + \frac{2605\overline{\omega}_1}{216\sqrt{3}} + \frac{443665}{1679616}\right) z \ ,$$

$$\Omega = \frac{121727\overline{\omega}_0^3}{8\sqrt{3}} + 645\overline{\omega}_1\overline{\omega}_0 + \frac{48623\overline{\omega}_0}{864\sqrt{3}} \ . \tag{2.93}$$

Recall that the index of the parabolic cylinder function $D_a((-1+i)g(z))$ is given by $a = -1/2 + i\lambda/2$. With the perturbation in Eq. (2.64) and the result in Eq. (2.89), we may write $a = n + i\epsilon\sqrt{27} + \mathcal{O}\left(L^{-1}\right)$.

We now have all the necessary components to write the interior wavefunction. For the parabolic cylinder function, we use Eq. (D.1.8) and Eq. (3.22) of Ref. [153], with $z \to g(z)$. For $\eta = i\epsilon\sqrt{27}$, this produces solutions of the form

$$\psi \sim (g'(z))^{-1/2} D_{n+\eta+\mathcal{O}\left(\frac{1}{L}\right)}[(-1+i)g(z)] \ . \tag{2.94}$$

Since we are concerned only with the fundamental QNM in this calculation, we emphasise that we set $n = 0$ from this point.

Recall also that the interior function in the Dolan-Ottewill framework is given by the ansatz $u_0 = f^{-1/2}\psi$. With the introduction of the $r \to z$ replacement of Eq. (2.72), the asymptotic behaviour of this prefactor is

$$\begin{aligned} f(z)^{-1/2} &\sim \left(1 - \frac{2}{r_p + \alpha^{-1}z}\right)^{-1/2} \\ &\sim \sqrt{3}\left[1 - \frac{z}{\sqrt{3}L} + \left(\frac{2i}{3} + \frac{5z^2}{6}\right)\frac{1}{L} + \left(-\frac{13z^3}{6\sqrt{3}} - \frac{4iz}{3\sqrt{3}}\right)\frac{1}{L^{3/2}} + \left(\frac{139z^4}{72} + iz^2 - \frac{115}{162}\right)\frac{1}{L^2} + ...\right] \ . \end{aligned} \tag{2.95}$$

For the sake of brevity, we shall present only the asymptotic forms here and impose that $n = 0$ for the

overtone. In the eikonal limit,

$$\psi_{z\to-\infty} \sim e^{+ig(z)^2/2}\left(\frac{dg}{dz}\right)^{-1/2} \tag{2.96}$$

$$\psi_{z\to+\infty} \sim e^{+ig(z)^2/2}\left(\frac{dg}{dz}\right)^{-1/2} - e^{-ig(z)^2/2}\left(\frac{dg}{dz}\right)^{-1/2}\frac{\sqrt{2\pi}e^{-3i\pi/4}2^{-1/2}}{\Gamma\{-n-\eta+\mathcal{O}\left(\frac{1}{L}\right)\}}\frac{1}{g(z)}\left[1+\frac{i}{2}g(z)^{-2}-\frac{3}{4}g(z)^{-4}+...\right], \tag{2.97}$$

where the asymptotics of each component are given by:

$$e^{\pm ig(z)^2/2} \sim \exp\left\{\pm\frac{iz^2}{2}\pm\frac{(20z-10iz^3)}{3\sqrt{27}}\frac{1}{L^{1/2}}\pm\left[-\frac{200i}{243}-\frac{595z^2}{3888}+\frac{185iz^4}{216}\right]\frac{1}{L}\mp\left[\frac{839iz^5}{405\sqrt{3}}+\frac{527z^3}{131220\sqrt{3}}+\frac{93269iz}{65610\sqrt{3}}\right]\frac{1}{L^{3/2}}\pm\left[\frac{60547iz^6}{34992}+\frac{853499z^4}{7558272}-\frac{27982081iz^2}{45349632}+\frac{8837}{177147}\right]\frac{1}{L^2}+...\right\}. \tag{2.98}$$

$$\left(\frac{dg}{dz}\right)^{-1/2} \sim 1+\frac{10z}{9\sqrt{3L}}+\left[-\frac{155z^2}{432}+\frac{2605i}{7776}\right]\frac{1}{L}+\left[\frac{51323z^3}{87480\sqrt{3}}+\frac{215767iz}{524880\sqrt{3}}\right]\frac{1}{L^{3/2}} + \left[-\frac{11897483z^4}{30233088}-\frac{1100411iz^2}{10077696}+\frac{100425053}{362797056}\right]\frac{1}{L^2}+... . \tag{2.99}$$

$$\begin{aligned}&\frac{1}{g(z)}\left[1+\frac{i}{2g(z)^2}-\frac{3}{4g(z)^4}+...\right]\\ &\sim\frac{1}{z}+\frac{i}{2z^3}-\frac{3}{4z^5}+\left[\frac{10}{9\sqrt{3}}+\frac{35i}{9\sqrt{3}z^2}-\frac{5\sqrt{3}}{2z^4}-\frac{25i}{3\sqrt{3}z^6}\right]\frac{1}{L^{1/2}}+\left[-\frac{155z}{648}+\frac{5005i}{1944z}-\frac{9505}{972z^3}-\frac{44875i}{1728z^5}+\frac{500}{27z^7}\right]\frac{1}{L}\\ &+\left[\frac{70000i}{729\sqrt{3}z^8}+\frac{762343}{3888\sqrt{3}z^6}-\frac{32791703i}{349920\sqrt{3}z^4}+\frac{15737z^2}{43740\sqrt{3}}-\frac{583061}{32805\sqrt{3}z^2}+\frac{79477i}{131220\sqrt{3}}\right]\frac{1}{L^{3/2}}+\left[-\frac{2800000}{19683z^9}\right.\\ &\left.+\frac{30926495i}{78732z^7}+\frac{32239603847}{120932352z^5}-\frac{1743973z^3}{7558272}-\frac{9730444495i}{181398528z^3}-\frac{329953iz}{15116544}-\frac{152696747}{45349632z}\right]\frac{1}{L^2}+... .\end{aligned} \tag{2.100}$$

Finally, applying the $\Gamma\{-n-\eta+\mathcal{O}\left(L^{-1}\right)\}$ approximation in the $n=0$ limit yields,

$$\frac{1}{\Gamma\{-n-\eta+\mathcal{O}\left(\frac{1}{L}\right)\}}\sqrt{2\pi}e^{-3i\pi/4}2^{-1/2} \sim \left(-i\sqrt{27}\epsilon\right)\left[1+\frac{5i}{36L}-\frac{659}{7776L^2}+...\right]\sqrt{\pi}e^{-3i\pi/4}. \tag{2.101}$$

2.4.3 Exterior solution: using the Dolan-Ottewill ansatz

For the exterior solution, we closely follow the method described in Ref. [50] (c.f. Appendix D.2) for

$$u^{\pm}(r) = \exp\left\{\pm i\omega\int_3^r\left(1+\frac{6}{r}\right)^{1/2}\left(1-\frac{3}{r}\right)dr_\star\right\}v^{\pm}(r). \tag{2.102}$$

To obtain the exponential component of the wavefunction, we perform a power series expansion on the

integrand around $r = 3$, and then integrate directly with respect to the tortoise coordinate. We then perform the substitution of $r \to r_p + \alpha^{-1} z$, $\omega \to \omega_{\ell 0}^{(2)} \approx \overline{\omega}_{-1} L + \overline{\omega}_0 + \overline{\omega}_1 L^{-1} + \overline{\omega}_2 L^{-2}$, and $\overline{\omega}_k$ given in Eq. (2.64), which gives

$$\begin{aligned}
&\pm i\omega \int_3^r \left(1+\frac{6}{r}\right)^{1/2} \left(1-\frac{3}{r}\right) dr_\star \\
&\quad \sim \pm \Bigg[\frac{iz^2}{2} + \left[\frac{2z}{\sqrt{3}} - \frac{10iz^3}{9\sqrt{3}}\right] \frac{1}{L^{1/2}} + \left[-\frac{2i}{3} + \frac{z^2}{36} + \frac{185iz^4}{216} + \right] \frac{1}{L} - \left[\frac{95iz}{54\sqrt{3}} + \frac{10z^3}{27\sqrt{3}} + \frac{839iz^5}{405\sqrt{3}}\right] \frac{1}{L^{3/2}} \\
&\qquad + \left[-\frac{4}{27} - \frac{1135iz^2}{1944} + \frac{1457z^4}{3888} + \frac{60547iz^6}{34992}\right] \frac{1}{L^2} + \mathcal{O}(L^{-5/2}) \Bigg] \,.
\end{aligned} \tag{2.103}$$

To construct the higher-order expressions for the function $v^{\pm(k)}$, we require the higher-order $\widetilde{S}_{kn}(r)$ functions (see Eqs. (2.44) and (D.2.13)). For $n = 0$, we can express this as

$$v^{\pm(k)}(r) = \exp\{\widetilde{S}^{\pm}_{00}(r) + \widetilde{S}^{\pm}_{10}(r) L^{-1} + ... + \widetilde{S}^{\pm}_{k0}(r) L^{-k}\} \,. \tag{2.104}$$

To extract these terms, we follow the same iterative Dolan-Ottewill QNF calculation. Recall that to determine each components of the QNF series expansion $\overline{\omega}_k$, we require $S_{kn}(r)$ and its derivatives with respect to r. Recall also that $v^{\pm}(r)$ and $\widetilde{S}^{\pm}_{kn}(r)$ are the functions after introducing the QNF perturbation (see Eq. (2.64), together with Eq. (2.64)) into Eq. (D.2.13), such that we solve for $\widetilde{S}^{\pm}_{k0}(r)$ order by order. Their explicit forms are provided in Appendix E, up to and including $k = 2$. To determine the asymptotics of these perturbed $\widetilde{S}^{\pm}_{k0}$ functions, we evaluate the functions at the perturbed QNF $\widetilde{\omega}^{(k)}_{\ell 0}$, perform the substitution $r \to r_p + \alpha^{-1} z$, and subject the result to a power series expansion about $L \to \infty$ to second order in L. Using these asymptotic forms of the components, together with Eqs. (2.103) and (2.104), the explicit forms of Eq. (2.102), $u^{\pm(k=2)}$, may produce at the order of $\mathcal{O}(L^{-2})$,

$$\begin{aligned}
u^{+(2)} \approx \sqrt{2} e^{+iz^2/2} \left(\frac{\xi}{4\sqrt{27}}\right)^{1/2} \times \exp\Bigg\{ &\left[\frac{7z}{3\sqrt{3}} - \frac{10iz^3}{9\sqrt{3}}\right] \frac{1}{\sqrt{L}} + \left[-\frac{367i}{324} + \frac{67i}{144\sqrt{3}} - \frac{11z^2}{216} + \frac{185iz^4}{216}\right] \frac{1}{L} \\
&+ \left[-\frac{166iz}{81\sqrt{3}} - \frac{151z^3}{486\sqrt{3}} - \frac{839iz^5}{405\sqrt{3}}\right] \frac{1}{L^{3/2}} + \left[-\frac{11687}{93312} - \frac{47}{2592\sqrt{3}} - \frac{9289iz^2}{23328} + \frac{5581z^4}{15552} + \frac{60547iz^6}{34992}\right] \frac{1}{L^2} \Bigg\} \,,
\end{aligned} \tag{2.105}$$

and

$$\begin{aligned}
u^{-(2)} \approx \sqrt{2} e^{-iz^2/2} \left(\frac{z}{L^{1/2}}\right)^{-1} \left(\frac{\xi}{\sqrt{27}}\right)^{-1/2} \exp\Bigg\{ &-\frac{5}{8z^4} + \frac{i}{2z^2} + \left[-\frac{5i}{\sqrt{3}z^5} - \frac{5}{\sqrt{3}z^3} + \frac{10i}{3\sqrt{3}z} \right. \\
&\left. - \frac{z}{\sqrt{3}} + \frac{10iz^3}{9\sqrt{3}}\right] \frac{1}{\sqrt{L}} + \left[\frac{679i}{324} - \frac{67i}{144\sqrt{3}} + \frac{25}{3z^6} - \frac{13i}{z^4} - \frac{265}{54z^2} - \frac{41z^2}{216} - \frac{185iz^4}{216}\right] \frac{1}{L} \\
&+ \left[\frac{100i}{3\sqrt{3}z^7} + \frac{8243}{108\sqrt{3}z^5} - \frac{1991i}{54\sqrt{3}z^3} - \frac{55}{9\sqrt{3}z} + \frac{32iz}{81\sqrt{3}} + \frac{77z^3}{162\sqrt{3}} + \frac{839iz^5}{405\sqrt{3}}\right] \frac{1}{L^{3/2}} \\
&+ \left[\frac{6031}{93312} + \frac{47}{2592\sqrt{3}} - \frac{350}{9z^8} + \frac{19615i}{162z^6} + \frac{73271}{864z^4} - \frac{56915i}{3888z^2} + \frac{23945iz^2}{23328} \right. \\
&\left. - \frac{18679z^4}{46656} - \frac{60547iz^6}{34992}\right] \frac{1}{L^2} \Bigg\} \,.
\end{aligned} \tag{2.106}$$

2.4.4 Matching procedure

Within the matching regions, the expression

$$r - 3 \propto \frac{z}{\sqrt{L}} + \dots , \tag{2.107}$$

governs the behaviour of the in-going and out-going solutions, following the form of Eq. (D.1.3) and Eq. (2.69). Specifically, $r-3$ is small and L is large. In other words, when we apply a power series expansion to the exponential function, terms of the order $\mathcal{O}(z^a L^{-b/2})$ for $a \leq |b|$ are affected. In so doing, exponential terms of appropriate order in $z/\sqrt{L}$ reduce to polynomial form. For the interior solutions, $z \to \pm\infty$, we match these against the exterior solutions.

We find that we can obtain constant (i.e. z-independent) terms for C_{in}, B_{in}, and B_{out} as a consequence of the cancellation of higher-order terms during the matching procedure. For terms with powers of z in the denominator that do not cancel, we have determined their contribution to be negligible. This is evidenced when we solve for these constant coefficients at increasingly higher orders: terms that retain powers of z in the denominator at order k cancel at orders $k+1$ and higher during the matching procedure; only constant and L-dependent terms remain unmodified as we progress to higher orders. Finally, we note that each of these reduce to their leading-order form for $L \to \infty$ (c.f. Section D.3).

To obtain $C_{in} \sim u_0^{r\to-\infty}/u^+$

Through the perturbative power series expansion, the exterior solution in the region $r < r_p$ becomes

$$\begin{aligned} u^{+(2)} \sim \left(\frac{\xi}{2\sqrt{27}}\right)^{1/2} \exp\left\{ + \frac{iz^2}{2} - \frac{10iz^3}{9\sqrt{3}}\frac{1}{\sqrt{L}} + \frac{185iz^4}{216}\frac{1}{L} - \frac{839iz^5}{405\sqrt{3}}\frac{1}{L^{3/2}} + \frac{60547iz^6}{34992}\frac{1}{L^2} \right\} \\ \times \left[1 + \frac{7z}{3\sqrt{3}}\frac{1}{\sqrt{L}} + \left[-\frac{367i}{324} + \frac{67i}{144\sqrt{3}} + \frac{185z^2}{216} \right]\frac{1}{L} + \left[\frac{469iz}{1296} - \frac{4561iz}{972\sqrt{3}} + \frac{179z^3}{648\sqrt{3}} \right]\frac{1}{L^{3/2}} \right. \\ \left. + \left[-\frac{2696959}{3359232} + \frac{23743}{46656\sqrt{3}} - \frac{103657iz^2}{34992} + \frac{12395iz^2}{31104\sqrt{3}} + \frac{6517z^4}{31104} \right]\frac{1}{L^2} \right] . \end{aligned} \tag{2.108}$$

For the interior solution, we retain only the $z \to -\infty$ asymptotic forms presented in Section 2.4.2. Recall that the complete solution is given by

$$u_0^{z\to-\infty} \sim f^{-1/2} e^{+ig(z)^2/2} \left(\frac{dg}{dz}\right)^{-1/2} . \tag{2.109}$$

Following the same linearisation for terms of order $\mathcal{O}(z^a L^{-b/2})$ for $a \leq |b|$, we find that

$$\begin{aligned} u_0^{z\to-\infty} \sim \exp\left\{ + \frac{iz^2}{2} - \frac{10iz^3}{9\sqrt{3}}\frac{1}{\sqrt{L}} + \frac{185iz^4}{216}\frac{1}{L} - \frac{839iz^5}{405\sqrt{3}}\frac{1}{L^{3/2}} + \frac{60547iz^6}{34992}\frac{1}{L^2} \right\} \\ \times \sqrt{3}\left[1 + \frac{7z}{3\sqrt{3}}\frac{1}{\sqrt{L}} + \left[\frac{463i}{2592} + \frac{185z^2}{216} \right]\frac{1}{L} + \left[-\frac{12695iz}{7776\sqrt{3}} + \frac{179z^3}{648\sqrt{3}} \right]\frac{1}{L^{3/2}} \right. \\ \left. + \left[-\frac{1623193}{13436928} - \frac{1029697iz^2}{559872} + \frac{6517z^4}{31104} \right]\frac{1}{L^2} \right] + \dots . \end{aligned} \tag{2.110}$$

Terms that are higher-order in z cancel, leaving us with

$$C_{in}^{(2)} \sim \sqrt{2}\left(\frac{\xi}{3\sqrt{27}}\right)^{-1/2}\left[1+\left[\frac{1133i}{864}-\frac{67i}{144\sqrt{3}}\right]\frac{1}{L}+\left(\frac{78167}{124416\sqrt{3}}-\frac{1307101}{1492992}\right)\frac{1}{L^2}\right]. \tag{2.111}$$

To obtain $B_{out} \sim u_0^{r\to+\infty}/u^+$

To obtain $B_{out}^{(2)}$, we must match the asymptotics of $f^{-1/2}\psi_{z\to+\infty}^{(2)}(e^{+iz^2/2})$ over $u^{+(2)}$, where $\psi_{z\to+\infty}^{(2)}(e^{+iz^2/2})$ is the first term of Eq. (2.97). Up to and including $\mathcal{O}(L^{-2})$, this gives

$$B_{out}^{(2)} \sim \sqrt{2}\left(\frac{\xi}{3\sqrt{27}}\right)^{-1/2}\left[1+\left[\frac{1133i}{864}-\frac{67i}{144\sqrt{3}}\right]\frac{1}{L}+\left(\frac{78167}{124416\sqrt{3}}-\frac{1307101}{1492992}\right)\frac{1}{L^2}\right] = C_{in}^{(2)}. \tag{2.112}$$

To obtain $B_{in} \sim u_0^{r\to+\infty}/u^-$

To obtain $B_{in}^{(2)}$, we must match the asymptotics of $f^{-1/2}\psi_{z\to+\infty}^{(2)}(e^{-iz^2/2})$ over $u^{-(2)}$, where $\psi_{z\to+\infty}^{(2)}(e^{-iz^2/2})$ is the second term of Eq. (2.97) at $\mathcal{O}(L^{-2})$. Through the perturbative power series expansion, the exterior solution in the region $r > r_p$ becomes

$$\begin{aligned}
u^{-(2)} \sim{}& \left(\frac{z}{L^{1/2}}\right)^{-1}\left(\frac{\xi}{2\sqrt{27}}\right)^{-1/2}\exp\left\{-\frac{iz^2}{2}-\frac{10iz^3}{9\sqrt{3}}\frac{1}{\sqrt{L}}+\frac{185iz^4}{216}\frac{1}{L}+\frac{839iz^5}{405\sqrt{3}}\frac{1}{L^{3/2}}-\frac{60547iz^6}{34992}\frac{1}{L^2}\right\}\\
&\times\left[1-\frac{i}{3z^6}-\frac{3}{4z^4}+\frac{i}{2z^2}+\left[\mathcal{O}\left(\frac{1}{z^7}\right)-\frac{29i}{3\sqrt{3}z^5}-\frac{71}{12\sqrt{3}z^3}+\frac{17i}{6\sqrt{3}z}-\frac{z}{\sqrt{3}}\right]\frac{1}{\sqrt{L}}\right.\\
&+\left[\mathcal{O}\left(\frac{1}{z^6}\right)-\frac{26135i}{1296z^4}+\frac{67i}{192\sqrt{3}z^4}-\frac{14431}{2592z^2}+\frac{67}{288\sqrt{3}z^2}-\frac{5z^2}{216}+\frac{1261i}{1296}-\frac{67i}{144\sqrt{3}}\right]\frac{1}{L}\\
&+\left[\mathcal{O}\left(\frac{1}{z^5}\right)+\frac{4757i}{5184z^3}-\frac{190799i}{3888\sqrt{3}z^3}+\frac{1139}{2592z}-\frac{45023}{7776\sqrt{3}z}+\frac{67iz}{432}-\frac{1909iz}{1296\sqrt{3}}+\frac{395z^3}{648\sqrt{3}}\right]\frac{1}{L^{3/2}}\\
&+\left[\mathcal{O}\left(\frac{1}{z^4}\right)-\frac{103604815i}{6718464z^2}+\frac{970261i}{373248\sqrt{3}z^2}+\frac{694049iz^2}{559872}+\frac{335iz^2}{31104\sqrt{3}}-\frac{52981z^4}{93312}+\frac{118373}{209952}\right.\\
&\left.\left.+\frac{87871}{186624\sqrt{3}}\right]\frac{1}{L^2}\right].
\end{aligned} \tag{2.113}$$

Since terms satisfying the condition $\mathcal{O}(z^aL^{-b/2})$ for $a \leq |b|$ are linearised through the power series expansion, we are left with terms in inverse powers of z. The contribution of these terms can be neglected as discussed above.

As before, for the interior solution, we retain only the $z \to +\infty$ asymptotic forms presented in Section 2.4.2. Here, however, we are concerned only with the $\exp\{-ig(z)^2/2\}$ component. Recall that the complete solution is given by

$$u_0^{z\to+\infty} \sim -f^{-1/2}e^{-ig(z)^2/2}\left(\frac{dg}{dz}\right)^{-1/2}\frac{\sqrt{2\pi}}{\Gamma\{-n-\eta+\mathcal{O}\left(\frac{1}{L}\right)\}}e^{-3i\pi/4}2^{-1/2}\frac{1}{g(z)}\left[1+\frac{i}{2}g(z)^{-2}-\frac{3}{4}g(z)^{-4}+...\right]. \tag{2.114}$$

Following the same linearisation for terms of order $\mathcal{O}(z^a L^{-b/2})$ for $a \leq |b|$, we find that

$$
\begin{aligned}
u_0^{z\to+\infty} \sim \frac{9}{z}\sqrt{\frac{\pi}{i}}\epsilon \exp\left\{ -\frac{iz^2}{2} + \frac{10iz^3}{9\sqrt{3}}\frac{1}{\sqrt{L}} - \frac{185iz^4}{216}\frac{1}{L} + \frac{839iz^5}{405\sqrt{3}}\frac{1}{L^{3/2}} - \frac{60547iz^6}{34992}\frac{1}{L^2}\right\} \\
\times \left[1 - \frac{3}{4z^4} + \frac{i}{2z^2} + \left[-\frac{25i}{3\sqrt{3}z^5} - \frac{71}{12\sqrt{3}z^3} + \frac{17i}{6\sqrt{3}z} - \frac{z}{\sqrt{3}}\right]\frac{1}{\sqrt{L}}\right. \\
+ \left[\frac{5963i}{2592} + \frac{500}{27z^6} - \frac{74573i}{3456z^4} - \frac{32303}{5184z^2} - \frac{5z^2}{216}\right]\frac{1}{L} + \left[\frac{70000i}{729\sqrt{3}z^7} + \frac{4043783}{23328\sqrt{3}z^5}\right. \\
- \frac{5544353i}{93312\sqrt{3}z^3} - \frac{148543}{15552\sqrt{3}z} - \frac{7259iz}{2592\sqrt{3}} + \frac{395z^3}{648\sqrt{3}}\Big]\frac{1}{L^{3/2}} + \Big[-\frac{23383681}{13436928} \\
\left.\left. - \frac{2800000}{19683z^8} + \frac{56938865i}{157464z^6} + \frac{30705895193}{161243136z^4} - \frac{629568725i}{26873856z^2} + \frac{169211iz^2}{139968} - \frac{52981z^4}{93312}\Big]\frac{1}{L^2}\right] + \dots .
\end{aligned}
\tag{2.115}
$$

Upon performing the matching procedure, we then obtain

$$
\begin{aligned}
B_{in}^{(2)} \sim \epsilon\left(\frac{27\pi\xi}{i2\sqrt{3}L}\right)^{1/2}\left[1 + \mathcal{O}\left(\frac{1}{z^6}\right) + \mathcal{O}\left(\frac{1}{z^5}\right)\frac{1}{L^{1/2}} + \left[\frac{1147i}{864} + \frac{67i}{144\sqrt{3}} + \mathcal{O}\left(\frac{1}{z^4}\right)\right]\frac{1}{L} + \mathcal{O}\left(\frac{1}{z^3}\right)\frac{1}{L^{3/2}}\right. \\
\left. + \left[-\frac{1619197}{1492992} - \frac{79105}{124416\sqrt{3}} + \mathcal{O}\left(\frac{1}{z^2}\right)\right]\frac{1}{L^2}\right] .
\end{aligned}
\tag{2.116}
$$

We find constant coefficients only for the terms with integer powers of $(1/L)$, but not the ones with half-integer powers. Though we have retained coefficients with inverse powers of z, we expect them to be cancelled by higher order contributions, while the constant coefficients as shown in Eq. (2.116) will remain unmodified. To illustrate this explicitly, let us consider the above procedure only to order $\mathcal{O}(L^{-1})$,

$$
B_{in}^{(1)} \sim \epsilon\left(\frac{27\pi\xi}{i2\sqrt{3}L}\right)^{1/2}\left[1 + \mathcal{O}\left(\frac{1}{z^4}\right) + \mathcal{O}\left(\frac{1}{z^3}\right)\frac{1}{L^{1/2}} + \left[\frac{1147i}{864} + \frac{67i}{144\sqrt{3}} + \mathcal{O}\left(\frac{1}{z^2}\right)\right]\frac{1}{L}\right] . \tag{2.117}
$$

If we compare Eq. (2.116) and Eq. (2.117), we observe that despite the changes in the functions of z, the constant coefficients of L^{-1} remain the same.

We note also that when we compare our higher-order matching variables, $C_{in}^{(2)}$, $B_{out}^{(2)}$, $B_{in}^{(2)}$, with the $n = 0$ the leading-order results of Eqs. (D.3.29), (D.3.30), and (D.3.32), respectively, there is a $\sqrt{3}$ discrepancy for the leading coefficients. This is due to our necessary inclusion of the prefactor $f^{-1/2}$ in Eqs. (2.109) and (2.114). For the leading order, the prefactor is just a constant $\sqrt{3}$ and will fully cancel out in the calculation of the $A_{\ell n}^{\pm(0)}$ coefficients. As such, the leading order results will not change when excluding this prefactor. However, for the higher-order studies, the prefactor provides a polynomial of $\mathcal{O}(z^a L^{-b/2})$ as in Eq. (2.95), which contributes to the cancellation of z-dependent terms in the higher-order matching.

2.4.5 The quasinormal excitation factor

Finally, we can bring together the components of the calculation in order to construct the QNEF. To define the QNEF, we use Eq. (2.25) for $k = 2$ and $n = 0$,

$$
\mathcal{B}_{\ell 0}^{(2)} \equiv \frac{A_{\ell 0}^{+(2)}}{2\omega}\left(\frac{\partial A_{\ell 0}^{-(2)}}{\partial\omega}\right)^{-1}\Bigg|_{\omega\to\omega_{\ell 0}^{(2)}} , \tag{2.118}
$$

where the constants $A_{\ell 0}^{\pm(2)}$ are defined as

$$A_{\ell 0}^{+(2)} = \frac{\beta_1^{(2)}\beta_2^{(2)}}{\alpha_1^{(2)}\alpha_2^{(2)}}\frac{B_{out}^{(2)}}{C_{in}^{(2)}}\,, \qquad A_{\ell 0}^{-(2)} = \frac{\gamma_1^{(2)}\gamma_2^{(2)}}{\alpha_1^{(2)}\alpha_2^{(2)}}\frac{B_{in}^{(2)}}{C_{in}^{(2)}}\,, \tag{2.119}$$

with the "phase factors" [50] extended to higher order as,

$$\begin{aligned}
\alpha_1^{(2)} &= \exp\left\{+i\omega\int_{r=3}^{r=2}\left(1+\frac{6}{r}\right)^{1/2}\left(1-\frac{3}{r}\right)\frac{dr}{f}\right\}\exp\{+i\omega r_\star\} \\
&= \exp\{i\omega[6-\sqrt{27}+8\ln 2-3\ln\xi]\}\,, &(2.120)\\
\beta_1^{(2)} &= \exp\left\{+i\omega\int_{r=3}^{r=\infty}\left(1+\frac{6}{r}\right)^{1/2}\left(1-\frac{3}{r}\right)\frac{dr}{f}\right\}\exp\{-i\omega r_\star\} \\
&= \exp\{i\omega[3-\sqrt{27}+4\ln 2-3\ln\xi]\} &(2.121)\\
\gamma_1^{(2)} &= \exp\left\{-i\omega\int_{r=3}^{r=\infty}\left(1+\frac{6}{r}\right)^{1/2}\left(1-\frac{3}{r}\right)\frac{dr}{f}\right\}\exp\{+i\omega r_\star\} = 1/\beta_1^{(2)}\,, &(2.122)\\
\alpha_2^{(2)} &= \lim_{r\to 2}\ \exp\left\{\sum_{k=0}^{2}\widetilde{S}_{k0}^{+}(r)L^{-k}\right\} = 1\,, &(2.123)\\
\beta_2^{(2)} &= \lim_{r\to\infty}\ \exp\left\{\sum_{k=0}^{2}\widetilde{S}_{k0}^{+}(r)L^{-k}\right\} = \left(2-\sqrt{3}\right)^{-1/2}\exp\left\{+\frac{47i}{144\sqrt{3}L}-\frac{145}{2592\sqrt{3}L^2}\right\}\,, &(2.124)\\
\gamma_2^{(2)} &= \lim_{r\to\infty}\ \exp\left\{\sum_{k=0}^{2}\widetilde{S}_{k0}^{-}(r)L^{-k}\right\} = \left(2-\sqrt{3}\right)^{+1/2}\exp\left\{-\frac{47i}{144\sqrt{3}L}+\frac{145}{2592\sqrt{3}L^2}\right\}\,. &(2.125)
\end{aligned}$$

With the use of these definitions, we find that the out-going coefficient precisely matches Eq. (D.4.39) for $n=0$, with corrections in higher orders of L^{-k}. In the second line, we substitute the QNF up to order $\mathcal{O}(L^{-2})$,

$$\begin{aligned}
A_{\ell 0}^{+(2)}\Big|_{\omega\to\widetilde{\omega}_{\ell 0}^{(2)}} &\approx \xi^{1/4}\exp\left\{-i\omega[3+4\ln 2]+\frac{47i}{144\sqrt{3}}\frac{1}{L}-\frac{145}{2592\sqrt{3}}\frac{1}{L^2}+\mathcal{O}(\epsilon)\right\}\Bigg|_{\omega\to\omega_{\ell 0}^{(2)}} \\
&\approx \xi^{1/4}\exp\left\{-\frac{i(3+4\ln 2)}{3\sqrt{3}}L-\frac{(3+4\ln 2)}{6\sqrt{3}}+\left[\frac{127i}{432\sqrt{3}}-\frac{7i\ln 2}{162\sqrt{3}}\right]\frac{1}{L}\right. \\
&\qquad\left.+\left[-\frac{143}{1944\sqrt{3}}-\frac{137\ln 2}{5832\sqrt{3}}\right]\frac{1}{L^2}+\mathcal{O}(\epsilon)\right\}\,.
\end{aligned} \tag{2.126}$$

Similarly, the exponent of the in-going coefficient is precisely that of Eq. (D.4.40), albeit augmented here by higher-order L^{-k} terms. Note that this correction in L^{-k} within the exponential is the additive inverse of that of Eq. (2.126). With the higher-order terms in the polynomial, we find that the z terms cancel.

$$
\begin{aligned}
A^{-(2)}_{\ell 0}\Big|_{\omega\to\widetilde{\omega}^{(2)}_{\ell 0}} &\approx \epsilon \left(\frac{\left(26+5\sqrt{27}\right)\pi}{iL}\right)^{1/2} \frac{1619197i+316420i\sqrt{3}+\left(1982016+231552\sqrt{3}\right)L-1492992iL^2}{2614202i-625336i\sqrt{3}+\left(3915648-463104\sqrt{3}\right)L-2985984iL^2} \\
&\quad\times \exp\left\{-i\omega[9-2\sqrt{27}+12\ln 2-6\ln\xi]-\frac{47i}{144\sqrt{3}}\frac{1}{L}+\frac{145}{2592\sqrt{3}}\frac{1}{L^2}+\mathcal{O}(\epsilon)\right\}\Bigg|_{\omega\to\omega^{(2)}_{\ell 0}} \\
&\approx \epsilon \left(\frac{\left(26+5\sqrt{27}\right)\pi}{iL}\right)^{1/2} \frac{1619197i+316420i\sqrt{3}+\left(1982016+231552\sqrt{3}\right)L-1492992iL^2}{2614202i-625336i\sqrt{3}+\left(3915648-463104\sqrt{3}\right)L-2985984iL^2} \\
&\quad\times \exp\left\{\left[2i-i\sqrt{3}-\frac{4i\ln 2}{\sqrt{3}}+\frac{4i\ln\{2+\sqrt{3}\}}{\sqrt{3}}\right]L+\left[1-\frac{\sqrt{3}}{2}+\frac{2\ln\{2+\sqrt{3}\}}{\sqrt{3}}-\frac{2\ln 2}{\sqrt{3}}\right]\right. \\
&\quad+\left[\frac{7i}{108}-\frac{61i}{144\sqrt{3}}-\frac{7i\ln 2}{54\sqrt{3}}+\frac{7i\ln\{2+\sqrt{3}\}}{54\sqrt{3}}\right]\frac{1}{L}+\left[\frac{137}{3888}+\frac{1}{324\sqrt{3}}-\frac{137\ln 2}{1944\sqrt{3}}\right. \\
&\quad\left.\left.+\frac{137\ln\{2+\sqrt{3}\})}{1944\sqrt{3}}\right]\frac{1}{L^2}+\mathcal{O}(\epsilon)\right\}. \qquad (2.127)
\end{aligned}
$$

With all the necessary components of the QNEF computed explicitly to higher order, we present the final expressions for the QNEF at orders $\mathcal{O}(L^{(-1)})$ and $\mathcal{O}(L^{(-2)})$, respectively as:

$$
\mathcal{B}^{(1)}_{\ell 0} \approx \left(\frac{-1133+134\sqrt{3}+864iL}{-1147-134\sqrt{3}+864iL}\right)\left(\frac{\exp\left\{2i\omega^{(1)}_{\ell 0}\zeta+\frac{47i}{72\sqrt{3}}\frac{1}{L}\right\}}{\omega^{(1)}_{\ell 0}}\right)\left(\frac{\sqrt{L}}{\left(2+\sqrt{3}\right)\sqrt{-i\pi}}\right), \qquad (2.128)
$$

$$
\begin{aligned}
\mathcal{B}^{(2)}_{\ell 0} &\approx \left(\frac{-1307101+312688\sqrt{3}-1728iL\left(-1133+134\sqrt{3}+864iL\right)}{-1619197-316420\sqrt{3}-1728iL\left(-1147-134\sqrt{3}+864iL\right)}\right) \\
&\quad\times\left(\frac{\exp\left\{2i\omega^{(2)}_{\ell 0}\zeta+\frac{47i}{72\sqrt{3}}\frac{1}{L}-\frac{145}{1296\sqrt{3}}\frac{1}{L^2}\right\}}{\omega^{(2)}_{\ell 0}}\right)\left(\frac{\sqrt{L}}{\left(2+\sqrt{3}\right)\sqrt{-i\pi}}\right), \qquad (2.129)
\end{aligned}
$$

where the constant ζ is defined in Eq. (D.5.45).

We plot the real and imaginary contributions in Fig. 2.9 at leading order, and at the next two orders in L^{-k}. At order k, we evaluate the QNEF at the k-th order QNF, i.e. at order L^{-1} we evaluate at $\omega^{(1)}_{\ell 0} = \sqrt{27}L - i\sqrt{27}/2 + 7\sqrt{27}/216L^{-1}$. To improve the accuracy of our QNEFs, we subject Eq. (2.25) to an additional power series expansion in L^{-k}, where k refers to the order at which we compute the QNEF. In so doing, we can compute the elusive $\ell = 0$, $\ell = 1$ terms that are otherwise difficult to capture accurately.

In order to validate our results, we also compare our QNEF values against those generated in Ref. [193] through the method introduced by Mano, Suzuki, and Takasugi (MST) in Refs [194, 195]. This technique produces solutions to the radial component of the inhomogeneous QNM problem, as well as derived quantities such as the Wronskian, using Gaussian hypergeometric functions and Coulomb wave functions. In order to do this, two complementary infinite series are employed, whose radius of convergence extends towards spatial infinity and the event horizon, respectively. The approach is demonstrably accurate, particularly for small frequencies/late times.

We note with interest that, reminiscent of photon orbits in the $r \to r_+$ limit, the QNEFs tend towards zero in the large-ℓ regime. This reinforces the connection between unstable null geodesics and the behaviour of QNMs in the eikonal regime [157].

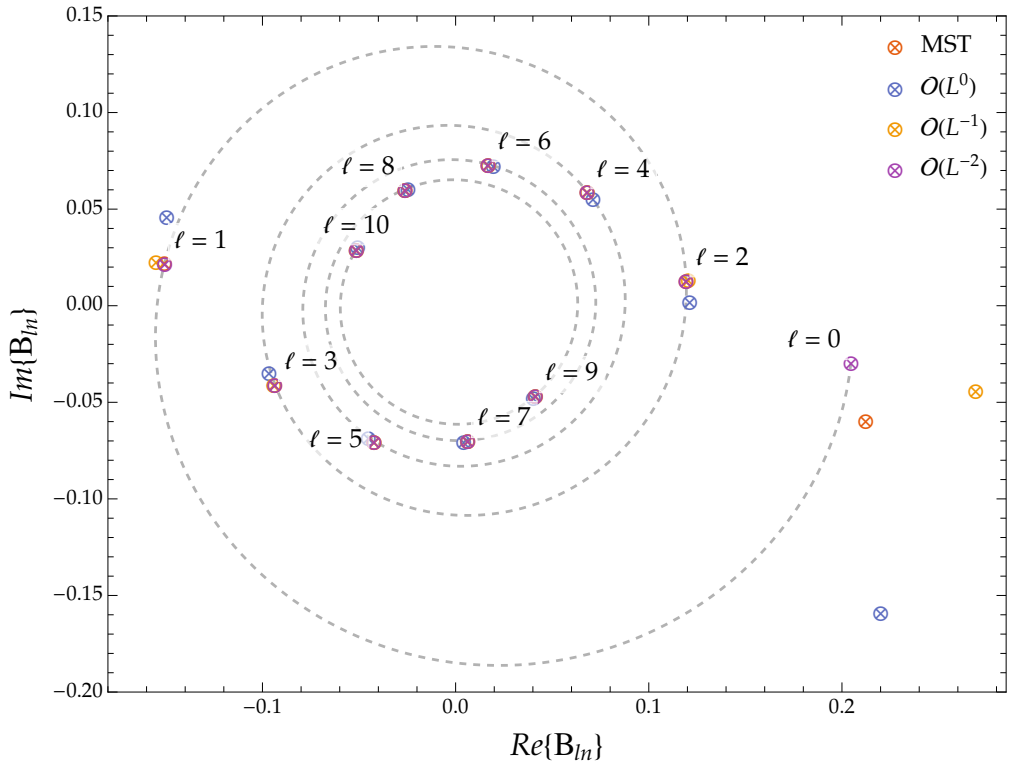

Figure 2.9: *The real and imaginary parts of the QNEF at orders L^0, L^{-1}, and L^{-2} for the fundamental mode. We compare against the numerical results generated using the MST formalism* [194, 195]*, listed in Table II of Ref.* [193].

2.4.6 Discussion

In this section, we have extended the Dolan-Ottewill method to calculate QNEFs to higher orders for the Schwarzschild black hole. By incorporating higher-order corrections using the WKB method, we achieved significantly greater accuracy in our QNEF calculations compared to leading-order results. Specifically, our higher-order treatment reduced the discrepancy between QNEFs computed using the Dolan-Ottewill method and those produced by the MST method, particularly for lower multipolar numbers (see Fig. 2.9).

The ability to extract QNEFs with higher accuracy has several important implications for future research and applications. These include enhanced GW modelling, where accurate QNEF calculations are crucial for modelling the post-merger phase of GWs from binary black hole mergers. Also, higher accuracy QNEF values will aid in better parameter estimation of post-merger black holes, facilitating more precise tests of GR in the strong-field regime.

Note that since the Dolan-Ottewill technique can be applied to a variety of spherically-symmetric black holes and perturbing fields of different spins, our higher-order extension enhances its utility across different contexts, including extremal black holes where traditional numerical methods may fail. In this way, we can perform more precise calculations while avoiding the use of computationally intensive approaches. Therefore, by providing a more accurate method for calculating QNEFs, our work supports the growing field of GW astronomy, offering a valuable resources for interpreting and analysing signals detected by the LVK collaboration.

As a final thought, we note that while gravitational perturbations of a Kerr black hole would be more closely aligned to the astrophysical reality, the comparatively simple setup produced here provides a suitable testing ground for our extension of this technique. We consider this work on static, spherically-symmetric black holes then a necessary precursor to the rotating case, which we will consider in a future work.

Table 2.2: *The real and imaginary components of the QNEF at orders L^0, L^{-1}, and L^{-2} for the fundamental mode.*

ℓ	$\mathfrak{Re}\{\mathcal{B}^{(0)}_{\ell 0}\}$	$\mathfrak{Im}\{\mathcal{B}^{(0)}_{\ell 0}\}$	$\mathfrak{Re}\{\mathcal{B}^{(1)}_{\ell 0}\}$	$\mathfrak{Im}\{\mathcal{B}^{(1)}_{\ell 0}\}$	$\mathfrak{Re}\{\mathcal{B}^{(2)}_{\ell 0}\}$	$\mathfrak{Im}\{\mathcal{B}^{(2)}_{\ell 0}\}$
0	$+0.22010$	-0.15859	$+0.26935$	-0.04343	$+0.20467$	-0.02932
1	-0.14952	$+0.04663$	-0.15502	$+0.02304$	-0.15062	$+0.02227$
2	$+0.12130$	$+0.00240$	$+0.12058$	$+0.01364$	$+0.11934$	$+0.01352$
3	-0.09660	-0.03438	-0.09412	-0.04071	-0.09363	-0.04050
4	$+0.07122$	$+0.05573$	$+0.06826$	$+0.05933$	$+0.06804$	$+0.05914$
5	-0.04515	-0.06821	-0.04224	-0.07005	-0.04215	-0.06990
6	$+0.01954$	$+0.07266$	$+0.01693$	$+0.07331$	$+0.01691$	$+0.07320$
7	$+0.00416$	-0.06992	$+0.00632$	-0.06976	$+0.00631$	-0.06968
8	-0.02450	$+0.06107$	-0.02615	$+0.06038$	-0.02613	$+0.06032$
9	$+0.04026$	-0.04746	$+0.04141$	-0.04646	$+0.04138$	-0.04643
10	-0.05062	0.03070	-0.05129	$+0.02957$	-0.05126	$+0.02956$

In this chapter, we have provided the underlying formalism needed to follow the QNM investigations performed in Chapters 4 and 6. For example, the semi-classical techniques introduced here inform the computational methods used therein; the influence of mass and the concepts of superradiance appear throughout our work. In the next chapters, we consider a more complicated framework, adding the space-time parameters of Q and Λ as well as the field parameter of q, in order to investigate the interplay of (M, Q, Λ) and (μ, q, ℓ) in the QNF spectra.

Chapter 3

Einstein-Hilbert-Maxwell theory in de Sitter space-time

> ... for one who has crossed the event horizon in the Reissner-Nordström geometry, there would appear to exist an infinite range of rich possibilities for experience, that are denied to one who crosses the event horizon in the Schwarzschild geometry...
>
> Subrahmanyan Chandrasekhar in *The Mathematical Theory of Black Holes* [131]

In the previous chapter, our focus was on the formalism required to describe the QNMs of the black hole exterior. To prioritise clarity over complexity in that discussion, we had concentrated on the simplest possible black hole configuration: the Schwarzschild solution in asymptotically flat space-time. In so doing, we were able to highlight explicitly the relationship between the behaviour of QNMs and the characteristics of their black hole source. Since QNMs are beholden to physically-motivated boundary conditions imposed by the black hole context, it is imperative that any QNM study is preceded by an analysis of the fixed background upon which these perturbations propagate. Since we are building towards an investigation into the QNMs of the RNdS black hole, we dedicate this chapter to the establishment of a concrete understanding of the space-time structure and parametric constraints of the RNdS solution.

The RNdS black hole represents the most generalised static and spherically-symmetric black hole for which $d = 4$ and $\Lambda > 0$. Since we consider the black hole to be isolated and at equilibrium, the "no-hair conjecture"[12] applies and the black hole is stable [32, 33]. As introduced in Chapter 1, the RNdS black hole serves as a rich testing ground for theoretical conjectures. Studies of the interplay between gravitational dynamics, electromagnetic charge, and the cosmological constant lead naturally to questions at both quantum and cosmological scales, allowing for investigations into black hole thermodynamics and the evolution of large-scale structure. As such, we begin this chapter with a review of the RNdS space-time structure, properties, and phase space; we rely heavily on Refs[89, 197–199] for Section 3.1. In Section 3.2, we provide a brief aside on the deviation of the FL bound from a study of the RNdS black hole decay, as an example of how bounds on particle mass and charge can be extracted from heuristic arguments in black hole mechanics. Finally, Section 3.3 explores the concept of cosmic censorship in the RNdS black hole context, which provides the necessary theoretical framework for our study of QNM applications set up in the next chapter.

[12] While a discussion on the "cosmic no-hair conjecture" [71] is beyond the scope of this thesis, evidence suggests that the hypothesis remains valid even for $\Lambda > 0$ [196].

3.1 The Reissner-Nordström de Sitter black hole

To begin our examination of the $(3+1)$-dimensional RNdS black hole, we consider the Einstein-Hilbert-Maxwell action in an asymptotically-de Sitter space-time under natural units,

$$S = \int d^4x\sqrt{-g}\left[\frac{1}{16\pi G}\left(R - 2\Lambda\right) - \frac{1}{4g_1^2}F_{\mu\nu}F^{\mu\nu}\right] . \tag{3.1}$$

As specified in Chapter 1, $\kappa^2 = 8\pi G = M_P^{-2}$ relates the gravitational coupling κ to Newton's gravitational constant G and the Planck mass M_P. The de Sitter radius L_{dS}, Hubble parameter H, and cosmological constant $\Lambda > 0$ can be expressed as $H^2 = L_{dS}^{-2} = \Lambda/3$. The geometry of the space-time is encoded in the Ricci scalar curvature $R = g^{\mu\nu}R_{\mu\nu}$ and the metric $g = \det|g_{\mu\nu}|$; the metric tensor $g_{\mu\nu}$ is in turn defined in terms of the characteristic black hole parameters, mass m_{BH} and charge q_{BH} per the "no-hair conjecture" [4], as well as Λ.[13] For the electromagnetic field strength tensor $F^{\mu\nu}$, g_1 is the $U(1)$ gauge coupling. Since we are concerned only with the electrically-charged RNdS case, the non-zero component of $F^{\mu\nu}$ is

$$F_{tr} = \frac{g_1^2}{4\pi}\frac{q_{\text{BH}}}{r} , \tag{3.2}$$

with a purely electric gauge potential

$$A = \Phi dt , \quad \Phi = \frac{g_1^2}{4\pi}\frac{q_{\text{BH}}}{r} . \tag{3.3}$$

The Lagrangian of Eq. (3.1) admits the static and spherically-symmetric black hole solution [9],

$$ds^2 = -f(r)dt^2 + f(r)^{-1}dr^2 + r^2\left(d\theta^2 + \sin^2\theta d\phi^2\right) , \tag{3.4}$$

written in terms of the usual Schwarzschild coordinates (t, r, θ, ϕ), with $t \in (-\infty, +\infty)$, $\theta \in (0, \pi)$, and $\phi \in (0, 2\pi)$. Setting $\hbar = c = 1$, we can express this metric function as

$$f(r) = 1 - \frac{2Gm_{\text{BH}}}{r} + \frac{Gg_1^2q_{\text{BH}}}{4\pi r^2} - \frac{\Lambda}{3}r^2 . \tag{3.5}$$

While the physical quantities m_{BH} and g_1q_{BH} lend themselves to characteristic black hole length scales [201], in fact, all three parameters have dimensions of length [89]:

$$Gm_{\text{BH}} = \frac{\kappa^2}{8\pi}m_{\text{BH}} = M , \tag{3.6}$$

$$\frac{G}{4\pi r^2}g_1^2q_{\text{BH}} = \frac{\kappa^2}{32\pi^2r^2}g_1^2q_{\text{BH}} = Q^2 , \tag{3.7}$$

$$\Lambda = \frac{3}{L_{dS}^2} . \tag{3.8}$$

In introducing these parametrisations, we have reduced the characterising space-time information to the

[13] Recall that Λ is a parameter of the "space of theories", a model-dependent degree of freedom, rather than a black hole parameter. In our standard model of (big bang) cosmology, it is understood that Λ is associated with the vacuum energy of the scalar field that once drove inflation. In other words, the potential of the inflaton acts as an effective cosmological constant whose value is near-zero in our present epoch [200].

Table 3.1: *RNdS space-time regions (Fig. 3.1) and the dominant force within each.*

Region		$f(r)$		*Dominant force*
$0 < r < r_-$	(III)	$\sim Q^2/r^2$	> 0	*repulsive electromagnetic force*
$r_- < r < r_+$	(II)	$\sim -2M/r$	< 0	*attractive gravitational force*
$r_+ < r < r_c$	(I)	~ 1	> 0	*no subdominant contributions*
$r_c < r$	(IV)	$\sim -r^2$	< 0	*positive vacuum energy*

dimensionless triple (M, Q, Λ). This allows us to compare mass and charge directly

$$\frac{M^2}{Q^2} = \frac{\kappa^2}{2}\frac{m_{\rm BH}^2}{g_1^2 q_{\rm BH}^2}\,, \tag{3.9}$$

which proves useful in our considerations of constraints on the RNdS phase space. Furthermore, we can express the metric function in its simplified form,

$$f(r) = 1 - \frac{2M}{r} + \frac{Q^2}{r^2} - \frac{r^2}{L_{dS}^2}\,. \tag{3.10}$$

From Eq. (3.10) alone, we can extract substantial information about the black hole structure and phase space. In the sections that follow, we shall demonstrate this explicitly, and highlight how these provide constraints for the field behaviour discussed throughout this chapter and the QNM calculations that follow in Chapter 4.

3.1.1 RNdS black hole structure

The global structure of the black hole space-time is predicated on the nature at the horizons and at the boundaries (i.e. the scalar curvature singularity $r \to 0$ and, in asymptotically flat space-time, spatial infinity $r \to \infty$). The roots of the metric function dictate the causal structure of the space-time, and depend strongly on the values of M, Q, and L_{dS}. From the four real roots of Eq. (3.10), we can identify three Killing horizons: the Cauchy horizon r_-, the event horizon r_+, and the cosmological horizon r_c, where

$$0 < r_- \leq r_+ \leq r_c \leq L_{dS} < \infty\,. \tag{3.11}$$

The fourth (and unphysical) root is given by $r_0 = -(r_- + r_+ + r_c)$. These allow for an alternate expression of the metric function,

$$f(r) = \frac{1}{r^2 L_{dS}^2}(r - r_-)(r - r_+)(r_c - r)(r - r_0)\,. \tag{3.12}$$

The physical horizons of Eq. (3.11) divide the black hole space-time into four causally-connected regions. In Table 3.1, we summarise the dominant contribution from $f(r)$ in each one [89]; in Fig. 3.1, we sketch the corresponding extended conformal space-time diagram for the RNdS black hole, following the conventions set out in Appendix B. There, we highlight the exterior space-time and the black hole interior. Respectively, these are the static patch $\mathcal{M}_{ext}$ (Region I), bounded by the bifurcate event horizon $\mathscr{H}_R^+ \cup \mathscr{H}_R^-$ and the cosmological horizon $\mathscr{C}_R^+$, and $\mathcal{M}_{int}$ (Region II), bounded by the bifurcate event horizon $\mathscr{H}_L^+ \cup \mathscr{H}_R^+$ and the Cauchy horizon $\mathscr{CH}_R^+$.

For each non-degenerate horizon specified in Eq. 3.11, we can calculate a surface gravity κ_i (see Appendix

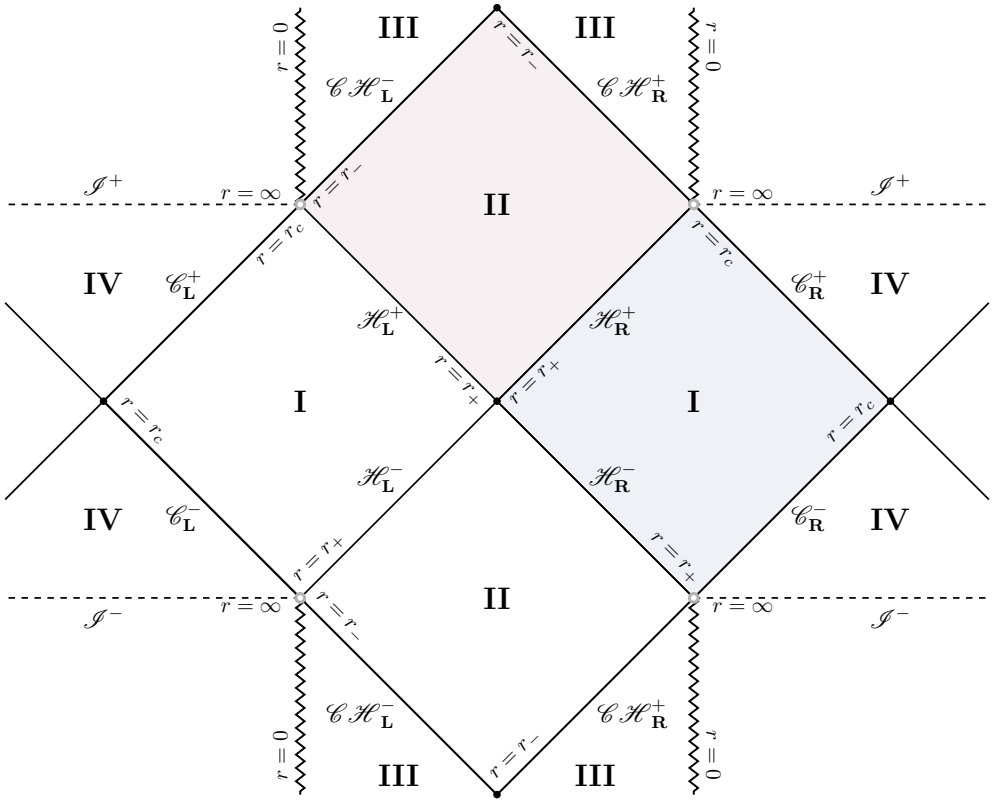

Figure 3.1: *The conformal diagram for the extended RNdS space-time.*

B for details) and an associated Hawking temperature T_i [86]. For $i \in \{-,+,c\}$, we define these as

$$\kappa_i = \frac{1}{2}\frac{d}{dr}f(r)\Big|_{r=r_i}, \qquad T_i = \frac{\kappa_i}{2\pi}\,. \tag{3.13}$$

Explicitly, the surface gravities corresponding to each horizon are

$$\kappa_- = -\frac{(r_+ - r_-)(r_c - r_-)(r_- - r_0)}{2r_-^2 L_{dS}^2}\,, \tag{3.14}$$

$$\kappa_+ = +\frac{(r_+ - r_-)(r_c - r_+)(r_+ - r_0)}{2r_+^2 L_{dS}^2}\,, \tag{3.15}$$

$$\kappa_c = -\frac{(r_c - r_-)(r_c - r_+)(r_c - r_0)}{2r_c^2 L_{dS}^2}\,.\,, \tag{3.16}$$

with $|\kappa_-| > |\kappa_+|$ [202]. Generally, the Hawking radiation emanates from each horizon at a different temperature.

While thermal radiation isotropically pervades de Sitter space-time [71], the black hole is not necessarily in thermal equilibrium with the de Sitter edge. However, there are two black hole solutions that represent thermal equilibrium: the "lukewarm" and the "charged Nariai" families of RNdS black hole solutions. The former represents the case for which $M = Q$ while the latter corresponds to the condition $r_+ = r_c$ [197]. These solutions are discussed in further detail in Section 3.1.2 and Appendix C. In Section 3.2, we will elaborate on the black hole decay process that leads to thermal equilibrium.

These correspond to non-extremal black holes. However, degenerate horizons have vanishing surface gravities. Since $T_i = 0$ in these cases, these black holes are classified as "cold". For asymptotically flat space-time, the RN black hole develops a degenerate horizon when $M = Q$. As we shall demonstrate explicitly in the next section, the presence of the cosmological constant affects the (M, Q) parameter space in the RNdS case. For the RNdS black hole, $\kappa_- = \kappa_+ = 0$ when $Q_{ext} \sim r_+$, as suggested in [203] and shown in Ref. [204] particularly for low Q. The definition of Q_{ext} is provided in Ref. [203], *viz.*

$$Q_{ext} \equiv y_+ r_c \sqrt{\frac{1+2y_+}{1+2y_+ + 3y_+^2}} \,, \quad y_+ = \frac{r_+}{r_c} \,. \tag{3.17}$$

To discuss the black hole solutions more thoroughly, let us consider the black hole phase space of the RNdS black hole, following Refs [89, 200]. As we shall see, much of the analysis we perform is based on the metric function Eq. (3.10) and the "sharkfin" diagram of Fig. 3.2.

3.1.2 RNdS black hole phase space

In order to delineate the RNdS (M, Q) phase space, we begin with the polynomial,

$$\Pi(r) \equiv -r^2 f(r) = -r^2 + 2Mr - Q^2 + L_{dS}^2 r^4 \,. \tag{3.18}$$

We then determine the discriminant thereof,

$$\Delta \equiv -16 L_{dS}^{-2} \left[27 M^4 L_{dS}^{-2} - M^2 (1 + 36 Q^2 L_{dS}^{-2}) + (Q + 4Q^3 L_{dS}^{-2})^2 \right] \,, \tag{3.19}$$

set $L_{dS}^2 = 1$, and plot $\Delta = 0$. Note also that if we set $\Delta = 0$ and solve for M in terms of Λ and Q, we reproduce the known analytical bound on $M^2\Lambda$ [197, 200],

$$M^2 \Lambda \leq \frac{1}{18} \left[1 + 12 Q^2 \Lambda + (1 - 4Q^2 \Lambda)^{3/2} \right] \,. \tag{3.20}$$

We deduce then that $M^2\Lambda$ has an upper bound of $1/9$. In Fig. 3.2, where we parametrise $L_{dS}^{-2} = \Lambda/3 = 1$. $M = \sqrt{2/27}$ is marked on the tip of the sharkfin as Point U. Traditionally [197, 200], the constraint on the black hole charge in 4D comes from the Bogomoln'yi bound for small values of $M^2\Lambda$ [197],

$$\frac{Q^2}{M^2} \lesssim 1 + \frac{1}{3}(M^2\Lambda) + \frac{4}{9}(M^2\Lambda)^2 + \frac{8}{9}(M^2\Lambda)^3 + \mathcal{O}(M^8\Lambda^4) \,. \tag{3.21}$$

For $\Lambda = 3$ and $M = \sqrt{2/27}$, Eq. (3.21) approximately produces the $Q = 1/\sqrt{12}$ result obtained by solving for Q from $\Delta = 0$ and observed at the tip of the sharkfin. Note also that the presence of the cosmological constant raises the upper-bound of the black hole charge-mass ratio: in asymptotically-flat space-time, $Q/M \leq 1$, whereas in asymptotically-de Sitter space-time, $Q/M \leq 1.0607$.

Finally, observe that if we set $L_{dS}^2 = 1$ and $\underline{\Delta} = -\Delta/16$, we can write the complicated analytical expressions corresponding to the black hole horizons as functions of M and Q, *viz.*

$$\underline{r_-} = -a + b \,, \quad \underline{r_+} = +a - b \,, \quad \underline{r_c} = +a + b \,, \quad \underline{r_0} = -a - b \,. \tag{3.22}$$

In our convention, underlined quantities are derived from the parametrised Eq. (3.19). Here,

$$a = \frac{1}{2\sqrt{3}} \sqrt{\frac{(1+X)^2 - 12Q^2}{X}} \qquad , b = \frac{1}{2} \sqrt{\frac{4}{3} - \frac{1 - 12Q^2}{3X} - \frac{X}{3} + \frac{2M}{a}} \,, \tag{3.23}$$

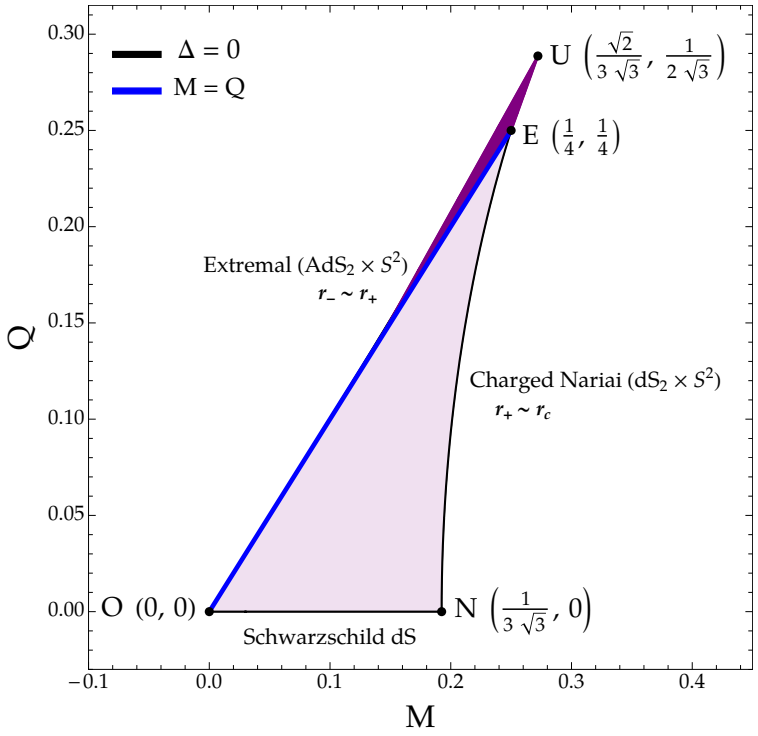

Figure 3.2: *A two-dimensional projection of the parameter space for $H^2 = \Lambda/3 = 1$ for the 4D RNdS black hole. Dark (light) shading corresponds to cold (warm) black holes.*

and

$$X = \left(-1 + 54M^2 - 36Q^2 - 2\sqrt{27}\sqrt{\Delta}\right)^{1/3} . \tag{3.24}$$

Let us now consider the phase space itself. The boundary of Fig. 3.2 corresponds to extremised[14] conditions. At Point O lies pure de Sitter space ($Q = M = 0$). Along Line ON, there is the Schwarzschild de Sitter family of solutions ($Q = 0, M > 0$), with the uncharged Nariai case at point N. The Nariai limit, discussed in Appendix C, corresponds to the upper limit of the black hole mass in de Sitter space-time. The charged Nariai branch of Line NU, for which $r_+ \sim r_c$, extends along NU, and represents the upper mass limit of the charged black hole. The opposite branch of Line OU corresponds to "cold" black hole solutions, with $r_- = r_+$. On this branch, $Q \sim Q_{ext} \sim r_+$, with Q_{ext} defined in Eq. (3.17). These branches terminate in the "ultracold" solution at Point U, where $r_- = r_+ = r_c$: Hawking temperature goes to zero and the local geometry is $\mathbb{M}_2 \times \mathbb{S}^2$.

As mentioned earlier, the $Q = M$ line reflects the "lukewarm" solutions to which black holes in the phase space evolve [197, 205–207]. With this in mind, we can divide the phase diagram of Fig. 3.2 into two regions: the "colder" OEU region, where $Q > M$, and the warmer OEN region, where $Q < M$.

Black hole solutions in the shaded $Q > M$ region are colder than the lukewarm solution and absorb radiation from the cosmological horizon until they become lukewarm. This is evidenced also by $T_c < 0$. The $Q > M$ region is bounded by the OU line: if Q increases with respect to M, the inner and outer black hole horizons eventually coincide, leading to the extremal cold RNdS black hole condition.

Below the lukewarm line is the $Q < M$ region. In this region, black holes are warmer than the cosmological horizon, and will evaporate until they become lukewarm. Note that because these black holes are stabilised by the Gibbons-Hawking radiation from the cosmological horizon, they cannot become arbitrarily cold. The region is bounded by the NU line, upon which $r_+ = r_c$. The outer and cosmological horizons are

[14] For clarity, we use the term "extremise" to refer to black holes with degenerate horizons and "extremal" to refer to the specific case where inner and outer horizons coincide, $r_- = r_+$.

in thermal equilibrium, leading to the charged Nariai solution where the mass is maximal at a given charge [200].

Finally, let us close this section with a few additional constraints that can be derived for the RNdS black hole space-time. As explained in appendix A of Refs [137, 208], we can examine the extremised conditions with respect to the black hole charge-mass relationship, and the useful constraint on L_{dS},

$$0 < L^2_{dS_\pm} = \frac{1}{2}\frac{(3M \pm \sqrt{9M^2 - 8Q^2})^3}{M \pm \sqrt{9M^2 - 8Q^2}} \,. \tag{3.25}$$

Here, we shall observe how this corresponds to the region within the sharkfin diagram.

(i) For $Q^2 > M^2$, above the $M = Q$ line, we have a number of extremising configurations:

(a) We can impose extremal conditions on Q, such that $Q^2 = 9M^2/8$. This yields the "RN-type" extremal condition that extremises the cosmological constant at the upper value such that $L^2_{dS} = L^2_{dS_+}$ i.e. $\Lambda = 2/9M^2$. This yields the "ultra-extremal" case [197, 205] at Point U where there is only one real positive root,

$$r_- = r_+ = r_c = \frac{3M}{2} \,. \tag{3.26}$$

(b) Alternatively, we can extremise Λ. For $\lambda = \lambda_-$, we have the "RN-type" extremal condition that gives two positive roots: one at $r = r_c$ and a degenerate horizon at

$$r_- = r_+ = \frac{3M - \sqrt{9M^2 - 8Q^2}}{2} \,. \tag{3.27}$$

This is the "cold" black-hole case [197, 205] on line OU.

(ii) For $Q^2 \leq M^2$, under the $M = Q$ line, the "dS-type extremal condition" $L^2_{dS} = L^2_{dS_+}$ gives two positive roots,

$$r_+ = r_c = \frac{3M + \sqrt{9M^2 - 8Q^2}}{2} \,. \tag{3.28}$$

This is the "extreme" or "marginal" naked-singularity case, falling on Line NU [197, 205]

From our analysis of the RNdS phase space, we have derived a number of limits on the mass and charge of the black hole with respect to a de Sitter radius of $L_{dS} = 1$. The phase space diagram of Fig. 3.2 shall serve as the foundation of our QNM analyses of Chapter 4. In the next section, we shall extract a constraint on the mass of a charged particle, in the spirit of the WGC. This, the FL limit introduced in Chapter 1, shall similarly inform our QNM investigations into the mass and charge of the scalar field.

3.2 The Festina-Lente mass bound

As discussed in Chapter 1, the WGC is based on the consideration of the emission of elementary particles of mass m and charge q from black holes of mass M and charge Q in Minkowski space-time. Upon introducing $\Lambda > 0$, however, the qualitative and quantitative implications discussed in this chapter strongly influence the black hole decay process. In the RNdS case, black hole emission serves as a transition towards thermal equilibrium mediated by an exchange of mass and charge between cosmological horizon and black hole. This process was recently investigated by Refs [91, 92], in an attempt to understand how RNdS black holes decay and to extend the principles of the WGC to de Sitter space-times. This led to the FL bound for elementary particles of mass m and charge q discharging the black hole,

$$\frac{m^4}{8\pi\alpha} \geq V \,, \tag{3.29}$$

where $\alpha = g_1^2 q^2/4\pi \sim 1/137$ is the fine structure constant, with g_1 as the $U(1)$ gauge coupling, and $V = \Lambda/8\pi G = 3M_P^2 H^2$, with $H^2 = \Lambda/3$, as the gravitating vacuum energy. We can write this as $m^2 \geq \sqrt{6} g_1 q M_P H$. In natural units, the Planck scale is $M_P \sim 10^{27}$ eV and the current Hubble scale is $H \sim 10^{-33}$ eV.

Since we consider the $U(1)$ to be electromagnetism, the scale is set at $\sqrt{g_1 M_P H} \sim 10^{-3}$ eV, around the vacuum energy density scale/neutrino mass scale.[15] The bound is therefore the geometric mean between our current Hubble scale and the Planck scale [91]. For the lightest electrically-charged particle in the SM, the electron, the particle mass $m_e \sim 10^5$ eV comfortably satisfies the FL bound. On the other hand, the electron saturates the WGC by 19 orders of magnitude.

Provided the charge carrier is sufficiently heavy, Eq. (3.29) demonstrates that the RNdS black hole will evaporate to de Sitter space-time, in the usual fashion [81]. However, in the case of very light particles (i.e. $m^2 \ll \sqrt{6} g_1 q M_P H$) discharging from very large charged black holes, such that $r_{\rm BH} \sim r_{\rm dS}$, the charge depletion is near-instantaneous and the result is a Big Crunch solution. In other words, the black hole passes from sub-extremal to super-extremal, leading to a naked curvature singularity, which is a violation of cosmic censorship [211–213]. We shall return to this point in a moment.

As shown in Ref. [92], we can combine Eqs (1.5) and (3.29) to determine an upper and lower limit, respectively, on the mass of the elementary particle being discharged from a RNdS black hole,

$$\sqrt{8\pi\alpha V} \sim \sqrt{6} g_1 q M_P H < m^2 < 2 g_1^2 q^2 M_P^2 \sim 8\pi\alpha M_P^2 \,. \tag{3.30}$$

This corresponds to 10^{-3} eV $\lesssim m \lesssim 10^{26}$ eV in the case of a $U(1)$ charge in our current universe. For consistency, the WGC-based limit is derived under the assumption that $r_{\rm BH} \ll r_{\rm dS}$ and that cosmic censorship must be preserved [92]. In contrast, the FL bound is derived for black holes of size $r_{\rm BH} \sim r_{\rm dS}$. These black hole solutions correspond to the Nariai black hole solution, referred to in Fig. 3.2 and discussed in Appendix C.

For completeness, let us briefly summarise the argument used to derive Eq. 3.29 in Ref. [91]. Extremal black holes in Minkowski space-time are expected to decay through the emission of massive charged particles whose "elementary" electric and magnetic charge obey a mass-ratio $\mu/|q| < M/|Q| \leq 1$ [77]. When embedded in de Sitter space-time, however, the evaporation of charged black holes is complicated by the exchange of mass and charge between the event horizon and the cosmological horizon.

The decay of the RNdS black hole is triggered by the Schwinger mechanism, whose decay rate is governed by

$$\Gamma \sim \exp\left\{ -\frac{m^2}{qE} \right\} . \tag{3.31}$$

The near-horizon electric field is of the order $E \sim \mathcal{O}(g M_P H)$, the usual electric field for a Nariai black hole.[16]

If $m \ll q g M_P H$, the electric field of the charged Nariai black hole is quickly screened by Schwinger pair production; it discharges instantaneously such that the black hole charge becomes $Q = 0$ but its mass remains above the neutral Nariai mass limit $M^2\Lambda > 1/9$. This marks a super-extremal black hole solution, lying beyond the sharkfin, and thus in violation of the WCC. In the cosmologists' parlance, this is a "Big Crunch" solution where the two-sphere collapses to zero.

In contrast, if $m \gg q g M_P H$, the black hole gradually evaporates to empty de Sitter space, as expected [87, 200, 207, 214]. In Minkowski space-time, the prohibition of super-extremal black holes and the preservation of WCC leads to the WGC [77]. If we follow these same principles in de Sitter space-time, we must forbid $m \ll q g M_P H$. In so doing, Refs [91, 92] utilise the charged Nariai black hole as a laboratory in which to

[15] Since neutrinos are electrically neutral, the FL bound does not apply. Attempts to extend the FL bound beyond fields charged under $U(1)$ are being explored, such as in Ref. [209]. As the electron mass is determined by the vacuum expectation value (VEV) of the Higgs, the shape of the Higgs potential is constrained by the FL bound as discussed in Ref. [210].

[16] At *Point U* of Fig. 3.2, $E = \sqrt{6} g M_P H$.

construct a de Sitter analogue for the WGC, namely the FL bound of Eq. (3.30).

Since we consider the $U(1)$ to be electromagnetism, the scale is set at $\sqrt{g_1 M_P H} \sim 10^{-3}$ eV, around the vacuum energy density scale/neutrino mass scale.[17] The bound is therefore the geometric mean between our current Hubble scale and the Planck scale (see Fig. 5 of Ref. [91]). For the lightest electrically-charged particle in the SM, the electron, the particle mass $m_e \sim 10^5$ eV comfortably satisfies the FL bound. On the other hand, the electron saturates the WGC by 19 orders of magnitude.

Provided the charge carrier is sufficiently heavy, Eq. (3.30) demonstrates that the RNdS black hole will evaporate to de Sitter space-time, in the usual fashion [81]. However, in the case of very light particles (i.e. $m^2 \ll \sqrt{6} g_1 q M_P H$) discharging from very large charged black holes, such that $r_{\rm BH} \sim r_{\rm dS}$, the charge depletion is near-instantaneous and the result is a Big Crunch solution. In other words, the black hole passes from sub-extremal to super-extremal, leading to a naked curvature singularity, which is a violation of cosmic censorship [211–213].

Eq. (3.30) is a strong indication of the value of studying the RNdS black hole within the broader context of well-established principles like cosmic censorship, and under the assumption of black hole stability. In the case of a RNdS space-time, these ideas are interlinked and can be investigated through the study of the perturbations of the black hole in question. In the next chapter, we shall demonstrate this explicitly: through QNM analyses, we shall explore the properties of massive scalar QNFs within the RNdS background, their stability and superradiant amplification, and how QNFs can be used as evidence for or against the preservation of cosmic censorship.

However, the topic of cosmic censorship is a delicate one that requires a formal mathematical treatment, and that can benefit from historical and philosophical context. While a critical analysis of the conjecture itself is beyond the scope of this thesis, we include a short review of the developments in the field in the following section, focused in particular on "Strong Cosmic Censorship" (SCC). For the QNM studies that shall be performed in Chapter 4, one need only consider Eq. (3.32): for SCC to be preserved in the RNdS black hole space-time, this is the criterion that must be satisfied. For the interested reader, we include the following brief introduction to the topic of cosmic censorship within GR, with supplementary material on GR formalism included in Appendices A and B.

3.3 Strong Cosmic Censorship

Within the framework of GR, a curvature singularity exists at $r = 0$. For much of the twentieth century, this was accepted as unphysical: Einstein and his contemporaries considered the singularity to be an artefact of the theory; Oppenheimer and Snyder [215] suggested it to be an unfortunate consequence of imposing unrealistic symmetry idealisations on stellar collapse (see Ref. [66] for a comprehensive historical review). The 1960s, however, saw a shift in the paradigm, beginning with Penrose's seminal 1965 paper on gravitational collapse [211]. There, he demonstrated that in the wake of the inward stellar collapse to $r = 0$ and the subsequent formation of a trapped surface (*viz.* a surface from which light cannot escape outwards), a space-time $(\mathcal{M}, g)$ cannot be future null-geodesically complete: in other words, a light-like trajectory incoming from spatial infinity terminates in an undefined point at $r = 0$. With this, a vague suggestion of a physical manifestation of the singularity came to be.

In isolation, Ref. [211] makes no claims on the nature of the singularity nor on the implications of its existence. To do so would have been impossible since its publication preceded the definition of an event horizon and, by extension, a black hole. In [212], however, Penrose provides the outstanding definition of the black hole event horizon as the absolute boundary of the set of all events (i.e. the space-like boundary of the past of future null infinity $\mathscr{I}^+$), corresponding to the coordinate singularity $r = r_+$, which can be

[17] Caution is required in the application of the FL limit. Since neutrinos are electrically neutral, the FL bound does not apply. Attempts to extend the FL bound beyond fields charged under $U(1)$ are being explored, such as in Ref. [209]. For example, as the electron mass is determined by the vacuum expectation value of the Higgs, the shape of the Higgs potential is constrained by the FL bound as discussed in Ref. [210].

observed in principle by an external inertial observer. The black hole is then defined as the region bounded by the event horizon (see Appendix B for details).

With these definitions in place, the formulation of the cosmic censorship conjecture could follow, forbidding naked singularities within GR [212]. Today, we refer to this requirement for cloaked singularities as the "Weak Cosmic Censorship" (WCC) conjecture. Despite the absence of a formalised proof, WCC serves as an implicit assumption throughout the GR literature, serving as the cornerstone of black hole uniqueness theorems and models; as we have seen in Section 3.1, the WCC conjecture is crucial to our understanding of the black hole structure and phase space.

In this section, however, we are concerned with the notion of "Strong Cosmic Censorship" (SCC).[18] The underlying logic of the SCC conjecture lies in the inextendability of a physically-reasonable space-time metric past the space-like $r = 0$ singularity [211, 216]. Intuitively, we may consider an infalling object whose journey past the event horizon must end at $r = 0$. To define this formally, however, is highly non-trivial, as we need to specify the precise genericity criteria that must be satisfied for a space-time to be considered "physically-reasonable" as well as the requirements for "inextendability".

Further complications arise when we consider the Kerr-Newman family of black holes. As we have seen in Section 3.1, the region bounded by the event horizon includes an additional Killing horizon, the Cauchy horizon, as well as a time-like singularity. The criteria for "physically-reasonable" must be adapted to accommodate this structure. Worse still, SCC preservation becomes conceptually entangled with determinism in this setup: an observer that crosses the Cauchy horizon can, upon looking back whence they came, see the entire future of the asymptotically-flat spacetime exterior to the black hole within a finite time.

In other words, the Cauchy horizon marks the limit where initial data evolves uniquely. If the metric cannot be extended past this horizon within the GR framework, then there is a possibility to rescue SCC. Upon closer inspection, the Cauchy horizon is in fact demonstrably unstable. Infalling radiation becomes infinitely "blue-shifted" (i.e. its oscillation frequency increases) as it approaches $r = r_-$ and accumulates at the Cauchy horizon. This leads to a curvature divergence. As such, this "blue-shift" mechanism results in a singularity, preventing causal curves from being extended past $r = r_-$ [217]. The criterion for whether this holds true in a space-time with a non-zero cosmological constant shall be the focal point of our discussion.

Cosmic censorship continues to draw interest, with recent investigations concerning its relationship to Swampland conjectures [218] and especially possible violations in the presence of a non-zero cosmological constant (see Ref. [219] and references therein). The SCC conjecture itself has been challenged and adapted several times; the literature on the subject is scattered across multiple sub-disciplines, and includes philosophical deconstructions, rigorous mathematical arguments, and numerical analyses. According to the definitions provided for the singularity and the horizon, the preservation of SCC is predicated on the inextendability of the space-time under specific conditions. For this reason, the arguments in favour of and in opposition to SCC have become dominated by the "initial-value approach" to GR, referred to also as the "partial differential equations programme". There, SCC preservation is posed as an initial-value problem that seeks to prove whether for "generic" initial data, the maximal globally hyperbolic data, is inextendible as a solution to the vacuum Einstein equations [66]. This allows for the establishment of specific criteria that, once met, formally prove that SCC holds. In this manner, six decades after its formulation, a formal proof of the (C^0-)inextendibility of the Schwarzschild space-time was presented in Ref. [220].

With these perspectives in mind, we produce a short and pedagogical treatment of SCC, with a particular focus on how QNMs have come to contribute to this ongoing debate. We address several of the most recent revisions to the statement, to provide the necessary context for the study of SCC within the RNdS space-time.

[18] While this follows the GR convention of referring to conjectures as "strong" or "weak", this does not indicate the relative strength of one to another. In fact, the link between the two is demonstrably tenuous (see Ref. [66]).

Formal definitions for the cosmic censorship conjectures

Intuitively, singularities were understood to correspond to "places" in space-time where curvature "blows up" or showcases "pathological behaviour" [7]. To construct a precise singularity theorem proved difficult; the starting point, however, was this understanding that null and time-like geodesic completeness was a minimal requirement for a space-time to be devoid of singularities [6]. For our purposes, we shall define the singularity with respect to its relationship with to metric, following the statements used in Refs [6, 221, 222],

Proposition 3.3.1 (Singularity)**.** *Consider $(\mathcal{M}, g)$ to be a 4D time-orientable Lorentzian manifold. Then a singularity is denoted by a future-directed future-inextendible time-like curve $C \subset \mathcal{M}$.*

With the singularity defined, we can proceed to the definition for the WCC conjecture,

Conjecture 3.3.1 (**Weak Cosmic Censorship**)**.** *Consider the strongly causal space-time $(\mathcal{M}, g)$ that is asymptotically-flat at null infinity. Then $(\mathcal{M}, g)$ contains no naked singularities with respect to $J^-(\mathscr{I}^+)$ if and only if $J^-(\mathscr{I}^+)$ is globally hyperbolic.*[19]

Then the definition of the SCC conjecture can be encapsulated by the statement from Ref. [223],

Conjecture 3.3.2 (**Strong Cosmic Censorship**)**.** *For generic vacuum data sets, the maximal Cauchy development $(\mathcal{M}, g_{ab})$ defined in Theorem A.5 is inextendible as a suitably regular Lorentzian manifold.*

However, as we shall see in the following discussion, a single version of the SCC conjecture is too rigid to suit the wide variety of space-times to which the conjecture is applied. Rather, the criterion of extendability is expanded to establish multiple versions of the SCC, with varying relative "strength". Using the usual conventions in the literature [6, 7, 224] and the definitions of smoothness and differentiability introduced in Appendix A, we list here the different versions of the SCC considered in this chapter, in order of decreasing strength. We begin with the most satisfactory condition for the SCC conjecture [225],

Conjecture 3.3.3 (C^0-formulation of Strong Cosmic Censorship)**.** *For generic vacuum data sets, the maximal Cauchy development $(\mathcal{M}, g_{ab})$ is inextendible past the Cauchy horizon as a C^0 manifold.*

This implies that there are no extensions of the metric beyond the Cauchy horizon that preserve the continuity of the metric, without requiring further differentiability. The Cauchy horizon is treated like a singularity. The next strongest statement is is attributed to Christodoulou [225],

Conjecture 3.3.4 (Christodoulou-formulation of Strong Cosmic Censorship)**.** *For generic vacuum data sets, the maximal Cauchy development is inextendible past the Cauchy horizon as a weak solution of the Einstein field equations, such that the Christoffel symbols associated with the C^0 metric are locally L^2 (i.e. square-integrable when multiplied by any smooth test function of compact support).*

With this reformulation of the SCC conjecture, the metric is not continuous across the Cauchy horizon as a weak solution such that the "blow up" is in H^1_{loc}. In other words, this is the least regular case for which the metric continuously satisfies the Einstein field equations, albeit as a weak solution. Finally, we come to the weakest version of the SCC conjecture considered here,

Conjecture 3.3.5 (C^2-formulation of Strong Cosmic Censorship)**.** *For generic vacuum data sets, the maximal Cauchy development $(\mathcal{M}, g_{ab})$ is inextendible past the Cauchy horizon as a C^2 manifold.*

This serves as the lowest threshold to cross when testing the SCC conjecture, thereby serving as a useful test case but not a satisfactory proof for the preservation of SCC.

With these definitions in place for the different versions of the SCC conjecture and their relative hierarchy, we can proceed to a study of the conjecture in the context of spherically-symmetric space-times. In so doing, we shall describe how each of these conjectures came to be and how they have been applied to date.

[19] For additional details on the notation used here, see Table B.1 and Appendix B.

3.3.1 Preserving strong cosmic censorship in spherically-symmetric space-times

Now that we have developed the necessary formalism to describe the SCC conjecture in a mathematically precise way, let us begin in earnest our discussion of the preservation of SCC with the simple case of the Schwarzschild black hole.

SCC in Schwarzschild black holes

Recall that for a Schwarzschild black hole space-time, the event horizon is located at $r = 2M$ and corresponds to a coordinate singularity. The curvature singularity at $r = 0$ is space-like. Considerations of the SCC conjecture in this space-time can be traced back to sources such as Ref. [4], where an observer falling past the horizon and towards the Schwarzschild singularity was discussed rigorously for the first time, with the observer ripped apart by tidal forces before ever reaching $r = 0$. While this "spaghettification" of the in-falling observer captured the popular imagination as an indictment of black hole interiors, a formal proof that supported the strongest case for SCC remained elusive until recently. As mentioned at the beginning of this section, Sbierski proved that the metric cannot be extended continuously past the $r = 0$, formally demonstrating that the C^0-formulation of SCC is valid in the Schwarzschild black hole [220].

Let us now move on to the RN black hole space-time, which we sketch in Fig. 3.3. There, the shaded regions refer to the asymptotically-flat universe exterior to the black hole (Region I) and the black hole interior (Region II). The future and past Cauchy horizons are denoted, respectively, by $\mathscr{CH}^+$ and $\mathscr{CH}^-$. Our discussion is concerned only with the "right" of "ingoing" horizons, denoted by the subscript "R". Recall that the internal structure of the Kerr and the RN black hole space-times are similar, such that arguments corresponding to one can apply also to the other. For this reason, we mention results concerning the Kerr space-time here, even though the (axisymmetric) rotating space-time is beyond the scope of this thesis.

SCC in RN black holes

For RN black holes (as well as rotating Kerr black holes), the interior is complicated by the presence of the Cauchy horizon at $r = r_-$. For $r < r_-$, surfaces of constant r are time-like such that the curvature singularity $r = 0$ is time-like. The solution is thus time-like geodesically complete but space-like (and null) geodesically incomplete. Consider a space-like surface, Σ, upon which we prescribe initial data for the asymptotically-flat metric M. The metric can then be determined uniquely up to the Cauchy horizon, but not beyond; past $r = r_-$, the evolution of the initial data is governed by unknown boundary conditions at $r = 0$. Mathematically, the maximal future Cauchy development of initial data posed on the Cauchy surface is considered incomplete but smoothly extendible beyond the Cauchy horizon. All incomplete geodesics can pass this horizon. For the in-falling observer, this means a safe journey past the Cauchy horizon; for the theory, this corresponds to a failure in determinism.

However, in 1973 Penrose put forth a statement for the Kerr black hole suggesting that for generic asymptotically-flat initial data, the maximal future Cauchy development is inextendible as a continuous Lorentzian metric [216]. In other words, this is a claim for the C^0-formulation of SCC and a possible way in which SCC could be preserved. If we consider the scalar field Φ as a linear proxy for the full non-linear Einstein equations, then Penrose's formulation relies on the notion that the scalar field is badly behaved at the Cauchy horizon. For the non-linear case, this corresponds to the energy blowing up at $r = r_-$. The reasoning for this is as follows. Consider two observers external to the RN black hole: a time-like observer A remaining in the exterior region and a time-like observer B falling into the black hole. Observer A will reach future infinity at infinite proper time; observer B will reach the Cauchy horizon at finite proper time. If observer A sends periodic (in A's time) signals to observer B, observer B will perceive them as incoming with greater frequency. By this logic, the frequency of an oscillating scalar field Φ entering the black hole will increase infinitely as it reaches the Cauchy horizon, leading to the infinite "blue-shift" effect. This renders the scalar field inextendible past the Cauchy horizon; in the non-linear problem, the equations blow up.

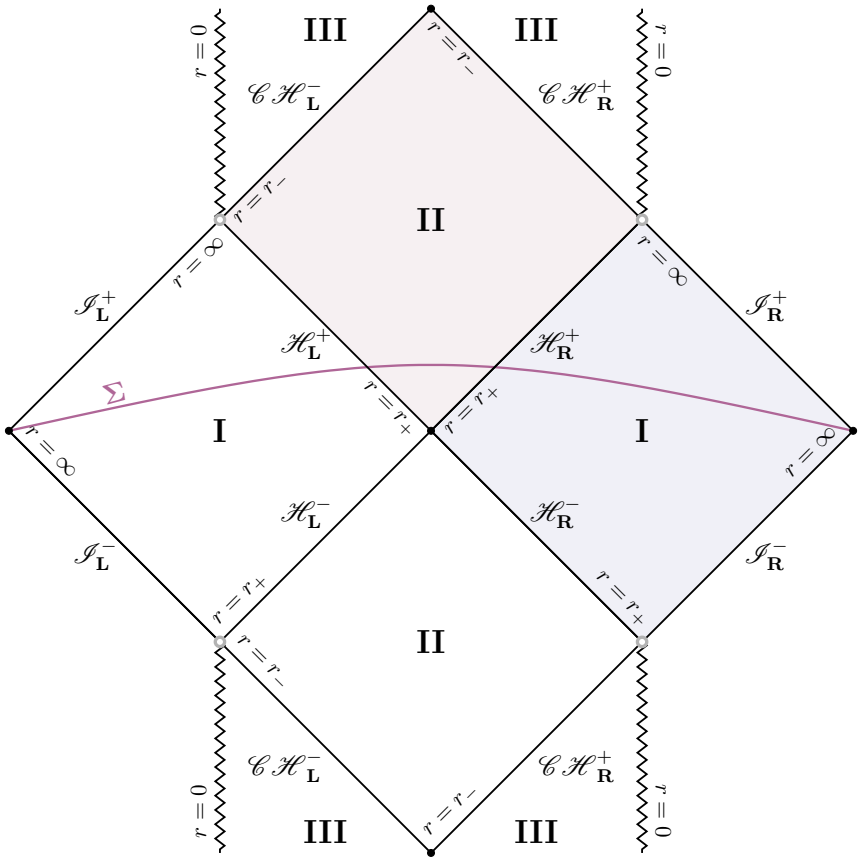

Figure 3.3: *Conformal diagram for the extended RN black hole space-time, with Cauchy surface* Σ.

However, Penrose's formulation does not take into account the global black hole metric. It was recently argued by Dafermos *et al.* [226, 227] that the well-known stability of the Kerr metric exterior in the wake of some space-time perturbation [228, 229] implies that the incoming scalar field experiences an inverse polynomial decay in time along the event horizon. Decay in the exterior is therefore in competition with the blue-shift mechanism at the Cauchy horizon. The consequence of this argument is that for smooth localised initial data in sub-extremal Kerr − and, equivalently, RN − black hole space-times, the local energy of Φ blows up at the Cauchy horizon. Here, the local energy is the integral of the energy as measured by a local observer i.e. the first derivative of Φ in L^2. Formally, Φ is then inextendible in H^1_{loc} across the Cauchy horizon. Thus, the Christodoulou version of SCC holds in the case of the RN black hole [230]. Recall that this "blowing-up" of the energy is a requirement for Christodoulou's formulation of SCC (see Conjecture 3.3.4). As such, this was perceived as a possible means of "saving" SCC by weakening the C^0 requirement further, such that only the maximal future Cauchy development of the metric need be inextendible as a continuous Lorentzian manifold whose Christoffel symbols are locally square-integrable. We can consider this loosely as a relaxation of the C^0-formulation of SCC, where the metric cannot be interpreted even as a weak solution of the Einstein equations past the Cauchy horizon.

It is interesting to observe that stability in the metric challenges SCC. For SCC to be preserved, the blue-shift mechanism must win over the exterior decay: the exponential growth of the derivatives at the Cauchy horizon must exceed the inverse polynomial decay of Φ. To ensure this, the decay of Φ must not be too fast as to overwhelm the blue-shift. We shall see that it is this requirement that leads us to the works of Refs [231, 232], where QNMs dominate the exponential behaviour for $\Lambda > 0$.

However, to finalise our discussion on the current state of the SCC, we note that as discussed by Franzen [233], the blue-shift may not be enough to rescue SCC if we consider also the amplitude of Φ. This is

because the blue-shifting − the increasing frequency of the oscillations entering the black hole − affects the derivatives of Φ but has no influence on its amplitude. Under this argument, it may be shown that Φ remains uniformly bounded on the black hole interior for the sub-extremal RN black hole and extends continuously past the Cauchy horizon, violating the C^0 formulation of SCC.

Let us now proceed to the case of the RNdS black hole space-time, where we shall see the effect of the positive cosmological constant on the preservation of SCC. Specifically, we shall discuss the relationship between the "blue-shift" (i.e. the mechanism responsible for the exponential growth of the perturbations) affecting the derivatives of Φ in the interior, and a competing "red-shift" effect emergent in the case of de Sitter space-times. This is constructed in analogy to "Price's Law" in asymptotically-flat space-time [234], where a "red-shift" corresponds to a shift of late-stage radiation to spatial infinity. In asymptotically-de Sitter space-time, if an observer A crossing $\mathscr{H}_R^+$ emits a signal at a constant rate with respect to his own proper time, the frequency of the signal as received by an observer B crossing $\mathscr{H}_R^+$ at a later time is shifted to $\mathscr{C}_R^+$.

SCC in RNdS black holes

Finally, let us turn to the case of the RNdS black hole. Once again, the stability of the metric in Region I of Fig. 3.4 (for which $r_+ < r < r_c$) has been proven (see Ref. [235]). However, the decay of Φ differs: while generic initial data defined on the Cauchy surface decays inverse polynomially on the event horizon in asymptotically-flat space-time, the decay becomes exponential in asymptotically-de Sitter space-time [236]. Intuitively, we understand this to be a consequence of $\Lambda > 0$, which naturally leads to cosmological expansion, and therefore results in a "red-shifting" effect. Φ at the exterior then experiences exponential damping (i.e. the asymptotics of Φ demonstrate QNM behaviour).

This faster decay rate is promising for proving instability, provided it does not overcome the blue-shifting at the Cauchy horizon. However, to quantify the exponential rates precisely, one must take into account the influence of all three physical horizons. This problem was recently resolved through Refs [231], which focused on the behaviour of the linear perturbations of smooth initial data. This analytical means of scaling the competing blue- and red-shifting phenomena makes use of the exponential dependence on κ_- at the Cauchy horizon and the infinum of the imaginary component of the fundamental QNF (i.e. the "spectral gap").

The main finding of [231] is as follows. For a non-degenerate RNdS black hole of dimension $d \geq 4$, there exists some $\beta > 0$ dependent only on the black hole parameters such that the exponential decay for massive and neutral scalar fields is governed by the expression,

$$|\Phi| \leq Ce^{-\beta t} \,, \quad \beta \equiv -\frac{\mathfrak{Im}\{\omega^{n=0}\}}{|\kappa_-|} \,. \tag{3.32}$$

for small mass $m > 0$. As before, Φ is a linear scalar perturbation; $C \geq 0$ is a constant and $\mathfrak{Im}\{\omega^{n=0}\}$ is the least-damped QNF.

In this case, Φ becomes continuous up to the Cauchy horizon; the derivatives of Φ lie in the Sobolev space $H^{\left(\beta+\frac{1}{2}\right)-\epsilon}$ $\forall \epsilon > 0$. To satisfy the C^2 formulation of the SCC, $\beta < 1$. However, the stronger Christodoulou formulation requires that $\beta < 1$ for Φ to be inextendible across $\mathscr{C}\mathscr{H}_R^+$ in H^1_{loc} for SCC to be preserved [231, 232].

As such, the QNM study on SCC preservation that we shall perform in Chapter 4 will be predicated on the condition,

$$\beta \equiv -\frac{\mathfrak{Im}\{\omega^{n=0}\}}{|\kappa_-|} < \frac{1}{2} \,. \tag{3.33}$$

In particular, we shall investigate where in the RNdS phase space we are more likely to observe a violation of the Christodoulou formulation of SCC. Certain examples have already been noted in the literature. In the

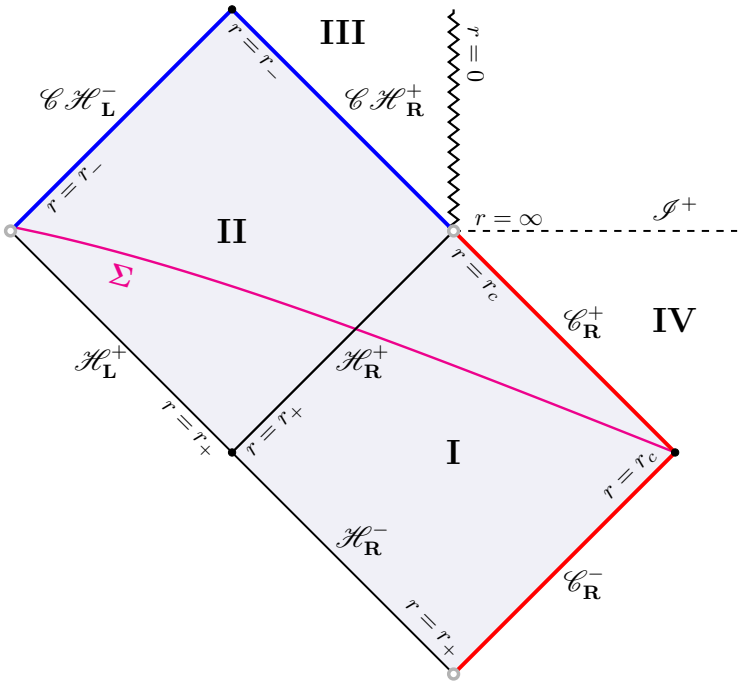

Figure 3.4: *From the RNdS Penrose diagram of Fig. 3.1, we consider the competing blue-shift and red=shift mechanisms.*

case of a RNdS black hole sufficiently close to extremality, Φ becomes extendible in H^1_{loc} across the Cauchy horizon [227]. Similarly, the C^2 and Christodoulou formulations of SCC were found to be violated near extremality in Ref. [237].

This indicates that Λ can cause a failure of SCC. However, we add as a final comment on the SCC that if we accept a relaxation on the requirement of the smoothness of the initial data, the SCC can remain valid. Specifically, to rescue the Christodoulou formulation of SCC, Dafermos *et al.* proved in Ref. [224] that by relaxing the requirement on the regularity class – considering initial data that is in the class $H^1_{loc} \times L^2_{loc}$ – the local energy does indeed blow up at the Cauchy horizon for sub-extremal RNdS black holes. That the preservation of SCC depends on the use of rough initial data is further corroborated in Ref. [237].

In this chapter, we have provided a pedagogical treatment of the RNdS black hole space-time, with a particular focus on its structure and the insights that we might thereof glean. The chapters that follow shall rely heavily on the formalism herein introduced, where we shall use Fig. 3.2 as the foundation of our QNM investigations. While the phase space diagram delineates the constraints on the space-time parameters (M, Q, Λ), our discussion on the FL bound in Section 3.2 offered constraints on the field parameters (μ, q). Beyond this, Section 3.2 served as an illustrative example of the manner in which we can probe fundamental physics using black hole mechanics; through a study of black hole decay, constraints on elementary particles can be derived. Similarly, our discussion on the SCC conjecture in Section 3.3 allowed us to explore the causal structure of the RNdS black hole more carefully. While the notion of determinism and its preservation within GR is a fascinating topic in and of itself, we wish to highlight in particular the vital role of QNMs in the maintaining cosmic censorship. In this vein, we have alluded to the antithetical role of horizon stability in the preservation of WCC and SCC (where a similar observation was made in Ref. [66]): where singularities exist, the WCC conjecture requires the existence and stability of event horizons. The SCC conjecture, on the other hand, requires the absence or instability of Cauchy horizons in all cases. These inform the QNM analyses of Chapter 4.

Chapter 4

Probing the RNdS black hole space-time with QNMs

> ...observers in such a universe live in a cavity bathed by the Hawking radiation emanating from the cosmic horizon, and are constrained to the observations they make on their finite size lab wall... the question of how to make sense of the cosmic thermal cavity, known as the static patch, becomes vexingly relevant.
>
> Dionysios Anninos in *De Sitter Musings* [81]

In Chapter 2, we introduced the QNM formalism, providing the underlying theoretical foundations required to engage in QNM computation and analysis. In Chapter 3, we provided a detailed study of the background space-time of interest, *viz*. the RNdS black hole. In this chapter, we bring together the main concepts developed in these chapters in order to investigate the range of QNM applications in the exploration of a charged black hole embedded in de Sitter space-time. We focus in particular on the interplay and influence of parameters associated with the space-time (M, Q, Λ) and the perturbing field (μ, q, ℓ), the related phenomena of superradiance and instability, and the preservation of SCC.

We begin by extending the discussions of Sections 2.1 and 2.3 from the simple case of a massive scalar field in a fixed Schwarzschild background to the more complicated scenario of a scalar field with non-zero mass and charge within a RNdS black hole space-time. For this reason, the "sharkfin" parameter space diagram illustrated in Section 3.1.2 shall prove especially useful within this chapter. To perform the QNM computations in this setup, we introduce the modified WKB technique of Ref. [238] to the list of methods specified in Section 2.2; this is discussed in Section 4.2 and used throughout this chapter. We rely on the established arguments of Section 2.1 for our discussion on superradiance and Sections 3.2 and 3.3, respectively, to contextualise the results we present in the final sections of this chapter.

4.1 QNMs for a charged massive scalar field in the RNdS space-time

To begin our discussion on the QNMs of a charged and massive scalar test field within the RNdS black hole space-time, we consider the generic action for the Einstein-Hilbert-Maxwell system (as studied in Chapter 3) minimally coupled to complex scalar test field charged under $U(1)$. As before, we take $U(1)$ to be electromagnetism. The mass and charge of the field is given by $\mu = \mu c/\hbar$ and $q = qc/\hbar$, respectively. In natural units, μ has units of inverse length; a physical value for q should be a multiple of the electron charge $|e| \sim$

0.1 [203]. Following the conventions of Eqs 2.3 and 3.1,

$$S = \int d^4x\sqrt{-g}\left[\frac{1}{2\kappa^2}\left(R - 2\Lambda\right) - \frac{1}{4g_1^2}F_{\mu\nu}F^{\mu\nu}\right] + \int d^4x\sqrt{-g}\mathcal{L}_{sc.}\,, \tag{4.1}$$

where $g = \det|g_{\mu\nu}|$ refers to the RNdS metric. The Lagrangian $\mathcal{L}_{sc.}$ represents the complex scalar field, which is itself a linear combination of two real scalar fields Φ_1 and Φ_2, such that $\Phi = \Phi_1 + i\Phi_2$. The full Lagrangian [6, 133] is then given by

$$\mathcal{L}_{sc.} = -\frac{1}{2}\left(\mathcal{D}_\mu\Phi\right)^\dagger\left(\mathcal{D}^\mu\Phi\right) - \frac{1}{2}\mu^2\Phi^\dagger\Phi\,. \tag{4.2}$$

Here, $\mathcal{D}_\mu = (\partial_\mu - iqA_\mu)$. The interaction of the charged scalar field with the external electromagnetic field of the black hole $F_{\mu\nu} = \partial_\mu A_\nu - \partial_\nu A_\mu$ is introduced through the minimal coupling prescription, in which ∂_μ is replaced by its covariant counterpart, $\mathcal{D}_\mu$. Recall that in this stationary black hole context, the only nonzero component of A_μ is $A_t(r) = -Q/r\,dt$, the electrostatic four-potential of the black hole.

The full, non-linear evolution of the system can be described using the corresponding equations of motion. These separate into the massive, charged Klein-Gordon equation in curved space-time and the Einstein field equations, *viz*.

$$\nabla_\mu\nabla^\mu\Phi - \mu^2\Phi = 0\,, \quad G_{\mu\nu} + \Lambda g_{\mu\nu} = 8\pi G T_{\mu\nu}\,, \tag{4.3}$$

for which the stress-energy tensor becomes quadratic in Φ for this particular model. Higher-order perturbations in the scalar field induce changes in the space-time geometry, as well as in the vector potential [133]. As explained in Chapter 2, we avoid these complications by following introducing the linear approximations for the fields Φ and $g_{\mu\nu}$,

$$g'_{\mu\nu} = g^{\rm BH}_{\mu\nu} + \delta_{\mu\nu}\,, \quad \Phi' = \Phi^{\rm BG} + \Psi\,. \tag{4.4}$$

The unperturbed fields, $g^{\rm BH}_{\mu\nu}$ and $\Phi^{\rm BG}$, are referred to as the "backgrounds"; the "perturbations", $\delta_{\mu\nu}$ and Ψ, are considered to be very small. If we substitute $g'_{\mu\nu}$ and Φ' (with $\Phi^{\rm BG} = 0$) and linearise the system of equations with respect to $\delta_{\mu\nu}$ and Ψ, we find that $\delta_{\mu\nu}$ and Ψ decouple; the metric fluctuations for $\delta_{\mu\nu}$ can then be set to zero and $g^{\rm BH}_{\mu\nu}$ satisfies the vacuum Einstein field equations. In this way, the gravitational sector can be described by the vacuum solution $R_{\mu\nu} = 0$ and the backreaction emergent at quadratic order in Φ is neglected.

Let us proceed to the equation of motion for Ψ,

$$\frac{1}{\sqrt{-g}}\left(\partial_\mu - iqA_\mu\right)\left(\sqrt{-g}g^{\mu\nu}\left(\partial_\nu - iqA_\nu\right)\Psi\right) = \mu^2\Psi\,. \tag{4.5}$$

Recall that we can formulate an ansatz for Ψ derived from the symmetries of the fixed background space-time: in the RNdS case (static, non-rotating, and spherically-symmetric), the wave-function is written in variable-separable form,

$$\Psi_{n\ell m}(t, r, \theta, \phi) = \sum_{n=0}^{\infty}\sum_{\ell,m}^{\infty}\frac{\psi_{n\ell m}(r)}{r}\,Y_{\ell m}(\theta, \phi)\,e^{-i\omega_{n\ell m}t}\,. \tag{4.6}$$

As before, we are concerned only with the $n = 0$ "fundamental mode", representing the least-damped and thus longest-lived QNM. The angular contribution is expressed using spherical harmonics, for which ℓ and m represent the angular momentum (multipolar) and azimuthal numbers. The spherical harmonic function $Y_{\ell m}(\theta, \phi)$ satisfies Eq. (2.6), repeated here for completeness,

$$\nabla^2 Y_{\ell m}(\theta, \phi) = -\frac{\ell(\ell+1)}{r^2}Y_{\ell m}(\theta, \phi)\,. \tag{4.7}$$

Since the black hole is static, the corresponding ordinary differential equations are time independent. Consequently, the defining QNM behaviour is then fully encapsulated by the radial component. For convenience, we drop the subscripts and write,

$$\frac{d}{dr}\left(r^2 f(r)\frac{d\psi}{dr}\right) + \left(\frac{r^2(\omega + qA_t(r))^2}{f(r)} - \ell(\ell+1) - \mu^2 r^2\right)\psi(r) = 0\,. \tag{4.8}$$

Then, redefining $\psi(r)$ as $\psi(r) = \varphi(r)/r$ and employing the tortoise coordinate $r_\star$, we obtain

$$\frac{d^2\varphi(r_\star)}{dr_\star^2} + \Big[\omega^2 - V(r)\Big]\,\varphi(r_\star) = 0\,, \tag{4.9}$$

$$\text{with} \quad V(r) = f(r)\left[\frac{\ell(\ell+1)}{r^2} + \frac{f'(r)}{r} + \mu^2\right] - 2\omega q A_t(r) - q^2 A_t(r)^2\,. \tag{4.10}$$

Note that in the RNdS space-time, where $r_\star = r_\star(r)$ serves as a bijection from (r_+, r_c) to $(-\infty, +\infty)$, the general tortoise coordinate becomes

$$r_\star(r) = \int \frac{dr}{f(r)} = \sum_{i=1}^{4} \frac{1}{2\kappa_i} \ln\left(1 - \frac{r}{r_i}\right)\,, \tag{4.11}$$

if we set $r_\star(r=0) = 0$. Here, κ_i is the usual surface gravity at the horizon (see Appendix B for details).

For a massive charged scalar field in a RNdS background, the QNM problem to solve can be written in the form of Eq. (2.49),

$$\frac{d^2\varphi(r_\star)}{dr_\star^2} + \left[\left(\omega - \frac{qQ}{r}\right)^2 - f(r)\left[\frac{\ell(\ell+1)}{r^2} + \frac{f'(r)}{r} + \mu^2\right]\right]\varphi(r_\star) = 0\,, \tag{4.12}$$

where ω is shifted by the qQ/r term. Similarly, the boundary conditions of Eqs (2.20) and (2.21) become

$$\varphi(r_\star) \sim \begin{cases} e^{-i\left(\omega - \frac{qQ}{r_+}\right)r_\star}\,, & r \to r_+ \quad (r_\star \to -\infty)\,, \\ e^{+i\left(\omega - \frac{qQ}{r_c}\right)r_\star}\,, & r \to r_c \quad (r_\star \to +\infty)\,, \end{cases} \tag{4.13}$$

with radiation purely outgoing at the de Sitter horizon [203, 239–241].

These QNM boundary conditions are applied to perturbations exterior to the event horizon. Recall that, classically, the event horizon serves as a one-sided membrane through which energy is lost to the black hole interior. Furthermore, energy cannot enter into the system from beyond the de Sitter horizon. Consequentially, the system is not time-symmetric; the eigenvalue problem is non-Hermitian and the eigenvalues are complex. The corresponding eigenfunctions are then not normalisable and do not form a complete set (see reviews [14, 47, 130] for further discussion). As discussed in Section 2.2, a host of QNM techniques have been developed to confront these technical difficulties.

Several of these are semi-classical methods, informed by the Schutz-Iyer-Will WKB-based technique [151–153], that take advantage of the QNM problem's likeness to a scattering problem. Specifically, these require a bell-shaped confining potential and particular asymptotic behaviour (i.e. $V(r_\star)$ tends towards constant values as $r_\star \to \pm\infty$) for their applicability [155]. As discussed in Section 2.3, the scalar field parameters strongly influence the shape of the potential and, in turn, the nature of the QNFs. There, we demonstrated that the damping of the QNFs decreases with increasing field mass. In this way, for particular values of μ and ℓ, QNFs within the Schwarzschild black hole space-time enter the "quasiresonance" regime and become arbitrarily long-lived.

Through Fig. 2.4, we showed that an analysis of the behaviour of the potential allows us to estimate the values of μ and ℓ at which the potential barrier is smoothed out, serving as a rough precursor to the onset

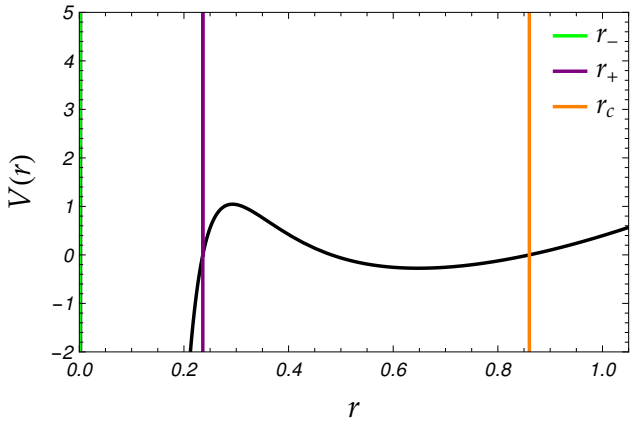

Figure 4.1: *For* $L_{dS}^2 = 1$, $M = 0.112$, *and* $Q = 0.016$, *we plot the scalar QNM potential with* $\mu = q = 0.1$ *and* $\ell = 0$. *Observe the "valley" following the barrier potential indicative of superradiant amplification.*

of the quasiresonant regime. Similarly, we shall see that certain features of the QNM effective potential provide physical insights, including indications of superradiant amplification of reflected waves. For the QNM analysis performed here within the RNdS black hole space-time, we need to account for field parameters (μ, q, ℓ) and space-time parameters (M, Q, Λ). While our QNM analysis focuses on the $\ell = 1$ modes, we shall dedicate a brief discussion to the $\ell = 0$ case: while perturbations within the RNdS black hole space-time are demonstrably stable for $d = 4$ [47, 137], the discovery of an instability for small scalar field charge and vanishing multipolar number [242], with a superradiant origin [239], stimulated great interest within the QNM literature on the charged QNFs of the RNdS space-time. We shall outline the necessary QNF condition for superradiant instabilities and demonstrate how the shape of the potential suggests superradiant amplification of incident waves reflected off of the potential in Section 4.1.1. Thereafter, we shall describe the behaviour of the potential for $\ell > 0$ within the "sharkfin", which informs our subsequent QNF analyses.

4.1.1 Superradiance for $\ell = 0$ in the RNdS black hole space-time

For the RNdS black hole, stability had been well established for $d < 7$ for massless fields [137, 235, 243]. However, attention was refocused on the stability of the 4D RNdS black hole in the wake of the observed instability for the $\mu = \ell = 0$ case [242]. This led to a number of studies scrutinising the parameter space of unstable RNdS QNFs e.g. [239, 244, 245] confirming instability for a vanishing field mass, as well as a small field charge and cosmological constant.

An exponentially growing mode can be caused by superradiance. We introduced this idea in Section 2.3.1, where a "superradiant instability" can be associated with the massive QNMs within the vicinity of a Kerr black hole. Recall that this superradiant instability is a consequence of the local minimum generated by the massive term far from the black hole, such that waves reflected off the potential barrier become reflected and amplified within this "valley" [184]. Superradiance has also been studied in the context of charged black holes. The connection between the rotating and charged black holes lies in the so-called "charge-angular momentum analogy", where near-extremal charge corresponds to fast rotating black holes [246].

Consider the scattering problem of Section 2.1.1. In the RNdS case, the ingoing wave from $r = r_c$ partially passes through the potential barrier, passing $r = r_+$ to fall inside the event horizon, while the rest is reflected from the potential barrier back towards the cosmological horizon $r = r_c$. The RNdS boundary conditions of Eq. (4.13) are modified to those of a scattering problem, such that

$$\varphi \sim \begin{cases} \mathcal{T} e^{-i\left(\omega - \frac{qQ}{r_+}\right) r_\star}, & r \to r_+ \ \ (r_\star \to -\infty), \\ e^{-i\left(\omega - \frac{qQ}{r_c}\right) r_\star} + \mathcal{R} e^{+i\left(\omega - \frac{qQ}{r_c}\right) r_\star}, & r \to r_c \ \ (r_\star \to +\infty). \end{cases} \tag{4.14}$$

As before, $\mathcal{R}$ is the amplitude of the reflected wave (i.e. the reflection coefficient), and $\mathcal{T}$ is the transmitted-wave amplitude (i.e. transmission coefficient). We have set the incident amplitude $\mathcal{I}$ to unity. Superradiance corresponds to $\mathcal{R} > 1$ i.e. the amplitude of the reflected wave exceeds that of the incident wave. For the linear-independent solutions, the Wronskian will be constant, and Eq. (2.12) becomes

$$1 - |\mathcal{R}|^2 = \frac{\omega - qQ/r_+}{\omega - qQ/r_c}|\mathcal{T}|^2 \,. \tag{4.15}$$

With this expression in mind, a necessary condition for superradiance can be derived from Eq. (4.12). Following Ref. [239], this is given by

$$\frac{qQ}{r_c} < \mathfrak{Re}\{\omega\} < \frac{qQ}{r_+} \,. \tag{4.16}$$

In Ref. [239], it was observed that the growing modes satisfied Eq. (4.16). However, some stable modes also satisfied this superradiance condition. The authors there concluded that superradiance can imply instability but does not necessarily prove instability. In other words, superradiant modes are not necessarily unstable modes.

A superradiant amplification of reflected charged perturbations within RNdS space-times can be inferred directly from a study of the QNM effective potential. In Fig. 4.1, we plot the $\ell = 0$ case for $L_{dS}^2 = 1$, $M = 0.112$, $Q = 0.016$, and $\mu = q = 0.1$. These parameters correspond to a central position in the phase space, Fig. 3.2. There is a single "peak" in the barrier potential, the local maximum, followed by a local minimum. A wave scattering off the potential barrier will become amplified in this "valley", resulting in a superradiance that destabilises the black hole. For fixed Q, increasing M shrinks the amplitude of the potential.

As we shall see in the next section, increasing ℓ or μ lifts the potential, restoring stability. We note with interest that for the extremised conditions showcased in Figures 4.2 and 4.3, where the local maximum is suppressed and a local minimum follows, the "valley" appears beyond the physically-relevant domain $r_+ < r < r_c$. As confirmed in [247], a single peak remains in the region defined as the black hole exterior.

Finally, we note that a QNF analysis of instability and superradiance is beyond the scope of this thesis. For a harmonic time dependence $\psi \sim e^{-i\omega t}$, a negative imaginary component reveals an exponentially decaying system, in accordance with a return to an equilibrium state [44]. An unstable QNM is indicated by $\mathfrak{Im}\{\omega\} > 0$, corresponding to an exponential growth in the oscillations. As we shall discuss in Section 4.1, the RNdS QNF spectrum is complicated by the introduction of a non-zero q and the consequent breaking of the $\omega \to -\omega^+$ QNM reflection symmetry. To capture the unstable and/or superradiant behaviour of the imaginary component, we require a more precise method than the WKB-based technique we use here (e.g. direct integration or pseudospectral techniques); results with WKB-based methods in this case would be misleading. Within the literature, however, there has been no evidence of instability in the RNdS space-time for $\ell \neq 0$.

4.1.2 The behaviour of the potential within the RNdS phase space for $\ell > 0$

Let us consider the QNM potential of a massive and charged scalar test field with respect to key benchmark points within the RNdS phase space of Fig. 3.2. In these sketches of the potential, we demarcate the locus of each horizon as defined by the roots of the metric function for each given benchmark: green, purple, and orange vertical lines demarcate the Cauchy ($r = r_-$), event ($r = r_+$), and cosmological ($r = r_c$) horizons, respectively. As we shall see, a single peak in the potential is defined in each case on the black hole exterior $r \in (r_+, r_c)$, framed by the purple and orange delineators. The barrier potential established in this context suggests that QNM propagation is maintained and supports the application of WKB-based techniques. This behaviour of the potential was recently confirmed in Ref. [247], which determined that for general spherically-symmetric black holes, the WKB method is indeed quite accurate for $\Lambda > 0$, particularly if $\mu M \gg 1$. Note how this is in direct contrast with the Schwarzschild case of Section 2.3, where the local

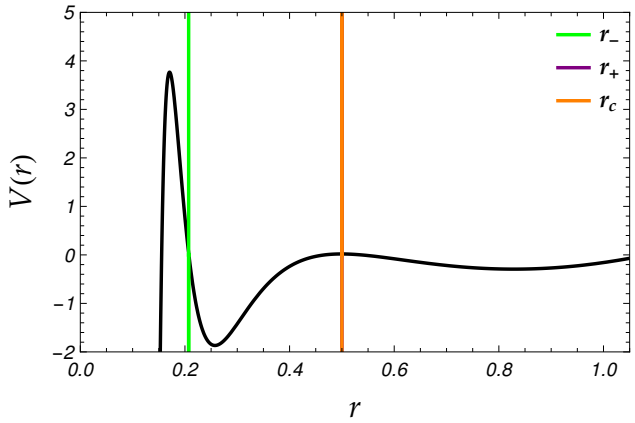

Figure 4.2: *For $M = Q = 0.25$ and $L^2_{dS} = 1$ (point E of Fig. 3.2), we plot the scalar QNM potential with $\ell = 1$ and $\mu = q = 0.1$.*

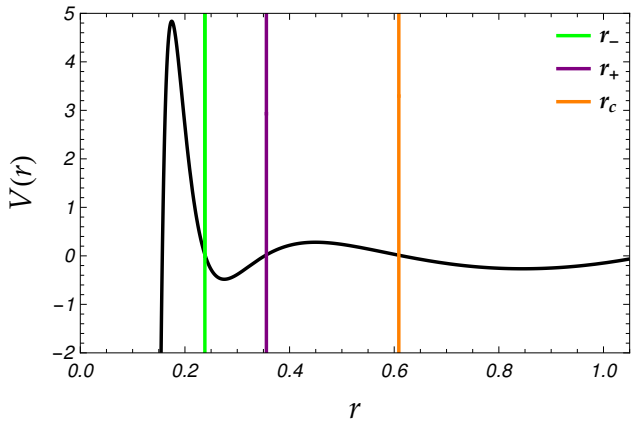

Figure 4.3: *For $M = 0.2425$, $Q = 0.249$, and $L^2_{dS} = 1$ (above the $M = Q$ line of Fig. 3.2), we plot the scalar QNM potential with $\ell = 1$ and $\mu = q = 0.1$.*

maximum of the potential is suppressed by large values of μ and the WKB method fails to produce reliable results. Once we have discussed the behaviour of the potential, we shall return to this point at the end of this section.

In Fig. 4.2, we plot the potential for $\mu = q = 0.1$ and $\ell = 1$ for $M = Q = 1/4$. This is point E of Fig. 3.2, corresponding to a charged Nariai case at the maximum point of the $M = Q$ "lukewarm" line. In setting $r_+ \to r_c$ (see Appendix C for details on the Nariai limit), there is no physical exterior black hole region; the de Sitter space-time is dominated entirely by the black hole. This renders QNM analyses impossible, as we cannot impose the boundary conditions necessary to isolate the discrete set of frequencies. In this configuration, we see explicitly the effect of the cosmological constant on the parameter space: the $M = Q$ solution, which in asymptotically flat space-times corresponds to a coalescence of the Cauchy and event horizons, is associated with a meeting of the event and de Sitter horizons. Similarly, for the "ultracold" case (point U on Figure 3.2), all horizons converge on this line at $r = 3M/2 \sim 0.408$.

To our knowledge, there has been little discussion in the literature on the nature of QNMs within "cold" black holes, such that $Q > M$. To determine if there is a significant behavioural shift upon crossing the "lukewarm" line, we plot the potential for $M = 0.2425$ and $Q = 0.249$ in Fig. 4.3 for these same field parameters of $\ell = 1$ and $\mu = q = 0.1$. The barrier potential is present, but suppressed. Interestingly, for the slightly "warmer" $M > Q$ solution corresponding to $M = 0.2425$ and $Q = 0.239$, the event and de Sitter horizons are relatively closer and the potential's amplitude becomes more suppressed.

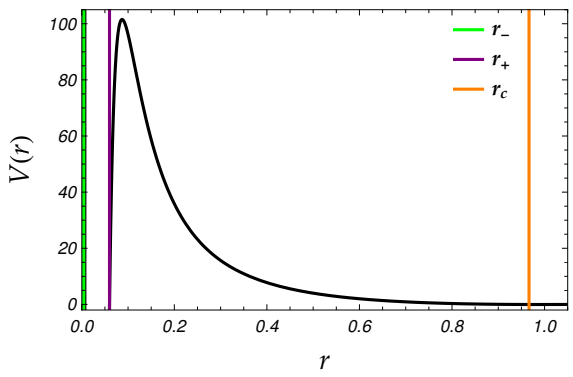

(a) *For* $M = 0.032$ *and* $Q = 0.016$, $V(r_{peak}) \sim 100$.

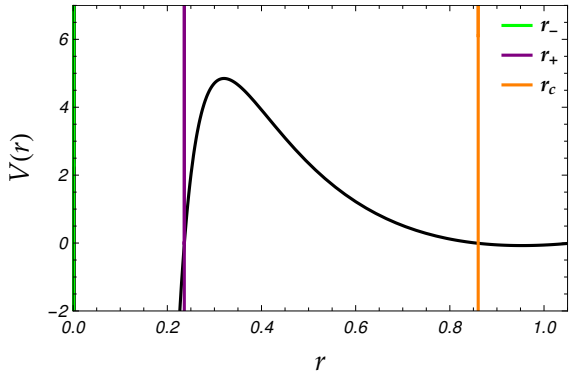

(b) *For* $M = 0.112$ *and* $Q = 0.016$, $V(r_{peak}) \sim 5$.

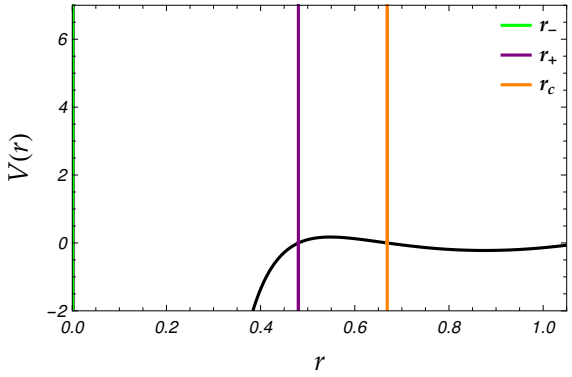

(c) *For* $M = 0.185$ *and* $Q = 0.016$, $V(r_{peak}) < 0.5$.

Figure 4.4: *The evolution of the QNM scalar potential within Fig. 3.2 for* $L_{dS}^2 = 1$, $\ell = 1$, *and* $\mu = q = 0.1$.

After exploring the full available phase space depicted in Fig. 3.2, we can summarise the general behaviour of the potential. As a visual aide, we illustrate a examples of these trends in Figs 4.4 and 4.5. For a fixed Q, $V(r_{peak})$ is largest near point O and decreases towards U, remaining largest along the extremal branch OU. The amplitude of the potential decreases significantly as we increase M from the near-extremal OU branch to the near-Nariai NU branch. Despite this, the potential retains its shape on $r_+ < r < r_c$. We can also identify the effect of the scalar field parameters on the barrier potential. For example, raising ℓ increases the magnitude of $V(r)$, as expected. From Fig. 4.5, we see that even for the suppressed peak of Fig. 4.4c, elevating μ increases the amplitude of the peak and smoothes out the local minimum. As suggested in Ref. [247], a strong barrier potential emerges in the $\mu M \gg 1$ regime on the region of interest $r_+ < r < r_c$. Raising q, on the other hand, suppresses the effective potential.

From these observations, the application of QNM techniques dependent on barrier potentials (e.g. WKB-based, potential-based, and photon-orbit techniques) seems permissible throughout the sharkfin (except for the extremised regions), provided the field parameters support a barrier potential. Recall from Section 2.3 that the standard WKB method (e.g. the Schutz-Iyer-Will approach) remains a good approximation provided the local maximum of the potential is "high enough" for $\ell \geq 1$. Even if a local minimum follows the local maximum, WKB-based methods remain fairly reliable provided $V(r_{peak})$ exceeds the value to which $V(r)$ asymptotes as $r \to \infty$. In this case, Ref. [155] claims that neglecting the local minimum does not result in significant error.

With these arguments in mind, we shall make use of a modified WKB method in our QNM investigations within the RNdS phase space. This method was established in Ref. [238] and employed for scalar QNMs of nonzero mass and charge in the RNdS context in Refs [248, 249]. The value of this method lies in the fact

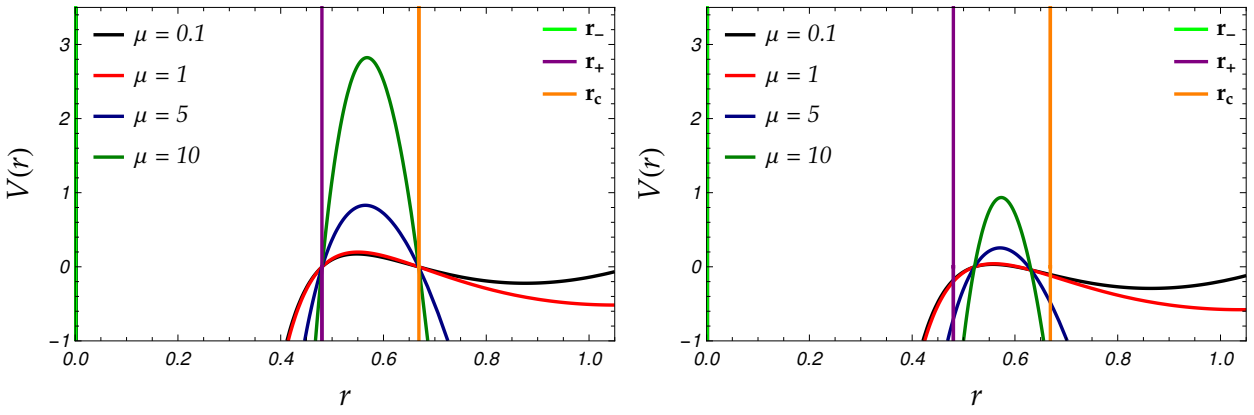

(a) *For* $q = 0.1$, $V(r_{peak})$ *scales with* μ.

(b) *For* $q = 5$, *the amplitude is suppressed.*

Figure 4.5: *The influence of scalar field parameters on the QNM scalar potential within Fig. 3.2 for* $L_{dS}^2 = 1$, $M = 0.185$, $Q = 0.016$, *and* $\ell = 1$.

that it allows us to define the position of the potential peak explicitly through Eq. (4.19) and to produce the QNF as a series expansion à la Eq. (2.43) that maintains the space-time and field parameters $-$ (M, Q, Λ) and (μ, q, ℓ), respectively $-$ as free parameters. We shall introduce this method in Section 4.2.1. There, we shall also discuss a number of limitations associated with this method.

4.2 The QNF spectrum in RNdS space-time

4.2.1 The semi-classical calculation of QNFs in a RNdS background

In this section, we compute the QNFs using a modified WKB approach applied to the RNdS black hole space-time by Fontana *et al.* [248, 249] in the eikonal regime for small Q/M and qM. The method is based a Borel-resummation technique proposed in Ref. [238] that exploits the well-cultivated relationship between the bound states of anharmonic oscillators [250] and black hole QNFs [150, 162, 163].

Like the Dolan-Ottewill multipolar expansion method [156] discussed in Section 2.2, the QNF is expressed as a series expansion in inverse powers of L,

$$\omega = \sum_{k=-1} \omega_k L^{-k} \,. \tag{4.17}$$

Note, however, that $L = \sqrt{\ell(\ell+1)}$ in this case. The series expansion is then inserted into

$$\begin{aligned} \omega &= \sqrt{V(r_\star^{max}) - 2iU}\,, \\ U &\equiv \qquad\qquad\qquad\qquad U(V^{(2)}, V^{(3)}, V^{(4)}, V^{(5)}, V^{(6)})\,. \end{aligned} \tag{4.18}$$

The objective of the method is to solve iteratively for the ω_k coefficients for increasing orders of k. $V(r_\star^{max})$ corresponds to the peak of the barrier potential, located at

$$\begin{aligned} r_\star^{max} &\approx r_0 + r_1 L^{-2} + \dots\,, \\ V(r_\star^{max}) &\approx V_0 + V_1 L^{-2} + \dots\,, \end{aligned} \tag{4.19}$$

where subscripts refer to terms in a series expansion around the peak. The explicit expressions for U,

$V(r_\star^{max})$, and $r_\star^{max}$ are presented in Appendix F.

The numbered superscripts in Eq. (4.18) refer to derivatives V^j, taken with respect to a generalised tortoise coordinate, such that

$$V^j = \frac{d^j V(r_\star^{max})}{dr^j} = f(r)\frac{d}{dr}\left[f(r)\frac{d}{dr}\left[...\left[f(r)\frac{dV(r)}{dr}\right]...\right]\right]_{r\to r_\star^{max}} . \tag{4.20}$$

This method is most reliable in the large-ℓ regime, and for small values of Q and q. Beyond these limitations, the method allows us to maintain the black hole and scalar field parameters as free variables. In other words, the iterative procedure required to produce an expression for the QNF, Eq. (4.17), can be computed with reasonable accuracy without pre-defining the masses, charges, overtones, or harmonics (which is required for many other semi-classical methods e.g. consider Refs [155, 251] and references therein). It is for this reason that we employ this method here: to provide analytical insight into the behaviour of the QNFs throughout the phase space, in order to identify the parameters that warrant further exploration in a follow-up investigation based on more accurate techniques.

However, we must address a number of weaknesses in this method for our particular QNM analyses. As already mentioned, the method itself does not yield very precise results. The Borel-resummation technique of Ref. [238] derives the function U in a simplified manner, which is equivalent to the result of Ref. [153]; the higher-order corrections to Ref. [153], summarised in [155], are not included. Furthermore, the WKB method is most accurate in the eikonal regime. When $\ell \to \infty$, $\Im m\{\omega\}$ is independent of ℓ. Recall that in asymptotically flat and de Sitter space-times, the imaginary component tends towards the Lyapunov constant describing the decay time scale of the perturbations [157]. Techniques that capture the behaviour of the imaginary component of the QNF more precisely are better suited to investigations concerning the imaginary component.

As we shall discuss in the next section, the QNF frequency spectrum associated with the RNdS black hole space-time and a massive charged test-field is complicated by the number of free parameters and the breaking of the QNF reflection symmetry. For these reasons, it is useful to employ a flexible technique like the WKB-based method to scan the parameter space for general trends in the QNF behaviour and to identify key benchmark points that warrant further investigation (which we reserve for a follow-up work).

4.2.2 Classifying charged QNMs in the RNdS space-time

Within spherically-symmetric black holes with $\Lambda > 0$, Ref. [247] asserts that the QNMs can be categorised into two main branches:

- (I) "Schwarzschild modes": the modes of an asymptotically flat black hole corrected by a $\Lambda > 0$ term;
- (II) "de Sitter modes": the modes of an empty de Sitter spacetime corrected by the presence of a black hole.

When $\Lambda \to 0$ and $M \to 0$, these reduce to Schwarzschild an pure de Sitter modes, respectively. While there are both real and imaginary components for large-μM, the real modes vanish for smaller values of μM for the de Sitter branch [247].

As first stipulated in Ref. [246], and further explored in Refs [203, 241, 249, 252], QNMs in the RNdS space-time can be classified into three qualitatively distinct types based on the structure of their QNF solution: a (i) "photon-sphere" type, a (ii) "de Sitter" type, and a (iii) "near-extremal" type. The photon-sphere type connects smoothly to the "Schwarzschild" branch, while the de Sitter type connects to the "de Sitter" branch [253]. The near-extremal type, on the other hand, is unique to the RNdS space-time. We find that each of these can be loosely associated with a particular region in the Fig. 3.2. With this in mind, we can categorise the QNFs according to their structure [246] and position in the phase space, *viz*

(i) photon-sphere modes occupy a wide space beneath the $M = Q$ line and approach the NU line, characterised by large $\mathfrak{Re}\{\omega\}$ and for which $\mathfrak{Im}\{\omega\}$ is related to the instability time scale of null geodesics near the black hole photon sphere in the eikonal regime. Closely following the charged Nariai NU branch for smaller Q values,

$$\mathfrak{Im}\{\omega_{PS}\} \approx -i\left(n+\frac{1}{2}\right)\kappa_+ \,; \tag{4.21}$$

(ii) de Sitter modes can be found near Point O, following closely along branch OU and in competition with the near-extremal modes. Here, $\kappa_c \sim 1/L_{dS}$ and

$$\omega_{dS_{n=0}} \approx -i\ell\kappa_c \,, \quad \omega_{dS_{n\neq 0}} \approx -i(\ell+n+1)\kappa_c \,; \tag{4.22}$$

(i) near-extremal modes arise near the OU line where $r_- \sim r_+$,

$$\omega_{NE} \approx -i(\ell+n+1)\kappa_- = -i(\ell+n+1)\kappa_+ \,. \tag{4.23}$$

These hold for electrically-neutral and charged scalar test fields. We note that we observe a non-zero $\mathfrak{Re}\{\omega\}$ part in each of these regions for low values of μ and q. However, in the case of the near-Nariai region, this contribution is very small: $\mathfrak{Re}\{\omega\} \sim \mathcal{O}(0.01)$ for $Q < 0.1$.

Let us now consider the QNM spectrum itself. Irrespective of the space-time parameters, when studying $q = 0$ QNM problems in spherically-symmetric space-times, there are two sets of QNFs for which the imaginary parts are identical and the real parts are of equal magnitude but opposite sign. This is a natural consequence of the QNM reflection symmetry $\omega \to -\omega^*$, such that the complex conjugate ω^* is the QNF corresponding to the QNM φ^* which satisfies Eq. (4.12). Upon introducing a non-zero field charge, the QNM reflection symmetry is broken, leaving us with two distinct sets of QNF solutions, such that if φ has a charge q, then φ^* has a charge $-q$. To elaborate: if $\omega = \omega_a + i\omega_b$ is a QNF associated with the QNM φ, then $-\omega^* = -\omega_a + i\omega_b$ is a QNF associated with the QNM φ^*. In other words, we must allow for both positive and negative values of $\mathfrak{Re}\{\omega\}$. We assume $q > 0$.

Furthermore, we find that our WKB-based analysis yields two families of QNFs for nonzero q, as observed in Refs [203, 249]. Following the convention of Ref. [203], we refer to the two families of solutions as a "black-hole family" ω_+ and a "cosmological horizon family" ω_c. For a fixed q, we find that $|\mathfrak{Re}\{\omega_+\}| < |\mathfrak{Re}\{\omega_c\}|$ and $|\mathfrak{Im}\{\omega_+\}| < |\mathfrak{Im}\{\omega_c\}|$.

In the next section, we shall focus on the influence of μ on the QNF spectrum. We highlight the anomalous decay first noted in Ref. [183] for the Schwarzschild case, in which the QNF damping decreases with the angular momentum number for μ below a critical field mass μ_{crit}.

4.2.3 On the scalar field mass of the QNF

In Section 2.3, we initiated our investigation into the relationship between μ and ℓ for the QNF spectrum in spherically-symmetric black holes. There, we determined that an increase in ℓ or an increase in μ leads to increased $|\mathfrak{Re}\{\omega\}|$. Similarly, $|\mathfrak{Im}\{\omega\}|$ scales with ℓ. On the other hand, $|\mathfrak{Im}\{\omega\}|$ decays with increasing scalar field mass μ. As such, heavier modes are expected to be less damped and longer lived. This is demonstrated in Fig. 4.6, where we plot the imaginary part of the QNF for increasing values of μ. There, we set $M = 1/\sqrt{27}$ and $Q = 0$, corresponding to Point N of Fig. 3.2: the uncharged Nariai solution at which $r_+ \sim r_c$. Irrespective of the value of ℓ, the magnitude of the imaginary part of the QNF $|\mathfrak{Im}\{\omega\}|$ decreases with μ.

For (massive) scalar QNMs in a spherically-symmetric space-time, it is expected that $|\mathfrak{Im}\{\omega\}|$ scales with ℓ [14, 47]. However, this relationship was only observed for heavier modes in Fig. 2.7. Similarly, we do

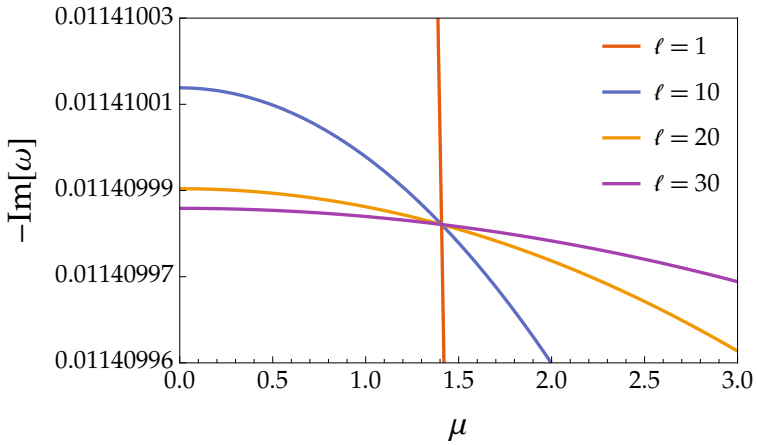

Figure 4.6: *A graphical indication of the critical mass* $\mu_{cit} \sim 1.4083$ *at Point N, where* $r_+ \sim r_c$ *for* $L_{dS}^2 = 1$, $M = 1/\sqrt{27}$, *and* $Q = 0$.

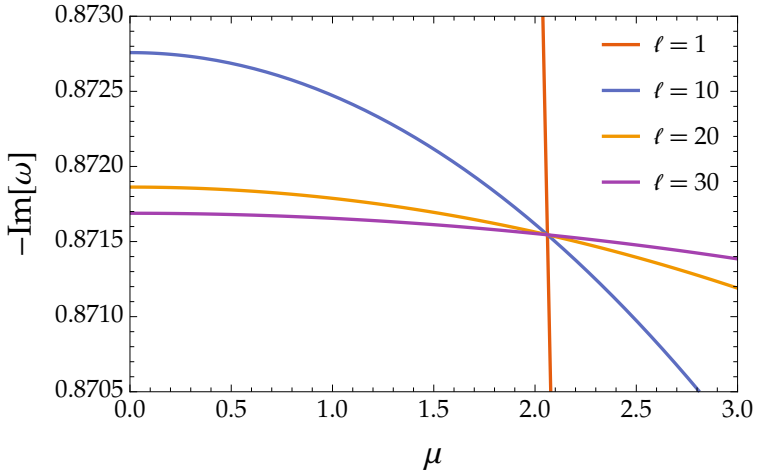

Figure 4.7: *At Point E, where* $M = Q = 0.104$ *for* $L_{dS}^2 = 1$, *the critical mass is* $\mu_{crit} \sim 2.065$ *for* $q = 0$.

not see this throughout Fig. 4.6: $|\mathfrak{Im}\{\omega_{\ell=10}\}| > |\mathfrak{Im}\{\omega_{\ell=30}\}|$ for lower values of μ and $|\mathfrak{Im}\{\omega_{\ell=10}\}| < |\mathfrak{Im}\{\omega_{\ell=30}\}|$ for larger values of μ. In other words, only past a certain mass value do we observe "regular" QNF behaviour. In Fig. 4.6, this "critical mass" is given by $\mu_{crit} \sim 1.4083$ and corresponds to a very small $\mathfrak{Im}\{\omega\} \sim -0.0114$. We observe that for these values of $\mu = \mu_{crit}$ and $(M, Q) = (1/\sqrt{27}, 0)$, $M\mu \sim 0.3$; this is the smallest possible μ_{crit} for the RNdS black hole parameterised as $L_{dS} = 1$.

This "critical mass" μ_{crit} value has been observed in Schwarzschild (and Kerr) black hole space-times beyond which the magnitude of the imaginary part increases with larger values of ℓ [183]. This has been noticed also for the charged, massive scalar field in the RN and RNdS space-times [248, 249]. Here, we study this effect in greater detail, to determine the parameter range for which it is valid.

We can solve for μ_{crit} by setting $\mathfrak{Im}\{\omega_{-2}\} = 0$ [249] (see Appendix F). At the lowest order in Q,

$$\mu_{crit}^2 = \frac{18045\Lambda M^2 + 137}{29160 M^2} \,. \tag{4.24}$$

As shown in Fig. 4.6, we can also determine μ_{crit} graphically by plotting $-\mathfrak{Im}(\omega)$ vs μ. A common point of intersection, irrespective of the hierarchy in ℓ, denotes the value of μ_{crit}. We observe that this coalescence indicates a negligible dependence of the QNF on ℓ at $\mu = \mu_{crit}$, and confirm it analytically.

In particular, we observe in Fig. 4.6 that for the uncharged Nariai case, the critical mass corresponds to

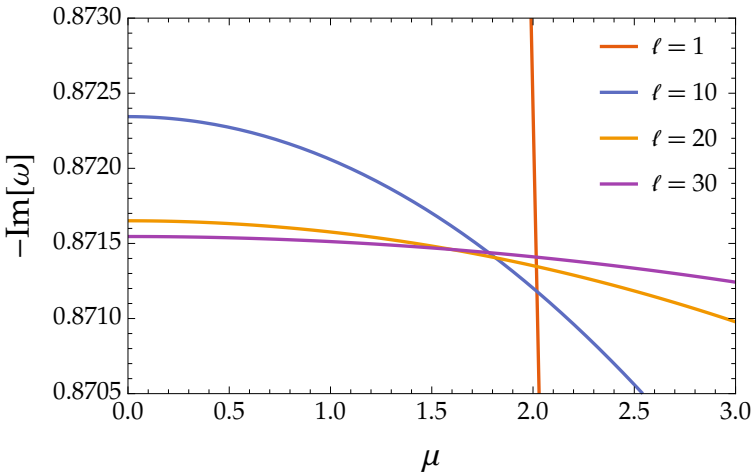

Figure 4.8: *At Point E, where* $M = Q = 0.104$ *for* $L_{dS}^2 = 1$*, there is no longer an intersection to denote* μ_{crit} *for* $q = 0.1$.

$\mu_{crit} \sim 1.4083$ for all q. This same result is found using Eq. (F6) for $q = 0$. This is the maximum M for which we see an intersection. We do not observe further intersections along the NU branch, and since $Q = 0$, the charge q has no influence on the QNF at point N (recall that q and Q couple in the potential, Eq. (4.12)). For $q \approx 0$, the intersection point shifts to the right of Fig. 3.2 as we increase Q, and as we increase M (from zero) the intersection point shifts left. For fixed values of M and Q, the intersection point shifts left as we increase q (along the small domain of q).

When $q = 0$, the influence of Q is negligible on μ_{crit}. We find that large M corresponds to a small μ_{crit}; μ_{crit} decreases with increasing M, such that for $M \sim 0$, $\mu_{crit} \sim 20$. When $M > 1/\sqrt{9\Lambda}$ for non-zero Q, we observe growing rather than decaying modes for large values of μ e.g. when $\mu > 5$ for $\ell \sim 10$ and $\mu > 15$ for $\ell \sim 30$. For $q > 0$, we do not observe an intersection of all lines, but the anomalous behaviour in which $|\mathfrak{Im}\{\omega_\ell\}| > |\mathfrak{Im}\{\omega_{\ell+1}\}|$ is noted for smaller values of μ (see Fig. 4.8). As we would expect from the coupling between q and Q, Q has a more obvious effect for the nonzero q, such that the spacing between modes increases with Q.

As a final comment and brief aside on the scalar field mass, we consider whether scalar QNFs with a non-zero mass and charge satisfying the FL bound could be observable. To do so, we invoke the arguments presented in Section 2.3.1, where we derived Eq. (2.56). For convenience, we repeat it here

$$m = \frac{1}{m_{\rm BH}} \frac{\hbar c}{G} M\mu \, .$$

As before, we scale the black hole mass as $m_{\rm BH} \sim 10^{\chi} M_\odot$ to obtain Eq. (2.57), *viz.*

$$m \sim 10^{-(\chi+10)} M\mu \text{ eV} \, .$$

We have seen that for the critical mass in the regime $\mu M \gg qQ$, $\mu_{crit} M \leq 0.3$. To satisfy the FL bound of $m > 10^{-3}$ eV, this means we can only consider compact objects corresponding to $\chi < -8$, such as micro black holes. With this, we surmise that the FL bound rules out the possibility of observing weakly-charged scalar QNMs from astrophysical black holes.

In this section, we focused on the scaling of the imaginary part of the QNF with respect to the black hole and field parameters. We shall continue our QNM investigation of the RNdS black hole with a semi-classical analysis of the preservation of cosmic censorship. We shall rely on the arguments presented in Section 3.3 to do so, invoking the criterion for the preservation of SCC determined in Ref. [231].

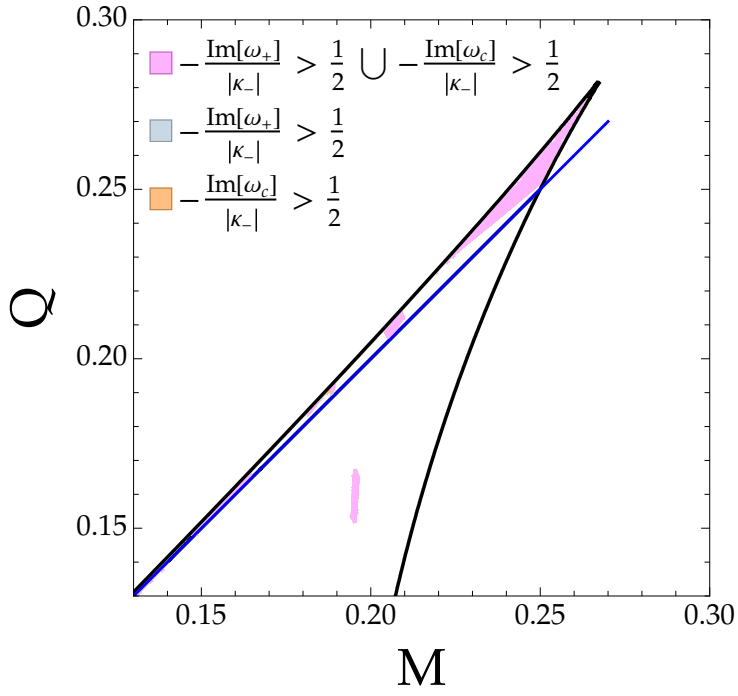

Figure 4.9: *With $L_{dS}^2 = 1$ and for $\mu = \ell = 1$ and $q = 0.1$, we shade the parameter space in which ω_+ (blue), ω_c (orange), and both families (magenta) violate the condition for SCC preservation.*

4.3 On the issue of Strong Cosmic Censorship

As discussed in Section 3.3, there is an expectation based on Penrose's SCC conjecture that the presence of a Cauchy horizon in the RN back hole interior leads to the infinite amplification of perturbations in the interior region through a "blue-shift" mechanism. The Cauchy horizon then is destabilised and behaves as a singularity beyond which the initial data cannot be extended. Such a phenomenon allows for determinism to be protected within GR.

For the RNdS case, the presence of the cosmological horizon complicates matters, as the resultant "red-shift" effect introduced by the positive vacuum energy competes against the blue-shifting in the black hole interior. This leads to a delicate balance between the damping of the perturbations in the exterior and the amplifications from the black hole interior. As discussed in Section 3.3, the criterion for the preservation of (the Christodoulou formulation of) SCC is provided in Eqs (3.32) and (3.33), *viz.*

$$\beta \equiv -\frac{\mathfrak{Im}\{\omega^{n=0}\}}{|\kappa_-|} < \frac{1}{2}\,.$$

Using the semi-classical technique described in Section 4.2, we explore the RNdS (M, Q) parameter space in order to determine for which space-time and scalar field parameters we find evidence for $\beta > 1/2$ for $\ell = 1$. The SCC is largely preserved within the sharkfin; we only find evidence of its violation for intermediate and large values of M and Q. In particular, we consistently find evidence that SCC is violated within the shaded *OEU* region of the sharkfin and on certain points on the *OU* line, particularly near $M \sim Q \sim 0.089$ for near-zero mass and charge. For $\ell = 1$ and $q = 0.1$, we find that $\mu = 0.1$ and $\mu = 1$ violate identical regions, yielding Fig. 4.9. When $q = 1$, however, a larger region of the parameter space is violated, extending from the extremal $r_- \sim r_+$ regime.

Finally, we note with interest that for a very small parameter space on the *OU* line corresponding to

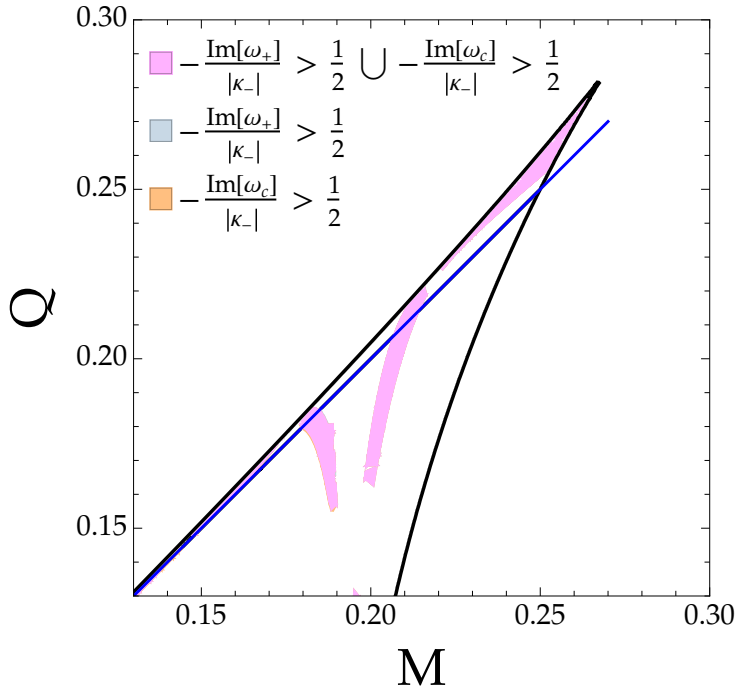

Figure 4.10: *With $L_{dS}^2 = 1$ and for $\mu = 0.1$, $q = 1$, and $\ell = 1$, we shade the parameter space in which ω_+ (blue), ω_c (orange), and both families (magenta) violate the condition for SCC preservation.*

extremal black holes, we observe in Fig. 4.11 a μ_{crit} for which $\beta > 1/2$. Only in the extremal region $r_- \sim r_+$ do we observe β values that approach or exceed $1/2$.

4.3.1 Comparisons with other works

Irrespective of the scalar field parameters, we have found that scalar QNFs satisfy the condition for SCC preservation in the near-Nariai limit $r_+ \sim r_c$.This result is confirmed in Refs [252, 254] for the massless charged case for small q. Only in the regime $\mu M \gg 1$ and $qQ \gg 1$ do we observe $\beta > 1/2$ for $Q \gtrsim 0.2$.

As we mentioned earlier, we find that violations of the SCC occur only for intermediate and large values of M and Q. Near *Point O*, where r_+ is significantly smaller than r_c, $\beta \ll 1/2$. This follows from Ref. [255], where a universal result for spherically-symmetric black holes was determined: provided $r_+ \ll r_c$ and irrespective of the near-horizon geometry, $\Im m\{\omega\{ < \kappa_-/2$.

In Ref. [203], it is shown that even for large q, there is always a region in the extremal $r_- \sim r_+$ regime for which SCC is violated. In this work, the authors considered a WKB-based analysis of their own, following the Dolan-Ottewill method outlined in Ref. [256] and using a series expansion in inverse powers of q, i.e.

$$\overline{\omega} = \sum_{k=-1}^{+\infty} \frac{\omega^{(k)}}{q^k} + \text{non-perturbative}\,. \tag{4.25}$$

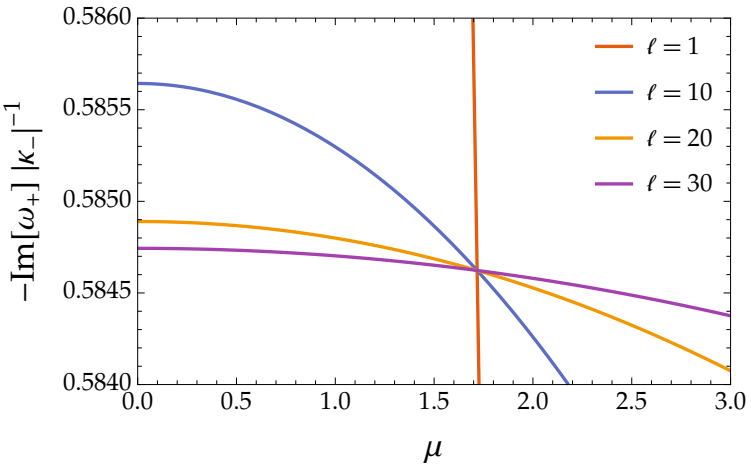

Figure 4.11: *For $L_{dS}^2 = 1$, $M = 0.157$, and $Q = 0.158$, we plot the critical mass $\mu_{crit} \sim 1.7$ corresponding to a violation of the condition for SCC preservation.*

Let us consider the series up to the order $\mathcal{O}(q^{-2})$ for the "black hole" family of solutions, where

$$\begin{aligned}
\omega_+^{(-1)} &= \frac{Q}{r_+} \\
\omega_+^{(0)} &= -\frac{i}{2}\kappa_+ \,, \\
\omega_+^{(1)} &= \frac{\kappa_+}{2Q}\left\{ r_+^2\mu^2 + \ell(\ell+1) + \frac{1}{4}\left[9\frac{r_c^3 + (Q^2+r_c^2)r_+}{r_c(r_c^2 + r_c\, r_+ + r_+^2)} - 7 - \frac{Q^2}{r_+^2}\right]\right\} \,, \\
\omega_+^{(2)} &= \frac{i\,\kappa_+^2}{16Q^2 r_c\, r_+}\left[r_c\left(8r_+^4\mu^2 + 3Q^2 - r_+^2\right) + 15\frac{r_+^3\,(Q^2 - r_c\, r_+)}{r_c^2 + r_c\, r_+ + r_+^2}\right] \,,
\end{aligned}$$

where

$$\omega r_c = \overline{\omega} - \frac{qQ}{r_+} \,.$$

While the WKB-based analysis of Ref. [203] is tailored to the large-q regime, we find reasonable agreement between our result and theirs for the point showcased in Fig. 4.11: $M = 0.157$, $Q = 0.158$. There, for $\mu = 0.1$, $q = 0.1$, and $\ell = 1$,

$$\begin{aligned}
\beta_{large-q} &\approx 0.531576 \,, \\
\beta_{large-\ell} &\approx 0.532152 \,.
\end{aligned}$$

4.4 Discussion on the behaviour of QNMs within the RNdS space-time

Within Chapters 3 and 4, we have explored the full range of the RNdS phase space and the behaviour of QNMs within it. In so doing, we have investigate the wide array of applications of QNMsFurthermore, we have evaluated the implications of scalar field mass and charge on the behaviour of the QNFs; we can observe directly how each of these behaviours manifest in different regions of the sharkfin, i.e. for different values of M and Q, and how these affect principles such as cosmic censorship.

Through this study of the interplay of black hole and scalar field parameters, we have determined the

maximum black hole mass for which a μ_{crit} exists in the case of massive charged scalar QNMs, at point N corresponding to the uncharged Nariai solution. Black hole mass scales inversely with μ_{crit}: for $M \sim 0$, $\mu_{crit} \sim 20$ whereas for the maximum $M \sim 1/\sqrt{27}$, we obtained the minimum $\mu_{crit} \sim 1.4$. For fixed values of M and Q, the value of μ_{crit} decreases as we increase q. When $q = 0$, the influence of Q is negligible on μ_{crit}. For larger values of $q > 1$, we did not observe an intersection in the $-\mathfrak{Im}\{\omega\}$ vs μ plot but the anomalous behaviour in which $|\mathfrak{Im}\{\omega_\ell\}| > |\mathfrak{Im}\{\omega_{\ell+1}\}|$ is noted when $\mu > 0$ is sufficiently small. Due to the coupling between q and Q, Q has a more obvious effect for the nonzero q, such that the spacing between modes increases with Q (see Figs 4.6, 4.7, 4.8). This value of μ_{crit} corresponds to a point in the QNF spectrum for which dependence on the angular momentum number is negligible. It is interesting to note that the introduction of charge offsets this value, suggesting perhaps that the behaviour of the charged scalar field cannot be decoupled from angular momentum.

Furthermore, using dimensional analysis, we also found evidence suggesting that the FL bound rules out the possibility of observing weakly-charged scalar QNFs from astrophysical black holes. For scalar test fields oscillating within the exterior of an astrophysical black hole, recent studies [133, 188–190] suggest that modes scaling as $M\mu \sim \mathcal{O}(1)$ may undergo a superradiant amplification on timescales of suitable length to be observed by current and next-generation GW detectors. Here, we find that $M\mu_{crit} \sim 0.3$. By Eq. (2.57), we infer that only from compact objects of the order $m \lesssim 10^{-8}\ M_\odot$ can we expect to observe QNMs satisfying the FL bound.

From our analysis of the evolution of the potential within the phase space, we found that a barrier potential characteristic of QNM behaviour was shown to exist on $r_+ \leq r \leq r_c$ for $\ell > 0$ (with the "valley" suggestive of superradiant amplification suppressed or lying beyond $r = r_c$). The only exception to this could be found in extremised regions of the RNdS parameter space, where the coalescence of horizons suppressed the potential (i.e. Figs 4.2 and 4.3) and the $\ell = 0$ case (see Fig. 4.1, where the "valley" falls within $r_+ < r < r_c$). However, as demonstrated in Figure 4.5, increasing μ can uplift the local maximum of a suppressed potential within non-extremised regimes.

Finally, we note that in Section 3.3, the condition for the preservation of SCC was violated within the shaded OEU region of the RNdS phase space and on certain points on the OU line, particularly near $M \sim Q \sim 0.089$. For non-zero μ, black holes "colder" than the cosmological horizon were associated with SCC violations. In fact, this question of whether large, cold black holes respect SCC has recently been investigated in Ref. [257]. Moreover, we noted also that a $\mu = \mu_{crit}$ value could be observed on the extremal OU line, corresponding to a β in violation of SCC.

A more qualitative aspect of these chapters was to demonstrate the value in beginning QNM studies by first contextualising the space-time in which we perform our QNM analysis; for this reason, we established a means by which we could observe the evolution of the QNF spectrum, throughout the available phase space. This process allowed for a clarification of the effect of the non-zero cosmological constant on the black hole solution space:

(*i*) the widening of the parameter space to include black hole solutions where $Q > M$, as well as analytical limitations on the possible black hole mass;

(*ii*) the presence of a cosmological horizon that confines the size of the black hole such that $r_+ \leq r_c \leq L_{dS}$;

(*iii*) the near-Nariai solution which, although unphysical, represents a black hole in which event horizon and cosmological horizon are infinitesimally close but never overlapping.

This concludes our investigation into the QNMs of charged black holes in de Sitter space-time. We now proceed to the next component of our investigation into the applications of black hole perturbations, focusing here on the possibility of detecting evidence of extra dimensions.

Chapter 5

Compact negative spaces as higher-dimensional manifolds

...negative curvature means nothing or, equivalently, permits everything...

Marcel Berger in *A Panoramic View of Riemannian Geometry* [258]

Compact negative-curvature spaces (i.e. spaces with negative Ricci scalar curvature) have been interrogated extensively within the mathematical literature [258, 259]. Among members of the string theory community, a burgeoning interest in such spaces is developing in the wake of a recent observation that negatively-curved manifolds are a requirement for classical de Sitter solutions with orientifold planes [260–262]. In the context of particle physics, extra-dimensional models characterised by partial or total negative scalar curvature remain comparatively under-explored.

Phenomenologically, studies on compact negative spaces are promising for their capacity to include cosmological observations such as homogeneity and flatness [263–265]. Moreover, these models could be used to address the hierarchy problem between the Planck and the electroweak scale by virtue of their geometrical properties. Compact negative-curvature spaces possess two characteristic length scales: ℓ_c, associated with local properties like the curvature and fixed by the equations of motion, and ℓ_G, associated with global properties like the volume and independent of the equations of motion. Their volume grows exponentially with ℓ_c/ℓ_G, leading to an exponential reduction of the Planck length, which in turn yields a natural explanation for the perceived discrepancy in energy scales [266]. Furthermore, the KK mass spectra associated with such spaces are usually similar to those of Randall-Sundrum models [267] in that they accommodate the electroweak-Planck scale hierarchy without introducing light KK modes [266].

Motivated by these implications, a series of investigations [128, 268–271] have focused model-building efforts on a compact, negatively-curved manifold whose tangent vectors form a Lie algebra that is nilpotent *viz.* a nilmanifold $\mathcal{N}_3$ (see Refs [272, 273]). In the sections that follow, we shall outline how the nilmanifold is constructed from the Heisenberg algebra and demonstrate the KK expansion of a scalar field in this context, as established in Ref. [128]. With these elements in place, we may proceed to the construction of our Schwarzschild-nilmanifold setup, and the KK reduction that allows us to treat the oscillations travelling through the 7D product space-time as a massive 4D scalar field.

5.1 Constructing the 3D nilmanifold

Any Lie group of dimension d can be understood as a d-dimensional differentiable manifold. Under certain conditions (see Ref. [274] for a review), a solvable[20] Lie group G can be divided by a lattice Γ, a discrete subgroup of G, to construct a compact solvmanifold (i.e. a twisted torus) by means of discrete identifications [275]. "Nilpotent"[21] groups are a special subclass of solvable groups. For them, the compactness criterion requires the structure constants to be rational in some basis [276]. We refer to their corresponding compact manifolds as "nilmanifolds".

Consider the d-dimensional Lie algebra $\mathfrak{g}$ generated by the vectors $\{Z_a, a = 1, ..., d\}$ satisfying

$$[Z_b, Z_c] = f^a{}_{bc} Z_a \, . \tag{5.1}$$

Here, the structure constants satisfy $f^a{}_{bc} = -f^a{}_{cb}$. The corresponding d-dimensional manifold admits a globally-defined orthonormal frame $\{e^a, a = 1, ..., d\}$ (where this basis defines the dual space of one-forms $\mathfrak{g}^\star$). This frame obeys the Maurer-Cartan equation

$$\mathrm{d}e^a = -\frac{1}{2} f^a{}_{bc} e^b \wedge e^c = -\sum_{b<c} f^a{}_{bc} e^b \wedge e^c \, , \tag{5.2}$$

with the exterior derivative d. Since the dual space $\mathfrak{g}^\star \approx T_e G^\star$, $\{e^a, a = 1, ..., d\}$ provides – by left invariance – a basis for the cotangent space $T_x G^\star$ at every point $x \in G$, the one-forms are globally defined on the manifold. These one-forms will have their non-trivial identification through the "lattice action" when G is divided by Γ. Note that $f^a{}_{bc}$ is related to the spin connection.

In flat indices and for a unimodular Lie algebra, the Ricci tensor is given by

$$\mathcal{R}_{cd} = \frac{1}{2}\Big(- f^b{}_{ac} f^a{}_{bd} - \delta^{bg}\delta_{ah} f^h{}_{gc} f^a{}_{bd} + \frac{1}{2}\delta^{ah}\delta^{bj}\delta_{ci}\delta_{dg} f^i{}_{aj} f^g{}_{hb}\Big) \, , \tag{5.3}$$

with δ_{ab} serving as a Euclidean metric. For the nilpotent algebra, and thus for the nilmanifold case, the first term vanishes. The Ricci tensor is thus nowhere-vanishing and the corresponding Ricci scalar emerges as

$$\mathcal{R} = -\frac{1}{4}\delta_{ad}\delta^{be}\delta^{cg} f^a{}_{bc} f^d{}_{eg} \, . \tag{5.4}$$

The Ricci scalar is strictly negative.

From Eq. (5.2), we can see that $d = 3$ is the lowest dimensionality for which this expression is non-trivially satisfied. For $d = 3$, there is the trivial Abelian algebra that leads to a three-torus, as well as three different solvable algebras. Of these, one is nilpotent: the "Heisenberg" algebra

$$[Z_1, Z_2] = -\mathtt{f} Z_3 \, , \quad [Z_1, Z_3] = [Z_2, Z_3] = 0 \, , \tag{5.5}$$

with $\mathtt{f} = -f^3_{12} \neq 0$ such that the Maurer-Cartan equation becomes

$$\mathrm{d}e^3 = \mathtt{f} e^1 \wedge e^2 \, , \quad \mathrm{d}e^1 = 0 \, , \quad \mathrm{d}e^2 = 0 \, . \tag{5.6}$$

The only nonzero structure constant $\mathtt{f} = -f^3{}_{12} \in \mathbb{R}$ is the "geometric flux" serving as the nilmanifold's "twist parameter". The corresponding geometric properties of the nilmanifold can be relayed through the

[20] A Lie group G is solvable if its Lie algebra $\mathfrak{g}$ terminates in the null algebra i.e. the sequence $\mathfrak{g}_0 = \mathfrak{g}$, $\mathfrak{g}_{n+1} = [\mathfrak{g}_n, \mathfrak{g}_n]$ for $n \geq 0$ reduces to the null algebra after a finite number of steps.

[21] A Lie group G is nilpotent if the sequence $\mathfrak{g}_{n+1} = [\mathfrak{g}, \mathfrak{g}_n]$ reduces to the null algebra after a finite number of steps.

Maurer-Cartan equation Eq. (5.6), from which we define

$$e^1 = r^1 \mathrm{d}y^1 \ , \ \ e^2 = r^2 \mathrm{d}y^2 \ , \ \ e^3 = r^3(\mathrm{d}y^3 + N y^1 \mathrm{d}y^2) \tag{5.7}$$

for the constant radii $r^{1,2,3} > 0$, angular coordinates $y^m \in [0,1]$, and the integer $N = r^1 r^2 \mathtt{f}/r^3$ [128].

The discrete identifications that make the compactification possible are

$$y^1 \sim y^1 + n^1 \ , \ \ y^2 \sim y^2 + n^2 \ , \ \ y^3 \sim y^3 + n^3 - n^1 N y^2 \ , \tag{5.8}$$

for $n^{m=1,2,3} \in [0,1]$. In other words, these identifications correspond to the lattice action responsible for establishing $\mathcal{N}_3$ as a nilmanifold. Eq. (5.8) leaves Eq. (5.7) invariant.

In this way, the compact manifold is fully characterised as a twisted S^1 fibration over layered tori T^2. The twist is along the fibre coordinate y^3, while the base is parameterised by the coordinates (y^1, y^2). Physically, $y^{m=1,2,3}$ are angles defined on $[0,1]$. The constant radii r^m have units of length, the coordinates y^m are dimensionless, and $\mathtt{f}$ has units of inverse length (i.e. energy).

The most general left-invariant metric for the nilmanifold is given by

$$\mathrm{d}s^2 = \delta_{ab} E^a E^b \ , \quad E^a = \left(L^{-1}\right)^a_{\ b} e^b, \tag{5.9}$$

where we use E^a to denote the one-forms related to the orthonormal basis e^a through the constant $GL(3,\mathbb{R})$ transformation L.

To demonstrate the construction of the scalar mass spectrum, we shall consider the simplified special case in which $r^m = 1$ and $\mathtt{f} = 1$. The nilmanifold metric then becomes

$$\mathrm{d}s^2_{\mathrm{nil}} = \delta_{ab} e^a e^b = (\mathrm{d}y^1)^2 + (\mathrm{d}y^2)^2 + (\mathrm{d}y^3 + y^1 \mathrm{d}y^2)^2 \ . \tag{5.10}$$

To understand the behaviour of a scalar field on this space, we consider the massive Klein-Gordon equation. Let us begin with the Laplacian

$$\nabla^2 \Phi = \frac{1}{\sqrt{g}} \delta_m \left(\sqrt{g} g^{mn} \delta_n \Phi\right) \ , \tag{5.11}$$

where the determinant $\sqrt{g} = r^1 r^2 r^2$ reduces to 1 in our simplified metric. We may write

$$\nabla^2 u = \left(\partial_1^2 + \left(\partial_2 - y^1 \partial_3\right)^2 + \partial_3^2\right) u \ , \tag{5.12}$$

as we shall consider the expansion of u on the space of functions invariant under Eq. (5.8), beginning with the functions depending only on the base coordinates (y^1, y^2). In this case, the Laplacian is easily diagonalised:

$$\left(\nabla^2 + \mu^2_{\beta,\gamma}\right) \tilde{v}_{\beta,\gamma} = 0 \ , \tag{5.13}$$

where we define

$$\tilde{v}_{\beta,\gamma}(y^1, y^2) = e^{2\pi i \beta y^1} e^{2\pi i \gamma y^2} \ , \tag{5.14}$$

for $\beta, \gamma \in \mathbb{Z}$, as invariant under Eq. (5.8), and the Klein-Gordon masses as

$$\mu^2_{\beta,\gamma} = 4\pi^2 \left(\beta^2 + \gamma^2\right) \ . \tag{5.15}$$

We can present a more generalised expression using the "Weil-Brezin-Zak" transforms [277] for a basis

of invariant functions $u_{\kappa,\lambda}$,

$$u_{\kappa,\lambda}(y^1,y^2,y^3) = e^{2\pi\kappa i(y^3+y^1y^2)}e^{2\pi\lambda i y^1} \times \sum_\sigma e^{2\pi\kappa\sigma i y^1} f(y^2+\sigma)\ , \tag{5.16}$$

for $\kappa,\lambda,\sigma\in\mathbb{Z}$. Since $u_{\kappa,\lambda}$ is invariant under Eq. (5.8) for all values of $f(x)$, the functions remain well-defined across our nilmanifold $\mathcal{N}_3$. Upon substituting Eq. (5.16) into Eq. (5.12), we obtain

$$\nabla^2 u_{\kappa,\lambda} = e^{2\pi\kappa i(y^3+y^1y^2)}e^{2\pi\lambda i y^1}\sum_\sigma e^{2\pi\kappa\sigma i y^1} \times \left[\partial_2^2 - 4\pi^2\left(\kappa^2+(\kappa(y^2+\sigma)+\lambda)^2\right)\right] f(y^2+\sigma)\ , \tag{5.17}$$

where we require that $\kappa\neq 0$ to retain the y^3-dependent terms.

If we introduce $z_\sigma = y^2+\sigma+\lambda/\kappa$ and $g(z_\sigma)=f(y^2+\sigma)$, we can rewrite the above Laplacian as

$$\nabla^2 u_{\kappa,\lambda} = e^{2\pi\kappa i(y^3+y^1y^2)}e^{2\pi\lambda i y^1}\sum_\sigma e^{2\pi\kappa\sigma i y^1} \times \left[\partial_{z_\sigma}^2 - (2\pi\kappa)^2\left(z_\sigma^2+1\right)\right] g(z_\sigma)\ . \tag{5.18}$$

From the normalised Hermite functions

$$X_\nu(z) = e^{-z^2/2}H_\nu(z)\ ,\quad \nu\in\mathbb{N}\ , \tag{5.19}$$

where H_ν represents the Hermite polynomials, we may define

$$X_\nu^\rho(z) = |\rho|^{1/4}X_\nu(|\rho|^{1/2}z) \tag{5.20}$$

for $\rho\in\mathbb{R}^*$ [277]. By the properties of Hermite polynomials, Eq. (5.20) satisfies the differential equation

$$(\partial_z^2-\rho^2z^2)X_\nu^\rho(z) = -(2\nu+1)|\rho|X_\nu^\rho(z)\ . \tag{5.21}$$

With the insertion of $g(z_\sigma)=X_\nu^{2\pi\kappa}(z_\sigma)$ into Eq. (5.18), we obtain the 3D Klein-Gordon equation

$$\left(\nabla^2+M_{\kappa,\lambda,\nu}^2\right)\tilde{u}_{\kappa,\lambda,\nu}=0\ , \tag{5.22}$$

where the masses and wavefunctions are, respectively,

$$M_{\kappa,\lambda,\nu}^2 = (2\pi\kappa)^2\left(1+\frac{2\nu+1}{2\pi|\kappa|}\right)\ , \tag{5.23}$$

$$\tilde{u}_{\kappa,\lambda,\nu}(y^1,y^2,y^3) = e^{2\pi\kappa i(y^3+y^1y^2)}e^{2\pi\lambda i y^1}\sum_\sigma e^{2\pi\kappa\sigma i y^1} \times X_\nu^{2\pi\kappa}\left(y^2+\sigma+\frac{\lambda}{\kappa}\right) \tag{5.24}$$

for $\sigma\in\mathbb{Z}$, $\nu\in\mathbb{N}$, $\kappa\in\mathbb{Z}^*$, and $\lambda=0,...,|\kappa|-1$. The range of λ is derived from the fact that λ itself is defined modulo κ, which in turn is a consequence of the identity

$$\tilde{u}_{\kappa,\lambda+\kappa\tau,\nu}(y^1,y^2,y^3) = \tilde{u}_{\kappa,\lambda,\nu}(y^1,y^2,y^3)\ \ \forall\ \tau\in\mathbb{Z}\ . \tag{5.25}$$

By virtue of Eq. (5.23)'s independence of λ, there exists a mass degeneracy. The wavefunctions are parameterised by a finite number of inequivalent values of λ such that the level of the degeneracy is $|\kappa|$. Note that only one zero-mode (i.e. with vanishing mass) exists for this Klein-Gordon equation, $\tilde{v}_{0,0}$, corresponding to the modes of the torus base.

We conclude this discussion on the nilmanifold space with the physical spectrum associated with a scalar field propagating on $\mathcal{N}_3$. This is achieved by reintroducing dimensional parameters r^m and $\mathtt{f}$ [128]. We may distinguish between "torus modes",

$$v_{\beta,\gamma}(y^1,y^2) = \frac{1}{\sqrt{V}} e^{2\pi i\beta y^1} e^{2\pi i\gamma y^2} , \tag{5.26}$$

$$\mu^2_{\beta,\gamma} = \beta^2 \left(\frac{2\pi}{r^1}\right)^2 + \gamma^2 \left(\frac{2\pi}{r^2}\right) , \tag{5.27}$$

and "fibre modes",

$$u_{\kappa,\lambda,\nu}(y^1,y^2,y^3) = \sqrt{\frac{r^2}{|N|V}} \frac{1}{\sqrt{2^\nu \nu! \sqrt{\pi}}} e^{2\pi\kappa i(y^3+Ny^1y^2)} \times e^{2\pi\lambda i y^1} \sum_\sigma e^{2\pi\kappa\sigma i y^1} X^\rho_\nu(w_\sigma) , \tag{5.28}$$

$$M^2_{\kappa,\lambda,\nu} = \kappa^2 \left(\frac{2\pi}{r^3}\right)^2 + (2\nu+1)|\kappa| \frac{2\pi\mathtt{f}}{r^3} , \tag{5.29}$$

for which we define

$$\rho = \frac{2\pi\mathtt{f}}{r^3}\kappa , \quad w_\sigma = r^2\left(y^2 + \frac{\sigma}{N} + \frac{\lambda}{N\kappa}\right) ,$$

and the volume

$$V = \int d^3y \sqrt{g} = r^1 r^2 r^3 . \tag{5.30}$$

The scalar spectrum on the nilmanifold contains a complete tower of modes on the torus that is independent of the fibre coordinate and radius. The fibre modes, whose mass spectrum is a function of the radial components and the curvature-related energy scale $\mathtt{f}$, have been shown to be tunable in Ref. [128] by varying parameters in the generalised case; the fibre modes can be made lighter than their toroidal counterparts and the energy gaps in the spectrum may be enhanced. From the structure of Eq. (5.29) itself, we understand that the fibre modes present with a unique mass spectrum: added to the typical $1/R$ KK term is the novel $\mathtt{f}$-dependent term that enforces more finely-spaced modes, which follow a linear Regge trajectory. From the characteristic fibre-mode spectrum, we would expect a unique experimental signature.

To see clearly the distinctive spectrum of the nilmanifold, let us compare the fibre-mode masses of Eq. (5.29) to the KK masses of a standard compactification $M_{st;\kappa,\lambda,\nu}$ on a three-dimensional torus $\mathbb{T}^3$,

$$M^2_{st;\kappa,\lambda,\nu} = \kappa^2 \left(\frac{2\pi}{r^1}\right)^2 + \lambda^2 \left(\frac{2\pi}{r^2}\right)^2 + \nu^2 \left(\frac{2\pi}{r^3}\right)^2 , \tag{5.31}$$

where $\kappa, \lambda, \nu \in \mathbb{Z}$. For simplicity we shall take all internal radii to be equal, $r^1 = r^2 = r^3$. Moreover we shall consider a nilmanifold $\mathcal{N}_3$ with minimal twist, $N = 1$. The ratio R of excited KK masses to the lowest-lying one is then independent of the size of the radii of the internal manifold. For $\mathcal{N}_3$, R^2_{nil} is given by

$$R^2_{nil} = \frac{M^2_{\kappa,\lambda,\nu}}{M^2_{1,0,0}} = \frac{2\pi\kappa^2 + (2\nu+1)|\kappa|}{1+2\pi} . \tag{5.32}$$

In contrast, for the standard $\mathbb{T}^3$, R^2_{st} is given by

$$R^2_{st} = \frac{M^2_{st;\kappa,\lambda,\nu}}{M^2_{st;1,0,0}} = \kappa^2 + \lambda^2 + \nu^2 \,. \tag{5.33}$$

Table 5.1: *Mass ratios R_{nil} for the 3D nilmanifold $\mathcal{N}^3$, corresponding to Eq. (5.32) for $\kappa = 1, 2$.*

ν	0	1	2	3	4	5	6	7	8	9	10
R^2_{nil} $(\kappa = 1)$	1.0	1.3	1.6	1.8	2.1	2.4	2.6	2.9	3.2	3.5	3.7
R^2_{nil} $(\kappa = 2)$	3.7	4.3	4.8	5.4	5.9	6.5	7.0	7.6	8.1	8.7	9.2

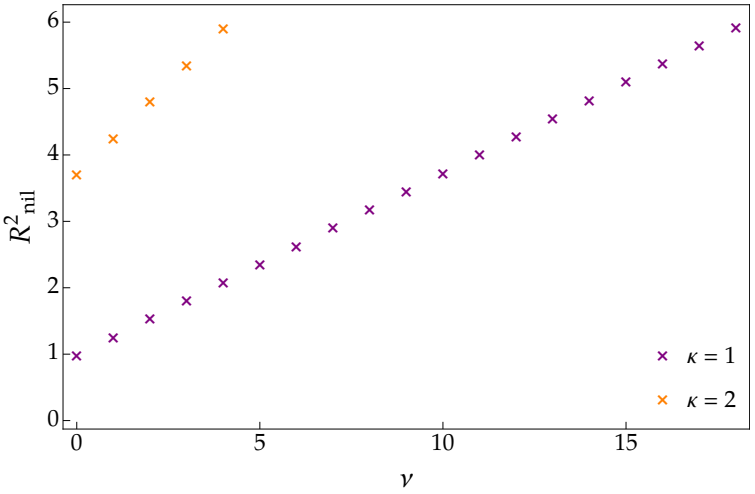

Figure 5.1: *Mass ratios $R^2_{nil} \leq 6$ corresponding to Eq. (5.32) for $\mathcal{N}_3$ for $\kappa = 1$ (purple) and $\kappa = 2$ (orange).*

Table 5.2: *Mass ratios R^2_{st} for the standard 3D torus $\mathbb{T}^3$, corresponding to Eq. (5.33).*

$(\kappa\lambda\nu)$	(100)	(110)	(111)	(200)	(210)	(211)
R^2_{st}	1	2	3	4	5	6

Since nilmanifolds allow for the possibility of analytically calculating the spectrum of propagating fields, they can be promising tools in the construction of effective BSM frameworks. Such models may be embeddable in string theory compactifications [128]. As mentioned in the introduction, recent investigations into GW signatures of compact extra dimensions predict observables at frequencies of the order of $10^{12} - 10^{14}$ Hz and higher [35, 37, 108, 109, 112, 113] – several orders of magnitude beyond the 10^4 Hz upper bound on modern detectors. However, these investigations suggest also that the KK GW spectrum is sensitive to changes in geometry. For example, introducing a non-trivial warp factor, as shown in Ref. [113], can lower the first KK mass by at least 69% as compared against the standard KK spectrum on a torus $\mathbb{T}^d$. This is promising for the high-frequency GWs in extra-dimensional frameworks, as the relationship between frequency and KK mass implies that lower KK mass corresponds to GW frequencies closer to the sensitivity of modern instruments.

In Figs. 5.1 and 5.2, we see a similarly encouraging behaviour when we compare the fibre-mode spectrum with that of the standard torus modes. While we centre this investigation on the feasibility of detection

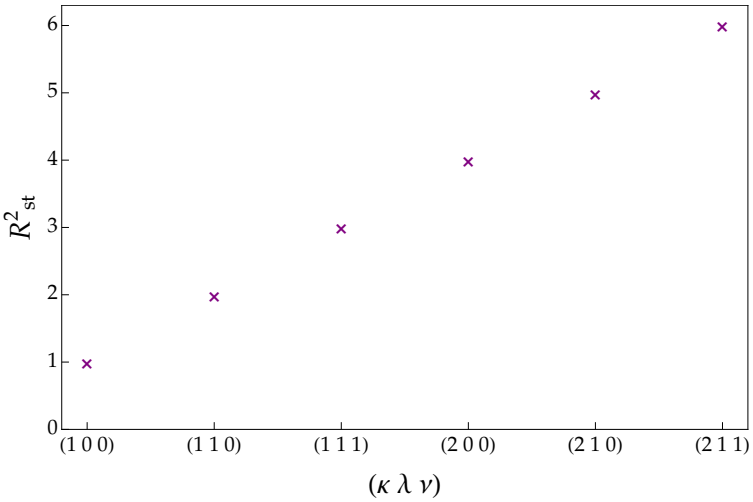

Figure 5.2: *Ratios* $R^2_{st} \leq 6$ *corresponding to Eq.* (5.33) *and Table* 5.2 *for* $\mathbb{T}^3$.

with present-day data from the LVK Collaboration, this effect motivates further investigation into the GWs propagating in nilmanifold spaces.

In the next section, we shall consider a case study for the investigation of black hole QNMs in an extra-dimensional setup constructed using the nilmanifold. Before we move on to this analysis, however, we include a brief aside on a toy dark matter model introduced in Ref. [128] that demonstrates how structures produced in this section can be incorporated into a BSM framework. While such a study is beyond the scope of this thesis, it is a useful illustration of the phenomenological applications of negative compact spaces.

5.1.1 Constraints from a dark matter model

In Ref. [128], a simplified dark matter model was set up as a proof of concept for the nilmanifold framework. There, a neutral scalar field singlet under the SM was allowed to propagate throughout the bulk while the 4D SM fields were confined to a point on the nilmanifold. For consistency, the setup requires an orbifold containing the singular points where the 4D brane supporting the SM fields can be localised. For this scalar field to be a dark matter candidate, a minimum requirement is that at least one additional symmetry is imposed upon the orbifold space: a dark matter parity under which KK modes are labelled, such that the lightest KK state serves as the dark matter candidate. The lightest KK state is odd under this parity, such that a decay to SM fields or zero modes is forbidden. The only coupling permitted between the bulk scalar field and the SM is via a Higgs portal coupling.

The symmetries of the nilmanifold space can be summarised as follows:

$$\begin{aligned} \text{orbifold:} \quad & y^1 \longleftrightarrow y^2\ ,\ \ y^3 \to -y^3 - N y^1 y^2\ ; \\ \text{dark matter parity:} \quad & y^{1,2} \longleftrightarrow -y^{1,2}\ ,\ \ y^3 \to y^3\ . \end{aligned}$$

As specified in Section 5.1, we focus on the fibre modes whose mass spectrum is defined in Eq. (5.23). Here, $k > 0$; for even (odd) k, we consider $0 < j < k/2$ ($0 < j < (k+1)/2$). For even k, the degeneracy of the mass spectrum is consistently $k/2$ for the dark matter-odd and dark matter-even states of both the orbifold-even and the orbifold-odd scalar fields. In the case of the odd k, the degeneracy is $(k+1)/2$ for dark matter-even states and $(k-1)/2$ for dark matter-odd states for both the orbifold-even and orbifold-odd fields. Following

Ref. [128], the fibre mode mass spectrum is expressed in terms of units of the torus radius $(r/2\pi)^2$ as

$$\mu_{KK}^2 = |N| \left(k^2 \xi + \frac{k(2p+1)}{2\pi} \right) , \qquad \xi \equiv \frac{1}{|N|} \left(\frac{r}{cr^3} \right)^2 . \tag{5.34}$$

Here, ξ is a dimensionless parameter and $N = r^1 r^2 \mathtt{f}/r^3$. There are dark matter-even and dark matter-odd states for all mass levels, except for $k = 1$: in this case, there are no dark matter-odd fibre modes. The lightest KK state is thus the dark matter-even mode for which $k = 1$, $j = p = 0$, and

$$\xi < \frac{2\pi - |N|}{2\pi |N|} . \tag{5.35}$$

If we set $N = 1$, $\xi = 0.84$ and $\mu = 0.9996$. The dark matter state lives in the dark matter-odd (i.e. $k = 2$, $j = p = 0$) fibre tier for

$$\xi < \frac{\pi - |N|}{4\pi |N|} , \tag{5.36}$$

where $\xi = 0.17$ for $N = 1$, and $\mu = 0.9992$. From Eq. (5.34), we understand that a dense spectrum of fibre states forms above a mass gap determined by the radius of the torus base, provided ξ is small (and/or r^3 is large). Since these states are lifted and the torus modes dominate for $\xi > 1$ [128], we avoid increasing ξ (i.e. decreasing r^3).

Let us look to some of the limits considered in the literature for the nilmanifold structure as it is set up in this work. In Refs [112, 113, 268], the "small fibre/large base" limit is presented with the intention of generating a hierarchy between the geometric flux $\mathtt{f}$ and the KK scales $1/r^m$ for $m = 1, 2, 3$ ($r^m > 0$). From the definition of $\mathtt{f}$, the approximation is proposed as

$$|N| r^3 \ll r^1 , \quad |N| r^3 \ll r^2 , \tag{5.37}$$

to suggest that the fibre along e^3 is much smaller than the toroidal base along the e^1, e^2 directions. The consequential hierarchy is then

$$|\mathtt{f}| \ll \frac{1}{r^1} , \quad \frac{1}{r^2} \ll \frac{1}{r^3} , \tag{5.38}$$

i.e. the energy scale generated by the geometric flux is light compared to the KK scale of the base, which is in turn light compared to the fibre KK scale. To that end, we consider $r^3 \gg r^1, r^2$.

We shall conclude our example here, and reserve a deeper investigation into the applications of the nilmanifold to such dark matter models for the future. In the next section, we shall consider the development of a "Schwarzschild-nilmanifold" metric and the perturbations thereof.

5.2 The effective 4D QNM problem

In combining the Schwarzschild metric with the nilmanifold metric of Eq. (5.10), we can construct our extra-dimensional manifold

$$ds_{7D}^2 = ds_{\rm BH}^2 + ds_{\rm nil}^2 . \tag{5.39}$$

In the absence of mixing terms, we consider a 7D scalar field propagating on this direct product space to be expressible as

$$\Psi_{n\ell m}^s(\mathbf{z}) = \sum_{n=0}^{\infty} \sum_{\ell,m}^{\infty} \frac{\psi_{sn\ell}(r)}{r} \, Y_{m\ell}^s(\theta, \phi) \, Z(y^1, y^2, y^3) \, e^{-i\omega t} . \tag{5.40}$$

To determine the QNM behaviour, we have shown that we may use the Klein-Gordon equation. Recall that the Laplacian of a product space is the sum of its parts, such that

$$\nabla^2\Psi(\mathbf{z}) = \left(\nabla^2_{\rm BH} + \nabla^2_{\rm nil}\right)\Phi^s_{n\ell m}(\mathbf{x})Z(\mathbf{y})\,. \tag{5.41}$$

However, if we choose to impose a KK reduction, we may encode the higher-dimensional behaviour through an effective mass term representing a KK tower of states. This allows us to formulate the 7D scalar field evolution as a 4D "massive" Klein-Gordon equation,

$$\frac{1}{\sqrt{-g}}\partial_\mu\left(\sqrt{-g}g^{\mu\nu}\partial_\nu\Psi\right) - \mu^2\Psi = 0\,, \tag{5.42}$$

where

$$\nabla^2_{\rm nil}Z(\mathbf{y}) = -\mu^2 Z(y^1, y^2, y^3)\,. \tag{5.43}$$

Using the derivative of the tortoise coordinate $dr_\star = dr/f(r)$, we extract the radial component of the QNM to produce a characteristic wave-like equation containing the QNF and the effective scalar potential,

$$\frac{d^2\psi}{dr_\star^2} + \left(\omega^2 - V(r)\right)\psi = 0\,, \tag{5.44}$$

where

$$V(r) = \left(1 - \frac{2M}{r}\right)\left(\frac{\ell(\ell+1)}{r^2} + \frac{2M}{r^3} + \mu^2\right)\,. \tag{5.45}$$

Eq. (5.45) exactly resembles the effective potential of the massive scalar QNM considered in Section 2.3. This proves advantageous, as it allows us to apply our knowledge of QNM techniques to the extra-dimensional problem at hand. However, recall also that the parameter space of μ is confined in the QNM context. Recall Fig. 2.4, in which we highlight that QNM behaviour is preserved provided the barrier potential remains intact. This places an upper bound on μ, such that $\Re e\{\omega^2\} > \mu^2$. For a scalar test field in the Schwarzschild black hole space-time, we therefore consider the bound from the semi-classical analysis to be $\mu \lesssim 0.6$.

We shall demonstrate in Chapter 6 how constraining μ can serve in our search for evidence of extra dimensions. As an aside, however, we first discuss the possible roles this mass-like term may play in various scenarios of new physics, reframing arguments from Section 2.3.

5.2.1 The interpretation of a mass-like term in the context of new physics

In Eq. (5.45), we demonstrate how a mass-like term incorporated into the effective QNM potential can be used as an artefact of the extra-dimensional submanifold, representing the KK tower of states on the compact space. This mass-like term results in QNM behaviour corresponding to that of a massive scalar test field. As addressed in Section 2.3, when considering massive bosonic fields in the region of an astrophysical black hole, the dimensionless parameter $M\mu$ acts as a scaling for the suppression of the instability timescale. Specifically, when the Compton wavelength of the perturbing field is of the order of the black hole's radius, the dimensionless parameter scales as $M\mu \sim 1$, leading to the strongest super-radiant instabilities [14, 47]. Recall also that a number of BSM conjectures depend on the existence of light or even ultralight particles (e.g. light scalars of mass $10^{-32} \leq m \leq 10^{-10}$ eV as in the "string axiverse" scenarios [191], dark or hidden photons, and other candidates [3]). For this reason, massive QNMs may be useful in complementary searches for a variety of exotic signatures.

Although we have positioned the extra-dimensional μ parameter as a component of the QNM potential, our next step is to connect it to parameters that are physical. To obtain a sense of magnitude of this term,

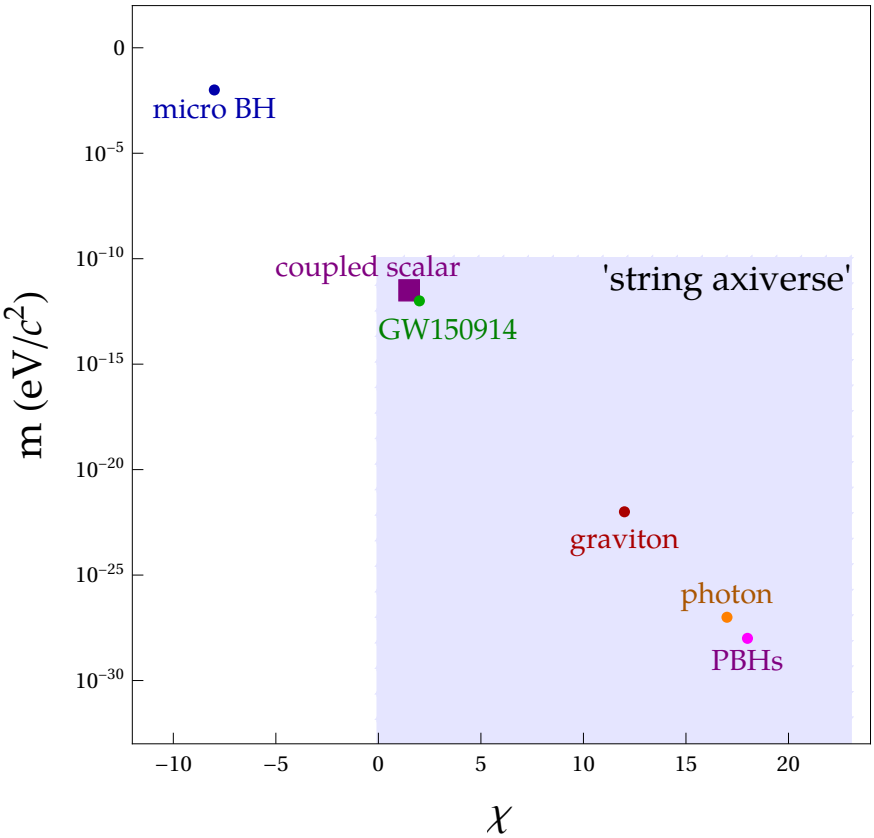

Figure 5.3: *An illustration of the scales probed by QNFs for* $M\mu \sim 1$ *using Eqs* (5.47) *and* (5.48).

recall that we can revert back to SI units such that the mass of the black hole and the μ parameter become

$$M = \frac{Gm^{\rm BH}}{c^2} \quad \text{and} \quad \mu = \frac{mc}{\hbar} \,. \tag{5.46}$$

From dimensional analysis, we can show that M and μ have dimensions of length and inverse-length, respectively, such that $M\mu$ is indeed dimensionless. It is straightforward then that

$$\begin{aligned} M\mu &= \frac{Gm^{\rm BH}m}{\hbar c} \\ \Rightarrow \quad m &= \frac{1}{m^{\rm BH}}\frac{\hbar c}{G}M\mu \,. \end{aligned} \tag{5.47}$$

With the values $\hbar c/G \sim 10^{-16}$ kg^2, $1M_\odot \sim 10^{30}$ kg, and $M\mu \sim \mathcal{O}(1)$, we can scale the black hole mass as $m^{\rm BH} = 10^{\chi}M_\odot$ and thereby express the extra-dimensional contribution through

$$m \sim 10^{-\chi}10^{-46}\text{kg} \sim 10^{-(\chi+10)}\text{eV/c}^2 \,. \tag{5.48}$$

We may use this expression to explore possible constraints. From the well-known mass limit for non-evaporating primordial black holes $m_{\rm PBH} \gtrsim 10^{15}$ g [40], $m \lesssim 10^{-28}$eV/c^2 such that $\chi \gtrsim 18$. On the other hand, $\chi \sim -8$ corresponds to a micro black hole of the same mass as the moon. For the $\sim 62M_\odot$ black hole remnant corresponding to the GW150914 event [43], $\chi \sim 2$.

We can also contrast this against the dynamical lower bound on the graviton Compton wavelength $\lambda_g \geq 10^{13}$ km, as determined by the LVK Collaboration at a 90% confidence (using null tests against the modified

dispersion relation of massive-graviton theory introduced in Ref. [278]). This in turn corresponds to the upper bound on the graviton mass $m_g \lesssim 10^{-22}$ eV/c^2 [60], which leads to the bound $\chi \gtrsim 12$.

As a visual aide, we sketch the magnitudes of m and χ in Fig. 5.3. We include the upper bounds for the photon mass [165] and the graviton [3], as well as the lower mass bound for massive primordial black holes [40]. We note that particles of these magnitudes correspond to those of the "string axiverse" scenarios [191].

In this chapter, we have considered an extra-dimensional setup comprised of a Schwarzschild black hole embedded in a 7D product space-time whose extra dimensions form a negative compact space − specifically, a nilmanifold built from Heisenberg algebra. By positioning the extra-dimensional contribution as an effective mass-like μ^2 term in the QNM potential, we have demonstrated that we can apply our experience in massive QNMs from Section 2.3) to place a possible upper bound on this μ. For the scalar test-field and Schwarzschild space-time background considered here, $\mu \lesssim 0.6$.

In the next chapter, we take this QNM analysis further by considering constraints we can extract from GW data. These shall be combined with our QNM computations of Section 2.3 to establish a rough sensitivity bound on observable QNFs to traces of new physics. To pursue this avenue of inquiry, however, we must first engage in a short overview of the data capturing, processing, and analysis strategies of the LVK Collaboration. For this reason, Chapter 6 begins with a pedagogical introduction to the Bayesian techniques favoured by the LVK Collaboration before focusing on the ringdown analysis tools and concluding with the extraction of the sensitivity bound on the QNF spectrum.

Chapter 6

Searching for extra-dimensions in gravitational-wave ringdown

> In physics, we live and breathe for discoveries like the one reported by LIGO, but the best is yet to come...
>
> Emanuele Berti in *The First Sounds of Merging Black Holes* [279]

On 14 September 2015, the twin LIGO detectors observed a GW transient signal GW150914; its false alarm rate was estimated to be less than 1 event per 203 000 years, equivalent to a significance of 5.1σ. The signal was consistent with the inspiral-merger-ringdown waveform of a binary black hole merger whose progenitor (source-frame) masses were $36.3^{+5.3}_{-4.5}\ M_\odot$ and $28.6^{+4.4}_{-4.2}\ M_\odot$, with a final black hole mass of $62.0^{+4.4}_{-4.0}\ M_\odot$. Approximately 3.0 $M_\odot$ of energy ($\sim 5.4 \times 10^{47}$ J) was radiated in the form of GWs, at a distance 1.4 ± 0.6 $\times 10^9$ light years ($\sim$ 410 Mpc) from Earth. The combined matched-filter SNR ratio (SNR) was a striking $\rho \sim 24$, with $\rho \sim 14$ for frequencies $f > 154.7$ Hz in the post-peak region [43, 114]. For these reasons, GW150914 is considered a "golden" event whose sufficiently high SNR allows for separate analyses of pre- and post-merger phases. As such, the first direct detection of GWs presents as an ideal candidate for studies of binary black hole dynamics and the nature of warped space-time under extreme conditions, a wide variety of tests of GR, and even searches for modifications to gravity [280].

For our purposes, this high post-merger SNR invites investigations centred on the ringdown phase, to which we can apply the QNM theory that we have outlined in Chapters 1 and 2 to the data captured by the LVK Collaboration. We are particularly interested in the possibility of finding evidence of new physics, where we focus on the extra-dimensional scenario of Chapter 5. However, to proceed along this line of inquiry, we must begin with a brief foray into the the methodology employed by the LVK Collaboration to capture, process, and analyse GW data. Specifically, we shall highlight this last point.

It is important to remember that the statistical analyses favoured by the LVK consortium is distinct from that used in collider-based experiments: while the frequentist approach dominates the latter, the former relies primarily on Bayesian techniques. In the frequentist picture, probabilities are based on repeated events collected over extended periods, such that probabilities are considered fixed and objective; in other words, probabilities are assigned to data rather than to models or hypotheses. Bayesian statistics, on the other hand, considers probabilities to be adaptable. The Bayesian approach acknowledges assumptions in the analysis by incorporating prior knowledge, and then updates hypotheses as additional data is collected. Data is then considered to be fixed and objective, and probabilities are assigned to hypotheses.

In the context of GW studies, the signal-processing method preferred is known as the "matched-filtering technique". It involves a correlation between a set of observed data and a bank of theoretical templates tuned with the appropriate source parameters to identify a GW signal. The technique itself is a subset of the "maximum likelihood" detection method, for which the likelihood function is maximised over the parameter space to find the best-fit parameters of the GW signal. In so doing, the SNR can be enhanced and the physical properties of astrophysical events can be extracted with greater precision. Furthermore, the matched-filtering technique was noted in Ref. [281] to be sensitive to post-Newtonian effects of the waveforms for coalescing binaries, making it ideal for analyses related to compact merger events.

Following the *modus operandi* of the LVK Collaboration, we shall briefly outline how the processing of deterministic GW signals with a Gaussian noise background is performed. We will then discuss the ringdown analysis tool that we employed in our work, *viz.* the Python package pyRing. Thereafter, we shall elaborate on the comparison made between our semi-classical QNM computation and our search for GR deviations in the ringdown data of GW150914, after which we shall conclude with the constraint we have determined on the application of QNMs in the search for new physics. Specifically, the objective of this chapter is to outline a means by which we can determine the sensitivity range of observable black hole QNMs to new physics.

6.1 Identifying and processing signals with the LVK network

GW detection operates on the principle of Michelson interferometry. For example, each of the twin LIGO detectors are arranged in an L-shaped configuration; each is made up of two perpendicular arms within ultra-high vacuum environments, terminating in carefully positioned and highly reflective mirrors. A laser beam is split and directed down each orthogonal arm, reflected, and recombined to form an interference pattern. Passing GWs introduce minute changes in the length of the path travelled, thereby altering the relative phases of the returning laser beams by as little as 10^{-18} m. Thanks to this precision, LIGO can detect GW strains of the order of 10^{-21}, over frequency ranges from 10 Hz to several kilohertz.

While GW detectors represent a triumph in both engineering and physics, the acquisition of GW data is made meaningful by the careful statistical interpretation thereof. In this section, we shall review how a GW signal is isolated from raw data, closely following the guide issued by the LVK Collaboration, Ref. [15].

6.1.1 Model comparisons: the matched filter

GW searches rely on the comparison between a null hypothesis $\mathcal{H}_0$ (claiming that the observed data represent only noise) and the signal hypothesis $\mathcal{H}_1$ that asserts the data detected contains both noise and a GW signal. The likelihood of observing data corresponding to each of these hypotheses is quantified as

$$p(\mathbf{d}|\mathcal{H}_0) = p_0(\mathbf{d}) \quad \text{and} \quad p(\mathbf{d}|\mathcal{H}_1) = p_1(\mathbf{d}) \tag{6.1}$$

Here, $\mathbf{d} = \mathbf{n} + \mathfrak{h}$: the sum of the GW response of the detector $\mathfrak{h}$ and all the noise sources in the detector $\mathbf{n}$ gives the time series $\mathbf{d}$ collected from the interferometer. To accommodate the fact that true GW signals in the detector are not known, $\mathbf{h} = \mathbf{h}(\boldsymbol{\theta})$ is used instead, which represents a signal model defined in terms of a set of parameters $\boldsymbol{\theta}$ (e.g. masses and spins of the binary black hole system).

One of the main quantities reported by the LVK Collaboration is the "posterior probability", which describes the probability of the signal hypothesis given the observed data,

$$p(\mathcal{H}_1|\mathbf{d}) = \frac{p(\mathcal{H}_1)p_1(\mathbf{d})}{p(\mathcal{H}_0)p_0(\mathbf{d}) + p(\mathcal{H}_1)p_1(\mathbf{d})} = \frac{p_1(\mathbf{d})}{p_0(\mathbf{d})}\left[\frac{p_1(\mathbf{d})}{p_0(\mathbf{d})} + \frac{p(\mathcal{H}_0)}{p(\mathcal{H}_1)}\right]^{-1}. \tag{6.2}$$

The values $p(\mathcal{H}_0)$ and $p(\mathcal{H}_1)$ denote our prior beliefs of whether, respectively, a signal is absent or present

within the data. The "likelihood ratio"

$$\Lambda(\mathbf{d}|\boldsymbol{\theta}) = \frac{p(\mathbf{d}|\mathcal{H}_1)}{p(\mathbf{d}|\mathcal{H}_0)} \frac{p_1(\mathbf{d})}{p_0(\mathbf{d})} , \tag{6.3}$$

is independent of prior beliefs, and is therefore considered an optimal test statistic. The log of the likelihood ratio is often presented in the literature,

$$\log \Lambda(\mathbf{d}|\boldsymbol{\theta}) = (\mathbf{d}|\mathbf{h}(\boldsymbol{\theta})) - \frac{1}{2}(\mathbf{h}(\boldsymbol{\theta})|\mathbf{h}(\boldsymbol{\theta})) . \tag{6.4}$$

From here, we obtain another optimal test statistic: the "matched filter" $(\mathbf{d}|\mathbf{h}(\boldsymbol{\theta}))$.

6.1.2 Signal-to-noise ratio and template banks

The parameters $\boldsymbol{\theta}$ are not known *a priori*. The optimal detection statistic must therefore be obtained by "marginalising" the likelihood ratio $\Lambda(\mathbf{d}|\boldsymbol{\theta})$ over the unknown parameters. This is achieved by integrating the likelihood ratio over the unknown parameters. Consider, for example, the inclination ι of the binary orbit relative to the line of sight for a compact binary GW source: the signal probability density over ι is uniform in $\cos\iota$.

As a linear function of the signal model, the exponential of the log likelihood ratio (i.e. the likelihood ratio itself) is sharply peaked about its maximum. For this reason, the maximum value of $\Lambda(\mathbf{d}|\theta)$ over the unknown parameters θ is expected to be a good approximation to the marginalised likelihood ratio (with the inclusion of a possible rescaling constant). The maximisation procedure is equivalent to minimising the residuals ($\mathbf{r} = \mathbf{d} - \mathbf{h}$) This becomes more clear when we write the log likelihood ratio as

$$\Lambda(\mathbf{d}|\theta) = -\frac{1}{2}\left[\mathbf{d} - \mathbf{d}(\boldsymbol{\theta})\right|\left(\mathbf{d} - \mathbf{d}(\boldsymbol{\theta})\right] + \frac{1}{2}(\mathbf{d}|\mathbf{d}) , \tag{6.5}$$

where we see that the parameters $\boldsymbol{\theta}$ that maximise the log likelihood ratio are those that minimise the residuals.

The parameter θ through which the observed strain in the detector is described represents the amplitude A observed in the detector (which is inversely proportional to the distance to the source of the GW), the phase ϕ is the sinusoidally-varying signal that is observed in the detector, the arrival time t of the signal (i.e. the moment the GW signal reaches its peak), and the set of physical parameters $\boldsymbol{\mu}$ to characterise the GW source (e.g. mass, spin, etc. of the components). These are related by

$$h(\boldsymbol{\theta}) = A\left[\mathbf{p}(t,\boldsymbol{\mu})\cos\phi + \mathbf{q}(t,\boldsymbol{\mu})\sin\phi\right] , \tag{6.6}$$

where $\mathbf{p}(t,\boldsymbol{\mu})$ and $\mathbf{q}(t,\boldsymbol{\mu})$ are waveforms that are, respectively, in-phase (cosine) and quadrature-phase (sine). These are normalised such that $(\mathbf{p}|\mathbf{p}) = 1 = (\mathbf{q}|\mathbf{q})$ and orthogonal to one another i.e. $(\mathbf{p}|\mathbf{q}) = 0$.

We maximise over the phase and the amplitude by substituting Eq. (6.6) into (6.4) to obtain

$$\log \Lambda(\mathbf{d}|\boldsymbol{\theta}) = A\rho(t,\boldsymbol{\mu})\cos(\phi - \varphi) - \frac{1}{2}A^2 , \tag{6.7}$$

for

$$\varphi \equiv \arctan\frac{(\mathbf{d}|\mathbf{q}(t,\boldsymbol{\mu}))}{(\mathbf{d}|\mathbf{p}(t,\boldsymbol{\mu}))} ; \tag{6.8}$$

$$\rho(t,\boldsymbol{\mu}) \equiv \sqrt{(\mathbf{d}|\mathbf{p}(t,\boldsymbol{\mu}))^2 + (\mathbf{d}|\mathbf{q}(t,\boldsymbol{\mu}))^2} . \tag{6.9}$$

This is the "SNR time series" for waveform templates with parameters $\boldsymbol{\mu}$ (i.e. the set of parameters of the

binary constituents, e.g. masses, spins, etc.). Log Λ, the log-likelihood, is maximised for the amplitude $\hat{A} = \rho$ and $\hat{\phi} = \varphi$, such that

$$\max_{A,\phi} \log \equiv \log \Lambda(t, \hat{A}, \hat{\phi}, \boldsymbol{\mu}) = \frac{1}{2}\rho^2(t, \boldsymbol{\mu}) \, . \tag{6.10}$$

Times for which the signal is most likely to be present are indicated by peaks in the time series.

The parameters represented by $\boldsymbol{\mu}$ affect the morphology of the GW. To accommodate the wide range of possible masses, spins, etc. that a binary system might present, a "bank" of signal templates spanning the parameter space is produced, and each template in the bank can then be used as a matched filter. A condition specified in Ref. [15] for the template bank used in the signal search is that its density in parameter space is sufficiently high such that the loss in SNR between a true signal and the best-fit template is no more than 3%.

6.1.3 Inferring waveforms and physical parameters

Since GW signals are notoriously weak, the uncertainties in the physical parameters of the system whence the signal emerged can be large. This necessitates *a priori* assumptions about the amplitude and phase of the GW signals, which in turn affects the reconstruction efforts. This motivates the use of "Bayesian parameter estimation" in GW analyses, which allows for the inference of a GW signal waveform based on physical parameters of the system and the background. Specifically, we may apply Bayes' theorem to define the "posterior probability density function" i.e. the posterior for $\boldsymbol{\theta}$,

$$p(\boldsymbol{\theta}|\mathbf{d}, M, I) \equiv p(\boldsymbol{\theta}|M, I)\frac{p(\mathbf{d}|\boldsymbol{\theta}, M, I)}{p(\mathbf{d}|M, I)} \, . \tag{6.11}$$

Here, M is the GW signal model constructed from the physical parameters of the system $\boldsymbol{\theta}$ that allows for the waveform prediction, I is the background or "prior" information, and $\mathbf{d}$ is the set of observed data. Three terms are introduced through this expression: the "prior probability density function" $p(\boldsymbol{\theta}|M, I)$, the "likelihood function" $p(\mathbf{d}|\boldsymbol{\theta}, M, I)$, and the "evidence"

$$p(\mathbf{d}|M, I) = \int d\boldsymbol{\theta} p(\boldsymbol{\theta}|M, I) p(\mathbf{d}|\boldsymbol{\theta}, M, I) \, . \tag{6.12}$$

The Bayesian parameter estimation used by the LVK Collaboration centres on the computation of the posterior for $\boldsymbol{\theta}$ from the model M and the analysis assumptions I, from which the prior distribution and the likelihood function may be uniquely determined.

Let us first consider the latter. The signal model M determines the functional form of $h(t; \boldsymbol{\theta})$ necessary for the calculation of the likelihood function; the parametric forms of $h(t; \boldsymbol{\theta})$ are computed by solving Einstein's equations. Since exact analytical solutions are not easily obtained, the models used are based on perturbative solutions (e.g. "Taylor" family of waveforms), effective-one-body approximations, or phenomenological approaches (e.g. the "Phenom" family of waveforms). The latter two employ full inspiral-merger-ringdown modelling and are particular popular in GW studies. In the case of GW150914, `SEOBNRv2`[22] and `IMRPhenomPv2`[23] were appropriate and effectively equivalent choices for the GW data analysis as the binary system was approximately "face-off" i.e. with the orbital angular momentum vector pointing away from the Earth.

The former refers to the prior probability distributions for the physical parameters required to characterise the GW signal emergent from the coalescing binaries. If we consider a quasicircular orbit, there are 15

[22] Spin-aligned effective-one-body numerical-relativity model that models the dynamics of spin vector components along the direction of orbital angular momentum.

[23] Models precessing binaries, based on inspiral-merger-ringdown model `IMRPhenomD` – which models spinning, but non-precessing, binaries. `IMRPhenomPv2` takes into account the in-plane spin vector components, as well as those along the direction of the orbital angular momentum.

parameters [11, 15] are required to describe fully the coalescence within a GR framework. These can be subdivided into "intrinsic parameters", *viz.*

- ⋆ the masses of the coalescing bodies M_1 and M_2 (where $M_1 \geq M_2$, by convention);
- ⋆ the spin vectors $\vec{S}_1$ and $\vec{S}_2$.

Then we have the "extrinsic parameters",

- ⋆ a reference time t_c (typically associated with the peak of the GW strain) and phase ϕ_c;
- ⋆ the sky position of the binary, in terms of the source's right ascension α and declination δ;
- ⋆ the luminosity distance d_L;
- ⋆ the binary's orientation, described through the its inclination ι and its polarisation angle ψ.

We can also introduce the angle θ_{jn} between the total angular momentum $\vec{J}$ and the direction in which the GW propagates $\hat{n}$. Furthermore, there is the total source mass $M = M_1 + M_2$, the dimensionless symmetric mass ratio $\nu = (M_1 + M_2)/M$, and the mass ratio $q = M_1/M_2 \geq 1$. Finally, we must also take into account the detector masses, $M_1^{det} = (1+z)M_1$ and $M_2^{det} = (1+z)M_2$, where z is the redshift. Note that if the black holes have spins aligned or anti-aligned with the orbital angular momentum, only 11 parameters need to be considered. In such a case, we define $\chi_i = |\vec{S}_i|/M_i^2$ for $i = 1, 2$.

A number of these "priors" are defined according to symmetries of the parameter space. Notable examples include the priors d_L, α, and δ. From the Friedmann-Lemaître-Robertson-Walker model, we understand that the number density of GW sources is uniform in the cosmological co-moving volume. As such,

$$p(D_L, \alpha, \delta | M, I) \propto dV$$

reduces to

$$p(D_L, \alpha, \delta | M, I) \propto D_L^2 |\cos(\delta)|$$

for redshift $z \ll 1$. When we cannot apply invariance arguments, we opt for forms of priors that produce the most easily interpretable results. For the spin vectors $\vec{S}_1$ and $\vec{S}_2$, as well as the orientation angles ψ and θ_{jn}, priors are chosen such that these remain uniform for the azimuthal angles on $[0, 2\pi]$ and the cosine of the polar angle $[-1, 1]$. Several options are available for the magnitude of the spin vectors, such as $p(|\vec{S}_i| \mid M, I) \propto |\vec{S}_i|^2$ or $p(|\vec{S}_i| \mid M, I) \propto 1$. For the components of the coalescing binaries, $p(m_1, m_2 | M, I) \propto 1$, with a lower bound of $m_1, m_2 > 1M_\odot$.

We know that 15 (11) physical parameters must be inferred for quasicircular binary systems with spin vectors left unspecified (aligned with the orbital angular momentum). However, an additional $\mathcal{O}(10)$ parameters per detector must be considered when performing GW analyses in order to define the calibration uncertainty model needed to account for uncertainties in each detector's phase and amplitude response. For the LIGO-Virgo system currently in use, this gives a total of 45 parameters that must be sampled. A parameter space of such high dimensionality requires techniques beyond grid-based methods to be explored. Instead, we use the stochastic sampler library `LALInference` [282] that implements both the the parallel tempering Markov chain Monte Carlo[24] algorithm and a nested sampling[25] algorithm.

The output of the `LALInference` analysis are samples from the full posterior distribution for the parameters that characterise the GW waveform. To establish the nature of the components of the coalescing binary system, the focus is placed on the masses and spins (i.e. the "intrinsic" parameters).

Let us consider the binary black hole collision GW150914, the properties of which were published by LIGO in Ref. [114]. From Ref. [19], the constituent source-frame masses measured using a joint waveform model comprised of equal numbers of samples from `IMRPhenomPv2` and `SEOBNRv3` were $M_1 \sim 35.6M_\odot$ and

[24] generates samples from a multidimensional posterior distribution Eq. (6.11) [283]
[25] calculates Eq. (6.12), generating samples from the posterior distribution as a by-product [284]

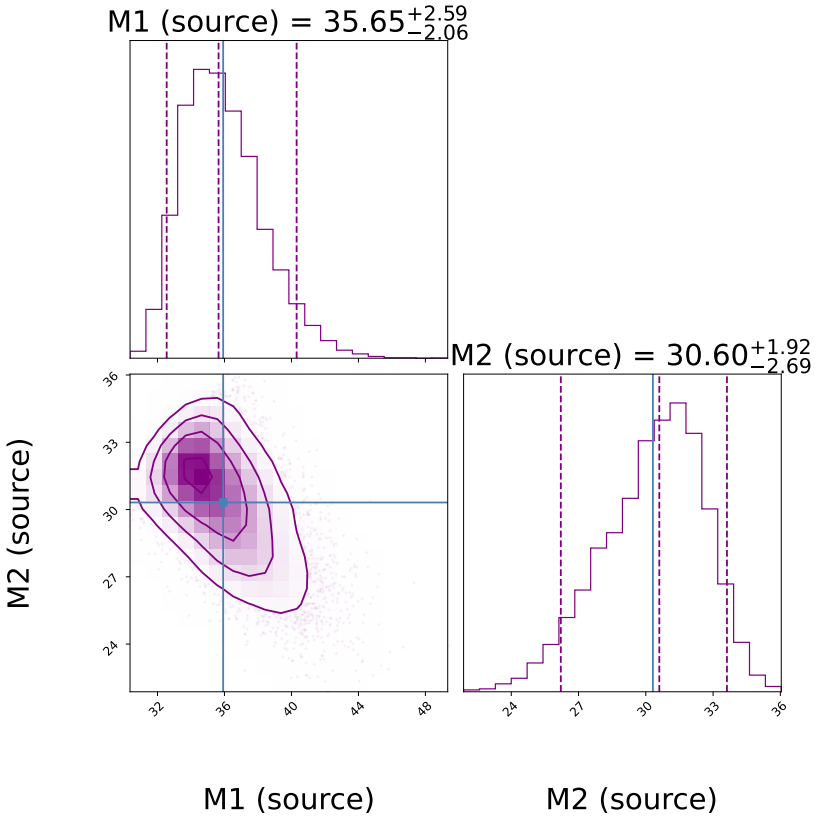

Figure 6.1: *1D and 2D marginal posteriors for source-frame masses, using O1 posterior samples.*

$M_2 \sim 30.6 M_\odot$. To determine M_1, for example, a marginalisation procedure is carried out over 14 of the 15 physical parameters, as well as the calibration parameters, to obtain a one-dimensional posterior distribution plot (see the top panel of Figure 6.1), from which the 90% credible region is then calculated. The same is performed for M_2 in the far-right panel of Figure 6.1. To establish a correlation between parameters, multidimensional posterior distributions can be plotted, as shown in the central panel of Figure 6.1. Dashed lines and contours indicate the 90% credible region while solid blue lines represent the mean.

With the fundamentals of GW analyses covered, we now turn specifically to the study of the ringdown phase in the wake of a binary black hole collision. To do so, we make use of one of the few tools dedicated to QNM analyses of GW data: the Python package PyRing [119, 123].

6.2 Using PyRing to search for deviations in GR

Within the GW community, searches for modified theories of gravity consider how GW signals may differ from those of GR in terms of their generation, propagation, and polarisation [58–60]. In the case of massive gravity theories, for example, it is well understood that additional polarisation states must be considered to describe the extra degrees of freedom. While GR has only two tensor modes (i.e. plus h_+ and cross $h_\times$ modes), a generalised metric theory of gravity can accommodate up to six polarisation modes: two tensor, two vector, and two scalar modes [285, 286]. Similar effects can be seen in extra-dimensional setups e.g. Ref. [35]; in such cases, however, these can often lie far beyond detectable range [37, 108]. The situation is complicated further by the known difficulty in relating these null tests to one another [287]. For these reasons, we suggest a new avenue of pursuit by which to probe extra dimensions within extant GW data,

inspired by tests for deviations from GR within the post-merger phase [59, 60].

PyRing was recently developed to perform Bayesian parameter estimation and ringdown studies through a combination of observed GW data with simulation and numerically-generated waveform templates, following the Bayesian framework detailed in Ref. [15]. Using a reference time t_0 computed directly from an approximation of the peak of the strain $(h_+^2 + h_\times^2)$, PyRing is focused exclusively on analyses of the post-merger signal through a native time-domain likelihood formulation. The software is fully integrated into the LVK infrastructure, where it serves as a vital component of hierarchical tests of GR covered in Refs [59, 60]. Treating GR as the null hypothesis, PyRing tests for deviations from the QNF oscillation frequency $(\Re e\{\omega\} = \omega)$ and decay timescale $(1/\Im m\{\omega\} = \tau)$ at the linear level,

$$\begin{aligned} \delta\omega &= \omega^{\rm GR}(1+\delta\omega)\ , \\ \delta\tau &= \tau^{\rm GR}(1+\delta\tau)\ . \end{aligned} \tag{6.13}$$

Here, we run an agnostic test of GR deviation in GW data from the GW150914 black hole merger event [43] using the provided Kerr_{220} waveform template corresponding to the $\ell = m = 2$, $n = 0$ mode (see Fig. 6.2). The analysis through PyRing is conducted using the publicly-available data from the LVK Collaboration [288]. To reduce computational cost, we employ medium-resolution data, simplified noise estimation, and simplified sampler settings, as well as tight priors. Specifically, we follow Ref. [119] in sampling 4096s of data from the Hanford and the Livingston LIGO detectors, sampled at 4096 Hz with the raw strain band-passed over $f \in [20, 2028]$ Hz before being split into 2-second noise chunks. We set the trigtime in H1 to $t = 1126259462.423227$ s in GPS time.[26] We run the analysis over prior bounds for final mass $M_f \in [50.0, 90.0]\ M_\odot$, spin $a_f \in [0.6, 0.9]$, amplitude $A_{220} \in [0.0, 5.0 \times 10^{-20}]$, and phase $\phi_{220} \in [0, 2\pi]$. In testing for deviations from GR, we sample over $\delta\omega, \delta\tau \in [-1, 1]$.

To carry out its Bayesian inference, PyRing exploits the nested sampling algorithm of cpnest [284, 289]. The package's implementation is based on an ensemble Markov chain Monte Carlo (MCMC) sampler, for which we only need to input the specifics of the analysis. We use 2048 live points and set the maximum MCMC steps to 2048, with the default 1234 seeds; at the end of the analysis, we are left with $\sim$ 8000 independent samples. We visualise these results in Fig. 6.2. With Corner, we plot the 2D posteriors and 1D histograms on $(\delta\omega, \delta\tau)$, where $(0, 0)$ is the GR-predicted value. Dashed lines and contours demarcate the 90% credible region; the blue line indicates the mean. Pixelation is an unfortunate consequence of the narrow priors we have chosen, in an effort to reduce computation cost.

Our rudimentary analysis serves primarily as a proof-of-concept. Due to its focus on a single event and the loss of precision caused by the narrow priors, its results cannot serve as definitive evidence of deviations from GR. In fact, it is well known that GR remains the favoured hypothesis in all tests against gravity performed to date [3]. However, since the broader objective of this study is to examine the efficacy with which QNMs can be used in the search for evidence of new physics, we rely on the joint constraints reported by the latest series of test for GR deviations reported by the LVK Collaboration, *viz*.

$$\begin{aligned} \delta\omega_{220} &= 0.02^{+0.07}_{-0.07}\ , \\ \delta\tau_{220} &= 0.13^{+0.21}_{-0.22}\ . \end{aligned} \tag{6.14}$$

These joint constraints represent a hierarchical combination of the LVK Collaboration's strongest bounds on GR deviations to date, using the ringdown data of 21 events whose Bayesian evidence parameter favours the presence of signal over pure Gaussian noise when the most sensitive Kerr template is utilised (see Refs [19, 59] for detailed selection criteria). While the combined log odds ratio of -0.90 ± 0.44 at 90% uncertainty indicate that the null hypothesis of GR is favoured, we shall make use of Eq. (6.14) in the next section to indicate how statistically-significant deviations from GR could be exploited in the future.

[26] The "trigtime" is an estimate of the coalescence time of the signal. The time given here corresponds to 14 September 2015, 09:50:45 UTC, the merger time reported in Ref. [43]. See also the GW150914 data release page.

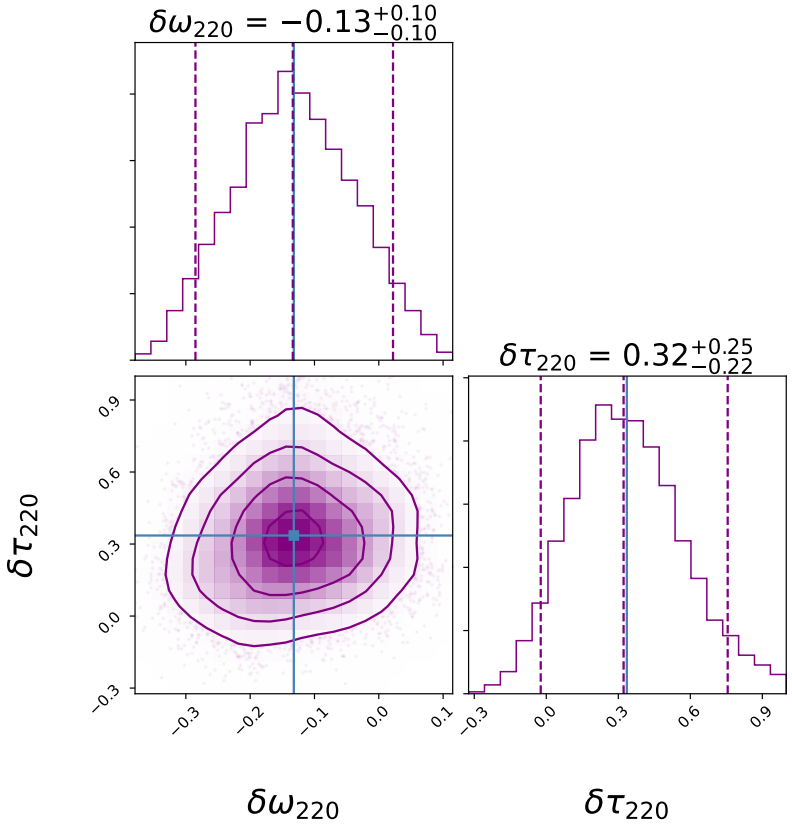

Figure 6.2: *A rudimentary parameter estimation of GR deviations using PyRing for event GW150914.*

6.3 Constraints from GWs using QNMs

In this section, we combine our semi-classical study of the massive QNM problem with our tests for deviations in GR. To create a correspondence between the two, we consider $\omega = \Re e\{\omega\}$ and the damping time $\tau = 1/\Im m\{\omega\}$ as $\omega = \omega^{\mu=0}(1+\delta\omega)$ and $\tau = \tau^{\mu=0}(1+\delta\tau)$, respectively. In other words, we interpret our $\mu = 0$ results to be equivalent to the GR prediction $(\delta\omega, \delta\tau) = (0,0)$ i.e. $\omega^{\rm GR} = \omega^{\mu=0}$. Our results for the semi-classically generated parametric deviations are provided in Table 6.1. We observe that the parametric deviations match the bounds predicted in Eq. (6.13) for $\mu \sim 0.2$.

If we exploit the QNF series expansion provided in Eq. (2.52), we can solve for μ explicitly. In doing so (for the real part and using the dominant $\ell = 2$, $n = 0$ mode), we find that we can impose the upper bound

$$\mu \lesssim 0.3681\ . \tag{6.15}$$

This serves as an upper bound on the sensitivity of QNFs to extra-dimensional KK resonances, as constructed in this framework. Using Eq. (5.47), we can explore the physical insights that can be extracted from this limit.

Since we have set $M = 1$, we can interpret this as a bound on the dimensionless parameter $M\mu$. As such, $M\mu \sim \mathcal{O}(0.1)$. Then for the final $M \sim 62M_\odot$ black hole remnant of GW150914, $\chi \sim 3$. This leads to the upper bound on the QNF probe,

$$m \lesssim 10^{-13}\text{eV}/\text{c}^2\ . \tag{6.16}$$

In other words, we observe that applying static black hole QNFs as a direct probe into an agnostic extra-dimensional model demonstrates that QNFs cannot detect KK masses beyond roughly $m \sim 10^{-13}\text{eV}/\text{c}^2$. We

Table 6.1: *QNFs computed with the Dolan-Ottewill method as parametric deviations from GR*

μ	$\omega(\ell, \mu)$	$\delta\omega$	$\delta\tau$
0.0	$0.4836 - 0.0968i$	0.0000	0.0000
0.1	$0.4868 - 0.0968i$	0.0065	0.0113
0.2	$0.4963 - 0.0924i$	0.0262	0.0473
0.3	$0.5124 - 0.0868i$	0.0594	0.1149
0.4	$0.5352 - 0.0787i$	0.1066	0.2302
0.5	$0.5653 - 0.0676i$	0.1687	0.4306
0.6	$0.6032 - 0.0532i$	0.2472	0.8206
0.7	$0.6500 - 0.0343i$	0.3440	1.8181

note that particles of this mass correspond to light scalar hypotheses rather than the TeV-scale KK masses of typical extra-dimensional conjectures [3]. Additional examples are illustrated in Fig. 5.3 and the surrounding discussion.

However, there are a number of improvements that could be made to this preliminary study that may lead to more stringent bounds, particularly in the application to other BSM scenarios. For example, we would expect minor corrections from the use of the more astrophysically-relevant Kerr black hole space-time and gravitational QNFs; this would be necessary for greater precision than the order-of-magnitude study conducted in this work. More significantly, we recognise that this investigation was limited by the need to adopt an agnostic approach to our pursuit of evidence of extra dimensions. As the LVK Collaboration develops more sophisticated and model-specific ringdown templates to test for parametric deviations in GR, it would be interesting to observe how theoretical frameworks can be adapted to the question of searches for extra-dimensional signatures in GWs.

A further point to consider is the application of our search for extra-dimensional signatures to other GW experiments. Recall that massive fields are short ranged; from Section 2.3, the relationship between field mass and Compton wavelength suggests that there is an effective observational cut-off at a distance which is related to the Compton wavelength of the field. The observational window exists only when the mass is very small and the wavelength is thus very large. As illustrated in Ref. [290], pulsar timing array observations by the likes of NANOGrav are sensitive to long-wavelength GWs (see Section 1.1), and therefore could be sensitive to the extra-dimensional signatures generated in our Schwarzschild-nilmanifold setup.

In this chapter, we have explored the analysis techniques employed by the LVK Collaboration, in order to provide a context for our study as well as to understand how QNMs are treated within the domain of GW astronomy. In so doing, we have demonstrated that combining GW considerations with the numerical approach to QNF calculations can lead to more stringent limits on the BSM parameter space that can be explored. With this, we conclude our investigation into the QNMs of extra-dimensional scenarios.

Chapter 7

Conclusions

Within this thesis, we have explored the applications of black holes and their perturbations in the search for a deeper understanding of fundamental physics as well as for evidence of new physics. As our investigations developed, we found that QNMs could be applied in several contexts: the more familiar, such as superradiance and instability, as well as the more formal case of cosmic censorship and the exotic case of detecting extra dimensions. In the spirit of GW astronomy, we have used QNFs as windows into different physical phenomena.

For this reason, we began with an investigation into the scalar QNMs of a Schwarzschild black hole space-time. This is the simplest black hole space-time in GR, with the scalar field acting as a proxy for the full non-linear gravitational field. First we studied the effect of field mass on the QNF spectrum. This demonstrated how mass can drive QNFs into the "quasiresonance" regime: beyond a certain field mass, QNFs become arbitrarily long-lived and lose their QNM character. From Fig. 2.4, it can be seen that the corresponding effective potential becomes suppressed; the potential barrier is made flat. We found that this occurred for $\mu \gtrsim 0.6$ when $\ell = 2$ and $n = 0$.

Moreover, massive QNFs display "anomalous" QNM behaviour for masses below a critical mass μ_{crit}, first shown here in Fig. 2.7. Recall that for scalar QNMs in a spherically-symmetric space-time, it is expected that $|\mathfrak{Im}\{\omega\}|$ scales with ℓ [14, 47]. However, this relationship was only observed for heavier modes in Fig. 2.7. This same "anomalous" behaviour for $\mu < \mu_{crit}$ was observed in the charged black hole case, provided $q = 0$ for the scalar field charge. For example, in Fig. 4.6, $|\mathfrak{Im}\{\omega_{\ell=10}\}| > |\mathfrak{Im}\{\omega_{\ell=30}\}|$ for lower values of μ and $|\mathfrak{Im}\{\omega_{\ell=10}\}| < |\mathfrak{Im}\{\omega_{\ell=30}\}|$ for larger values of μ. In other words, only past μ_{crit} do we observe "regular" QNF behaviour.

To embark on a more in-depth investigation into the relationships between space-time parameters (black hole mass M, black hole charge Q, and the cosmological constant Λ) and field parameters (scalar field mass μ, scalar field charge q, and multipolar number ℓ), we elevated our discussion to the case of a charged scalar QNM in the RNdS space-time. In so doing, we determined the maximum black hole mass for which a μ_{crit} exists in the case of massive charged scalar QNMs, at point N of Fig. 3.2 (i.e. $(M, Q, \Lambda) = (1/\sqrt{27}, 0, 1)$) corresponding to the uncharged Nariai solution. We have found that hole mass scales inversely with μ_{crit}: for $M \sim 0$, $\mu_{crit} \sim 20$ whereas for the maximum $M \sim 1/\sqrt{27}$, we obtained the minimum $\mu_{crit} \sim 1.4$. For fixed values of M and Q, the value of μ_{crit} decreases as we increase q.

From our analysis of the evolution of the potential within the phase space, we found that a barrier potential characteristic of QNM behaviour was shown to exist on the domain of the black hole exterior $r_+ < r < r_c$ for $\ell > 0$ (with the "valley" suggestive of superradiant amplification suppressed or lying beyond the cosmological horizon $r = r_c$). The only exception to this could be found in extremised regions of the RNdS parameter space, where the coalescence of horizons suppressed the potential (i.e. Figs 4.2 and 4.3) and the $\ell = 0$ case (see Fig. 4.1, where the "valley" falls within $r_+ < r < r_c$). With this in mind, we considered the use of a WKB-based method for our computations of the QNFs within the RNdS space-time to be accurate

enough to depict the trends in QNM behaviour, the goal of this investigation.

Finally, we note that in Section 3.3, the condition for the preservation of SCC was violated near $M \sim Q \sim 0.089$. For non-zero μ, black holes "colder" than the cosmological horizon were associated with SCC violations. In fact, this question of whether large, cold black holes respect cosmic censorship has recently been investigated in Ref. [257], where it was found that near-extremal charged black holes may collapse into naked singularities during photon emission. This certainly invites further study, particularly concerning the possible constraints we can consequentially apply to the black hole and the photon emitted, as well as the possible implications this may have for SCC preservation.

In our final investigation, we have considered a novel extra-dimensional setup comprised of a Schwarzschild black hole embedded in a 7D product space-time whose extra dimensions form a nilmanifold built from Heisenberg algebra. We have pursued a strategy for an extra-dimensional search using QNFs. By positioning the extra-dimensional contribution as an effective mass-like μ^2 term in the QNM potential, we have demonstrated through a numerical study a possible upper bound on this μ. For the scalar test-field and Schwarzschild space-time background considered here, $\mu \lesssim 0.6$.

Then, by using searches for parametric deviations from GR, we further constrain this probe to $\mu \lesssim 0.3681$. Via Eq. (5.47), we demonstrate that this corresponds to $m_{KK} \lesssim 10^{-13}\mathrm{eV/c^2}$. The limit provided in Eq. (6.15) can therefore be interpreted as a detectability bound on the QNM probe into extra dimensions. In other words, with currently available signals, we find that KK masses higher than roughly $m_{KK} \sim 10^{-13}\mathrm{eV/c^2}$ cannot be detected with QNMs.

Taking into account the limitations of present-day GW astronomy and the available LVK infrastructure, we have restricted our study, using dimensional analysis to determine an estimate on QNF sensitivity to new physics. As the LVK Collaboration develops more sophisticated and model-specific ringdown templates to test for parametric deviations in GR, it would be interesting to observe how theoretical frameworks can be adapted to the question of searches for extra-dimensional signatures in GWs.

A further open question is to what extent can we apply such constraints to place bounds on the size and number of extra dimensions. For example, a next step for this study could be to subject the mass spectrum of the toy dark matter model studied in Ref. [128] to this result in order to extract tangible bounds on the radius of the nilmanifold extra dimensions herein constructed. Moreover, a detailed investigation of the propagation of GWs in nilmanifold spaces is reserved for a future work.

As acknowledged in Ref. [60], there has been substantial progress in GW research from the analytical, numerical, and experimental fronts. GW phenomenology and our ability to perform precision-level testing of GR, however, are still in their infancy. It is our hope that the simple setup we have provided here may be refined as our understanding of the applicability of GW detection in fundamental physics grows, bringing these tests to a new level of accuracy.

Appendix A

Philosophical and mathematical preliminaries on cosmic censorship

Recall that a well-defined theory is predictable and deterministic. This innocuous statement, often an implicit assumption in our scientific thinking, has been the source of ongoing debate within the spheres of physics and philosophy alike. Through the Laplacian view of the universe [291], Werndl argues in Ref. [292] that determinism is an ontological position while predictability is an epistemological one. In other words, determinism is an inherent quality of the state, while predictability is our description of the state which is confirmed retrospectively by our observations of the evolution of the state. Determinism is the requirement that it evolves uniquely: the properties of a state are a direct consequence of its past and serve as the cause of its future. This can be considered a fundamental axiom in quantum mechanics, for example. Predictability, on the other hand, is a close cousin of reproducibility: it is the requirement that this unique evolution can be accurately described by the theory in place. Chaotic systems are then fine examples of deterministic models that are unpredictable.

Within the context of GR, the integrity of determinism is called into question when we consider a black hole interior within which a Cauchy horizon can be found [293, 294]. It is this question of determinism that serves as the underlying principle of the SCC conjecture. Particularly among mathematicians, the argument concerns the evolution of the metric over the Cauchy horizon and the regularity conditions that must be satisfied for the corresponding equations of motion to make sense. To understand the evolution of these partial differential equations and how regularity conditions influence the preservation of SCC, the massless scalar field serves as a convenient proxy for the full non-linear Einstein field equations. As such, our discussion shall lead to and then focus on the linear dynamics of a scalar field satisfying the massless Klein-Gordon equation, interacting with RN and RNdS black hole space-times.

However, to venture into these formal arguments, there are a number of mathematical preliminaries that must be specified first. To address these, we rely primarily on Refs [6, 7, 295].

Furthermore, when discussing the evolution of partial differential equations and the physical insights we might glean from them, it is imperative that we do so in the appropriate linear space. Note also that the principles of functional analysis usually employed for this purpose of interpreting the partial differential equation problem can only be applied after the problem of interest has been restructured in the form,

$$A : X \to Y \,, \tag{A.1}$$

where A serves as the operator encoding the structure, boundary conditions, etc. of the partial differential equation and X, Y are the spaces of functions. As we shall see, the appropriate space for the linear partial differential equations we consider here is the "Sobolev space".

Let us begin with the properties of smoothness and continuity. Generally, the "smoothness" of a function

is a property related to the highest order of its continuous derivatives. Consider a function f defined on an open set on the real line $\mathbb{R}$. Let $k \in \mathbb{Z}^+$. The function f is of differentiability class C^k if its derivatives f', f'', ..., $f^{(k)}$ exist and are continuous on $\mathbb{R}$. The function f is *at least* in the differentiability class C^{k-1} if it is k-differentiable, as this implies f', f'', ..., $f^{(k-1)}$ exist and are continuous on U. C^0 then denotes the space of continuous functions, so functions that are continuous but not differentiable; C^1 is the space of continuously differentiable functions (i.e. functions whose derivative is continuous over $\mathbb{R}$, such that f' is of differentiability class C^0). We can summarise this with the definition,

Definition A.1 (Differentiability class)**.** *A function f:$\mathcal{M} \subset \mathbb{R}^n \to \mathbb{R}$ belongs to differentiability class C^k if it is k-differentiable on $\mathcal{M}$ and its k-order gradient is continuous on $\mathcal{M}$.*

As such, f is considered to be in the class C^∞, "smooth" or "infinitely differentiable", if its derivatives of all orders exist and are continuous. For example, a C^∞ function such as $f(x) = e^{2x}$ has continuous derivatives to all orders. Formally, we can then define "smoothness":

Definition A.2 (Smoothness)**.** *A smooth curve C on a manifold $\mathcal{M}$ is a $\mathcal{C}^\infty$ map of $\mathbb{R}$ into $\mathcal{M}$, C: $\mathbb{R} \to \mathcal{M}$. At each point $p \in \mathcal{M}$ lying on the curve C, we can associate with C a tangent vector $T \in V_p$. Then the derivative of the function $f \circ C$: $\mathbb{R} \to \mathbb{R}$ evaluated at p is $T(f) = d(f \circ C)/dt$.*

A function that does not meet this criterion is then considered "rough".

We can see that there is a hierarchy of strictness in place, where higher values of k correspond to greater strictness. Recall also that differentiability is a stronger condition than continuity. For our purposes, the preservation of SCC hinges on the inextendability of the metric across the horizon: the strongest version of SCC therefore corresponds to a case C^0, where the metric cannot be extended continuously across the horizon. As already mentioned, this condition is not satisfied for the RN black hole's Cauchy horizon [225, 293].

In order to allow for a weakening of the condition for differentiability, it becomes necessary to introduce the "weak derivative", which we shall refer to simply as a generalisation of the derivative defined on the space for functions that are integrable but not assumed to be differentiable. We can introduce the more formal definition for a locally summable function v.

Definition A.3 (Weak partial derivative)**.** *Let us suppose that u and v are locally summable on the Lebesgue space L^1 $u, v \in L^1_{loc}(U)$, where $U \subset \mathbb{R}^n$ Suppose also that that α is a multi-index such that $\alpha = (\alpha_1, ..., \alpha_n)$ and $|\alpha| = \alpha_1 + ... + \alpha_n$. Then we can say that v is the α^{th}-weak partial derivative of u,*

$$D^\alpha u = v \,, \tag{A.2}$$

provided that for all test functions $\varphi \in C^\infty_c(U)$,

$$\int_U dx\; u D^\alpha \varphi = (-1)^{|\alpha|} \int_U dx\; v\varphi \,. \tag{A.3}$$

Note that the c subscript refers to compact support in U for the C^∞ function φ:$U \to \mathbb{R}$. With this, we can introduce the definition for the Sobolev space,

Definition A.4 (Sobolev space)**.** *Let us consider the open set $U \subset \mathbb{R}^n$ The Sobolev space $W^{k,p}(U)$ consists of all locally summable functions u:$U \to \mathbb{R}$ such that for each multi-index $|\alpha| \leq k$, the weak derivative $D^\alpha u$ exists and belongs to the space $L^p(U)$ for a fixed $1 \leq p \leq \infty$ and $k \in \mathbb{Z}^+$.*

Upon introducing the norm to $W^{k,p}(U)$,

$$||u||_{W^{k,p}(U)} \equiv \sum_{|\alpha| \leq k} ||D^\alpha u||_{L^p(U)} \,, \tag{A.4}$$

$W^{k,p}(U)$ becomes complete and Eq. (A.4) represents a Banach space. If we impose $p = 2$, $k \in \mathbb{N}_0$, and $U = \mathbb{R}^n$,

$$H^k(U) = W^{k,2}(U) \; ; \tag{A.5}$$

$H^k(U)$ is then a Hilbert space as well as a Banach space, and $H^0(U) = L^2(U)$.

The Sobolev space is ideal for defining functions and their weak derivatives. As in Definition A.1, k relays how differentiable a function is; p on the other hand tells us about a function's integrability. Spaces with larger k generally contain smoother functions whereas larger p implies more "roughness". For many cases, there is a trade-off between smoothness and integrability: a function that belongs to $W^{k,p}(\mathbb{R}^n)$ belongs to certain $W^{\ell,q}(\mathbb{R}^n)$ where $\ell < k$ and $p > q$. For a sufficiently large k and p, the function can be classified as classically differentiable.

To make precise our discussion on the nature of SCC and its preservation in various space-time configurations, we must specify one final point: unless otherwise stated, throughout our discussion on cosmic censorship, we consider the space-time $(\mathcal{M}, g)$ to be a 4D time-orientable Lorentzian manifold. Since we rely on the initial-value approach to GR to define the cosmic censorship conjectures, we cannot proceed without introducing the concept of "maximal Cauchy development" through the theorem of Choquet-Bruhat and Geroch (see Chapters 7.6 of Ref. [6] and 10.2 of Ref. [7]), *viz*.

Theorem A.5 (Maximal Cauchy development)**.** *Let Σ be a three-dimensional C^∞ manifold, let h_{ab} be a smooth Riemannian metric on Σ, and let K_{ab} be a smooth symmetric tensor field on Σ. Suppose that the initial data (Σ, h_{ab}, K_{ab}) satisfy the vacuum constraint equations,*

$$0 = D_b K^b{}_a - D_a K^b{}_b \; , \tag{A.6}$$

$$0 = \frac{1}{2}\left({}^{(3)}R + (K^a{}_a)^2 - K_{ab}K^{ab} \right) \; , \tag{A.7}$$

where D_a is the derivative operator associated with the metric h_{ab}. Then there exists a unique C^∞ space-time $(\mathcal{M}, g_{ab})$ known as the maximal Cauchy development of (Σ, h_{ab}, K_{ab}) that satisfies the following properties:

- (i) *$(\mathcal{M}, g_{ab})$ is a solution to the Einstein field equations.*
- (ii) *$(\mathcal{M}, g_{ab})$ is globally hyperbolic[27] with a Cauchy surface[28] Σ.*
- (iii) *h_{ab} and K_{ab} are the induced metric and extrinsic curvature, respectively, of Σ.*
- (iv) *A space-time $(\mathcal{M}', g'_{ab})$ satisfying properties $(i) - (iii)$ can be mapped isomterically into a subset of $(\mathcal{M}, g_{ab})$. To elaborate, suppose (Σ, h_{ab}, K_{ab}) and $(\Sigma', h'_{ab}, K'_{ab})$ are initial data sets with maximal developments $(\mathcal{M}, g_{ab})$ and $(\mathcal{M}', g'_{ab})$, respectively. Suppose also that there is a diffeomorphism between $S \subset \Sigma$ and $S' \subset \Sigma'$ that carries (h_{ab}, K_{ab}) on S into and (h'_{ab}, K'_{ab}) on S'. Then $D(S)$ in $(\mathcal{M}, g_{ab})$ is isometric to $D(S')$ in $(\mathcal{M}', g'_{ab})$. Finally, the solution g_{ab} on $\mathcal{M}$ depends continuously on the initial data (h_{ab}, K_{ab}) on Σ.*

[27] A set $\mathcal{N}$ is said to be globally hyperbolic if for any two points $p, q \in \mathcal{N}$, $J^+(p) \cap J^-(q)$ is compact and contained in $\mathcal{N}$. In other words, $J^+(p) \cap J^-(q)$ does not contain any points on the edge of space-time i.e. at spatial infinity or at a singularity [6].

[28] A Cauchy surface Σ in $\mathcal{M}, g_{ab})$ is a surface that is intersected exactly once by every inextendible null and time-like curve in $(\mathcal{M}, g_{ab})$ [211].

Appendix B

Horizons and conformal diagrams: the Schwarzschild example

A black hole is distinguished from other compact bodies by two features: its event horizon and the singularity it encloses [65]. Within this thesis, we consider the black hole through the (semi-)classical lens, such that infalling matter that passes the event horizon becomes trapped within the horizon but matter therein has no possibility of escape.[29] Since the causal relationship between the black hole interior $r < r_+$ and the exterior space-time $r > r_+$ prove fundamental to the physics herein pursued, we set aside this appendix to contextualise some of the terminology used, particularly in Chapters 3, 4, and 6. To do so, we largely follow Refs [6, 7, 66, 73] and refer to the simple case of a Schwarzschild black hole in asymptotically flat space-time when necessary.

We may begin with a formal definition of the black hole in an isolated system, *viz*.

Definition B.1 (Black hole)**.** *Consider a causal and asymptotically flat space-time* $(\mathcal{M}, g)$*. The space-time is said to contain a black hole if* $\mathcal{M}$ *is not contained in* $J^-(\mathscr{I}^+)$*. Then the black hole region is defined as* $\mathcal{B} \equiv \mathcal{M} - J^-(\mathscr{I}^+)$*. The event horizon is the boundary of* $\mathcal{B}$ *in* $\mathcal{M}$*,* $\mathscr{H} \equiv J^-(\mathscr{I}^+) \cap \mathcal{M}$*.*

Here, $\mathscr{I}^+$ refers to the future null infinity (see Table B.1) and J^- represents the chronological past. As such, the event horizon is the boundary of the past of $\mathscr{I}^+$; it is a null hypersurface comprised of future inextendible null geodesics without caustics.

We refer to this black hole as "stationary". For $\mathcal{B}$ to be stationary, there must exist a one-parameter group of isometries[30] on the space-time $(\mathcal{M}, g_{ab})$ whose orbits are time-like. These isometries are generated by a "Killing (vector) field" ξ^a that is unit time-like (i.e. $\xi^a\xi_a \to -1$) at infinity. A null surface $\mathcal{K}$ to which the Killing field ξ^a is normal is referred to as a "Killing horizon". By the "rigidity theorems" attributed to Carter [296] and Hawking [6], the event horizon of a stationary black hole must be a Killing horizon.

Since $\xi^a\xi_a = 0$ on $\mathscr{K}$, the vector $\nabla^b(\xi^a\xi_a)$ is also normal to $\mathscr{K}$, by definition. Then these vectors must be proportional at every point on the surface $\mathscr{K}$. As such, we can introduce the "surface gravity" κ through the expression,

$$\nabla^b(\xi^a\xi_a) = -2\kappa\xi^b \,. \tag{B.1}$$

where κ is constant along each generator [6, 296]. It can be shown [7, 73] that

$$\kappa = \lim_{r\to r_+} a(-\xi^a\xi_a)^{1/2} \,, \tag{B.2}$$

[29] Note, however, that the event horizon is not a "trapped surface": a closed, space-like 2-surface whose area decreases locally along any future direction, even along outgoing null (light-like) geodesics [211]. For stationary black holes, the event horizon is considered as the boundary of the region *containing* the trapped surface.

[30] Recall: an isometry $i : \mathcal{M} \to \mathcal{M}$ on a space-time $(\mathcal{M}, g)$ is a diffeomorphism that leaves the metric invariant.

where a is the magnitude of the acceleration of the orbits of (time-like) ξ^a in the region outside $\mathscr{H}$. The use of the term "surface gravity" for κ arises from the interpretation of $(-\xi^a\xi_a)^{1/2}$ as a "gravitational redshift factor", such that κ serves as the "redshifted proper acceleration" of the orbits of ξ^a near the horizon.

Finally, we introduce the "bifurcate Killing horizon": a pair of null surfaces $\mathscr{K}_A$ and $\mathscr{K}_B$ that intersect on a space-like 2-surface $\mathscr{S}$, the "bifurcation surface", such that $\mathscr{K}_A$ and $\mathscr{K}_B$ are each Killing horizons with respect to the same Killing field ξ^a. It then follows that ξ^a must vanish on $\mathscr{S}$. Assuming a non-zero κ, the event horizon of a "maximally-extended" black hole comprises a branch of a bifurcate Killing horizon (see, for example $\mathscr{H}_R^+$ and $\mathscr{H}_R^-$ of Figure B.1) [73]. The "extremal" black holes for which $\kappa_+ = 0$, on the other hand, do not possess this bifurcate event horizon.

Now that we have clarified our approach to black holes and their horizons, let us proceed to a discussion on the causal relationships between the regions of space-time they establish. A key visual aide in this is the "conformal space-time diagram". Known also as "Carter-Penrose diagrams", these were introduced by Brandon Carter and Roger Penrose to illustrate the structure of infinitely-large black hole space-times. These 2D projections are particularly useful as a concise geometric representation of space-time regions and the causal relationships between them, with key features such as event horizons and singularities clearly delineated. As demonstrated in our discussions on scattering in Section 2.1.1 and cosmic censorship in Section 3.3, conformal diagrams allow us to visualise complex field behaviours within curved space-times. In this section, we provide a brief overview of the construction of these space-time diagrams, using the maximally extended Schwarzschild solution as an example and following Refs [6, 7, 10].

Without loss of information, the conformal diagram must capture the characteristics of the $(3+1)$-dimensional space-time with a $(1+1)$-dimensional diagram. In the case of spherically-symmetric black holes, we are able to suppress the angular dimensions (θ, ϕ) while maintaining the integrity of the global and causal structure of the space-time. To do so, a coordinate transformation must be introduced such that

- ⋆ radial light rays are always at $\pm 45^\circ$ from the vertical axis (recall that $c = 1$);
- ⋆ points in the infinite past or future lie at a finite coordinate distance, at the boundary of the diagram.

In other words, the infinite space-time must be transformed into a finite diagram, with angles preserved but distances compactified. This is possible through a conformal rescaling of the metric,

$$g_{\mu\nu}(x^\mu) \to \overline{g}_{\mu\nu}(x^\mu) = \Omega(x^\mu)^2 g_{\mu\nu}(x^\mu) \,. \tag{B.3}$$

Locally, the metric on the conformal diagram is then conformally equivalent to the metric of the space-time depicted. Under such a conformal rescaling, the causal nature of a curve or vector field remains invariant: a vector field is space-like with respect to $\overline{g}_{\mu\nu}(x^\mu)$ if it is space-like with respect to $g_{\mu\nu}(x^\mu)$; a curve is time-like with respect to $\overline{g}_{\mu\nu}(x^\mu)$ if it is time-like with respect to $g_{\mu\nu}(x^\mu)$.

With these underlying ideas in place, let us proceed to the construction of the diagram itself. We begin with the introduction of new coordinates, motivated by the motion of physical particles. These are the advanced and retarded Eddington-Finkelstein coordinates, defined respectively as

$$u = t - r_\star \qquad \text{and} \qquad v = t + r_\star \,. \tag{B.4}$$

Here, t and $r_\star$ represent the Schwarzschild time coordinate and the tortoise coordinate, respectively. If we treat v as a new time coordinate, we can rewrite the metric in the form of ingoing Eddington-Finkelstein coordinates,

$$ds^2 = -\left(1 - \frac{2M}{r}\right) dv^2 + 2dvdr + r^2 d\Omega_{S^2}^2 \,. \tag{B.5}$$

Upon rewriting the (t, r)-component of the Schwarzschild metric in terms of both v and u, we obtain

$$ds^2 = -\left(1 - \frac{2M}{r}\right) dudv \,, \tag{B.6}$$

Table B.1: *Notation for asymptotic regions depicted in a standard conformal space-time diagram.*

Region	Symbol	*Coordinates*	
		Schwarzschild	*Eddington-Finkelstein*
Past horizon	$\mathscr{H}^-$	$t \to -\infty,\ r_\star \to -\infty$	$v \to -\infty,$ finite u
Future horizon	$\mathscr{H}^+$	$t \to +\infty,\ r_\star \to -\infty$	finite $v,\ u \to +\infty$
Past null infinity	$\mathscr{I}^-$	$t \to -\infty,\ r_\star \to +\infty$	finite $v,\ u \to -\infty$
Future null infinity	$\mathscr{I}^+$	$t \to +\infty,\ r_\star \to +\infty$	$v \to +\infty,$ finite u

with $r = r(u, v)$. Radial light rays correspond to $du\ dv = 0$; ingoing light rays follow curves of constant v while outgoing light rays follow curves of constant u. For $r > 2M$, outgoing light rays move towards larger r while for $r < 2M$, the move towards smaller r; for this reason, any observer following a time-like worldline eventually hits the space-like singularity $r = 0$. With these asymptotic behaviours in mind, we can summarise the asymptotic regions of the space-time using the notation provided in Table B.1.

Let us now proceed to the construction of the conformal diagram. To do so, we introduce the Kruskal coordinates,

$$X = \frac{1}{2}\left(e^{v/4M} + e^{-u/4M}\right) = (r - 2M)^{1/2} e^{r/4M} \cosh \frac{t}{4M}\,, \tag{B.7}$$

$$T = \frac{1}{2}\left(e^{v/4M} - e^{-u/4M}\right) = (r - 2M)^{1/2} e^{r/4M} \sinh \frac{t}{4M}\,, \tag{B.8}$$

$$X^2 - T^2 = (r - 2M)^{1/2} e^{r/2M}\,. \tag{B.9}$$

Here, $e^{v/4M}$ and $e^{-u/4M}$ are affine parameters along the outgoing and ingoing null geodesics, respectively. We may then rewrite Eq. (B.6) as

$$ds^2 = \frac{32M^3}{r} e^{-r/2M}(-dT^2 + dX^2)\,. \tag{B.10}$$

Due to the symmetries of the (X, T)-plane, each surface of constant $r$is represented twice − two hyperbolas have the same value of r. As a result, there are event horizons at $T = \pm X$, an asymptotic region for $X \gg 0$ and for $X \ll 0$, as well as a $r = 0$ singularity for $T > 0$ and for $T < 0$. These symmetries prove useful in the maximally-extended conformal diagram presented in Fig. B.1.

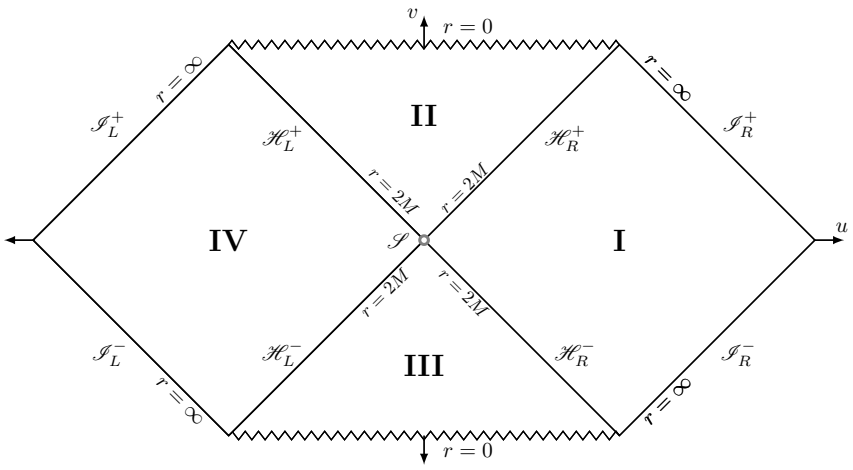

Figure B.1: *Conformal diagram for the maximally-extended Schwarzschild space-time.*

With a conformal rescaling of Eq. (B.10), we can generate Fig. B.1. Regions I and II are covered by the ingoing Eddington-Finkelstein coordinates of Eq. (B.5), where Region II is the black hole interior and Region I is the exterior asymptotically flat space-time. Here, $\mathscr{H}_R^+$ and $\mathscr{H}_R^-$ represent the future and past event horizons, respectively; they intersect at the bifurcation two-sphere $\mathscr{S}$. Hence, $\mathscr{H}_R^+$ and $\mathscr{H}_R^-$ are each branches of a bifurcate Killing horizon, and share an equivalent surface gravity κ_+.

When we discuss black holes formed from gravitational collapse, we consider only Regions I and II. Like Region I, Region IV is asymptotically flat, but it is causally disconnected from Region I. Region III is referred to as a "white hole": in antithesis to a black hole, it is an object from which information can escape but cannot enter. Regions III and IV are therefore treated as unphysical.

Appendix C

The Nariai black hole solution

The *NU* line of Fig. 3.2 is referred to in the text and literature as the "charged Nariai branch". While we loosely refer to it in the diagram as the solution for which $r_+ = r_c$, the horizons do not actually meet but instead become infinitesimally close. This is demonstrated explicitly in this appendix. Due to its relevance to the FL bound, we begin with a short discussion on the Nariai solution and how it relates to black holes in de Sitter space-time. The (uncharged) Nariai solution was constructed in 1950 [297, 298] from the isotropic form of the line element,

$$ds^2 = -e^{\nu(r)}dt^2 + e^{\mu(r)}(dr^2 + r^2 d\theta^2 + r^2 \sin^2\theta d\phi^2) \,. \tag{C.1}$$

Assuming a homogenous static universe with spherical symmetry, Nariai determined that

$$ds^2 = \frac{1}{\Lambda}\left[-(A\cos\{\log r\} + B\sin\{\log r\})^2 dt^2 + \frac{1}{r^2}(dr^2 + r^2 d\theta^2 + r^2\sin^2\theta d\phi^2)\right] \,, \tag{C.2}$$

for arbitrary constants A and B, satisfied the Einstein field equations for an empty universe with a non-zero cosmological constant. We can reformulate this into a more tractable expression with the introduction of a few transformations [298], *viz.*

$$\begin{aligned} t &= \tau\left(\frac{\Lambda}{A^2+B^2}\right)^{1/2} \,, \\ r &= \exp\left\{\pm\chi + \tan^{-1}\left\{\frac{B}{A}\right\}\right\} \,, \\ r_1 &= L\sin\{\chi\} \,, \end{aligned} \tag{C.3}$$

where $L^2 = 1/\Lambda$. Upon setting these transformations into Eq. (C.2), we obtain

$$ds^2 = -\cos^2\chi d\tau^2 + L^2(d\chi^2 + d\Omega^2) \,, \tag{C.4}$$

for $d\Omega^2 = d\theta^2 + \sin^2\theta d\phi^2$. Since $\sin\chi = r_1/L$, we can rewrite this expression as

$$ds^2 = -\left(1 - \frac{r_1^2}{L^2}\right)d\tau^2 + \left(1 - \frac{r_1^2}{L^2}\right)^{-1} dr_1^2 + L^2 d\Omega^2 \,. \tag{C.5}$$

We can compare this to the purely de Sitter solution, where $L_{dS}^2 = 3/\Lambda$,

$$ds^2 = -\cos^2\chi d\tau^2 + L_{dS}^2(d\chi^2 + \sin^2\chi d\Omega^2)\,, \tag{C.6}$$

$$= -\left(1 - \frac{r_1^2}{L_{dS}^2}\right) d\tau^2 + \left(1 - \frac{r_1^2}{L_{dS}^2}\right)^{-1} dr_1^2 + r_1^2 d\Omega^2\,. \tag{C.7}$$

For the purely radial case ($d\Omega^2 = 0$), Eq. (C.5) is nearly identical to pure de Sitter space. The Nariai space-time is spherically-symmetric, homogeneous and locally static; it is not isotropic or globally static. It has the geometry $dS_2 \times \mathbb{S}^2$ and a topology $\mathbb{R} \times \mathbb{S}^1 \times \mathbb{S}^2$. The space-time satisfies $R_{\mu\nu} = \Lambda g_{\mu\nu}$, where $\Lambda = 1/L^2$, and has constant Ricci scalar curvature, $R = 4\Lambda$. Furthermore, the space-time is symmetric $R_{\mu\nu\rho\sigma;\tau} = 0$ (see also Refs [200, 299–301] for further discussion).

Under a particular limiting procedure, Ginsparg and Perry [302] showed that the Nariai solution can be generated as the event and cosmological horizons of the Schwarzschild de Sitter approach one another: the extremal Schwarzschild de Sitter black hole, where $M = 1/\sqrt{9\Lambda}$, is often referred to as the "Nariai limit". Analogously, Hawking and Ross [303] obtained the charged Nariai solution of Bertotti [304] and Robinson [305] as a limiting case of the RNdS black hole.

Along the NU branch of Fig. 3.2, the proper distance between the two outer horizons remains finite in the $r_+ \to r_c$ limit, such that $r_+ \to \varrho - \epsilon$ and $r_c \to \varrho + \epsilon$ [81, 197, 303]. This is best illustrated by a change in coordinates, where we use the example from Ref. [91] that allows for a smooth transition of the black hole from a regular to extremal state. There, the coordinate $r = r_g$ is introduced, at which the competition between the gravitational attraction of the black hole and the accelerating expansion of the universe cancel and $f(r_g) = f'(r_g) = 0$. A "geodesic observer" situated at this point travels along a time-like Killing vector field which is also a geodesic. Suppose we let

$$\rho \to \frac{r - r_g}{\sqrt{|f(r_g)|}}\,, \quad \tau \to \sqrt{|f(r_g)|}\, t\,. \tag{C.8}$$

The metric then becomes

$$ds^2 = -\frac{f(r)}{\sqrt{|f(r_g)|}} d\tau^2 + \frac{\sqrt{|f(r_g)|}}{f(r)} d\rho^2 + r^2 d\Omega^2\,, \tag{C.9}$$

and the magnitude of the electric field is unchanged.

From the perspective of the geodesic observer, the two horizons become infinitesimally close along the NU branch, but they do not collide or overlap. There,

$$\frac{U(r)}{U(r_g)} \to 1 - \frac{\rho^2}{L_{dS_2}^2}\,, \quad r^2 \to r_c^2\,. \tag{C.10}$$

This produces the $dS_2 \times S^2$ metric,

$$ds^2 = -\left(1 - \frac{\rho^2}{L_{dS_2}^2}\right) d\tau^2 + \left(1 - \frac{\rho^2}{L_{dS_2}^2}\right)^{-1} d\rho^2 + r_c^2 d\Omega^2\,, \tag{C.11}$$

where

$$L_{dS_2}^2 = \frac{2}{f''(r_c)} = \frac{1}{6}\left(\frac{1}{\sqrt{1 - 12Q^2}} + 1\right) = \left(3 - \frac{Q^2}{r_c^4}\right)^{-1}\,. \tag{C.12}$$

The corresponding S^2 radius on the NU branch is

$$r_c(Q) = \sqrt{\frac{1}{6}\left(1+\sqrt{1-12Q^2}\right)}\,. \tag{C.13}$$

We can see that this is equivalent to the value of the cosmological horizon r_c in Eq. (3.22).

Appendix D

Quasinormal excitation factor computation at leading-order

In appendix A of Ref. [50], the method for the computation of the QNEF at leading-order is briefly outlined. In the interest of clarifying the procedure employed by Dolan and Ottewill, we review and explain the method in this appendix. As explained in Section 2.4, Dolan and Ottewill's method is characterised by a breakdown at the critical orbit $r = r_c = 3M$. To circumvent this, the solution space for the QNM wavefunction is divided into an "interior" region near $r = 3$ and "exterior" regions defined by $r > (3 + \epsilon')$ and $r < (3 - \epsilon')$ for some infinitesimally-small ϵ'. While the exterior solution is based on the photon-sphere arguments of the QNF calculation made in Refs [50, 156], the interior solution follows the low-order WKB method of Refs [151, 152]; specifically, the interior solution reduces to the asymptotic form of the parabolic cylinder function $\psi_1 \sim D_a((-1+i)z)$.

The first step of the Dolan-Ottewill procedure is the introduction of a perturbation factor into the QNF series expansion Eq. (2.43). At leading order,

$$\widetilde{\omega}_{\ell n} = \omega_{\ell n} + \epsilon \approx \omega^{(0)}_{\ell n} + \epsilon = \overline{\omega}_{-1} L + \overline{\omega}_0 + \epsilon \,. \tag{D.1}$$

Note that we refer to the "lowest-order" QNF as $\omega^{(-1)}_{\ell n} = \overline{\omega}_{-1} L = L/\sqrt{27}$ and the "leading-order" QNF as $\omega^{(0)}_{\ell n} = \overline{\omega}_{-1} L + \overline{\omega}_0 = (L - iN)/\sqrt{27}$. Furthermore, we make use of the superscript "(k)" to represent the "order" of each function or variable. Throughout, we indicate variables or functions subjected to a perturbation with an overhead tilde "$\sim$". We distinguish between terms independent of ϵ and coupled to ϵ as being of order $\mathcal{O}(\epsilon^0)$ and of order $\mathcal{O}(\epsilon)$, respectively. Note also that ϵ is not related to ϵ'.

D.1 Interior solution: using parabolic cylinder function

We begin by introducing $\ell = L - 1/2$ and the ansatz $u_{\ell\omega}(r) = f^{-1/2}\psi$ into

$$\left[\frac{d^2}{dr_\star^2} + \omega^2 - f(r)\left(\frac{\ell(\ell+1)}{r^2} + \frac{2M}{r^3}\right)\right] u_{\ell\omega}(r) = 0 \,. \tag{D.1.1}$$

This yields

$$f^{3/2}\psi'' + \frac{2M}{r^3} f^{1/2}\psi + \frac{M^2}{r^4} f^{-1/2}\psi + \left[\omega^2 - f\left(\frac{L^2 - 1/4}{r^2}\right) - f\frac{2M}{r^3}\right](f^{-1/2}\psi) = 0 \,,$$

which we multiply by $f^{-3/2}$ to obtain

$$\frac{d^2\psi}{dr^2} + U(r)\psi = 0\,, \qquad U(r) = f^{-2}\left[\omega^2 - f\left(\frac{L^2 - 1/4}{r^2}\right) + \frac{M^2}{r^4}\right]\,. \tag{D.1.2}$$

Let us now set $M = 1$. Then consider the lower-order change of variables

$$r = 3 + \sqrt{\frac{3}{L}}z\,, \tag{D.1.3}$$

and the first two terms of Eq. (2.43) evaluated at the leading-order QNF,

$$(\omega_{\ell n}^{(0)})^2 \approx (\overline{\omega}_{-1}L + \overline{\omega}_0)^2 = \frac{1}{27}L^2 + \frac{2\overline{\omega}_0 L}{\sqrt{27}} + \overline{\omega}_0{}^2\,. \tag{D.1.4}$$

Substituting these into Eq. (D.1.2) and extracting the dominant r-term, *viz.* $f^{-2}\omega^2$, produces the potential

$$U(r) = \left(2\sqrt{3}\overline{\omega}_0 + \frac{z^2}{3}\right)L + \mathcal{O}(L^{1/2}) \tag{D.1.5}$$

at leading order ($\mathcal{O}(L^1)$). Eq. (D.1.2) can then be written as

$$\frac{d^2\psi}{dz^2} + \left(2\sqrt{27}\overline{\omega}_0 + z^2\right)\psi = 0\,; \tag{D.1.6}$$

upon the replacement of $\overline{\omega}_0$ with the perturbed leading-order Eq. (D.1), we obtain

$$\frac{d^2\psi}{dz^2} + (-2iN + 2\sqrt{27}\epsilon + z^2)\psi = 0\,. \tag{D.1.7}$$

Note that an equivalent expression was determined in Ref. [55] using arguments based on the WKB results of Ref. [153]. Eq. (D.1.7) leads us to two independent solutions that can be expressed in terms of the parabolic cylinder functions [151, 152, 164],

$$\psi_1 = D_{n+\eta}\left[z(-1+i)\right]\,, \tag{D.1.8}$$

$$\psi_2 = D_{n+\eta}\left[z(+1-i)\right]\,. \tag{D.1.9}$$

Here, n is the overtone number and $\eta = i\epsilon\sqrt{27}$. The asymptotic behaviour of Eq. (D.1.8) is given by

$$\psi_1 \sim \begin{cases} 2^{(n+\eta)/2}e^{-i\pi(n+\eta)/4}|z|^{(n+\eta)}e^{+iz^2/2}\,, & z \to -\infty\,, \\ 2^{(n+\eta)/2}e^{+3i\pi(n+\eta)/4}|z|^{(n+\eta)}e^{+iz^2/2} & \\ \quad -\dfrac{(2\pi)^{1/2}}{\Gamma(-(n+\eta))}\dfrac{e^{+i\pi(n+\eta)}e^{-iz^2/2}}{e^{3i\pi(n+\eta+1)/4}\,2^{(n+\eta+1)/2}\,|z|^{(n+\eta+1)}}\,, & z \to +\infty\,. \end{cases} \tag{D.1.10}$$

The appropriate solution for this physical context is ψ_1: as $z \to \infty$, the two terms of ψ_1 correspond properly to outgoing and ingoing waves; ψ_2 on the other hand has both outgoing and ingoing parts for $z \to -\infty$. To satisfy the requirement that waves are purely ingoing at the horizon, ψ_2 cannot be used so we employ ψ_1 only.

We then take the lowest-order approximation in ϵ (through $\eta = i\epsilon\sqrt{27} \to 0$), such that Eq. (D.1.10)

becomes

$$\psi_1 \sim \begin{cases} 2^{n/2} e^{-i\pi n/4} |z|^n e^{+iz^2/2} , & z \to -\infty \\ 2^{n/2} e^{+3i\pi n/4} |z|^n e^{+iz^2/2} + \eta \dfrac{(2\pi)^{1/2} \Gamma(n+1) e^{-iz^2/2}}{e^{3i\pi(n+1)/4}\, 2^{(n+1)/2}\, |z|^{(n+1)}} , & z \to +\infty . \end{cases} \tag{D.1.11}$$

D.2 Exterior solution: using the Dolan-Ottewill ansatz

We utilise the Dolan-Ottewill ansatz introduced in Eq. (2.42),

$$u^{\pm}(r) = \exp\left\{ \pm i\omega \int_3^r \left(1 + \frac{6}{r}\right)^{1/2} \left(1 - \frac{3}{r}\right) dr_\star \right\} v^{\pm}(r) , \tag{D.2.12}$$

where the "$\pm$" superscripts indicate that we take into account the two types of boundary conditions in the exterior region. The "$+$" sign represents the purely ingoing wave near the event horizon and purely outgoing wave at spatial infinity. These are the QNM boundary conditions; as such, only u^+ corresponds to QNMs. On the other hand, the "$-$" sign represents the purely outgoing wave near the event horizon and the purely ingoing wave at spatial infinity. Note carefully, however, that under the perturbation of the QNFs as in Eq. (D.1), the first order correction of the ingoing coefficient in the matching region also contributes to the study of QNEFs. As such u^- is required to provide a linear combination of in- and outgoing waves in the matching region. With this setup, the subsequent wave equation is given by

$$f \frac{d^2 v^{\pm}}{dr^2} + \left[\frac{2}{r^2} \pm 2i\omega \left(1 + \frac{6}{r}\right)^{1/2} \left(1 - \frac{3}{r}\right) \right] \frac{dv^{\pm}}{dr} + \left[\frac{27\omega^2 - L^2}{r^2} \pm \frac{27 i\omega}{r^3} \left(1 + \frac{6}{r}\right)^{-1/2} + \frac{1}{4r^2} - \frac{2}{r^3} \right] v^{\pm} = 0 . \tag{D.2.13}$$

Near the critical orbit $r = r_c = 3$, we can make the approximation by taking $z = r(1 - 3/r)\sqrt{L/3}$ from Eq. (D.1.3),

$$\exp\left\{ \pm i\omega \int_3^{r_\star} \left(1 + \frac{6}{r}\right)^{-1/2} \left(1 - \frac{3}{r}\right) dr_\star \right\} \approx \exp\{ \pm iz^2/2 + \mathcal{O}(L^{-1}) \} . \tag{D.2.14}$$

With this, we have the exponential component of $u^{\pm}$. At leading order, $v^{\pm}(r)$ of Eq. (D.2.13) reduces to

$$v^{\pm(0)}(r) \approx \exp\left\{ \widetilde{S}^{\pm}_{0n}(r) L^0 \right\} . \tag{D.2.15}$$

For each side of the potential barrier, the perturbed $\widetilde{S}^{\pm}_{0n}(r)$ functions may be written as:

$$\widetilde{S}^{+}_{0n} = S_{0n}(r) + \eta Z_0(r) , \tag{D.2.16}$$

$$\widetilde{S}^{-}_{0n} = S_{0n}(r) - [2N + \eta] Z_0(r) . \tag{D.2.17}$$

To determine $S_{0n}(r)$, we substitute the leading-order expression for $v_{\ell n}(r)$ into Eq. (2.48) and solve for dS_{0n}/dr. We then integrate over r. Recall that to determine an explicit expression for dS_{0n}/dr, we need to introduce ω to order $\mathcal{O}(L^{-k})$. As such, for dS_{0n}/dr, we evaluate the function at $\omega_{\ell n} = (L - iN)/\sqrt{27}$. Note that this leading-order expression is independent of the spin of the perturbing field.

Similarly, for $\widetilde{S}^{\pm}_{0n}$ we insert $\omega \to \widetilde{\omega}_{\ell n} = (L - i/2)/\sqrt{27} + \epsilon$ and Eq. (D.2.15) into Eq. (D.2.13). After the integration, the term linear in ϵ (i.e. the $\mathcal{O}(\epsilon)$ term) in Eq. (D.2.16) can be realised as $\epsilon dZ_0/dr$. We then

integrate this term with respect to r and impose that $Z_0(r) \to 0$ as $r \to 2$. As such,

$$\frac{dZ_0(r)}{dr} = \frac{\sqrt{27}}{r^2(1-\frac{3}{r})\sqrt{1+\frac{6}{r}}} \tag{D.2.18}$$

$$\Rightarrow Z_0(r) = \ln|r-3| - \ln(3+2r+\sqrt{3r(r+6)}) + \ln\xi\,, \tag{D.2.19}$$

where $\xi = \left(2+\sqrt{3}\right)^2$. Note that $Z_0(r)$ is also independent of the spin of the field and the overtone number. We emphasise that solving for $\widetilde{S}^{-}_{0n}$, following the same procedure, yields $S_{0n}(r)$ and $[2N+\eta]Z_0(r)$; $S_{0n}(r)$ contributes terms of order $\mathcal{O}(\epsilon^0)$ while $[2N+\eta]Z_0(r)$ contributes terms of both $\mathcal{O}(\epsilon^0)$ and $\mathcal{O}(\epsilon)$. Using $\eta = \sqrt{27}i\epsilon$ and $y = \sqrt{1+6/r}$, the explicit expressions for Eqs. (D.2.16) and (D.2.17) may produced as

$$\widetilde{S}^{+}_{0n} = \frac{1}{2}\ln\left\{\frac{2}{y}\right\} + 2N\ln\left\{\frac{2+\sqrt{3}}{y+\sqrt{3}}\right\} + \eta\ln\left\{\frac{r-3}{3+2r+\sqrt{3}yr}\xi\right\} \tag{D.2.20}$$

$$\widetilde{S}^{-}_{0n} = \frac{1}{2}\ln\left\{\frac{2}{y}\right\} + 2N\ln\left\{\frac{2+\sqrt{3}}{y+\sqrt{3}}\right\} - [2N+\eta]\ln\left\{\frac{r-3}{3+2r+\sqrt{3}yr}\xi\right\}. \tag{D.2.21}$$

We then apply the change of variables from Eq. (D.1.3) into $S_{0n}(r)$ and $Z_0(r)$, and impose $z/\sqrt{L} \to 0$ (for $|z| \gg 1$). This yields[31]

$$S_{0n}(z) \approx \ln\left\{\left(\frac{4}{3}\right)^{1/4}\left(\frac{\xi}{12}\right)^N\right\}, \tag{D.2.22}$$

$$Z_0(z) \approx \ln\left(\frac{\xi|z|}{2\sqrt{27L}}\right). \tag{D.2.23}$$

Finally, we substitute the above approximations into Eq. (D.2.12) to obtain the asymptotics of $u^{\pm}$,

$$\begin{aligned} u^{+(0)} &\approx e^{+iz^2/2}\times\left(1-\frac{3}{r}\right)^n \exp\{S_{0n}(z)+\eta Z_0(z)\}\,, \\ &\approx \sqrt{2}e^{+iz^2/2}\left(\frac{z}{L^{1/2}}\right)^n\left(\frac{\xi}{4\sqrt{27}}\right)^N\left(\frac{\xi|z|}{2\sqrt{27L}}\right)^\eta, \end{aligned} \tag{D.2.24}$$

$$\begin{aligned} u^{-(0)} &\approx e^{-iz^2/2}\times\left(1-\frac{3}{r}\right)^n \exp\{S_{0n}(z)-[2N+\eta]Z_0(z)\} \\ &\approx \sqrt{2}e^{-iz^2/2}\left(\frac{z}{L^{1/2}}\right)^{-(n+1)}\left(\frac{\xi}{\sqrt{27}}\right)^{-N}\left(\frac{\xi|z|}{2\sqrt{27L}}\right)^{-\eta}. \end{aligned} \tag{D.2.25}$$

D.3 Matching procedure

We now match the solutions for the regions $r \sim 3$, $r > (3+\epsilon')$, and $r < (3-\epsilon')$. These correspond to the solutions $u^{(0)}_{r=3}$, $u^{(0)}_{r>3}$, and $u^{(0)}_{r<3}$, respectively. As an aside: note that for the interior solution, $u_{\ell\omega} = f^{-1/2}\psi$. At leading order, Dolan and Ottewill approximate this as $u_{\ell\omega} \sim \psi$. In Section 2.4, we shall see that this "prefactor" from the metric function contributes non-negligibly at higher orders. Here, for the region near $r = r_c = 3$, we have already justified that the ψ_1 is the appropriate choice for the interior solution, such that

$$u^{(0)}_{r=3} \approx \psi^{(0)}_1 D_{n+\eta}(z(-1+i))\,. \tag{D.3.26}$$

[31] In Eq. (D.2.23), we include the ξ missing from Eq. (A25) of the original work (c.f. the wavefunction of Eq. (A26) in Ref. [50], where ξ is included once again).

Then for the asymptotic regions,

$$u^{(0)}_{r<3} = C^{(0)}_{in} u^{+(0)} \,, \tag{D.3.27}$$

$$u^{(0)}_{r>3} = B^{(0)}_{out} u^{+(0)} + B^{(0)}_{in} u^{-\,(0)} \tag{D.3.28}$$

for $z \to -\infty (r < 3)$ and $z \to +\infty (r > 3)$, respectively. For the former, we determine $C^{(0)}_{in}$ by matching ψ_1 for $z \to -\infty$ of Eq. (D.1.10) to Eq. (D.2.24). For the latter, we determine $B^{(0)}_{out}$ by matching the first term of Eq. (D.1.10) for $z \to +\infty$ with Eq. (D.2.24) and $B^{(0)}_{in}$ by matching the second term of Eq. (D.1.10) for $z \to +\infty$ with Eq. (D.2.25). Note that these asymptotic limits for z are set for "mathematical convenience"; the exact matching region is described by a sufficiently large $|z|$ with a finite (sufficiently small) $|z|/\sqrt{L}$. This is because $\epsilon' \sim z/\sqrt{L}$, as presented in Eq. (D.1.3). With this in place, the matching region shall satisfy both interior and exterior solutions. We elaborate upon this in Section 2.4.4.

Explicitly, for $C^{(0)}_{in}$,

$$\begin{aligned}
\psi_{z\to-\infty} &= C^{(0)}_{in} u^{+(0)} \\
2^{n+\eta} e^{-i\pi(n+\eta)/4} e^{+iz^2/2} &= C_{in} \sqrt{2} e^{+iz^2/2} \left(\frac{z}{L^{1/2}}\right)^n \left(\frac{\xi}{4\sqrt{27}}\right)^N \left(\frac{\xi|z|}{2\sqrt{27L}}\right)^\eta \,, \\
\text{and by imposing } \eta \to 0: \qquad C^{(0)}_{in} &= 2^{2n} 2^{(n+1)/2} L^{n/2} \left(\frac{\xi}{\sqrt{27}}\right)^{-N} e^{-i\pi n/4} \,.
\end{aligned} \tag{D.3.29}$$

Similarly, for $B^{(0)}_{out}$, we use the $e^{+iz^2/2}$ term of Eq. (D.1.10) to obtain

$$\begin{aligned}
\psi^{(0)}_{z\to+\infty} &= B^{(0)}_{out} u^{+(0)} \\
2^{(n+\eta)/2} e^{+3i\pi(n+\eta)/4} |z|^{(n+\eta)} e^{+iz^2/2} &= B^{(0)}_{out} \sqrt{2} e^{+iz^2/2} \left(\frac{z}{L^{1/2}}\right)^n \left(\frac{\xi}{4\sqrt{27}}\right)^N \left(\frac{\xi|z|}{2\sqrt{27L}}\right)^\eta \,, \\
\text{and by imposing } \eta \to 0: \qquad B^{(0)}_{out} &= (-1)^n C^{(0)}_{in} \,.
\end{aligned} \tag{D.3.30}$$

Note how we have exploited $e^{+3i\pi n/4} = e^{i\pi n - i\pi n/4}$, where $(e^{i\pi})^n = (-1)^n$, to express $B^{(0)}_{out}$ as a function of $C^{(0)}_{in}$. Finally, for $B^{(0)}_{in}$ we use the $e^{-iz^2/2}$ term of Eq. (D.1.10) and Eq. (D.2.25).

$$\begin{aligned}
\psi^{(0)}_{z\to+\infty} &= B^{(0)}_{in} u^{-(0)} \\
-\frac{(2\pi)^{1/2}}{\Gamma(-(n+\eta))} \frac{e^{+i\pi(n+\eta)} e^{-iz^2/2}}{e^{3i\pi(n+\eta+1)/4}\, 2^{(n+\eta+1)/2}\, |z|^{(n+\eta+1)}} &= B^{(0)}_{in} \sqrt{2} e^{-iz^2/2} \left(\frac{z}{L^{1/2}}\right)^{-(n+1)} \left(\frac{\xi}{\sqrt{27}}\right)^{-N} \left(\frac{\xi|z|}{2\sqrt{27L}}\right)^{-\eta} \\
\text{up to order } \mathcal{O}(\epsilon): \qquad \eta \frac{(2\pi)^{1/2}\Gamma(n+1) e^{-iz^2/2}}{e^{3i\pi(n+1)/4}\, 2^{(n+1)/2}\, |z|^{(n+1)}} &= B^{(0)}_{in} \sqrt{2} e^{-iz^2/2} \left(\frac{z}{L^{1/2}}\right)^{-(n+1)} \left(\frac{\xi}{\sqrt{27}}\right)^{-N} .
\end{aligned} \tag{D.3.31}$$

Note in particular the use of the property $(\Gamma(-(n+\eta)))^{-1} = +\eta\, \Gamma(n+1)$. Through a number of algebraic manipulations to accommodate the introduction of the expression for $C^{(0)}_{in}$, we find that

$$B^{(0)}_{in} = \epsilon \Gamma(n+1) 2^{-n} L^{-n} \left(\frac{27\pi}{iL}\right)^{1/2} e^{-i\pi n/2} \left(\frac{\xi}{2\sqrt{27}}\right)^{2N} C^{(0)}_{in} \,, \tag{D.3.32}$$

where we have corrected a minor typographical error in the original work by including the $C^{(0)}_{in}$ omitted from Eq. (A34) of Ref. [50].

D.4 Ingoing and outgoing coefficients

To compute the in-going and out-going coefficients, $A^{\pm(0)}_{\ell n}$, we require the contribution from the "phase factors" [50]:

$$\alpha^{(0)}_1 = \exp\left\{+i\omega\int_{r=3}^{r=2}\left(1+\frac{6}{r}\right)^{1/2}\left(1-\frac{3}{r}\right)\frac{dr}{f}\right\}\exp\{+i\omega r_\star\}$$
$$= \exp\{i\omega[6-\sqrt{27}+8\ln 2-3\ln\xi]\}\,, \tag{D.4.33}$$
$$\beta^{(0)}_1 = \exp\left\{+i\omega\int_{r=3}^{r=\infty}\left(1+\frac{6}{r}\right)^{1/2}\left(1-\frac{3}{r}\right)\frac{dr}{f}\right\}\exp\{-i\omega r_\star\}$$
$$= \exp\{i\omega[3-\sqrt{27}+4\ln 2-3\ln\xi]\}\,, \tag{D.4.34}$$
$$\gamma^{(0)}_1 = \exp\left\{-i\omega\int_{r=3}^{r=\infty}\left(1+\frac{6}{r}\right)^{1/2}\left(1-\frac{3}{r}\right)\frac{dr}{f}\right\}\exp\{+i\omega r_\star\} = 1/\beta^{(0)}_1\,, \tag{D.4.35}$$
$$\alpha^{(0)}_2 = \lim_{r\to 2} e^{\widetilde{S}^{+}_{0n}} = 1\,, \tag{D.4.36}$$
$$\beta^{(0)}_2 = \lim_{r\to\infty} e^{\widetilde{S}^{+}_{0n}} = 2^{1/2}\left(\sqrt{\xi}/2\right)^{N}\,, \tag{D.4.37}$$
$$\gamma^{(0)}_2 = \lim_{r\to\infty} e^{\widetilde{S}^{-}_{0n}} = 2^{1/2}\left(2\sqrt{\xi}\right)^{-N}\,. \tag{D.4.38}$$

At leading order and evaluated at the perturbed QNF of Eq. (D.1),

$$A^{+(0)}_{\ell n}\Big|_{\omega\to\widetilde{\omega}^{(0)}_{\ell n}} = \frac{\beta^{(0)}_1\beta^{(0)}_2}{\alpha^{(0)}_1\alpha^{(0)}_2}\frac{B^{(0)}_{out}}{C^{(0)}_{in}}$$
$$\approx 2^{1/2}(-1)^n\left(\frac{\sqrt{\xi}}{2}\right)^{N}\exp\{-i\omega^{(0)}_{\ell n}[3+4\ln 2]+\mathcal{O}(\epsilon)\}\,, \tag{D.4.39}$$

since $\exp\{3\pi i n/4+\pi i n/4\} = (e^{i\pi})^n = (-1)^n$. Then, evaluating at the perturbed QNF of Eq. (D.1),

$$A^{-(0)}_{\ell n}\Big|_{\omega\to\widetilde{\omega}^{(0)}_{\ell n}} = \frac{\gamma^{(0)}_1\gamma^{(0)}_2}{\alpha^{(0)}_1\alpha^{(0)}_2}\frac{B^{(0)}_{in}}{C^{(0)}_{in}}$$
$$\approx \epsilon\Gamma(n+1)2^{-n}L^{-n}\left(\frac{27\pi}{iL}\right)^{1/2}\left(\frac{\xi}{2\sqrt{27}}\right)^{2N}2^{1/2}\left(2\sqrt{\xi}\right)^{-N}e^{-in\pi/2}$$
$$\times\exp\{-i\omega^{(0)}_{\ell n}[9-2\sqrt{27}+12\ln 2-6\ln\xi]+\mathcal{O}(\epsilon)\}\,. \tag{D.4.40}$$

From Eq. (D.4.40), it is clear that the in-going coefficient at order $\mathcal{O}(\epsilon^0)$ vanishes; it is from the perturbation in the QNF (see Eq. (D.1)) that we obtain a non-zero contribution from $A^{-(0)}_{\ell n}$. Eq. (D.4.40) can be viewed as a Taylor-expansion of $A^{-(0)}_{\ell n}$ with respect to $\tilde{\omega}^{(0)}_{\ell n}$ around the QNF $\omega^{(0)}_{\ell n}$. We can demonstrate this explicitly by writing the full perturbed expression for $A^{-(k)}_{\ell n}$,

$$A^{-(k)}_{\ell n}|_{\omega\to\widetilde{\omega}^{(k)}_{\ell n}} = 0+\epsilon\left(\frac{\partial A^{-(k)}_{\ell n}}{\partial\omega}\right)\Bigg|_{\omega\to\omega^{(k)}_{\ell n}}+\mathcal{O}(\epsilon^2). \tag{D.4.41}$$

In this case, Eq. (D.4.40) is naturally of order $\mathcal{O}(\epsilon)$ and higher, where the coefficient of ϵ shall be the first

partial derivative term of $A_{\ell n}^{-(k)}$ evaluated at $\omega_{\ell n}^{(k)}$. That is, for the leading order herewith studied,

$$\left(\frac{\partial A_{\ell n}^{-(0)}}{\partial\omega}\right)\Bigg|_{\omega\to\omega_{\ell n}^{(0)}} = \Gamma(n+1)2^{-n}L^{-n}\left(\frac{27\pi}{iL}\right)^{1/2}\left(\frac{\xi}{2\sqrt{27}}\right)^{2N}2^{1/2}\left(2\sqrt{\xi}\right)^{-N}e^{-in\pi/2} \times\exp\{-i\omega_{\ell n}^{(0)}[9-2\sqrt{27}+12\ln 2-6\ln\xi]\}\,. \tag{D.4.42}$$

The $\mathcal{O}(\epsilon^2)$ term will not contribute to the evaluation of the QNEFs. This is also the justification for maintaining $A_{\ell n}^{-(k)}$ only up to order $\mathcal{O}(\epsilon)$ for our higher-order L^{-k} results.

D.5 The leading-order quasinormal excitation factor

As shown in Eq. (2.25), the QNEF at order L^k is defined as

$$\mathcal{B}_{\ell n}^{(k)} \equiv \frac{A_{\ell n}^{+(k)}}{2\omega}\left(\frac{\partial A_{\ell n}^{-(k)}}{\partial\omega}\right)^{-1}\Bigg|_{\omega\to\omega_{\ell n}^{(k)}} \tag{D.5.43}$$

Using the expressions for Eqs. (D.4.39) and (D.4.40), we find that the leading-order QNEF for general n becomes

$$\mathcal{B}_{\ell n}^{(0)} = \frac{(-iL)^{n-1/2}}{n!(\sqrt{27}\omega_{\ell n}^{(0)}/L)}\frac{\exp\{2i\omega_{\ell n}^{(0)}\zeta\}}{\sqrt{8\pi}}\left(\frac{216}{\xi}\right)^{n+1/2}\,, \tag{D.5.44}$$

where we make use of the constant defined in Ref. [50],

$$\zeta = 3-\sqrt{27}+4\ln 2-6\ln\left(2+\sqrt{3}\right)\,, \tag{D.5.45}$$

and the property $\Gamma(n+1)=n!$. This is precisely Eq. (A34) of Ref. [50], where we have corrected a minor typographical error in the denominator. Note, however, that the QNEF result quoted in the main text of Ref. [50], Eq. (31), can be obtained by substituting $\omega_{\ell n}^{(0)}\approx(L-iN)/\sqrt{27}$ into the $\exp\{2i\omega_{\ell n}^{(0)}\zeta\}$ of Eq. (D.5.44), but only with the lowest-order $\omega_{\ell n}^{(-1)}\approx L/\sqrt{27}$ term being in the denominator. For the associated Fig. 4 of Ref. [50], the values plotted correspond to Eq. (D.5.44) evaluated at $\omega_{\ell n}^{(0)}\approx(L-iN)/\sqrt{27}$ for $n=0$, *viz.*

$$\mathcal{B}_{\ell n}^{(0)} = \left(\frac{i}{L}\right)^{1/2}\frac{B\,e^{2i\zeta L/\sqrt{27}}}{1-\frac{i\left(n+\frac{1}{2}\right)}{L}}\frac{(-i\kappa L)^n}{n!}\Bigg|_{n=0} = \left(\frac{i}{L}\right)^{1/2}\frac{B\,e^{2i\zeta L/\sqrt{27}}}{1-\frac{i}{2L}}\,, \tag{D.5.46}$$
$$B=\left(\frac{27}{\xi\pi}\right)^{1/2}e^{\zeta/\sqrt{27}}\,,\quad \kappa=\frac{216e^{2\zeta/\sqrt{27}}}{\xi}\,,$$

where we have made use of the constants B and κ introduced in Ref. [50]. We simplify Eq. (D.5.46) further,

$$\mathcal{B}_{\ell 0}^{(0)} = \left(\frac{\exp\{2i\omega_{\ell 0}^{(0)}\zeta\}}{\omega_{\ell 0}^{(0)}}\right)\left(\frac{\sqrt{L}}{\left(2+\sqrt{3}\right)\sqrt{-i\pi}}\right)\,, \tag{D.5.47}$$

where $\omega_{\ell 0}^{(0)}=\overline{\omega}_{-1}L+\overline{\omega}_0$ refers to the QNF for $n=0$ at leading order $L^{(0)}$.

Appendix E

Perturbed components of the QNM wavefunction at higher orders

For convenience and reproducability, we list the explicit perturbed $\widetilde{S}^{\pm}_{k0}$ functions for the fundamental QNM, discussed in Section 2.4.3 and featured in Eq. (2.104):

$$\begin{aligned}\widetilde{S}^{+}_{00}(r) &= \frac{1}{4}\ln\left(\frac{4r}{6+r}\right)+\frac{1}{2}\left(\ln\left(\frac{\xi r}{2}\right)-\ln\left(3+2r+\sqrt{3r(r+6)}\right)\right)\\ &\quad+i\sqrt{27}\epsilon\left(\ln(r-3)-\ln\left(3+2r+\sqrt{3r(r+6)}\right)+\ln(\xi)\right)\,, \qquad \text{(E.1)}\\ \widetilde{S}^{-}_{00}(r) &= \frac{1}{4}\ln\left(\frac{4r}{6+r}\right)+\frac{1}{2}\left(\ln\left(\frac{\xi r}{2}\right)-\ln\left(3+2r+\sqrt{3r(r+6)}\right)\right)\\ &\quad-(1+i\sqrt{27}\epsilon)\left(\ln(r-3)-\ln\left(3+2r+\sqrt{3r(r+6)}\right)+\ln(\xi)\right)\,; \qquad \text{(E.2)}\end{aligned}$$

$$\begin{aligned}\widetilde{S}^{+}_{10}(r) &= \left(\frac{67i}{144\sqrt{3}}+\frac{27i(r-2)}{4(r-3)^2(r+6)}-\frac{i\sqrt{\frac{r+6}{3r}}\left(1458-945r-90r^2+213r^3+10r^4\right)}{72\left((r-3)^2(r+6)^2\right)}\right)\\ &\quad+\epsilon\left(1-\frac{5\ln(\xi)}{4\sqrt{3}}-\frac{81\sqrt{3}(r-2)}{2(r-3)^2(r+6)}-\frac{\sqrt{r(r+6)}\left(90-45r+2r^2\right)}{4\left((r-3)^2(r+6)\right)}\right.\\ &\quad\left.-\frac{1}{12}\left(5\sqrt{3}\right)\ln(r-3)+\frac{1}{12}\left(5\sqrt{3}\right)\ln\left(3+2r+\sqrt{3r(r+6)}\right)\right)\,, \qquad \text{(E.3)}\\ \widetilde{S}^{-}_{10}(r) &= \left(-\frac{67i}{144\sqrt{3}}+\frac{27i(r-2)}{4(r-3)^2(r+6)}+\frac{i\sqrt{\frac{r+6}{3r}}\left(1458-945r-90r^2+213r^3+10r^4\right)}{72\left((r-3)^2(r+6)^2\right)}\right)\\ &\quad-\epsilon\left(1-\frac{5\ln(\xi)}{4\sqrt{3}}+\frac{81\sqrt{3}(r-2)}{2(r-3)^2(r+6)}-\frac{\sqrt{r(r+6)}\left(90-45r+2r^2\right)}{4\left((r-3)^2(r+6)\right)}\right.\\ &\quad\left.-\frac{1}{12}\left(5\sqrt{3}\right)\ln(r-3)+\frac{1}{12}\left(5\sqrt{3}\right)\ln\left(3+2r+\sqrt{3r(r+6)}\right)\right)\,; \qquad \text{(E.4)}\end{aligned}$$

$$\begin{aligned}\widetilde{S}^{+}_{20}(r) = &-\frac{47}{2592\sqrt{3}}+\frac{6237}{4(-3+r)^4(6+r)^3}-\frac{2187}{4(-3+r)^4r(6+r)^3}-\frac{17631r}{16(-3+r)^4(6+r)^3}+\frac{3267r^2}{8(-3+r)^4(6+r)^3}\\&-\frac{483r^3}{16(-3+r)^4(6+r)^3}-\frac{61r^4}{4(-3+r)^4(6+r)^3}-\frac{115r^5}{16(-3+r)^4(6+r)^3}-\frac{411\sqrt{3}r\sqrt{\frac{6+r}{r}}}{4(-3+r)^4(6+r)^3}\\&+\frac{685\sqrt{3}r^2\sqrt{\frac{6+r}{r}}}{8(-3+r)^4(6+r)^3}-\frac{2497r^3\sqrt{\frac{6+r}{r}}}{16\sqrt{3}(-3+r)^4(6+r)^3}+\frac{1355r^4\sqrt{\frac{6+r}{r}}}{32\sqrt{3}(-3+r)^4(6+r)^3}\\&+\frac{475r^5\sqrt{\frac{6+r}{r}}}{144\sqrt{3}(-3+r)^4(6+r)^3}+\frac{863r^6\sqrt{\frac{6+r}{r}}}{864\sqrt{3}(-3+r)^4(6+r)^3}-\frac{49r^7\sqrt{\frac{6+r}{r}}}{1296\sqrt{3}(-3+r)^4(6+r)^3}+\mathcal{O}(\epsilon)\,,\end{aligned} \tag{E.5}$$

$$\begin{aligned}\widetilde{S}^{-}_{20}(r) = &\frac{59}{864}+\frac{47}{2592\sqrt{3}}+\frac{729}{2(-3+r)^4(6+r)^3}-\frac{2187}{4(-3+r)^4r(6+r)^3}-\frac{1701r}{16(-3+r)^4(6+r)^3}\\&+\frac{4941r^2}{16(-3+r)^4(6+r)^3}-\frac{3975r^3}{32(-3+r)^4(6+r)^3}-\frac{r^4}{2(-3+r)^4(6+r)^3}-\frac{7r^5}{2(-3+r)^4(6+r)^3}\\&-\frac{59r^6}{144(-3+r)^4(6+r)^3}-\frac{59r^7}{864(-3+r)^4(6+r)^3}+\frac{411\sqrt{3}r\sqrt{\frac{6+r}{r}}}{4(-3+r)^4(6+r)^3}-\frac{685\sqrt{3}r^2\sqrt{\frac{6+r}{r}}}{8(-3+r)^4(6+r)^3}\\&+\frac{2497r^3\sqrt{\frac{6+r}{r}}}{16\sqrt{3}(-3+r)^4(6+r)^3}-\frac{1355r^4\sqrt{\frac{6+r}{r}}}{32\sqrt{3}(-3+r)^4(6+r)^3}-\frac{475r^5\sqrt{\frac{6+r}{r}}}{144\sqrt{3}(-3+r)^4(6+r)^3}\\&-\frac{863r^6\sqrt{\frac{6+r}{r}}}{864\sqrt{3}(-3+r)^4(6+r)^3}+\frac{49r^7\sqrt{\frac{6+r}{r}}}{1296\sqrt{3}(-3+r)^4(6+r)^3}+\mathcal{O}(\epsilon)\,.\end{aligned} \tag{E.6}$$

Upon imposing $r \to r_p + \alpha^{-1}z$ and the limit $\epsilon \to 0$, we can derive the asymptotics thereof, which contribute to Eqs (2.105) and (2.106):

$$\begin{aligned}\widetilde{S}^{+}_{00}(z) \sim &\ln\left[\left(\frac{4}{3}\right)^{\frac{1}{4}}\left(\frac{\xi}{12}\right)^{\frac{1}{2}}\right]+\left(\frac{\sqrt{3}}{9}z\right)\frac{1}{\sqrt{L}}-\left(\frac{2}{9}i+\frac{17}{216}z^2\right)\frac{1}{L}\\&+\left(\frac{29z^3}{486\sqrt{3}}-\frac{19iz}{54\sqrt{3}}\right)\frac{1}{L^{3/2}}+\left(-\frac{247z^4}{15552}+\frac{95iz^2}{486}-\frac{7}{243}\right)\frac{1}{L^2}\,,\end{aligned} \tag{E.7}$$

$$\begin{aligned}\widetilde{S}^{-}_{00}(z) \sim &\ln\left[\left(\frac{4}{3}\right)^{\frac{1}{4}}\left(\frac{\xi}{12}\right)^{\frac{1}{2}}\right]-\ln\left(\frac{\xi\,|z|}{2\sqrt{27L}}\right)+\left(\frac{2i}{\sqrt{3}z}+\frac{z}{\sqrt{3}}\right)\frac{1}{\sqrt{L}}\\&-\left(\frac{2}{3z^2}-\frac{4i}{3}+\frac{35}{216}z^2\right)\frac{1}{L}+\left(\frac{17z^3}{162\sqrt{3}}-\frac{8i}{9\sqrt{3}z^3}-\frac{73iz}{54\sqrt{3}}-\frac{151}{54\sqrt{3}z}\right)\frac{1}{L^{3/2}}\\&+\left(-\frac{1195z^4}{46656}+\frac{4}{9z^4}+\frac{71iz^2}{162}-\frac{151i}{81z^2}-\frac{43}{432}\right)\frac{1}{L^2}\,;\end{aligned} \tag{E.8}$$

$$\widetilde{S}^{+}_{10}(z) \sim \left(\frac{67i}{144\sqrt{3}} - \frac{79i}{324}\right) + \left(\frac{5iz}{81\sqrt{3}}\right)\left(\frac{1}{\sqrt{L}}\right) + \left(\frac{10}{243} - \frac{229iz^2}{23328}\right)\frac{1}{L} + \left(\frac{491z}{5832\sqrt{3}} + \frac{41iz^3}{6561\sqrt{3}}\right)\frac{1}{L^{3/2}} - \left(\frac{43iz^4}{26244} + \frac{1405z^2}{52488} + \frac{613i}{52488}\right)\frac{1}{L^2}\,, \tag{E.9}$$

$$\widetilde{S}^{-}_{10}(z) \sim \left(\frac{i}{2z^2}\right)L + \left(\frac{2i}{3\sqrt{3}}\right)\left(\frac{2}{z} + \frac{3i}{z^3}\right)\sqrt{L} + \left(\frac{31i}{324} - \frac{67i}{144\sqrt{3}} - \frac{26}{9z^2} - \frac{2i}{z^4}\right) + \left(\frac{16}{3\sqrt{3}z^5} - \frac{679i}{54\sqrt{3}z^3} - \frac{8}{3\sqrt{3}z} - \frac{iz}{81\sqrt{3}}\right)\frac{1}{\sqrt{L}} + \left(\frac{40i}{9z^6} + \frac{133}{9z^4} + \frac{101iz^2}{23328} - \frac{26963i}{3888z^2} - \frac{2}{243}\right)\frac{1}{L}\,; \tag{E.10}$$

$$\widetilde{S}^{+}_{20}(z) \sim \left(\frac{985}{93312} - \frac{47}{2592\sqrt{3}}\right) - \frac{11z}{5832\sqrt{3}}\frac{1}{\sqrt{L}} + \left(-\frac{947z^2}{839808} + \frac{11i}{8748}\right)\frac{1}{L} + \left(\frac{107z^3}{59049\sqrt{3}} + \frac{1739iz}{209952\sqrt{3}}\right)\frac{1}{L^{3/2}} - \left(\frac{845645z^4}{1088391168} - \frac{1675iz^2}{1889568} - \frac{4271}{1889568}\right)\frac{1}{L^2}\,, \tag{E.11}$$

$$\widetilde{S}^{-}_{20}(z) = -\frac{5}{8z^4}L^2 + \left(-\frac{\sqrt{3}}{z^3} - \frac{5i}{\sqrt{3}z^5}\right)L^{3/2} + \left(\frac{25}{3z^6} - \frac{11i}{z^4} - \frac{73}{54z^2}\right)L + \left(\frac{100i}{3\sqrt{3}z^7} + \frac{7667}{108\sqrt{3}z^5} - \frac{632i}{27\sqrt{3}z^3} - \frac{35}{54\sqrt{3}z}\right)L^{1/2} + \left(-\frac{350}{9z^8} + \frac{18895i}{162z^6} + \frac{60119}{864z^4} - \frac{473i}{81z^2} + \frac{2263}{93312} + \frac{47}{2592\sqrt{3}}\right)\,. \tag{E.12}$$

Appendix F

Details on the semi-classical method

When considering massive charged QNMs oscillating on the RNdS space-time, there are a number of free parameters that must be taken into account for the scalar QNF (μ, q, ℓ, n) and the black hole space-time (M, Q, Λ). To calculate the QNFs, we choose to make use of the semi-classical method of González *et al.* as it produces the QNF in the form of a series expansion in L, such that these black hole and scalar field input variables are left as free parameters (i.e. charges and masses do not need to be pre-defined, as is the case in a variety of other methods [47, 160]). In this way, black hole and scalar field input parameters can be substituted in after the iterative procedure has been applied, therefore allowing for a complete scan of the available phase space for a number of different combinations of variables.

For $N = n + 1/2$ and the derivative V^j taken with respect to a generalised tortoise coordinate, we compute the values of the QNF series terms using Eqs (4.18-4.20) [238, 249], for which

$$
\begin{aligned}
U = N\sqrt{\frac{-V^{(2)}}{2}} + \frac{i}{64}\left[-\frac{1}{9}\left(\frac{V^{(3)}}{V^{(2)}}\right)^2(7+60N^2) + \frac{V^{(4)}}{V^{(2)}}(1+4N^2)\right] \\
+ \frac{N}{2^{3/2}288}\left[\frac{5}{24}\left(\frac{(V^{(3)})^4}{(-V^{(2)})^{9/2}}\right)(77+188N^2) + \frac{3}{4}\left(\frac{(V^{(3)})^2V^{(4)}}{(-V^{(2)})^{7/2}}\right)(51+100N^2)\right. \\
\left. + \frac{1}{8}\left(\frac{(V^{(4)})^2}{(-V^{(2)})^{5/2}}\right)(67+68N^2) + \left(\frac{V^{(3)}V^{(5)}}{(-V^{(2)})^{5/2}}\right)(19+28N^2) + \left(\frac{V^{(6)}}{(-V^{(2)})^{3/2}}\right)(5+4N^2)\right], \quad \text{(F1)}
\end{aligned}
$$

as first derived in Eq. (1.5b) of Ref. [153]. The coefficients featured in the series expansion Eq. (4.19) are

$$
r_0 \approx 3M - \frac{2Q^2}{3M} - \frac{4Q^4}{27M^3} + \dots, \quad \text{(F2)}
$$

$$
\begin{aligned}
r_1 \approx 27\Lambda M^5\left(2\Lambda - 3\mu^2\right) - 3M^3\left(\Lambda - 3\mu^2\right) - \frac{M}{3} - 9\left(qM^2\omega\right)Q + \left[M\left(3q^2 + \frac{2\Lambda}{3} - 5\mu^2\right)\right. \\
\left. + 24\Lambda M^3\left(3\mu^2 - 2\Lambda\right) + \frac{5}{27M}\right]Q^2 + 2qQ^3\omega + Q^4\left[4\Lambda M\left(2\Lambda - 3\mu^2\right) - \frac{14}{81M^3}\right] + \dots. \quad \text{(F3)}
\end{aligned}
$$

Similarly, the contributions to the series expansion of the potential Eq. (4.19) are

$$\begin{aligned}
V_0 \approx & \frac{1}{27M^2}\left(1-9\Lambda M^2\right)+\frac{Q^2}{81M^4}+\frac{4Q^4}{729M^6}+... \\
V_1 \approx & -\frac{4\Lambda}{9}+\frac{\mu^2}{3}+2\Lambda^2M^2-3\Lambda\mu^2M^2+\frac{2}{81M^2}+\frac{2qQ\omega}{3M}+\left[-\frac{q^2}{9M^2}-\frac{8\Lambda^2}{9}+\frac{4\Lambda\mu^2}{3}\right. \\
& \left.+\frac{4}{729M^4}+\frac{4\Lambda}{81M^2}-\frac{\mu^2}{27M^2}\right]Q^2+\frac{4q\omega}{27M^3}Q^3+\left[-\frac{4q^2}{81M^4}+\frac{10}{6561M^6}+\frac{16\Lambda}{729M^4}\right. \\
& \left.-\frac{4\mu^2}{243M^4}-\frac{8\Lambda^2}{81M^2}+\frac{4\Lambda\mu^2}{27M^2}\right]Q^4+...
\end{aligned} \tag{F4}$$

The first term in the QNF series expansion is given by

$$\begin{aligned}
\omega_0 \approx & \frac{qQ}{3M}-\frac{i\sqrt{\frac{1}{3}-3\Lambda M^2}}{6M}+\frac{iQ^2\sqrt{\frac{1}{3}-3\Lambda M^2}\left(18\Lambda M^2+1\right)}{108M^3\left(9\Lambda M^2-1\right)}+\frac{2qQ^3}{27M^3} \\
& +\frac{iQ^4\left(1-18\Lambda M^2\right)^2}{432\sqrt{3}M^5\left(1-9\Lambda M^2\right)^{3/2}}+...
\end{aligned} \tag{F5}$$

We perform a crude error estimation using $\Delta\omega_{L^k}=|\omega_{L^k}-\omega_{L^{k-1}}|/2$ for order k, and tentatively consider the decreasing error for increasing k as indicative of convergence (see Table F.1).

Table F.1: *Error estimation for the WKB-based method used in Chapter 4, with* $M=Q=0.1$ *and* $L_{dS}=1$.

ℓ	$\mathfrak{Re}\{\omega_{L^2}\}$	$\mathfrak{Im}\{\omega_{L^2}\}$	$\Delta\mathfrak{Re}\{\omega_{L^0}\}$	$\Delta\mathfrak{Im}\{\omega_{L^0}\}$	$\Delta\mathfrak{Re}\{\omega_{L^1}\}$	$\Delta\mathfrak{Im}\{\omega_{L^1}\}$	$\Delta\mathfrak{Re}\{\omega_{L^2}\}$	$\Delta\mathfrak{Im}\{\omega_{L^2}\}$
1	3.2120	−0.9823	1.5160	0.4570	0.1808	0.4570	0.1808	0.0683
2	5.3550	−0.9367	2.6250	0.4570	0.3132	0.4570	0.3132	0.0683
3	7.500	−0.9254	3.7130	0.4570	0.4429	0.4570	0.4429	0.0683
4	9.6440	−0.9208	4.7930	0.4570	0.5718	0.4570	0.5718	0.0683
5	11.7900	−0.9185	5.8710	0.4570	0.7003	0.4570	0.7003	0.0683

To solve for the critical mass, we set $\mathfrak{Im}\{\omega_{-2}\}=0$[249]. Up to $\mathcal{O}(Q^4)$ and using $B=\Lambda M^2$,

$$\begin{aligned}
\mu^2_{crit} = & \frac{\left(3M^2\left(864c^2\left(9B\left(90B-17\right)+16\right)+\Lambda\left(252B\left(10593B+790\right)-93491\right)\right)+19231\right)}{17496M^2\left(6B+1\right)\left(126B-11\right)} \\
& -\frac{\left(8icQ^3\left(9B\left(1737B-470\right)+115\right)\right)\sqrt{1-9B}}{243\sqrt{3}\left(Q^4\left(6B+1\right)\left(126B-11\right)+4M^2Q^2\left(234B-11\right)\left(1-9B\right)+120M^4\left(1-9B\right)^2\right)} \\
& +\frac{\left(Q^2\left(9M^2\left(1080c^2\left(9B+2\right)-\Lambda\left(1350B+241\right)\right)+391\right)\right)\left(1-9B\right)}{3645\left(Q^4\left(6B+1\right)\left(126B-11\right)+4M^2Q^2\left(234B-11\right)\left(1-9B\right)+120M^4\left(1-9B\right)^2\right)} \\
& -\frac{16icM^2Q\left(99B-38\right)\left(1-9B\right)^{3/2}}{27\sqrt{3}\left(Q^4\left(6B+1\right)\left(126B-11\right)+4M^2Q^2\left(234B-11\right)\left(1-9B\right)+120M^4\left(1-9B\right)^2\right)}\,.
\end{aligned} \tag{F6}$$

References

[1] P. Laplace, *Exposition du système du monde*, 1st edition (L'imprimerie du Cercle-Social, Paris, 1796).

[2] C. Montgomery, W. Orchiston, and I. Whittingham, "Michell, Laplace and the origin of the black hole concept", Journal of Astronomical History and Heritage **12**, 90 (2009).

[3] R. L. Workman et al. (Particle Data Group), "Review of particle physics", PTEP **2022**, 083C01 (2022).

[4] C. W. Misner, K. S. Thorne, and J. A. Wheeler, *Gravitation* (W. H. Freeman, San Francisco, 1973).

[5] J. B. Hartle, *Gravity: An introduction to einstein's general relativity* (Cambridge University Press, Cambridge, 2021).

[6] S. W. Hawking and G. F. R. Ellis, *The large scale structure of space-time*, Cambridge Monographs on Mathematical Physics (Cambridge University Press, Cambridge, 1973).

[7] R. M. Wald, *General relativity* (Chicago Univ. Pr., Chicago, USA, 1984).

[8] R. d'Inverno, *Introducing einstein's relativity* (Oxford University Press, New York, 1992).

[9] H. Stephani, D. Kramer, M. MacCallum, C. Hoenselaers, and E. Herlt, *Exact solutions of einstein's field equations*, 2nd edition, Cambridge Monographs on Mathematical Physics (Cambridge University Press, Cambridge, 2003).

[10] G. T. Horowitz, "Black holes in four dimensions", in *Black holes in higher dimensions*, edited by G. T. Horowitz, 1st edition (Cambridge University Press, Cambridge, UK, 2012), pages 3–20.

[11] C. Van Den Broeck, "Probing dynamical spacetimes with gravitational waves", in *Springer handbook of spacetime*, edited by A. Ashtekar and V. Petkov (Springer, 2014), pages 589–613.

[12] C. Chirenti, "Black hole quasinormal modes in the era of LIGO", Braz. J. Phys. **48**, 102 (2018), arXiv:1708.04476 [gr-qc].

[13] V. Ferrari and L. Gualtieri, "Quasi-normal modes and gravitational wave astronomy", Gen. Rel. Grav. **40**, 945 (2008), arXiv:0709.0657 [gr-qc].

[14] E. Berti, V. Cardoso, and A. O. Starinets, "Quasinormal modes of black holes and black branes", Class. Quant. Grav. **26**, 163001 (2009), arXiv:0905.2975 [gr-qc].

[15] B. P. Abbott et al. (LIGO Scientific, Virgo), "A guide to LIGO–Virgo detector noise and extraction of transient gravitational-wave signals", Class. Quant. Grav. **37**, 055002 (2020), arXiv:1908.11170 [gr-qc].

[16] N. Christensen, "Stochastic gravitational wave backgrounds", Rept. Prog. Phys. **82**, 016903 (2019), arXiv:1811.08797 [gr-qc].

[17] P. Jaranowski and A. Krolak, "Gravitational-wave data analysis. Formalism and sample applications: The gaussian case", Living Rev. Rel. **8**, 3 (2005), arXiv:0711.1115 [gr-qc].

[18] J. L. Cervantes-Cota, S. Galindo-Uribarri, and G.-F. Smoot, "A brief history of gravitational waves", Universe **2**, 22 (2016), arXiv:1609.09400 [physics.hist-ph].

[19] B. P. Abbott et al. (LIGO Scientific, Virgo), "GWTC-1: A gravitational-wave transient catalog of compact binary mergers observed by LIGO and virgo during the first and second observing runs", Phys. Rev. X **9**, 031040 (2019), arXiv:1811.12907 [astro-ph.HE].

[20] R. Abbott et al. (LIGO Scientific, Virgo), "GWTC-2: Compact binary coalescences observed by LIGO and virgo during the first half of the third observing run", Phys. Rev. X **11**, 021053 (2021), arXiv:2010.14527 [gr-qc].

[21] R. Abbott et al. (KAGRA, VIRGO, LIGO Scientific), "GWTC-3: Compact binary coalescences observed by LIGO and Virgo during the second part of the third observing run", Phys. Rev. X **13**, 041039 (2023), arXiv:2111.03606 [gr-qc].

[22] K. Kuroda, "Status of LCGT", Class. Quant. Grav. **27**, edited by Z. Marka and S. Marka, 084004 (2010).

[23] S. L. Danilishin, F. Y. Khalili, and H. Miao, "Advanced quantum techniques for future gravitational-wave detectors", Living Rev. Rel. **22**, 2 (2019), arXiv:1903.05223 [gr-qc].

[24] C. S. Unnikrishnan, "IndIGO and LIGO-India: Scope and plans for gravitational wave research and precision metrology in India", Int. J. Mod. Phys. D **22**, 1341010 (2013).

[25] R. Abbott et al. (KAGRA, VIRGO, LIGO Scientific), "Sensitivity and performance of the Advanced LIGO detectors in the third observing run", Phys. Rev. D **102**, 062003 (2020), arXiv:2008.01301 [astro-ph.IM].

[26] Z. Arzoumanian et al., "The NANOGrav 12.5 yr data set: Search for an isotropic stochastic gravitational-wave background", Astrophys. J. Lett. **905**, L34 (2020).

[27] G. Agazie et al. (NANOGrav), "The NANOGrav 15 yr Data Set: Evidence for a Gravitational-wave Background", Astrophys. J. Lett. **951**, L8 (2023), arXiv:2306.16213 [astro-ph.HE].

[28] P. Amaro-Seoane et al., "Low-frequency gravitational-wave science with eLISA/NGO", Class. Quant. Grav. **29**, edited by M. Hannam, P. Sutton, S. Hild, and C. van den Broeck, 124016 (2012).

[29] D. Reitze et al., "Cosmic explorer: The U.S. contribution to gravitational-wave astronomy beyond LIGO", Bull. Am. Astron. Soc. **51**, 035 (2019).

[30] C. J. Moore, R. H. Cole, and C. P. L. Berry, "Gravitational-wave sensitivity curves", Class. Quant. Gravity **32**, 015014 (2014).

[31] C. M. Will, "The confrontation between general relativity and experiment", Living Rev. Rel. **17**, 4 (2014).

[32] W. Israel, "Event horizons in static vacuum space-times", Phys. Rev. **164**, 1776 (1967).

[33] W. Israel, "Event horizons in static electrovac space-times", Commun. Math. Phys. **8**, 245 (1968).

[34] B. Carter, "Axisymmetric black hole has only two degrees of freedom", Phys. Rev. Lett. **26**, 331 (1971).

[35] D. Andriot and G. Lucena Gómez, "Signatures of extra dimensions in gravitational waves", JCAP **06**, [Erratum: JCAP 05, E01 (2019)], 048 (2017), arXiv:1704.07392 [hep-th].

[36] L. Visinelli, N. Bolis, and S. Vagnozzi, "Brane-world extra dimensions in light of GW170817", Phys. Rev. D **97**, 064039 (2018), arXiv:1711.06628 [gr-qc].

[37] H. Yu, Z.-C. Lin, and Y.-X. Liu, "Gravitational waves and extra dimensions: a short review", Commun. Theor. Phys. **71**, 991 (2019), arXiv:1905.10614 [gr-qc].

[38] A. Kusenko and A. Mazumdar, "Gravitational waves from fragmentation of a primordial scalar condensate into Q-balls", Phys. Rev. Lett. **101**, 211301 (2008), arXiv:0807.4554 [astro-ph].

[39] M. Raidal, V. Vaskonen, and H. Veermäe, "Gravitational waves from primordial black hole mergers", JCAP **09**, 037 (2017), arXiv:1707.01480 [astro-ph.CO].

[40] M. Sasaki, T. Suyama, T. Tanaka, and S. Yokoyama, "Primordial black holes—perspectives in gravitational wave astronomy", Class. Quant. Grav. **35**, 063001 (2018), arXiv:1801.05235 [astro-ph.CO].

[41] E. Berti, V. Cardoso, J. A. Gonzalez, U. Sperhake, M. Hannam, S. Husa, and B. Bruegmann, "Inspiral, merger and ringdown of unequal mass black hole binaries: A Multipolar analysis", Phys. Rev. D **76**, 064034 (2007), arXiv:gr-qc/0703053.

[42] K. D. Kokkotas and B. G. Schmidt, "Quasinormal modes of stars and black holes", Living Rev. Rel. **2**, 2 (1999), arXiv:gr-qc/9909058.

[43] B. P. Abbott et al. (LIGO Scientific, Virgo), "Observation of gravitational waves from a binary black hole merger", Phys. Rev. Lett. **116**, 061102 (2016), arXiv:1602.03837 [gr-qc].

[44] C. V. Vishveshwara, "Stability of the Schwarzschild metric", Phys. Rev. D **1**, 2870 (1970).

[45] I. Kamaretsos, M. Hannam, and B. Sathyaprakash, "Is black-hole ringdown a memory of its progenitor?", Phys. Rev. Lett. **109**, 141102 (2012).

[46] N. Andersson and K. D. Kokkotas, Monthly Notices of the Royal Astronomical Society 1 **299**, 1059 (1998).

[47] R. A. Konoplya and A. Zhidenko, "Quasinormal modes of black holes: From astrophysics to string theory", Rev. Mod. Phys. **83**, 793 (2011), arXiv:1102.4014 [gr-qc].

[48] T. Nakamura, H. Nakano, and T. Tanaka, "Detecting quasinormal modes of binary black hole mergers with second-generation gravitational-wave detectors", Phys. Rev. D **93**, 044048 (2016), arXiv:1601.00356 [astro-ph.HE].

[49] E. Berti, V. Cardoso, and C. M. Will, "On gravitational-wave spectroscopy of massive black holes with the space interferometer LISA", Phys. Rev. D **73**, 064030 (2006), arXiv:gr-qc/0512160.

[50] S. R. Dolan and A. C. Ottewill, "Wave propagation and quasinormal mode excitation on schwarzschild spacetime", Phys. Rev. D **84**, 104002 (2011), arXiv:1106.4318 [gr-qc].

[51] N. Andersson, "Excitation of Schwarzschild black hole quasinormal modes", Phys. Rev. D **51**, 353 (1995).

[52] H.-P. Nollert and B. G. Schmidt, "Quasinormal modes of Schwarzschild black holes: Defined and calculated via Laplace transformation", Phys. Rev. D **45**, 2617 (1992).

[53] N. Fröman and P. O. Fröman, *JWKB approximation: Contributions to the theory*, 1st edition (North-Holland, Amsterdam, 1965).

[54] N. Andersson, M. E. Araujo, and B. F. Schutz, "The phase-integral method and black hole normal modes", Classical and Quantum Gravity **10**, 735 (1993).

[55] H. Yang, F. Zhang, A. Zimmerman, and Y. Chen, "Scalar Green function of the Kerr spacetime", Phys. Rev. D **89**, 064014 (2014), arXiv:1311.3380 [gr-qc].

[56] E. Berti and V. Cardoso, "Quasinormal ringing of kerr black holes. I. The excitation factors", Phys. Rev. D **74**, 104020 (2006), arXiv:gr-qc/0605118.

[57] N. Oshita, "Ease of excitation of black hole ringing: Quantifying the importance of overtones by the excitation factors", Phys. Rev. D **104**, 124032 (2021), arXiv:2109.09757 [gr-qc].

[58] B. P. Abbott et al. (LIGO Scientific, Virgo), "Tests of general relativity with the binary black hole signals from the LIGO-Virgo catalog GWTC-1", Phys. Rev. D **100**, 104036 (2019), arXiv:1903.04467 [gr-qc].

[59] R. Abbott et al. (LIGO Scientific, Virgo), "Tests of general relativity with binary black holes from the second LIGO-Virgo gravitational-wave transient catalog", Phys. Rev. D **103**, 122002 (2021), arXiv:2010.14529 [gr-qc].

[60] R. Abbott et al. (LIGO Scientific, VIRGO, KAGRA), "Tests of general relativity with GWTC-3", (2021), arXiv:2112.06861 [gr-qc].

[61] A. Ghosh, R. Brito, and A. Buonanno, "Constraints on quasinormal-mode frequencies with LIGO-Virgo binary–black-hole observations", Phys. Rev. D **103**, 124041 (2021), arXiv:2104.01906 [gr-qc].

[62] V. Baibhav, E. Berti, V. Cardoso, and G. Khanna, "Black hole spectroscopy: Systematic errors and ringdown energy estimates", Phys. Rev. D **97**, 044048 (2018), arXiv:1710.02156 [gr-qc].

[63] I. Ota and C. Chirenti, "Overtones or higher harmonics? Prospects for testing the no-hair theorem with gravitational wave detections", Phys. Rev. D **101**, 104005 (2020), arXiv:1911.00440 [gr-qc].

[64] V. Baibhav and E. Berti, "Multimode black hole spectroscopy", Phys. Rev. D **99**, 024005 (2019), arXiv:1809.03500 [gr-qc].

[65] E. Curiel, "The many definitions of a black hole", Nature Astron. **3**, 27 (2019), arXiv:1808.01507 [physics.hist-ph].

[66] K. Landsman, "Penrose's 1965 singularity theorem: from geodesic incompleteness to cosmic censorship", Gen. Rel. Grav. **54**, 115 (2022), arXiv:2205.01680 [physics.hist-ph].

[67] J. D. Bekenstein, "Quantum black holes as atoms", in 8th marcel grossmann meeting on recent developments in theoretical and experimental general relativity, gravitation and relativistic field theories (MG 8) (June 1997), arXiv:gr-qc/9710076.

[68] J. D. Bekenstein, "Black holes and the second law", Lett. Nuovo Cim. **4**, 737 (1972).

[69] J. D. Bekenstein, "The quantum mass spectrum of the Kerr black hole", Lett. Nuovo Cim. **11**, 467 (1974).

[70] S. W. Hawking, "Particle creation by black holes", Commun. Math. Phys. **43**, edited by G. W. Gibbons and S. W. Hawking, [Erratum: Commun.Math.Phys. 46, 206 (1976)], 199 (1975).

[71] G. W. Gibbons and S. W. Hawking, "Cosmological event horizons, thermodynamics, and particle creation", Phys. Rev. D **15**, 2738 (1977).

[72] H.-P. Nollert, "Quasinormal modes of Schwarzschild black holes: The determination of quasinormal frequencies with very large imaginary parts", Phys. Rev. D **47**, 5253 (1993).

[73] R. M. Wald, *Quantum field theory in curved space-time and black hole thermodynamics*, Chicago Lectures in Physics (University of Chicago Press, Chicago, IL, 1995).

[74] S. Hod, "Bohr's correspondence principle and the area spectrum of quantum black holes", Phys. Rev. Lett. **81**, 4293 (1998), arXiv:gr-qc/9812002.

[75] C. Vafa, "The String landscape and the swampland", (2005), arXiv:hep-th/0509212.

[76] E. Palti, "The swampland: Introduction and review", Fortsch. Phys. **67**, 1900037 (2019), arXiv:1903.06239 [hep-th].

[77] N. Arkani-Hamed, L. Motl, A. Nicolis, and C. Vafa, "The String landscape, black holes and gravity as the weakest force", JHEP **06**, 060 (2007), arXiv:hep-th/0601001.

[78] A. G. Riess et al. (Supernova Search Team), "Observational evidence from supernovae for an accelerating universe and a cosmological constant", Astron. J. **116**, 1009 (1998), arXiv:astro-ph/9805201.

[79] S. Perlmutter et al. (Supernova Cosmology Project), "Measurements of Ω and Λ from 42 high redshift supernovae", Astrophys. J. **517**, 565 (1999), arXiv:astro-ph/9812133.

[80] N. Aghanim et al. (Planck), "Planck 2018 results. VI. Cosmological parameters", Astron. Astrophys. **641**, [Erratum: Astron.Astrophys. 652, C4 (2021)], A6 (2020), arXiv:1807.06209 [astro-ph.CO].

[81] D. Anninos, "De sitter musings", Int. J. Mod. Phys. A **27**, 1230013 (2012), arXiv:1205.3855 [hep-th].

[82] A. Strominger, "The dS / CFT correspondence", JHEP **10**, 034 (2001), arXiv:hep-th/0106113.

[83] U. H. Danielsson and T. Van Riet, "What if string theory has no de Sitter vacua?", Int. J. Mod. Phys. D **27**, 1830007 (2018), arXiv:1804.01120 [hep-th].

[84] M. Dine, J. A. P. Law-Smith, S. Sun, D. Wood, and Y. Yu, "Obstacles to constructing de sitter space in string theory", JHEP **02**, 050 (2021), arXiv:2008.12399 [hep-th].

[85] B. P. Dolan, D. Kastor, D. Kubiznak, R. B. Mann, and J. Traschen, "Thermodynamic volumes and isoperimetric inequalities for de sitter black holes", Phys. Rev. D **87**, 104017 (2013), arXiv:1301.5926 [hep-th].

[86] S. W. Hawking, "Black hole explosions", Nature **248**, 30 (1974).

[87] R. Gregory, I. G. Moss, N. Oshita, and S. Patrick, "Black hole evaporation in de Sitter space", Class. Quant. Grav. **38**, 185005 (2021), arXiv:2103.09862 [gr-qc].

[88] B. P. Dolan, "The definition of mass in asymptotically de Sitter space-times", Class. Quant. Grav. **36**, 077001 (2019), arXiv:1808.09081 [gr-qc].

[89] I. Antoniadis and K. Benakli, "Weak gravity conjecture in de sitter space-time", Fortschritte der Physik **68**, 2000054 (2020), arXiv:2006.12512 [hep-th].

[90] R. M. Wald, "Gravitational collapse and cosmic censorship", in , EFI-97-43 (Oct. 1997), pages 69–85, arXiv:gr-qc/9710068.

[91] M. Montero, T. Van Riet, and G. Venken, "Festina lente: EFT constraints from charged black hole evaporation in de sitter", JHEP **01**, 039 (2020), arXiv:1910.01648 [hep-th].

[92] M. Montero, C. Vafa, T. Van Riet, and G. Venken, "The FL bound and its phenomenological implications", JHEP **10**, 009 (2021), arXiv:2106.07650 [hep-th].

[93] E. Berti et al., "Testing general relativity with present and future astrophysical observations", Class. Quant. Grav. **32**, 243001 (2015), arXiv:1501.07274 [gr-qc].

[94] R. Abbott et al. (LIGO Scientific, VIRGO, KAGRA), "Constraints on the cosmic expansion history from GWTC-3", (2021), arXiv:2111.03604 [astro-ph.CO].

[95] N. Yunes, K. Yagi, and F. Pretorius, "Theoretical physics implications of the binary black-hole mergers GW150914 and GW151226", Phys. Rev. D **94**, 084002 (2016), arXiv:1603.08955 [gr-qc].

[96] L. Barack et al., "Black holes, gravitational waves and fundamental physics: a roadmap", Class. Quant. Grav. **36**, 143001 (2019), arXiv:1806.05195 [gr-qc].

[97] D. J. Weir, "Gravitational waves from a first order electroweak phase transition: a brief review", Phil. Trans. Roy. Soc. Lond. A **376**, 20170126 (2018), arXiv:1705.01783 [hep-ph].

[98] R.-G. Cai, Z. Cao, Z.-K. Guo, S.-J. Wang, and T. Yang, "The gravitational-wave physics", Natl. Sci. Rev. **4**, 687 (2017), arXiv:1703.00187 [gr-qc].

[99] M. Bailes et al., "Gravitational-wave physics and astronomy in the 2020s and 2030s", Nature Rev. Phys. **3**, 344 (2021).

[100] N. Aggarwal et al., "Challenges and opportunities of gravitational-wave searches at MHz to GHz frequencies", Living Rev. Rel. **24**, 4 (2021), arXiv:2011.12414 [gr-qc].

[101] A. Alves, T. Ghosh, H.-K. Guo, K. Sinha, and D. Vagie, "Collider and gravitational wave complementarity in exploring the singlet extension of the standard model", JHEP **04**, 052 (2019), arXiv:1812.09333 [hep-ph].

[102] R. Caldwell et al., "Detection of early-universe gravitational-wave signatures and fundamental physics", Gen. Rel. Grav. **54**, 156 (2022), arXiv:2203.07972 [gr-qc].

[103] W.-C. Huang, F. Sannino, and Z.-W. Wang, "Gravitational waves from pati-salam dynamics", Phys. Rev. D **102**, 095025 (2020), arXiv:2004.02332 [hep-ph].

[104] S. Chigusa, Y. Nakai, and J. Zheng, "Implications of gravitational waves for supersymmetric grand unification", Phys. Rev. D **104**, 035031 (2021), arXiv:2011.04090 [hep-ph].

[105] S. F. King, S. Pascoli, J. Turner, and Y.-L. Zhou, "Confronting SO(10) GUTs with proton decay and gravitational waves", JHEP **10**, 225 (2021), arXiv:2106.15634 [hep-ph].

[106] J. A. Dror, T. Hiramatsu, K. Kohri, H. Murayama, and G. White, "Testing the seesaw mechanism and leptogenesis with gravitational waves", Phys. Rev. Lett. **124**, 041804 (2020), arXiv:1908.03227 [hep-ph].

[107] W. Buchmuller, V. Domcke, H. Murayama, and K. Schmitz, "Probing the scale of grand unification with gravitational waves", Phys. Lett. B **809**, 135764 (2020), arXiv:1912.03695 [hep-ph].

[108] V. Cardoso, L. Gualtieri, and C. J. Moore, "Gravitational waves and higher dimensions: Love numbers and Kaluza-Klein excitations", Phys. Rev. D **100**, 124037 (2019), arXiv:1910.09557 [gr-qc].

[109] O.-K. Kwon, S. Lee, and D. D. Tolla, "Gravitational waves as a probe of the extra dimension", Phys. Rev. D **100**, 084050 (2019).

[110] Y. Du, S. Tahura, D. Vaman, and K. Yagi, "Probing compactified extra dimensions with gravitational waves", Phys. Rev. D **103**, 044031 (2021).

[111] C. Ferko, G. Satishchandran, and S. Sethi, "Gravitational memory and compact extra dimensions", Phys. Rev. D **105**, 024072 (2022).

[112] D. Andriot and D. Tsimpis, "Gravitational waves in warped compactifications", JHEP **06**, 100 (2020), arXiv:1911.01444 [hep-th].

[113] D. Andriot, P. Marconnet, and D. Tsimpis, "Warp factor and the gravitational wave spectrum", JCAP **07**, 040 (2021), arXiv:2103.09240 [hep-th].

[114] B. P. Abbott et al. (LIGO Scientific, Virgo), "Properties of the binary black hole merger GW150914", Phys. Rev. Lett. **116**, 241102 (2016), arXiv:1602.03840 [gr-qc].

[115] B. P. Abbott et al. (LIGO Scientific, Virgo), "Tests of general relativity with GW150914", Phys. Rev. Lett. **116**, [Erratum: Phys.Rev.Lett. 121, 129902 (2018)], 221101 (2016), arXiv:1602.03841 [gr-qc].

[116] V. Baibhav, E. Berti, and V. Cardoso, "LISA parameter estimation and source localization with higher harmonics of the ringdown", Phys. Rev. D **101**, 084053 (2020), arXiv:2001.10011 [gr-qc].

[117] I. Ota and C. Chirenti, "Black hole spectroscopy horizons for current and future gravitational wave detectors", Phys. Rev. D **105**, 044015 (2022), arXiv:2108.01774 [gr-qc].

[118] S. Bhagwat, C. Pacilio, E. Barausse, and P. Pani, "The landscape of massive black-hole spectroscopy with LISA and Einstein Telescope", (2021), arXiv:2201.00023 [gr-qc].

[119] G. Carullo, W. Del Pozzo, and J. Veitch, "Observational black hole spectroscopy: A time-domain multimode analysis of GW150914", Phys. Rev. D **99**, [Erratum: Phys.Rev.D 100, 089903 (2019)], 123029 (2019), arXiv:1902.07527 [gr-qc].

[120] C. D. Capano, M. Cabero, J. Westerweck, J. Abedi, S. Kastha, A. H. Nitz, A. B. Nielsen, and B. Krishnan, "Observation of a multimode quasi-normal spectrum from a perturbed black hole", (2021), arXiv:2105.05238 [gr-qc].

[121] R. Cotesta, G. Carullo, E. Berti, and V. Cardoso, "Analysis of ringdown overtones in GW150914", Phys. Rev. Lett. **129**, 111102 (2022), arXiv:2201.00822 [gr-qc].

[122] G. Carullo et al., "Empirical tests of the black hole no-hair conjecture using gravitational-wave observations", Phys. Rev. D **98**, 104020 (2018), arXiv:1805.04760 [gr-qc].

[123] M. Isi, M. Giesler, W. M. Farr, M. A. Scheel, and S. A. Teukolsky, "Testing the no-hair theorem with GW150914", Phys. Rev. Lett. **123**, 111102 (2019), arXiv:1905.00869 [gr-qc].

[124] M. Isi and W. M. Farr, "Revisiting the ringdown of GW150914", (2022), arXiv:2202.02941 [gr-qc].

[125] L. Randall and R. Sundrum, "An alternative to compactification", Phys. Rev. Lett. **83**, 4690 (1999), arXiv:hep-th/9906064.

[126] T. Shiromizu, K.-i. Maeda, and M. Sasaki, "The Einstein equation on the 3-brane world", Phys. Rev. D **62**, 024012 (2000), arXiv:gr-qc/9910076.

[127] A. K. Mishra, A. Ghosh, and S. Chakraborty, "Constraining extra dimensions using observations of black hole quasi-normal modes", (2021), arXiv:2106.05558 [gr-qc].

[128] D. Andriot, G. Cacciapaglia, A. Deandrea, N. Deutschmann, and D. Tsimpis, "Towards kaluza-klein dark matter on nilmanifolds", JHEP **06**, 169 (2016), arXiv:1603.02289 [hep-th].

[129] M. Kac, "Can one hear the shape of a drum?", Am. Math. Mon. **73**, 1 (1966).

[130] H.-P. Nollert, "Quasinormal modes: the characteristic 'sound' of black holes and neutron stars", Class. Quant. Grav. **16**, R159 (1999).

[131] S. Chandrasekhar, *The mathematical theory of black holes* (Oxford Univerity Press, New York, 1983).

[132] J. A. H. Futterman, F. A. Handler, and R. A. Matzner, *Scattering from black holes*, Cambridge Monographs on Mathematical Physics (Cambridge University Press, Cambridge, 1988).

[133] R. Brito, V. Cardoso, and P. Pani, *Superradiance* (Springer International Publishing, 2020), arXiv:1501.06570 [gr-qc].

[134] T. Regge and J. A. Wheeler, "Stability of a schwarzschild singularity", Phys. Rev. **108**, 1063 (1957).

[135] H. Kodama and A. Ishibashi, "A Master equation for gravitational perturbations of maximally symmetric black holes in higher dimensions", Prog. Theor. Phys. **110**, 701 (2003), arXiv:hep-th/0305147.

[136] A. Ishibashi and H. Kodama, "Stability of higher dimensional Schwarzschild black holes", Prog. Theor. Phys. **110**, 901 (2003), arXiv:hep-th/0305185.

[137] H. Kodama and A. Ishibashi, "Master equations for perturbations of generalized static black holes with charge in higher dimensions", Prog. Theor. Phys. **111**, 29 (2004), arXiv:hep-th/0308128.

[138] F. J. Zerilli, "Gravitational field of a particle falling in a schwarzschild geometry analyzed in tensor harmonics", Phys. Rev. D **2**, 2141 (1970).

[139] N. Anderson and B. Jensen, "Chapter 5.1.1 - Scattering by black holes", in *Scattering*, edited by R. Pike and P. Sabatier (Academic Press, London, 2002), pages 1607–1626, arXiv:gr-qc/0011025.

[140] E. W. Leaver, "Spectral decomposition of the perturbation response of the Schwarzschild geometry", Phys. Rev. D **34**, 384 (1986).

[141] M. Davis, R. Ruffini, W. H. Press, and R. H. Price, "Gravitational radiation from a particle falling radially into a Schwarzschild black hole", Phys. Rev. Lett. **27**, 1466 (1971).

[142] C. Gundlach, R. H. Price, and J. Pullin, "Late time behavior of stellar collapse and explosions: 1. Linearized perturbations", Phys. Rev. D **49**, 883 (1994).

[143] E. W. Leaver, "An analytic representation for the quasi normal modes of Kerr black holes", Proc. Roy. Soc. Lond. A **402**, 285 (1985).

[144] O. J. C. Dias, P. Figueras, R. Monteiro, J. E. Santos, and R. Emparan, "Instability and new phases of higher-dimensional rotating black holes", Phys. Rev. D **80**, 111701 (2009).

[145] O. J. C. Dias, P. Figueras, R. Monteiro, H. S. Reall, and J. E. Santos, "An instability of higher-dimensional rotating black holes", JHEP **05**, 076 (2010).

[146] H. Ciftci, R. L. Hall, and N. Saad, "Asymptotic iteration method for eigenvalue problems", J. Phys. A. Math. Gen. **36**, 11807 (2003).

[147] H. T. Cho, A. S. Cornell, J. Doukas, and W. Naylor, "Black hole quasinormal modes using the asymptotic iteration method", Class. Quant. Grav. **27**, 155004 (2010), arXiv:0912.2740 [gr-qc].

[148] G. T. Horowitz and V. E. Hubeny, "Quasinormal modes of AdS black holes and the approach to thermal equilibrium", Phys. Rev. D **62**, 024027 (2000), arXiv:hep-th/9909056.

[149] G. Pöschl and E. Teller, "Bemerkungen zur quantenmechanik des anharmonischen oszillators", Z. Phys. **83**, 143 (1933).

[150] H.-J. Blome and B. Mashhoon, "Quasi-normal oscillations of a schwarzschild black hole", Physics Letters A **100**, 231 (1984).

[151] B. F. Schutz and C. M. Will, "Black hole normal modes - A semianalytic approach", Astrophys. J. **291**, L33 (1985).

[152] C. M. Will, "Approximation methods in gravitational-radiation theory", Can. J. Phys. **64**, 140 (1986).

[153] S. Iyer and C. M. Will, "Black-hole normal modes: A WKB approach. I. Foundations and application of a higher-order WKB analysis of potential-barrier scattering", Phys. Rev. D **35**, 3621 (1987).

[154] R. A. Konoplya, "Quasinormal behavior of the d-dimensional Schwarzschild black hole and higher order WKB approach", Phys. Rev. D **68**, 024018 (2003), arXiv:gr-qc/0303052.

[155] R. A. Konoplya, A. Zhidenko, and A. F. Zinhailo, "Higher order WKB formula for quasinormal modes and grey-body factors: recipes for quick and accurate calculations", Class. Quant. Grav. **36**, 155002 (2019), arXiv:1904.10333 [gr-qc].

[156] S. R. Dolan and A. C. Ottewill, "On an expansion method for black hole quasinormal modes and Regge poles", Class. Quant. Grav. **26**, 225003 (2009), arXiv:0908.0329 [gr-qc].

[157] C. J. Goebel, "Comments on the "vibrations" of a black hole", Astrophys. J. **172** (1972).

[158] C.-H. Chen, H.-T. Cho, A. Chrysostomou, and A. S. Cornell, "Quasinormal modes for integer and half-integer spins within the large angular momentum limit", Phys. Rev. D **104**, 024009 (2021), arXiv:2103.07777 [gr-qc].

[159] P. Grandclement and J. Novak, "Spectral methods for numerical relativity", Living Rev. Rel. **12**, 1 (2009), arXiv:0706.2286 [gr-qc].

[160] Ó. J. C. Dias, J. E. Santos, and B. Way, "Numerical methods for finding stationary gravitational solutions", Class. Quant. Grav. **33**, 133001 (2016), arXiv:1510.02804 [hep-th].

[161] N. Andersson, "On the asymptotic distribution of quasinormal-mode frequencies for Schwarzschild black holes", Class. Quant. Gravity **10**, L61 (1993).

[162] V. Ferrari and B. Mashhoon, "New approach to the quasinormal modes of a black hole", Phys. Rev. D **30**, 295 (1984).

[163] V. Ferrari and B. Mashhoon, "Oscillations of a black hole", Phys. Rev. Lett. **52**, 1361 (1984).

[164] M. Abramowitz and I. A. Stegun, *Handbook of mathematical functions with national bureau of standards applied mathematics series*, 6th edition (U.S. Government Printing Office, Washington D.C., 1964).

[165] J. Percival and S. R. Dolan, "Quasinormal modes of massive vector fields on the Kerr spacetime", Phys. Rev. D **102**, 104055 (2020), arXiv:2008.10621 [gr-qc].

[166] J. Matyjasek and M. Opala, "Quasinormal modes of black holes. The improved semianalytic approach", Phys. Rev. D **96**, 024011 (2017).

[167] J. Matyjasek and M. Telecka, "Quasinormal modes of black holes. II. Padé summation of the higher-order WKB terms", Phys. Rev. D **100**, 124006 (2019).

[168] V. Cardoso, A. S. Miranda, E. Berti, H. Witek, and V. T. Zanchin, "Geodesic stability, Lyapunov exponents, and quasinormal modes", Phys. Rev. D **79**, 4016 (2009).

[169] Q.-Y. Pan and J.-L. Jing, "Quasinormal modes of the Schwarzschild black hole with arbitrary spin fields: Numerical analysis", Mod. Phys. Lett. A **21**, 2671 (2006).

[170] F.-W. Shu and Y.-G. Shen, "Quasinormal modes in Schwarschild black holes due to arbitrary spin fields", Phys. Lett. B **619**, 340 (2005), arXiv:gr-qc/0501098.

[171] A. Zhidenko, "Quasi-normal modes of Schwarzschild-de Sitter black holes", Class. Quantum Gravity **21**, 273 (2004).

[172] R. A. Konoplya and A. Zhidenko, "Analytic expressions for quasinormal modes and grey-body factors in the eikonal limit and beyond", Class. Quant. Grav. **40**, 245005 (2023), arXiv:2309.02560 [gr-qc].

[173] R. A. Konoplya and Z. Stuchlík, "Are eikonal quasinormal modes linked to the unstable circular null geodesics?", Phys. Lett. B **771**, 597 (2017), arXiv:1705.05928 [gr-qc].

[174] R. A. Konoplya, "Further clarification on quasinormal modes/circular null geodesics correspondence", Phys. Lett. B **838**, 137674 (2023), arXiv:2210.08373 [gr-qc].

[175] J. M. Bardeen, W. H. Press, and S. A. Teukolsky, "Rotating black holes: Locally nonrotating frames, energy extraction, and scalar synchrotron radiation", Astrophys. J. **178**, 347 (1972).

[176] L. E. Simone and C. M. Will, "Massive scalar quasinormal modes of Schwarzschild and Kerr black holes", Class. Quant. Grav. **9**, 963 (1992).

[177] A. Ohashi and M.-a. Sakagami, "Massive quasi-normal mode", Class. Quant. Grav. **21**, 3973 (2004), arXiv:gr-qc/0407009.

[178] R. A. Konoplya and A. V. Zhidenko, "Decay of massive scalar field in a Schwarzschild background", Phys. Lett. B **609**, 377 (2005), arXiv:gr-qc/0411059.

[179] S. R. Dolan, "Instability of the massive Klein-Gordon field on the Kerr spacetime", Phys. Rev. D **76**, 084001 (2007), arXiv:0705.2880 [gr-qc].

[180] J. G. Rosa and S. R. Dolan, "Massive vector fields on the Schwarzschild spacetime: quasi-normal modes and bound states", Phys. Rev. D **85**, 044043 (2012), arXiv:1110.4494 [hep-th].

[181] Y. Decanini, A. Folacci, and B. Raffaelli, "Resonance and absorption spectra of the Schwarzschild black hole for massive scalar perturbations: a complex angular momentum analysis", Phys. Rev. D **84**, 084035 (2011), arXiv:1108.5076 [gr-qc].

[182] A. Chrysostomou, A. Cornell, A. Deandrea, É. Ligout, and D. Tsimpis, "Black holes and nilmanifolds: quasinormal modes as the fingerprints of extra dimensions?", Eur. Phys. J. C **83**, 325 (2023), arXiv:2211.08489 [gr-qc].

[183] M. Lagos, P. G. Ferreira, and O. J. Tattersall, "Anomalous decay rate of quasinormal modes", Phys. Rev. D **101**, 084018 (2020), arXiv:2002.01897 [gr-qc].

[184] H. Furuhashi and Y. Nambu, "Instability of massive scalar fields in Kerr-Newman space-time", Prog. Theor. Phys. **112**, 983 (2004), arXiv:gr-qc/0402037.

[185] A. A. Starobinsky, "Amplification of waves reflected from a rotating "black hole".", Sov. Phys. JETP **37**, 28 (1973).

[186] A. A. Starobinskil and S. M. Churilov, "Amplification of electromagnetic and gravitational waves scattered by a rotating "black hole"", Sov. Phys. JETP **65**, 1 (1974).

[187] J. D. Bekenstein, "Extraction of energy and charge from a black hole", Phys. Rev. D **7**, 949 (1973).

[188] R. Brito, S. Ghosh, E. Barausse, E. Berti, V. Cardoso, I. Dvorkin, A. Klein, and P. Pani, "Stochastic and resolvable gravitational waves from ultralight bosons", Phys. Rev. Lett. **119**, 131101 (2017), arXiv:1706.05097 [gr-qc].

[189] R. Brito, S. Ghosh, E. Barausse, E. Berti, V. Cardoso, I. Dvorkin, A. Klein, and P. Pani, "Gravitational wave searches for ultralight bosons with LIGO and LISA", Phys. Rev. D **96**, 064050 (2017), arXiv:1706.06311 [gr-qc].

[190] O. A. Hannuksela, K. W. K. Wong, R. Brito, E. Berti, and T. G. F. Li, "Probing the existence of ultralight bosons with a single gravitational-wave measurement", Nature Astron. **3**, 447 (2019), arXiv:1804.09659 [astro-ph.HE].

[191] A. Arvanitaki, S. Dimopoulos, S. Dubovsky, N. Kaloper, and J. March-Russell, "String axiverse", Phys. Rev. D **81**, 123530 (2010), arXiv:0905.4720 [hep-th].

[192] E. Berti, "A black-hole primer: Particles, waves, critical phenomena and superradiant instabilities", in (Oct. 2014), arXiv:1410.4481 [gr-qc].

[193] M. Casals, S. Dolan, A. C. Ottewill, and B. Wardell, "Self-force and green function in schwarzschild spacetime via quasinormal modes and branch cut", Phys. Rev. D **88**, 044022 (2013), arXiv:1306.0884 [gr-qc].

[194] S. Mano, H. Suzuki, and E. Takasugi, "Analytic solutions of the Teukolsky equation and their low frequency expansions", Prog. Theor. Phys. **95**, 1079 (1996), arXiv:gr-qc/9603020.

[195] S. Mano, H. Suzuki, and E. Takasugi, "Analytic solutions of the Regge-Wheeler equation and the postMinkowskian expansion", Prog. Theor. Phys. **96**, 549 (1996), arXiv:gr-qc/9605057.

[196] S. Bhattacharya and A. Lahiri, "Black-hole no-hair theorems for a positive cosmological constant", Phys. Rev. Lett. **99**, 201101 (2007), arXiv:gr-qc/0702006.

[197] L. J. Romans, "Supersymmetric, cold and lukewarm black holes in cosmological Einstein-Maxwell theory", Nucl. Phys. B **383**, 395 (1992), arXiv:hep-th/9203018.

[198] F. Belgiorno, S. L. Cacciatori, and F. Dalla Piazza, "Pair-production of charged Dirac particles on charged Nariai and ultracold black hole manifolds", JHEP **08**, 028 (2009), arXiv:0906.1520 [gr-qc].

[199] F. Belgiorno, S. L. Cacciatori, and F. Dalla Piazza, "Quantum instability for charged scalar particles on charged Nariai and ultracold black hole manifolds", Class. Quant. Grav. **27**, 055011 (2010), arXiv:0909.1454 [gr-qc].

[200] R. Bousso, "Charged Nariai black holes with a dilaton", Phys. Rev. D **55**, 3614 (1997), arXiv:gr-qc/9608053.

[201] J. D. Bekenstein, "Black holes and information theory", Contemp. Phys. **45**, 31 (2003), arXiv:quant-ph/0311049.

[202] P. R. Brady, I. G. Moss, and R. C. Myers, "Cosmic censorship: As strong as ever", Phys. Rev. Lett. **80**, 3432 (1998), arXiv:gr-qc/9801032.

[203] O. J. C. Dias, H. S. Reall, and J. E. Santos, "Strong cosmic censorship for charged de Sitter black holes with a charged scalar field", Class. Quant. Grav. **36**, 045005 (2019), arXiv:1808.04832 [gr-qc].

[204] A. Chrysostomou, A. S. Cornell, A. Deandrea, H. Noshad, and S. C. Park, "Reissner-Nordström black holes in de Sitter space-time: bounds with quasinormal frequencies", (2023), arXiv:2310.07311 [gr-qc].

[205] D. R. Brill and S. A. Hayward, "Global structure of a black hole cosmos and its extremes", Class. Quant. Grav. **11**, 359 (1994), arXiv:gr-qc/9304007.

[206] R. B. Mann and S. F. Ross, "Cosmological production of charged black hole pairs", Phys. Rev. D **52**, 2254 (1995), arXiv:gr-qc/9504015.

[207] R. Bousso, "Quantum global structure of de Sitter space", Phys. Rev. D **60**, 063503 (1999), arXiv:hep-th/9902183.

[208] J. Natário and R. Schiappa, "On the classification of asymptotic quasinormal frequencies for d-dimensional black holes and quantum gravity", Adv. Theor. Math. Phys. **8**, 1001 (2004), arXiv:hep-th/0411267.

[209] K. Ban, D. Y. Cheong, H. Okada, H. Otsuka, J.-C. Park, and S. C. Park, "Phenomenological implications on a hidden sector from the festina lente bound", PTEP **2023**, 013B04 (2023).

[210] S. M. Lee, D. Y. Cheong, S. C. Hyun, S. C. Park, and M.-S. Seo, "Festina-Lente bound on Higgs vacuum structure and inflation", JHEP **02**, 100 (2022), arXiv:2111.04010 [hep-ph].

[211] R. Penrose, "Gravitational collapse and space-time singularities", Phys. Rev. Lett. **14**, 57 (1965).

[212] R. Penrose, "Gravitational collapse: The role of general relativity", Riv. Nuovo Cim. **1**, 252 (1969).

[213] S. W. Hawking and R. Penrose, "The Singularities of gravitational collapse and cosmology", Proc. Roy. Soc. Lond. A **314**, 529 (1970).

[214] R. Bousso and S. W. Hawking, "Pair creation of black holes during inflation", Phys. Rev. D **54**, 6312 (1996), arXiv:gr-qc/9606052.

[215] J. R. Oppenheimer and H. Snyder, "On continued gravitational contraction", Phys. Rev. **56**, 455 (1939).

[216] R. Penrose, "The question of cosmic censorship", Journal of Astrophysics and Astronomy **20**, 233 (1999).

[217] M. Simpson and R. Penrose, "Internal instability in a reissner-nordstrom black hole", Int. J. Theor. Phys. **7**, 183 (1973).

[218] T. Crisford, G. T. Horowitz, and J. E. Santos, "Testing the weak gravity - cosmic censorship connection", Phys. Rev. D **97**, 066005 (2018), arXiv:1709.07880 [hep-th].

[219] F. Rossetti, "Strong cosmic censorship for the spherically symmetric Einstein-Maxwell-charged-Klein-Gordon system with positive Λ: stability of the Cauchy horizon and H^1 extensions", (2023), arXiv:2309.14420 [gr-qc].

[220] J. Sbierski, "The C_0-inextendibility of the Schwarzschild spacetime and the spacelike diameter in Lorentzian geometry", J. Diff. Geom. **108**, 319 (2018), arXiv:1507.00601 [gr-qc].

[221] S. Hawking, "Singularities and the geometry of spacetime (1966 Adams Prize Essay)", Eur. Phys. J. H **39**, 403 (2014).

[222] R. Penrose, "Naked singularities", Annals N. Y. Acad. Sci. **224**, 125 (1973).

[223] M. Dafermos, "Black holes without spacelike singularities", Commun. Math. Phys. **332**, 729 (2014), arXiv:1201.1797 [gr-qc].

[224] M. Dafermos and Y. Shlapentokh-Rothman, "Rough initial data and the strength of the blue-shift instability on cosmological black holes with $\Lambda > 0$", Class. Quant. Grav. **35**, 195010 (2018), arXiv:1805.08764 [gr-qc].

[225] D. Christodoulou, "The formation of black holes in general relativity", in 12th marcel grossmann meeting on general relativity (May 2008), pages 24–34, arXiv:0805.3880 [gr-qc].

[226] M. Dafermos and J. Luk, "The interior of dynamical vacuum black holes I: The C^0-stability of the Kerr Cauchy horizon", (2017), arXiv:1710.01722 [gr-qc].

[227] M. Dafermos, I. Rodnianski, and Y. Shlapentokh-Rothman, "A scattering theory for the wave equation on Kerr black hole exteriors", 10.24033/asens.2358 (2014), arXiv:1412.8379 [gr-qc].

[228] S. A. Teukolsky, "Perturbations of a rotating black hole. 1. Fundamental equations for gravitational electromagnetic and neutrino field perturbations", Astrophys. J. **185**, 635 (1973).

[229] W. H. Press and S. A. Teukolsky, "Perturbations of a rotating black hole. II. Dynamical stability of the kerr metric", Astrophys. J. **185**, 649 (1973).

[230] J. Luk and S.-J. Oh, "Proof of linear instability of the Reissner–Nordström Cauchy horizon under scalar perturbations", Duke Math. J. **166**, 437 (2017), arXiv:1501.04598 [gr-qc].

[231] P. Hintz and A. Vasy, "Analysis of linear waves near the Cauchy horizon of cosmological black holes", J. Math. Phys. **58**, 081509 (2017), arXiv:1512.08004 [math.AP].

[232] J. L. Costa and A. T. Franzen, "Bounded energy waves on the black hole interior of Reissner-Nordström-de Sitter", Annales Henri Poincare **18**, 3371 (2017), arXiv:1607.01018 [gr-qc].

[233] A. T. Franzen, "Boundedness of massless scalar waves on reissner-nordström interior backgrounds", Commun. Math. Phys. **343**, 601 (2016), arXiv:1407.7093 [gr-qc].

[234] M. Dafermos and I. Rodnianski, "A Proof of Price's law for the collapse of a selfgravitating scalar field", Invent. Math. **162**, 381 (2005), arXiv:gr-qc/0309115.

[235] A. Ishibashi and H. Kodama, "Perturbations and stability of static black holes in higher dimensions", Prog. Theor. Phys. Suppl. **189**, 165 (2011), arXiv:1103.6148 [hep-th].

[236] M. Dafermos and I. Rodnianski, "The Wave equation on Schwarzschild-de Sitter spacetimes", (2007), arXiv:0709.2766 [gr-qc].

[237] O. J. C. Dias, H. S. Reall, and J. E. Santos, "Strong cosmic censorship: taking the rough with the smooth", JHEP **10**, 001 (2018), arXiv:1808.02895 [gr-qc].

[238] Y. Hatsuda, "Quasinormal modes of black holes and Borel summation", Phys. Rev. D **101**, 024008 (2020), arXiv:1906.07232 [gr-qc].

[239] R. A. Konoplya and A. Zhidenko, "Charged scalar field instability between the event and cosmological horizons", Phys. Rev. D **90**, 064048 (2014), arXiv:1406.0019 [hep-th].

[240] S. Hod, "The instability spectra of near-extremal Reissner-Nordström-de Sitter black holes", Phys. Lett. B **786**, [Erratum: Phys.Lett.B 796, 256 (2019)], 217 (2018), arXiv:1808.04077 [gr-qc].

[241] O. J. C. Dias and J. E. Santos, "Origin of the reissner-nordström–de sitter instability", Phys. Rev. D **102**, 124039 (2020), arXiv:2005.03673 [hep-th].

[242] Z. Zhu, S.-J. Zhang, C. E. Pellicer, B. Wang, and E. Abdalla, "Stability of Reissner-Nordström black hole in de Sitter background under charged scalar perturbation", Phys. Rev. D **90**, [Addendum: Phys.Rev.D 90, 049904 (2014)], 044042 (2014), arXiv:1405.4931 [hep-th].

[243] R. A. Konoplya and A. Zhidenko, "Instability of higher dimensional charged black holes in the de-Sitter world", Phys. Rev. Lett. **103**, 161101 (2009), arXiv:0809.2822 [hep-th].

[244] R. A. Konoplya and A. Zhidenko, "Instability of D-dimensional extremally charged Reissner-Nordstrom(-de Sitter) black holes: Extrapolation to arbitrary D", Phys. Rev. D **89**, 024011 (2014), arXiv:1309.7667 [hep-th].

[245] O. J. C. Dias, F. C. Eperon, H. S. Reall, and J. E. Santos, "Strong cosmic censorship in de Sitter space", Phys. Rev. D **97**, 104060 (2018), arXiv:1801.09694 [gr-qc].

[246] V. Cardoso, J. L. Costa, K. Destounis, P. Hintz, and A. Jansen, "Quasinormal modes and strong cosmic censorship", Phys. Rev. Lett. **120**, 031103 (2018), arXiv:1711.10502 [gr-qc].

[247] R. A. Konoplya, "Two regimes of asymptotic fall-off of a massive scalar field in the Schwarzschild–de Sitter spacetime", Phys. Rev. D **109**, 104018 (2024), arXiv:2401.17106 [gr-qc].

[248] R. D. B. Fontana, P. A. González, E. Papantonopoulos, and Y. Vásquez, "Anomalous decay rate of quasinormal modes in Reissner-Nordström black holes", Phys. Rev. D **103**, 064005 (2021), arXiv:2011.10620 [gr-qc].

[249] P. A. González, E. Papantonopoulos, J. Saavedra, and Y. Vásquez, "Quasinormal modes for massive charged scalar fields in Reissner-Nordström dS black holes: anomalous decay rate", JHEP **06**, 150 (2022), arXiv:2204.01570 [gr-qc].

[250] C. M. Bender and T. T. Wu, "Anharmonic oscillator", Phys. Rev. **184**, 1231 (1969).

[251] R. A. Konoplya and A. Zhidenko, "Bernstein spectral method for quasinormal modes of a generic black hole spacetime and application to instability of dilaton–de Sitter solution", Phys. Rev. D **107**, 044009 (2023), arXiv:2211.02997 [gr-qc].

[252] Y. Mo, Y. Tian, B. Wang, H. Zhang, and Z. Zhong, "Strong cosmic censorship for the massless charged scalar field in the Reissner-Nordstrom–de Sitter spacetime", Phys. Rev. D **98**, 124025 (2018), arXiv:1808.03635 [gr-qc].

[253] V. Cardoso, J. L. Costa, K. Destounis, P. Hintz, and A. Jansen, "Strong cosmic censorship in charged black-hole spacetimes: still subtle", Phys. Rev. D **98**, 104007 (2018), arXiv:1808.03631 [gr-qc].

[254] Y. Gim and B. Gwak, "Charged particle and strong cosmic censorship in Reissner–Nordström–de Sitter black holes", Phys. Rev. D **100**, 124001 (2019), arXiv:1901.11214 [gr-qc].

[255] R. A. Konoplya and A. Zhidenko, "How general is the strong cosmic censorship bound for quasinormal modes?", JCAP **11**, 028 (2022), arXiv:2210.04314 [gr-qc].

[256] S. R. Dolan, "The Quasinormal Mode Spectrum of a Kerr Black Hole in the Eikonal Limit", Phys. Rev. D **82**, 104003 (2010), arXiv:1007.5097 [gr-qc].

[257] S. Hod, "Black holes that are too cold to respect cosmic censorship", Int. J. Mod. Phys. D **32**, 2341004 (2023), arXiv:2305.08918 [gr-qc].

[258] M. Berger, *A panoramic view of riemannian geometry* (Springer Berlin, Berlin, 2013).

[259] T. Needham, *Visual complex analysis* (Clarendon Press, Oxford, 2012).

[260] S. S. Haque, G. Shiu, B. Underwood, and T. Van Riet, "Minimal simple de Sitter solutions", Phys. Rev. D **79**, 086005 (2009), arXiv:0810.5328 [hep-th].

[261] D. Andriot and J. Blåbäck, "Refining the boundaries of the classical de Sitter landscape", JHEP **03**, [Erratum: JHEP 03, 083 (2018)], 102 (2017), arXiv:1609.00385 [hep-th].

[262] D. Andriot, L. Horer, and P. Marconnet, "Charting the landscape of (anti-) de Sitter and Minkowski solutions of 10d supergravities", JHEP **06**, 131 (2022), arXiv:2201.04152 [hep-th].

[263] G. D. Starkman, D. Stojkovic, and M. Trodden, "Homogeneity, flatness and 'large' extra dimensions", Phys. Rev. Lett. **87**, 231303 (2001), arXiv:hep-th/0106143.

[264] C.-M. Chen, P.-M. Ho, I. P. Neupane, N. Ohta, and J. E. Wang, "Hyperbolic space cosmologies", JHEP **10**, 058 (2003), arXiv:hep-th/0306291.

[265] I. P. Neupane, "Accelerating cosmologies from exponential potentials", Class. Quant. Grav. **21**, 4383 (2004), arXiv:hep-th/0311071.

[266] D. Orlando and S. C. Park, "Compact hyperbolic extra dimensions: a M-theory solution and its implications for the LHC", JHEP **08**, 006 (2010), arXiv:1006.1901 [hep-th].

[267] L. Randall and R. Sundrum, "A Large mass hierarchy from a small extra dimension", Phys. Rev. Lett. **83**, 3370 (1999), arXiv:hep-ph/9905221.

[268] D. Andriot and D. Tsimpis, "Laplacian spectrum on a nilmanifold, truncations and effective theories", JHEP **09**, 096 (2018), arXiv:1806.05156 [hep-th].

[269] D. Andriot, A. Cornell, A. Deandrea, F. Dogliotti, and D. Tsimpis, "A new mechanism for symmetry breaking from nilmanifolds", JHEP **05**, 122 (2020), arXiv:2002.11128 [hep-th].

[270] A. Deandrea, F. Dogliotti, and D. Tsimpis, "Gauge-Higgs models from nilmanifolds", Phys. Lett. B **829**, 137097 (2022), arXiv:2201.01151 [hep-ph].

[271] A. Deandrea, F. Dogliotti, and D. Tsimpis, "Dirac operator spectrum on a nilmanifold", Nucl. Phys. B **982**, 115895 (2022), arXiv:2202.11437 [hep-th].

[272] D. Andriot, "New supersymmetric vacua on solvmanifolds", JHEP **02**, 112 (2016), arXiv:1507.00014 [hep-th].

[273] C. Bock, "On low-dimensional solvmanifolds", Asian Journal of Mathematics **20**, 199 (2016), arXiv:0903.2926 [math.DG].

[274] M. Grana, R. Minasian, M. Petrini, and A. Tomasiello, "A Scan for new N=1 vacua on twisted tori", JHEP **05**, 031 (2007), arXiv:hep-th/0609124.

[275] D. Andriot, "String theory flux vacua on twisted tori and Generalized Complex Geometry", PhD thesis (Paris U., VI-VII, 2010).

[276] A. I. Malcev, "On a class of homogeneous spaces", Amer. Math. Soc. Translation **39** (1951).

[277] S. Thangavelu, "Harmonic analysis on heisenberg nilmanifolds", Revista de la Union Matematica Argentina **50**, 71 (2009).

[278] S. Mirshekari, N. Yunes, and C. M. Will, "Constraining generic lorentz violation and the speed of the graviton with gravitational waves", Phys. Rev. D **85**, 024041 (2012), arXiv:1110.2720 [gr-qc].

[279] E. Berti, "The First Sounds of Merging Black Holes", APS Physics **9**, 17 (2016), arXiv:1602.04476 [gr-qc].

[280] A. Ghosh et al., "Testing general relativity using golden black-hole binaries", Phys. Rev. D **94**, 021101 (2016), arXiv:1602.02453 [gr-qc].

[281] C. Cutler et al., "The last three minutes: issues in gravitational wave measurements of coalescing compact binaries", Phys. Rev. Lett. **70**, 2984 (1993), arXiv:astro-ph/9208005.

[282] LIGO Scientific Collaboration, *LIGO Algorithm Library - LALSuite*, free software (GPL), 2018.

[283] C. Rover, R. Meyer, and N. Christensen, "Coherent Bayesian inference on compact binary inspirals using a network of interferometric gravitational wave detectors", Phys. Rev. D **75**, 062004 (2007), arXiv:gr-qc/0609131.

[284] J. Veitch and A. Vecchio, "Bayesian coherent analysis of in-spiral gravitational wave signals with a detector network", Phys. Rev. D **81**, 062003 (2010), arXiv:0911.3820 [astro-ph.CO].

[285] D. M. Eardley, D. L. Lee, A. P. Lightman, R. V. Wagoner, and C. M. Will, "Gravitational-wave observations as a tool for testing relativistic gravity", Phys. Rev. Lett. **30**, 884 (1973).

[286] C. de Rham, J. T. Deskins, A. J. Tolley, and S.-Y. Zhou, "Graviton mass bounds", Rev. Mod. Phys. **89**, 025004 (2017), arXiv:1606.08462 [astro-ph.CO].

[287] N. K. Johnson-McDaniel, A. Ghosh, S. Ghonge, M. Saleem, N. V. Krishnendu, and J. A. Clark, "Investigating the relation between gravitational wave tests of general relativity", Phys. Rev. D **105**, 044020 (2022), arXiv:2109.06988 [gr-qc].

[288] R. Abbott et al. (LIGO Scientific, Virgo), "Open data from the first and second observing runs of Advanced LIGO and Advanced Virgo", SoftwareX **13**, 100658 (2021), arXiv:1912.11716 [gr-qc].

[289] J. Veitch, W. D. Pozzo, A. Lyttle, M. J. Williams, C. Talbot, M. Pitkin, G. Ashton, Cody, M. Hübner, A. Nitz, D. Mihaylov, D. Macleod, G. Carullo, G. Davies, and ttw, *Johnveitch/cpnest: v0.11.4*, version v0.11.4, Apr. 2022.

[290] R. A. Konoplya and A. Zhidenko, "Asymptotic tails of massive gravitons in light of pulsar timing array observations", Phys. Lett. B **853**, 138685 (2024), arXiv:2307.01110 [gr-qc].

[291] P. S. Laplace, *A philosophical essay on probabilities* (J. Wiley & Sons New York, New York, 1902).

[292] K. Timpe, M. Griffith, and N. Levy, editors, *Routledge companion to free will* (Routledge, New York, 2017).

[293] M. Dafermos, "The Interior of charged black holes and the problem of uniqueness in general relativity", Commun. Pure Appl. Math. **58**, 0445 (2005), arXiv:gr-qc/0307013.

[294] C. Smeenk and C. Wuthrich, "Determinism and general relativity", Phil. Sci. **88**, 638 (2021), arXiv:2009.07555 [physics.hist-ph].

[295] L. C. Evans, *Partial differential equations* (American Mathematical Society, Rhode Island, 2022).

[296] B. Carter, "Black holes equilibrium states", in Les Houches Summer School of Theoretical Physics: Black Holes (1973), pages 57–214.

[297] H. Nariai, "On some static solutions of Einstein's gravitational field equations in a spherically symmetric case", Sci. Rep. Tohoku Univ. Eighth Ser. **34**, 160 (1950).

[298] H. Nariai, "On a new cosmological solution of Einstein's field equations of gravitation", Sci. Rep. Tohoku Univ. Eighth Ser. **35**, 46 (1951).

[299] V. Cardoso and J. P. S. Lemos, "Quasinormal modes of the near extremal Schwarzschild-de Sitter black hole", Phys. Rev. D **67**, 084020 (2003), arXiv:gr-qc/0301078.

[300] V. Cardoso, O. J. C. Dias, and J. P. S. Lemos, "Nariai, Bertotti-Robinson and anti-Nariai solutions in higher dimensions", Phys. Rev. D **70**, 024002 (2004), arXiv:hep-th/0401192.

[301] M. Casals, S. R. Dolan, A. C. Ottewill, and B. Wardell, "Self-force calculations with matched expansions and quasinormal mode sums", Phys. Rev. D **79**, 124043 (2009), arXiv:0903.0395 [gr-qc].

[302] P. H. Ginsparg and M. J. Perry, "Semiclassical perdurance of de sitter space", Nucl. Phys. B **222**, 245 (1983).

[303] S. W. Hawking and S. F. Ross, "Duality between electric and magnetic black holes", Phys. Rev. D **52**, 5865 (1995), arXiv:hep-th/9504019.

[304] B. Bertotti, "Uniform electromagnetic field in the theory of general relativity", Phys. Rev. **116**, 1331 (1959).

[305] I. Robinson, "A solution of the maxwell-einstein equations", Bull. Acad. Pol. Sci. Ser. Sci. Math. Astron. Phys. **7**, 351 (1959).